Investigations of the structural dynamics of the water and proton channels in Photosystem II

Dissertation

zur Erlangung des akademischen Grades

Doctor rerum naturalium

(Dr. rer. nat.)

im Fach Biophysik
eingereicht an der Lebenswissenschaftlichen Fakultät
der Humboldt-Universität zu Berlin

von M.Sc. **Rana Emadeldin Hussein Ali**

Präsident (komm.) der Humboldt-Universität zu Berlin

Prof. Dr. Peter Frensch

Dekan der Lebenswissenschaftlichen Fakultät

Prof. Dr. rer. nat. Dr. rer. agr. Christian Ulrichs

Gutachter/innen: 1. Prof. Dr. Athina Zouni

2. Prof. Dr. Thomas Friedrich

3. Dr. rer. nat. Heiko Lokstein

Tag der mündlichen Prüfung: 15.03.2022

Zusammenfassung

Bei der lichtinduzierten Oxidation von Wasser im Photosystem II (PSII) werden zwei Substratwassermoleküle im katalytischen Zyklus des aktiven Metallclusters (Mn_4CaO_5) benötigt, eines während des $S_2 \rightarrow S_3$ Übergangs und ein zweites während des $S_3 \rightarrow S_0$ Übergangs. Bei dieser Reaktion werden vier Protonen aus dem Cluster in einer typischen Stöchiometrie von 1:0:1:2 entsprechend den S-Zustandsübergängen $S_0 \rightarrow S_1 \rightarrow S_2 \rightarrow S_3 \rightarrow S_0$ in den Lumen des PSII abgegeben. Daher ist es für das Verständnis des Mechanismus´ der Wasseroxidation von entscheidender Bedeutung, die Veränderung der Protonierungszustände am Mn_4CaO_5-Cluster einschließlich der umgebenden Proteinseitenketten während der Katalyse zu untersuchen. Hierbei sollten sowohl die Wasserkanäle für die Zuführung der Substratwassermoleküle als auch die Transportwege für die Freisetzung der Protonen untersucht werden. Eine mögliche Methode zur Bestimmung der Protonierungszustände von Substratwassermolekülen und Aminosäureseitenketten ist die Neutronenbeugung. Deshalb wurde in meiner ersten Veröffentlichung ein neues Protokoll entwickelt, um einzelne große Kristalle von PSII-Dimeren (dPSII) mit einer Länge von ~3 mm in der Längsachse zu züchten. Diese in D_2O-haltigem Puffer inkubierten Kristalle wurden am MaNDi-Instrument an der Spallationsneutronenquelle des Oak Ridge National Laboratory (ORNL, USA) mit einer Auflösung von ca. 8 Å gemessen. Um eine höhere Auflösung zu erzielen, ist die Verbesserung der Kristallqualität essenziell. Daher wurde in meiner zweiten Veröffentlichung die Struktur des Detergens-Protein-Komplexes von dPSII mit n-Dodecyl-ß-D-Maltosid (βDM), βDM -dPSII, durch Anwendung von Kleinwinkel-Neutronenstreuung (SANS) mit einem Kontrast von 5% D_2O und 75% D_2O in Kombination mit Kleinwinkel-Röntgenstreuung (SAXS) untersucht. Die Ergebnisse zeigten, dass βDM eine monomolekulare Schicht um dPSII bildet. Darüber hinaus konnten durch die SAXS-Daten freie Mizellen von βDM in der Lösung nachgewiesen werden, die während der Kristallisation einen negativen Einfluss auf das Wachstum der Kristalle und damit auf die Beugungsqualität haben. Damit ist eine weitere Optimierung der βDM-Konzentration in der Proteinlösung erforderlich, um die Bildung von freien Mizellen zu minimieren. In meiner dritten Veröffentlichung wurde die strukturelle Dynamik in den Wasserkanälen, die den Mn_4CaO_5 Cluster mit dem Lumen verbinden, während des $S_2 \rightarrow S_3$-Übergangs mit Hilfe der Seriellen Femtosekunden Röntgenkristallographie untersucht. Ein Datensatz mit einer hohen Auflösung von 1,89

Å wurde durch die Zusammenführung von Daten gewonnen, die bei Raumtemperatur während des gesamten katalytischen Zyklus gesammelt wurden. In Anbetracht der Analyse der zusammengeführten Daten und der einzelnen Zeitpunkte, die während des $S_2 \rightarrow S_3$ Übergangs gesammelt wurden, ist es wahrscheinlich, dass ein Substratwasser in die offene Koordinationsstelle des Mn1-Ions am Mn_4CaO_5-Cluster durch den O1-Kanal geliefert wird. Im Gegensatz dazu wird ein Proton aus dem Cluster durch den Cl1-A-Transportweg in Richtung Lumen freigesetzt. Die strukturelle Beobachtung legt nahe, dass die Protonenfreisetzung durch eine Protonenschranke reguliert wird, die aus den Aminosäuren D1-E65, D2-E312 und D1-R334 gebildet wird.

Abstract

The light-induced oxidation of water in Photosystem II (PSII) requires incorporating two water molecules in the catalytic cycle of the active metal cluster (Mn_4CaO_5), one during the $S_2 \rightarrow S_3$ transition and a second during the $S_3 \rightarrow S_0$ transition. Furthermore, four protons are released towards the bulk from the cluster in a typical stoichiometry of 1:0:1:2 corresponding to S-state transitions $S_0 \rightarrow S_1 \rightarrow S_2 \rightarrow S_3 \rightarrow S_0$, respectively. Therefore, tracking the change of protonation states at the active catalytic site and the surrounding protein side chains during catalysis and elucidating the pathways of water substrate insertion and proton release are crucial to understanding the water oxidation mechanism. A possible way to assess the protonation states of the ligand waters and side chains in the vicinity of the cluster is by using neutron diffraction. Therefore, in the first study of my work, a new protocol was developed to grow single large dPSIIcc crystals with a length of ~3 mm in the long axis. These crystals, soaked in D_2O containing buffer, diffracted to about 8 Å resolution at the MaNDi instrument at the Spallation Neutron Source at Oak Ridge National Laboratory (ORNL, USA). Improving the crystal quality is crucial for achieving a better resolution. Consequently, in the second study of my work, the structure of the detergent-protein complex of βDM-dPSIIcc has been investigated by applying small-angle neutron scattering (SANS) with a contrast of 5% D_2O and 75% D_2O in combination with small-angle X-ray scattering (SAXS). The results showed that βDM is forming a monomolecular layer around the dimeric PSII core complex (dPSIIcc). Moreover, the SAXS data detected a peak assigned to the free micelles of βDM. The presence of these aggregates during crystallization probably has a negative effect on the growth of the crystals and thus on the diffraction quality. These results raise the necessity to optimize the βDM concentration in the protein solution to avoid the possible excess of free micelles. In the third study of my work, the structural dynamics in the water channels connecting the cluster to the lumen during the $S_2 \rightarrow S_3$ transition were investigated using serial femtosecond XFEL. A high-resolution data set was obtained at a resolution of 1.89 Å by combining data collected at RT throughout the catalytic cycle. Considering the analysis of the combined data and the individual time points collected during the $S_2 \rightarrow S_3$ transition, it is likely that the substrate water insertion into the open coordination site of the Mn1 ion is delivered through the O1 channel. In contrast, a proton from the cluster is released towards the bulk through the Cl1 A channel. The structural observation suggests

that the proton release is regulated by a proton gate formed by D1-E65, D2-E312, and D1-R334.

Table of Contents

List of Abbreviations

ACF	Autocorrelation Function
ADP	Adenosine diphosphate
ATP	Adenosine triphosphate
$C_{12}E_8$	Octaethyleneglycolmonododecylether
Chl *a*	Chlorophyll *a*
Chl *b*	Chlorophyll *b*
CMC	Critical micelle concentration
CP	Chlorophyll binding protein
cryo-EM	cryogenic electron microscopy
CSC	Critical solubilization concentration
cyt	cytochrome
2,5 DCPQ	2,5-dichloro-p-benzoquinone
DEAE	Diethylaminoethyl
DLS	Dynamic light scattering
DPC	Detergent-protein complex
dPSIIcc	dimeric Photosystem II core complex
ENDOR	Electron Nuclear Double Resonance
EPR	Electron paramagnetic resonance
ET	Electron transfer
EXAFS	Extended X-ray Absorption Fine Structure
Fd	Ferredoxin
FID	Free interface diffusion
FIOP	Flash-induced oxygen evolution pattern
fm	femtometre
FNR	Ferredoxin-NADP-oxidoreductase
fs	femtosecond
FTIR	Fourier transform infrared spectroscopy
GOE	Great oxygen event
iF (i =0, 1, 2 or 3)	Flashes
kDa	kilodalton
LBHB	Low barrier H-bond
LCLS	Linac Coherent Light Source
LHC	Light harvesting complex

MaNDi	Macromolecular Neutron Diffractometer
MES	2-(N-morpholino)ethanesulfonic acid
MFX	Macromolecular femtosecond crystallography
MGy	Milligray
mPSIIcc	monomeric Photosystem II core complex
NADPH	Nicotinamide adenine dinucleotide phosphate
NMR	Nuclear Magnetic Resonance
OEC	Oxygen evolving complex
ORNL	Oak Ridge National Laboratory
PBS	phycobilisome
PC	plastocyanin
PCET	proton coupled electron transfer
PDB	protein data bank
PEG	Polyethylene glycol
Pheo	pheophytin
PhQ	phylloquinone
Pi	inorganic phosphate
PIPES-NaOH	1,4-piperazinediethanesulfonic acid
PQ	plastoquinone
PQH_2	plastoquinol
PS	Photosystem
ps	pico second
PsbA-Z	protein encoded by the corresponding PSII gene psbA-Z
PT	Proton transfer
Q_A	primary quinone electron acceptor
Q_B	secondary quinone electron acceptor
RC	reaction center
R_g	radius of gyration
R_H	hydrodynamic radius
RI	refractive index
ROS	Reactive Oxygen Species
RT	room temperature
S/N	signal-to-noise ratio
SANS	Small-angle Neutron scattering

SAXS	Small-angle X-ray scattering
SFX	Serial femtosecond Crystallography
Si	oxidation state of the OEC with (i=0–4)
SLAC	Stanford Linear Accelerator Center
SNS	Spallation Neutron Source
SR	Synchrotron Radiation
TOF	Time-of-flight
TR	Time-resolved
Tyr	tyrosine residue
UQ	ubiquinone
XAS	X-ray Absorption Spectroscopy
XES	X-ray Emission Spectroscopy
XFEL	X-ray Free Electron Laser
XRD	X-ray diffraction
Y_D	D2-tyrosine residue 160
Yz	D1-tyrosine residue 161
βDM	n-Dodecyl-β-D-maltoside
$\Delta G_{n.}$	Gibbs free energy

I. Introduction

I.1. **Photosynthesis**

More than 2.4 billion years ago, a significant transformation in our planet was triggered by the great oxidation event (GOE), resulting in rising the atmospheric oxygen on Earth[1]. Before that, there was almost no oxygen in the atmosphere, and the organisms on Earth were mainly anaerobic, utilizing the reducing compounds as a source of energy. It has been suggested that cyanobacteria were the leading player in this significant transformation by getting evolved, since 3.5 billion years ago[2], a light-driven enzyme capable of oxidizing the water into molecular oxygen and protons. This reaction was coupled with its capability to fix the carbon dioxide to carbohydrates. This whole process is called Photosynthesis. Over billions of years, the released dioxygen accumulated in our atmosphere encourages other aerobic life forms (Figure 1). Besides, it led to the formation of the ozone layer in the Stratosphere by absorbing UV-C radiation. The Stratospheric ozone layer provides us with efficient protection against UV radiation. In addition, Photosynthesis supplies us with our food and energy[3-5].

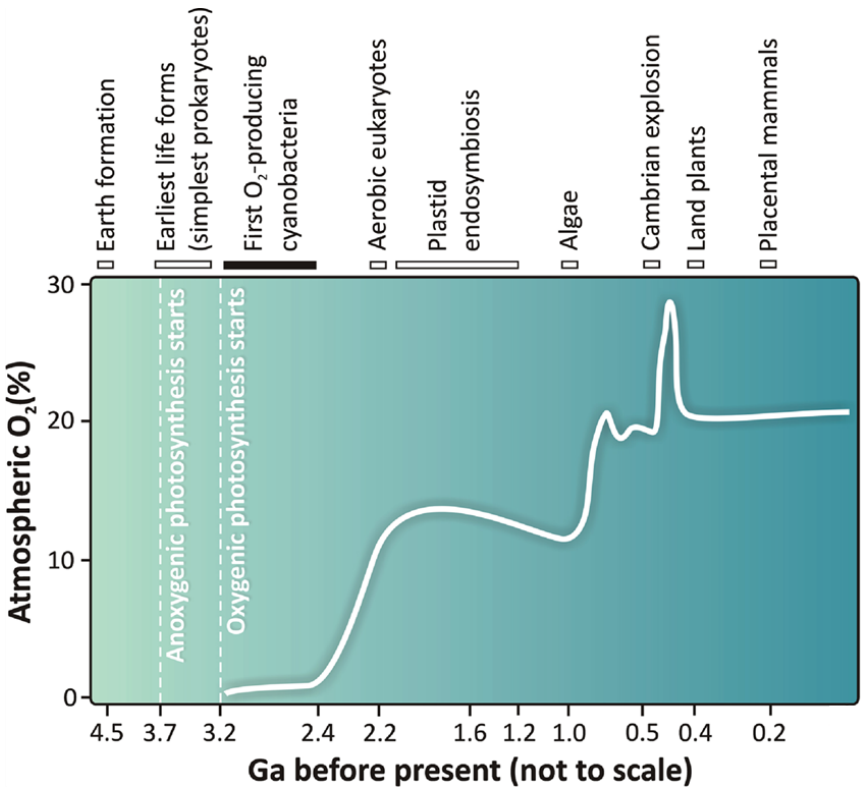

Figure 1 A scheme shows the relation between atmospheric oxygen accumulation and the major evolutionary events on our planet as a function of geological time (billion of years, Ga). *The figure is adapted from*[6].

The photosynthesis process is triggered by absorbing solar energy in a wavelength ranging from 300 nm to 700nm[7]. Capturing solar energy is done through antennas of light-harvesting protein, which can efficiently harvest sunlight. Several intrinsic pigments support cyanobacteria, including chlorophyll *a* (Chl *a*) that is considered the primary light-absorbing pigment, the carotenoids like β-carotene, zeaxanthin, and Lutein, besides the extrinsic light-harvesting proteins, the water-soluble phycobiliproteins[8, 9] (Figure 2 and Figure 3B). Chl *a* is a cyclic tetrapyrrole chelated in its center a magnesium ion[10] (Figure 2). On the other hand, the phycobiliproteins are open-chain tetrapyrroles that are covalently attached by colorless linker proteins to form the phycobilisomes PBSs[11] (Figure 2). The structure of PBSs showed that they formed mainly from a central core connected to six or eight peripheral rods (Figure 3B). The core domain could consist of either 2 or 3 or 5 cylinders. Each cylinder consists mainly of stacked phycobiliprotein and allophycocyanin (APC). The composition of the peripheral rods varies among different organisms. However, it typically consists of phycocyanin (PC)[11] (Figure 3). In cyanobacteria, β-carotene, Zeaxanthin, and Lutein are the major form of carotenoids. They are lipid-soluble, consisting of a linear C40 chain of isoprenoid compounds (Figure 2). In addition to their function as light-harvesting pigments, they also play a crucial role in protecting the organism from photo-oxidative damage[12, 13]. By primary endosymbiosis,

the photosynthesis has transferred from cyanobacteria to all the photosynthetic eukaryotes. From there, glaucophytes, rhodophytes (red line), green algae, and plants (green line) had evolved, and the cyanobacterial ancestor became the chloroplast. The light-harvesting antennas in these organisms have also developed (Figure 3A). The red line and the green line gain intrinsic antenna of light-harvesting complex (LHC). In the rhodophyte algae (red line), the solar light is harvested through the extrinsic antenna PBSs, in addition to the intrinsic antenna of light-harvesting complex (LHC), non-covalently bind to the Chl *a*. Whereas, the green algae and plants (green lines) have an only intrinsic antenna of light-harvesting complex (LHC) and have lost the extrinsic ones entirely. Their intrinsic light-harvesting complex (LHC) binds non-covalently to the Chl *a* as well as another variant of pigment molecule, Chl *b*[14, 15].

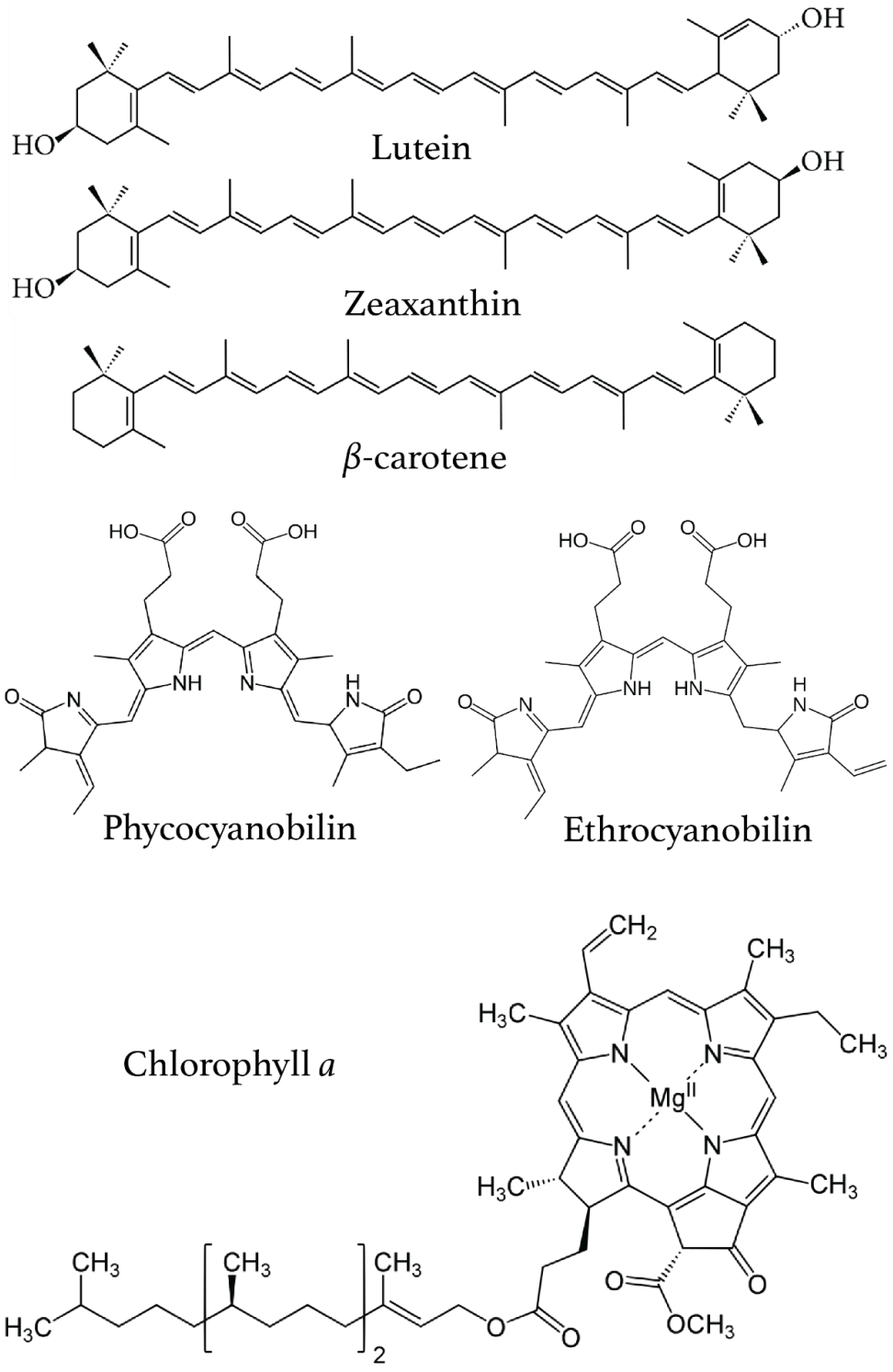

Figure 2 Chemical structure of photosynthetic pigments.

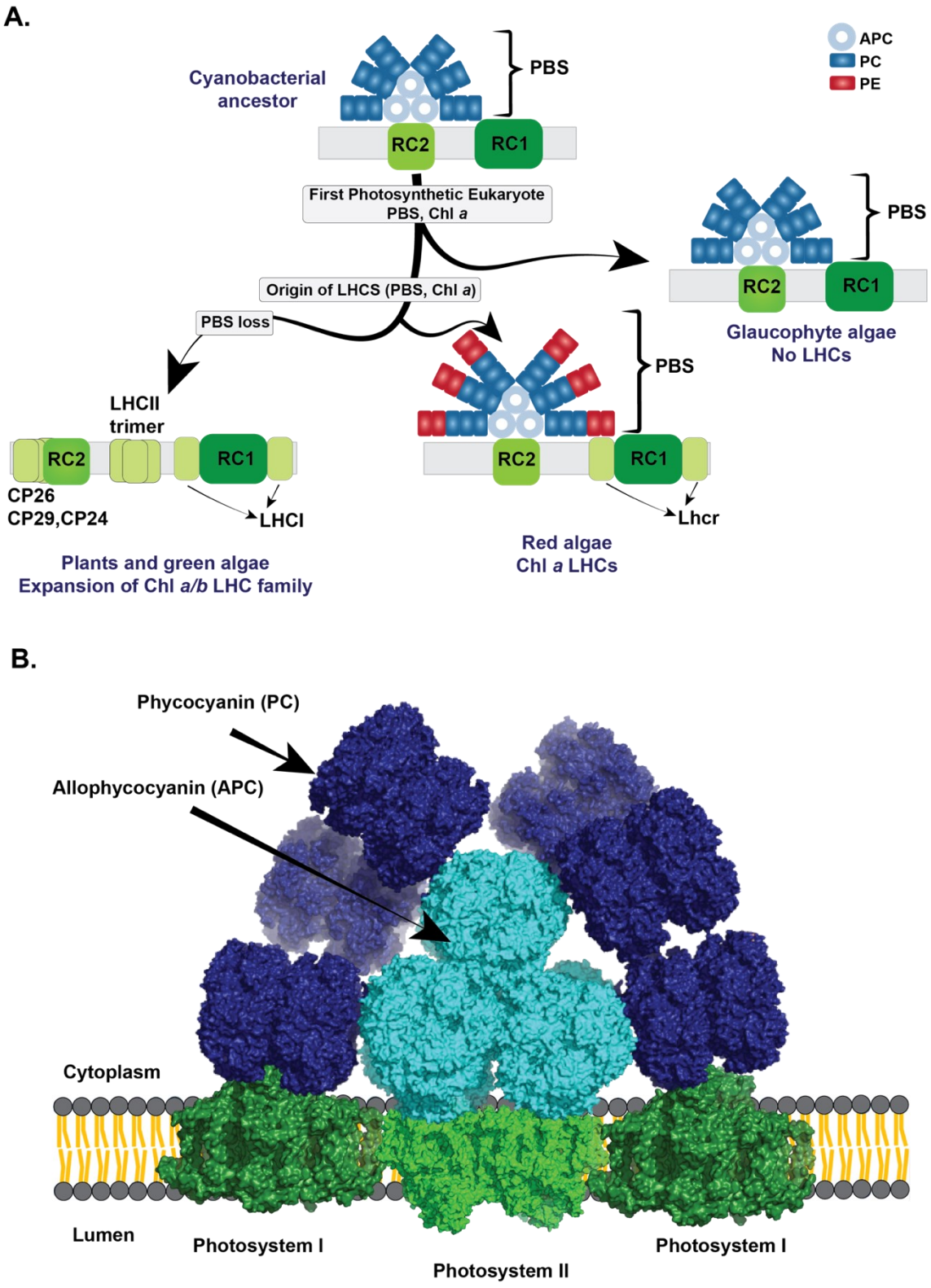

Figure 3 A. Schematic overview of the evolution of Light-harvesting antennas in cyanobacteria, algae, and plants. *In cyanobacteria, the photosynthetic core complexes are supported by the phycobilisomes (PBSs) as the light-harvesting antenna. Later, the first photosynthetic eukaryote got evolved into the glaucophyte, rhodophyte algae (red algae), green algae, and plants. The glaucophyte algae and rhodophyte algae are supported with PBSs similar to cyanobacteria. However, In rhodophyte algae, RC1 is supported with intrinsic light-harvesting complex (LHC), binding Chl a. Green algae and Plants have wholly lost the PBSs, and gained another pigment molecule Chl b. Both reaction centers in green algae and plants depend only on the intrinsic light-harvesting complex (LHC), binding Chl a/b*[15]*. Abbreviations of PBS: phycobilisome, APC: allophycocyanin, PC: phycocyanin, PE: phycoerythrin, RC1: reaction center type I referred to Photosystem I core complex, RC1: reaction center type II referred to Photosystem II core*

*complex, LHC: light-harvesting complex Figure adapted from[14]. **B. Phycobilisome megastructure model in cyanobacteria.** The model shows the arrangement on the top of PSI and PSII complexes in cyanobacteria. The Phycobilisome structure is based on the recent cryo-EM structure of the PBS from Synechococcus 7002 (PDB ID 7EXT)[16].*

Each of these pigments can absorb a specific wavelength range. Chl *a* maxima light absorption is at around 430 nm and 670 nm (Figure 4). The phycobiliprotein can absorb the light efficiently in the wavelengths ranging from 490 nm to 650 nm and act as a complementary to fill the green cap to Chl *a*[17, 18] (Figure 4A). β-carotene has a maxima light absorption at 425, 449, and 476 nm[12] (Figure 4). The phycobiliprotein pigments efficiently transfer the absorbed energy to the primary electron donor in the photochemical reaction center (RC) (Figure 4B). Together, these pigments with other pigments like Chl *a* and β-carotene result in almost harvesting the entire range of visible light (Figure 4A).

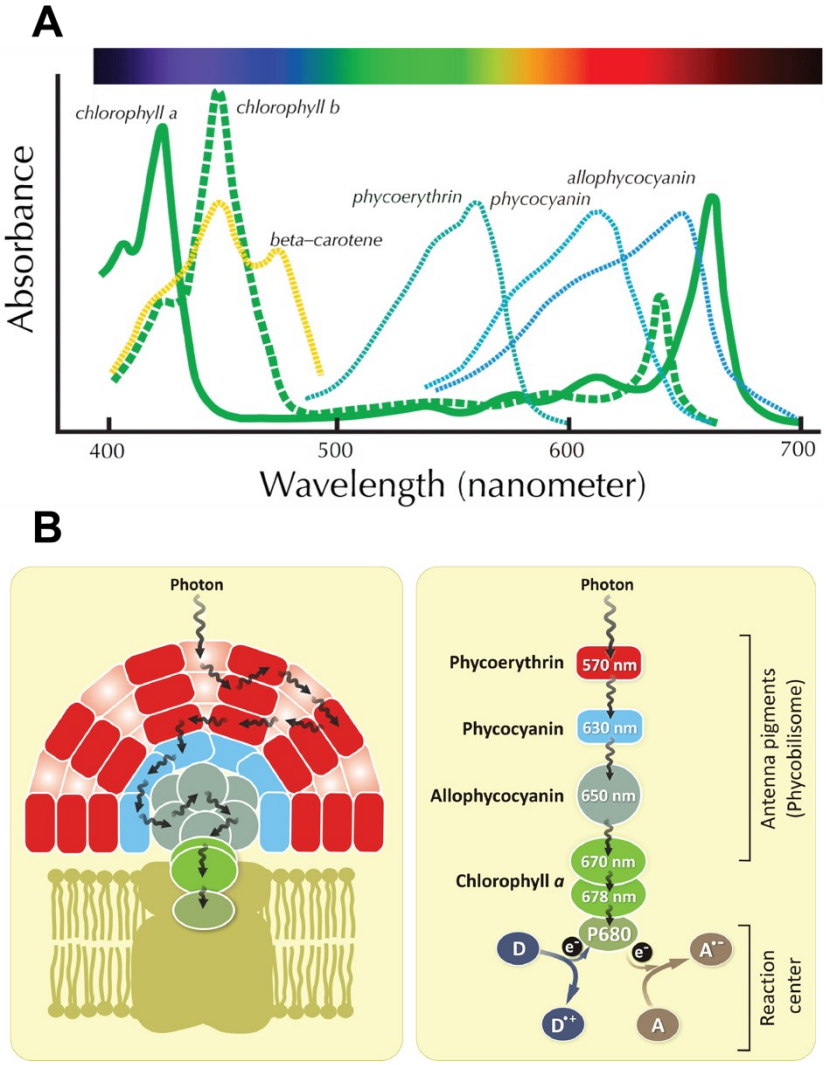

***Figure 4 A. Absorption spectra of most of the photosynthetic pigments.** The figure is modified and adapted from[19]. **B. Steps of Energy transfer from light-harvesting antennas to primary electron donor to achieve charge separation in red algae and cyanobacteria.** Abbreviations **:**D refers to the electron donor, and A refers to the electron acceptor. The figure is taken from The figure is taken from[6].*

Upon exposure to sunlight, charge separation occurs in the photo-activated Reaction Center (RC). One electron transfers from the primary donor to the primary electron acceptor and finally to the terminal electron acceptor. Based on the RC's terminal electron acceptor's chemical nature, the photosynthetic RC is classified into two types; the iron-sulfur type (RC type I) and the quinone type (RC type II) (Figure 5). Type I RCs, which reduces the iron-sulfur cluster as their terminal electron acceptor, is represented in green sulfur bacteria, heliobacteria, and photosystem I (PSI) as in cyanobacteria and plants. On the other hand, type II RCs, which reduces the pheophytin as their primary electron acceptor and quinones as their terminal electron acceptor, is represented in purple bacteria, green filamentous bacteria, and photosystem II. Some bacteria like green sulfur bacteria and heliobacteria are capable of performing anoxygenic Photosynthesis. They can only oxidize H_2S or other small organic molecules (i.e., acetate, succinate and propionate)[20] to get the required electrons to obtain the energy-rich compounds NADPH and ATP needed to fix the CO_2. Thus, they contain only one type of RCs[12, 21].

$$12\ H_2S + 6\ CO_2 \xrightarrow{\text{light}} 12\ S + C_6H_{12}O_6 + 6\ H_2O \quad (1)$$

While organisms performing oxygenic Photosynthesis like cyanobacteria, algae, and higher plants, can oxidize the water molecules to act as a leading source of electrons. For this reason, they are supported by both types of RCs[12]. Evolutionary, the RC tandem system of RC I and II developed in the more complex assembled proteins connected in series to protect the different systems. For example, in oxygenic photosynthesis, the dioxygen released during water splitting in RC II does not directly contact RC I of PSI, protecting the Fe-S centers there from getting oxidized upon direct contact with O_2. However, the redox-catalysis of the water oxidation process in the catalytic site of PSII to form O_2 leads to Reactive Oxygen Species (ROS) formation, resulting in protein damage[22].

$$12\ H_2O + 6\ CO_2 \xrightarrow{\text{light}} 6\ O_2 + C_6H_{12}O_6 + 6\ H_2O \quad [23] \quad (2)$$

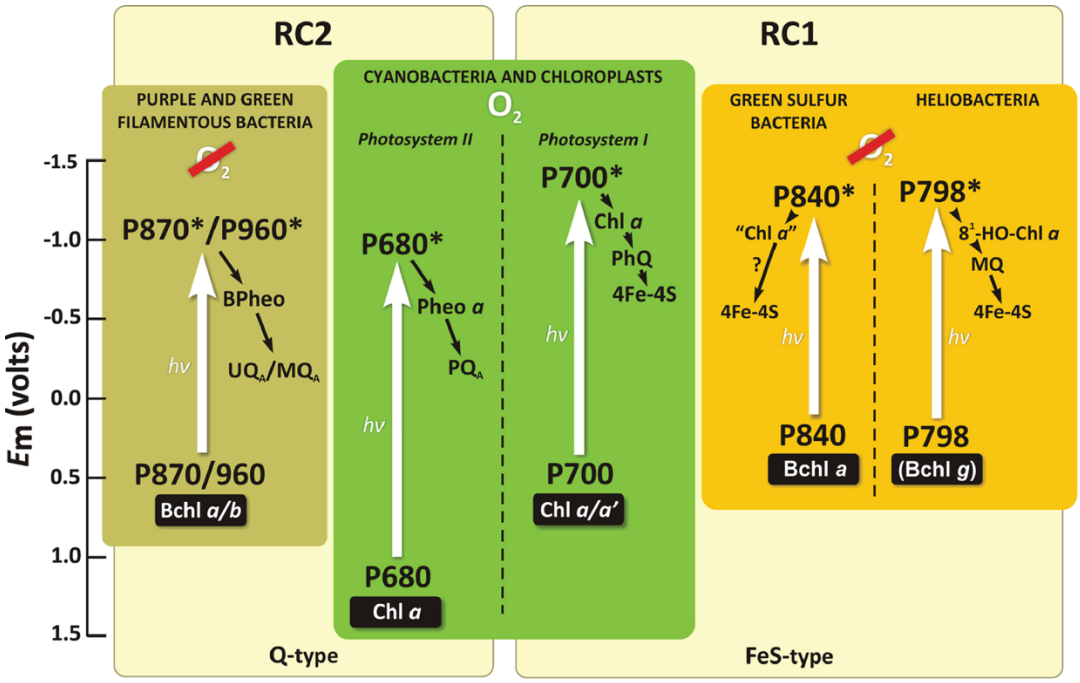

Figure 5 Scheme shows the classification and the Reaction center (RC) types in different photosynthetic organisms. *The primary donors of each RC are shown as (P), and the written number after (P) represents the wavelength (in nm) at which the maximum absorption occurs. In addition to the primary donor (P), the primary and the secondary electron acceptors are shown. Upon light absorption (hv), excitation of the primary electron donor takes place, and it is represented by the white arrows. Black arrows indicate the electron transfer from the excited electron donor to the electron acceptors. Abbreviations of BChl: bacteriochlorophyll, BPheo: bacteriopheophytin, Chl: Chlorophyll, Fe–S-type: iron-sulfur type of RC, Q-type: pheophytin–quinone type of RC, MQ: menaquinone, PhQ: phylloquinone, PQ: plastoquinone, and UQ: ubiquinone. The figure is taken from*[6].

I.2. **The oxygenic Photosynthesis**

The oxygenic Photosynthesis in cyanobacteria, which extended to algae and higher plants, is driven by several multisubunit-membrane-protein complexes embedded in the thylakoid membrane, photosystem II (PSII), and photosystem I (PSI), cytochrome *b6f (*cyt *b6f)*, and the ATP-synthase[24-28] (Figure 6). In addition, several soluble proteins, which are present either in the lumen side or stroma (higher plants)/cytoplasm, act as electron carriers; i.e., cytochrome *c6* (cyt *c6*) and plastocyanin (PC) that are located in the lumen, ferredoxin (Fd), and ferredoxin-$NADP^+$ reductase (FNR) that are situated in the stroma (higher plants)/the cytoplasm.

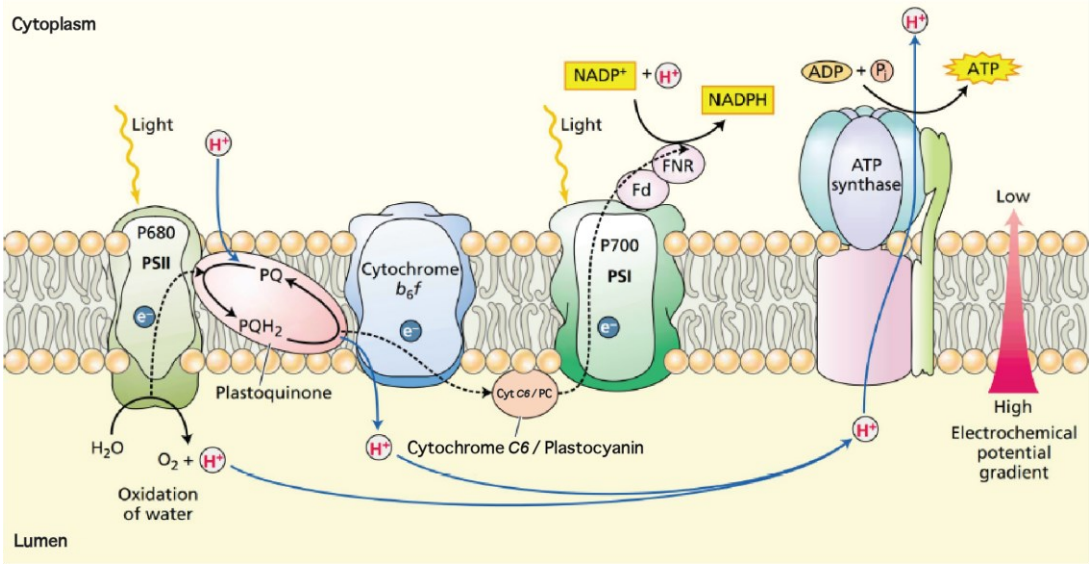

Figure 6 Schematic representation of the thylakoid membrane. *Schematic illustration shows the photosynthetic proteins embedded in the thylakoid membrane and the soluble electron transporters. Black arrows represent the pathways of electrons and the blue ones of protons. The figure is modified from*[29].

The electron transport (ET) reaction is initiated by absorption of light by the photosynthetic pigments of PSII and PSI, resulting in activating photosystem II to catalyze water oxidation, plastoquinone reduction, and releasing protons to the lumen side in addition to molecular oxygen that we breathe[30]. Once plastoquinone gets reduced to plastoquinone (Q_B^{-2}), it accepts two protons from the stroma (higher plants)/the cytoplasm and becomes plastoquinol (PQH_2) (3) Figure 7.

$$2\,H_2O + 2\,PQ + 4\,H^+_{\text{stroma/cytoplasm}} \xrightarrow{\text{light}} O_2 + 4\,H^+_{\text{lumen}} + 2\,PQH_2 \quad (3)$$

PQH_2 then diffuses in the membrane layer to bind to the Cyt *b6f* complex to get oxidized and deprotonated[31]. As a result, the protons are released towards the lumen. One of the electrons is transferred to the cyt *f* to initiate ET to plastocyanin (PC) which acts as an electron carrier between cytochrome *b6f* and PSI (4). The other electron is transferred to cyt *b6* to reduce plastoquinone (PQ) and produce PQH_2 in a Q cycle process to accumulate more protons in the lumen side[32].

$$PQH_2 + 2\,PC_{ox} + 2\,H^+_{\text{stroma/cytoplasm}} \longrightarrow PQ + 2\,PC_{red} + 4\,H^+_{\text{lumen}} \quad (4)$$

Photosystem I catalyze the reduced PC's oxidation and the reduction of ferredoxin (Fd)[33-35], which in turn reduces Ferredoxin-$NADP^+$-reductase (FNR) and generates NADPH. The reaction can be summarized in (5) and (6).

$$PC_{red} + Fd_{ox} \xrightarrow{light} PC_{ox} + Fd_{red}$$

(5)

$$4\ Fd_{red} + 2\ H^{+}_{stroma/cytoplasm} + 2\ NADP^{+} \xrightarrow{FNR} 4\ Fd_{ox} + 2\ NADPH$$

(6)

The ET generates potential across the thylakoid membrane, which drives the ATPase to pass the accumulated protons in the lumen side through it and synthesis ATP (adenosine triphosphate) from ADP (adenosine diphosphate) and Pi (inorganic phosphate) (7)[34, 36]. The illustration of the ET chain is shown in a Z-scheme (Figure 8).

$$2H_2O + 2NADP^{+} + 3ADP + 3Pi \xrightarrow{light} O_2 + 2NADPH + 3ATP + 2H^{+}$$

(7)

The generated NADPH and ATP provide the energy required for CO_2 fixation to generate the carbohydrates (8) in a process known as dark (light-independent) reactions or Calvin-Benson cycle[37, 38].

$$CO_2 + 2\ NADPH + 3\ ATP + 2\ H^{+} \rightarrow [CH_2O] + 2\ NADP^{+} + 3\ ADP + 3\ Pi + H_2O$$

(8)

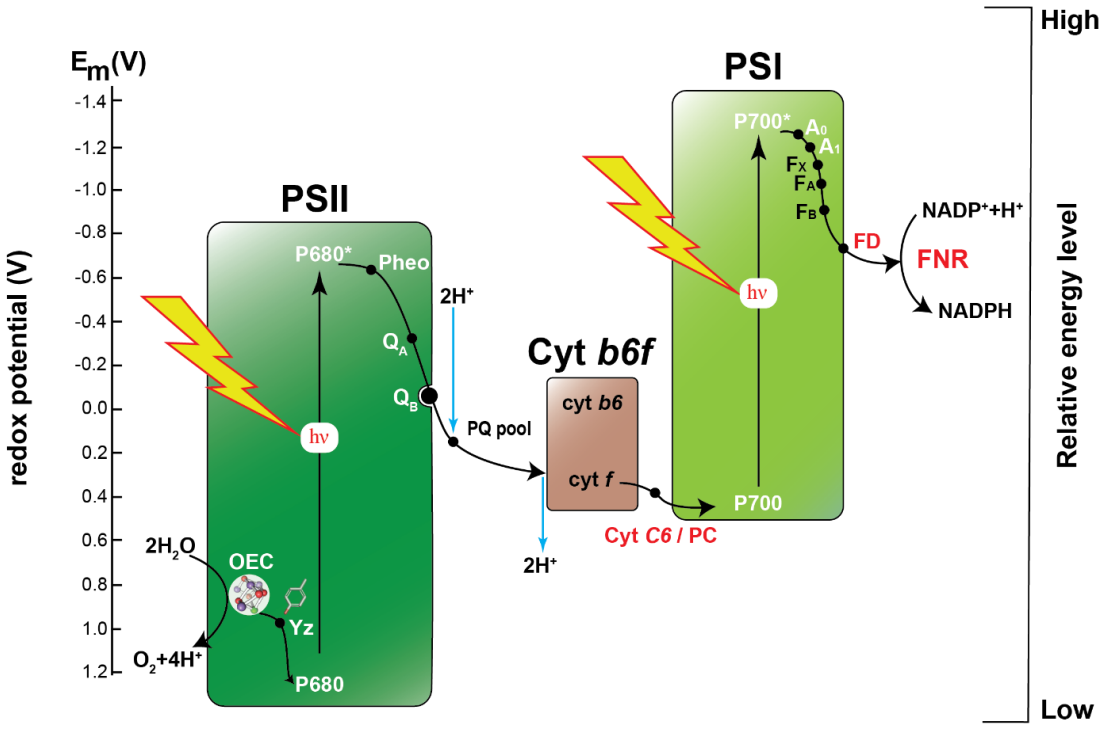

Figure 7 Z-Scheme shows the energy diagram of the light reaction by Photosynthesis. *The electron transfer pathway through the photosynthetic proteins starting from the water to FNR is represented by the black arrows. Photosynthetic membrane proteins are written in black, and soluble proteins are in red. OEC: oxygen-evolving complex, Yz: D1-tyrosine residue 161, P680: Primary electron donor in the RC of PSII, Pheo: pheophytin, Q: quinone molecule, Cyt: cytochrome, PC: plastocyanin, P700: reaction center Chl a of PSI, A_o: modified chlorophyll molecules and A_1: quinone acceptor, both A_o and A_1 are considered the early electron acceptors of PSI, (Fe_X, Fe_A, and Fe_B): bound iron-sulfur complex to PSI, Fd: soluble ferredoxin, FNR: ferredoxin NADP reductase.*

I.3. **Photosystem II**

Photosystem II (PSII) is a natural membrane protein complex in cyanobacteria, algae, and higher plants, capable of light-harvesting to drive water oxidization resulting in converting the light energy into chemical energy and releasing molecular oxygen (9).

$$2\,H_2O \xrightarrow{\text{light}} O_2 + 4\,H^+_{\text{lumen}} + 4\,e^- \quad (9)$$

Elucidating the crystal structure of PSII paves the way for our understanding of the molecular mechanism of PSII. The first crystal structure of the dimeric form of PSII core complex (dPSIIcc) from thermophilic cyanobacteria (*Thermosynechococcus elongatus*) was reported by Zouni et al. 2001[39] at 3.8 Å resolution. Several improvements had been achieved afterward[40-43] by applying conventional X-ray crystallography. In 2011, Umena and his co-workers made a leap in the crystal resolution of the dPSIIcc from *Thermosynechococcus vulcanus*, 1.9 Å. This data was the first data to provide atomic structural information of the catalytic center of PSII. However, the crystal structure was missing one subunit of the protein complex. The work of Hellmich et al. in 2014[44] reported the first native-like structure of dPSII retaining all the PSIIcc subunits at a resolution of 2.44 Å. The best resolution reported for dPSIIcc till now using conventional X-ray crystallography at cryogenic conditions is provided at a resolution of 1.85 Å by Tanaka and his co-workers[45]. Recently, applying X-ray free-electron laser radiation (XFEL) opened the doors to collecting radiation damage-free data at cryogenic and room temperatures[46-52].

I.3.1. The Protein subunits

The fully functional and highly purified PSII core complex (PSIIcc) from cyanobacteria showed that it is a homodimeric protein and consists of 20 protein subunits and several co-factors, including 35 molecules of chlorophyll *a*, 11 beta-carotenes, two plastoquinones, two pheophytins, two heme irons, one non-heme iron, two chloride ions, one bicarbonate ion, Mn_4CaO_5 cluster (Mn cluster), and more than 20 lipid molecules per monomer (Figure 8), in addition to the detergent belt. It is localized in the thylakoid membrane, having 17 intrinsic transmembrane subunits (D1, D2, CP43, CP47, PsbE, PsbF, PsbH, PsbI, PsbJ, PsbK, PsbL, PsbM, PsbT, PsbX, PsbY, PsbZ, and ycf12) and three extrinsic subunits (PsbU, PsbV, and PsbO) with total molecular weight around 350 kDa per monomer[53] Several transmembrane protein subunits, including D1, D2, CP43,

CP47, PsbE, PsbF, and PsbI, showed high similarity and are being conserved in algae and higher plants. However, the extrinsic subunits showed significant differences among the oxygenic photosynthesis organisms. In cyanobacteria, the extrinsic subunits are PsbU (12 kDa), PsbV(17 kDa), and PsbO (33 kDa), while in algae and higher plants, the extrinsic subunits are PsbP (23 kDa), PsbQ (16 kDa), and PsbO instead[1, 54] (Figure 9).

The structural analysis of the dimeric PSIIcc (dPSIIcc) showed that each monomer is interacting through two symmetry-related subunits PsbM and PsbM', which represent the *C2* rotation axis perpendicular to the membrane plane (Figure 8B). The seventeen intrinsic transmembrane subunits are embedded in the lipid bilayer of the thylakoid membrane. However, the three extrinsic subunits are anchored on the luminal side. The reaction center RC core of the PSII is built up mainly from the intrinsic subunits D1 (PsbA), D2 (PsbD)), and cytochrome *b*-559 (encoded by the *psbE* and *psbF* genes) (Figure 8). The subunits D1 and D2 contain all the redox-active co-factors that are necessary for the ET. They are surrounded by the heterodimer CP43 and CP47 subunits, which are mainly responsible for energy delivery to the RC as they harbor 13 and 16 Chl *a* molecules, respectively. While cytochrome *b*-559 is known not to be involved in the primary ET chain, serval studies showed that it plays a role in protecting the PSII from the Reactive Oxygen Species (ROS) that could lead to photoinhibition[55-57]. So far, despite intensive research, the role of cyt *b*-559 is still enigmatic. These subunits, which build the RC together with the three extrinsic subunits PsbO, PsbU and PsbV, represent the basic functional unit to oxidize the water molecules (Figure 10).

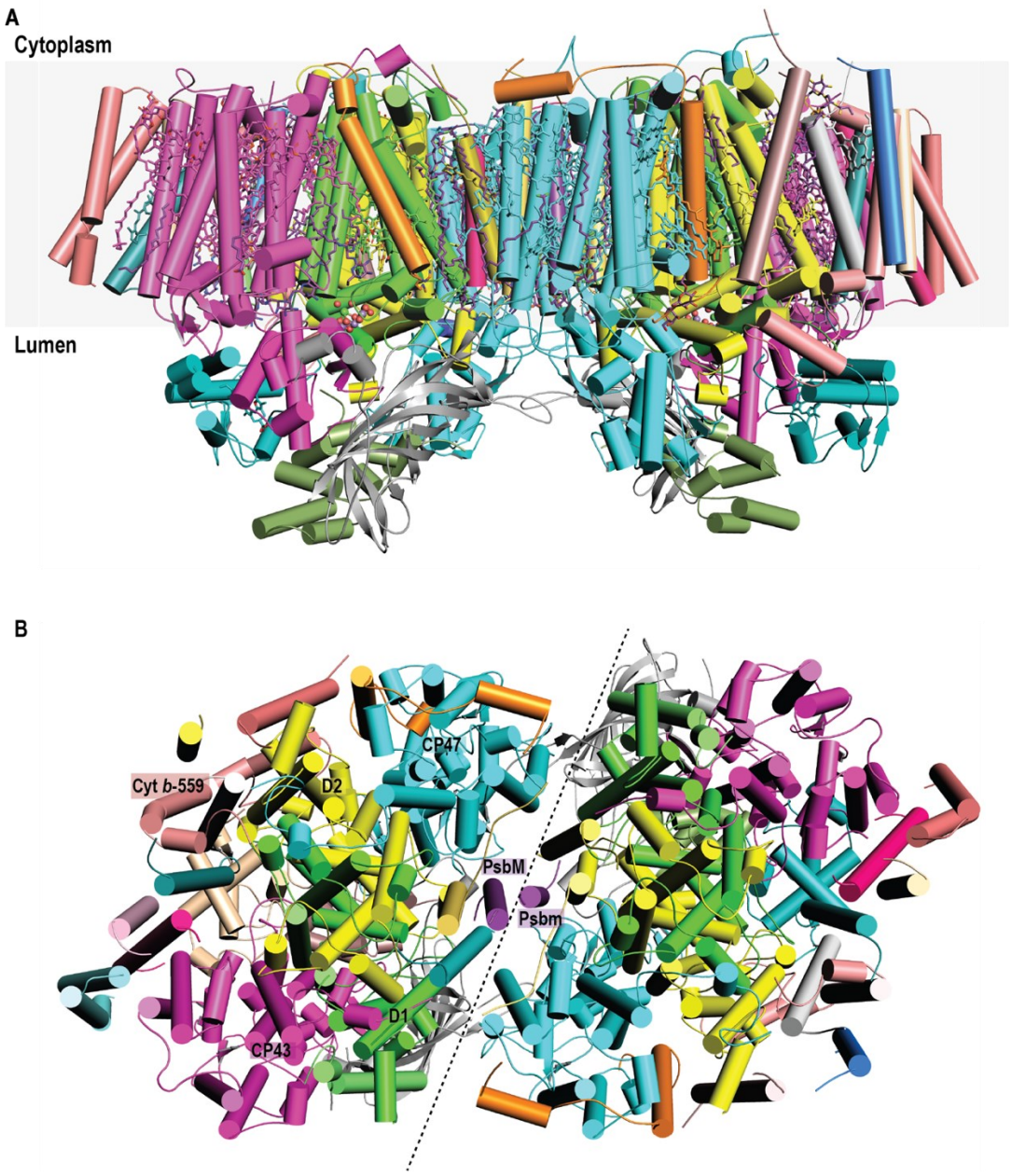

Figure 8 The homodimeric PSIIcc according to dark state RT crystal structure (PDB ID: 7RF2) at resolution 2.08 Å. *(A) Side View of the dimeric PSIIcc along the transmembrane plane. All the subunits and the co-factors are in cylinder cartoon and stick mode, respectively. The proteins subunits and co-factors are colored by chain (D1 (green), D2 (yellow), CP43 (magenta), CP47 (cyan), cyt b-559 (wheat), PsbO (gray), PsbU (smudge), and PsbV (green cyan)). (B)Top view from the cytoplasmic side of the dimeric PSIIcc. Intrinsic subunits are shown in the cylinder cartoon and have the same color code as in (A). The black dashed line represents the monomer-monomer interface.*

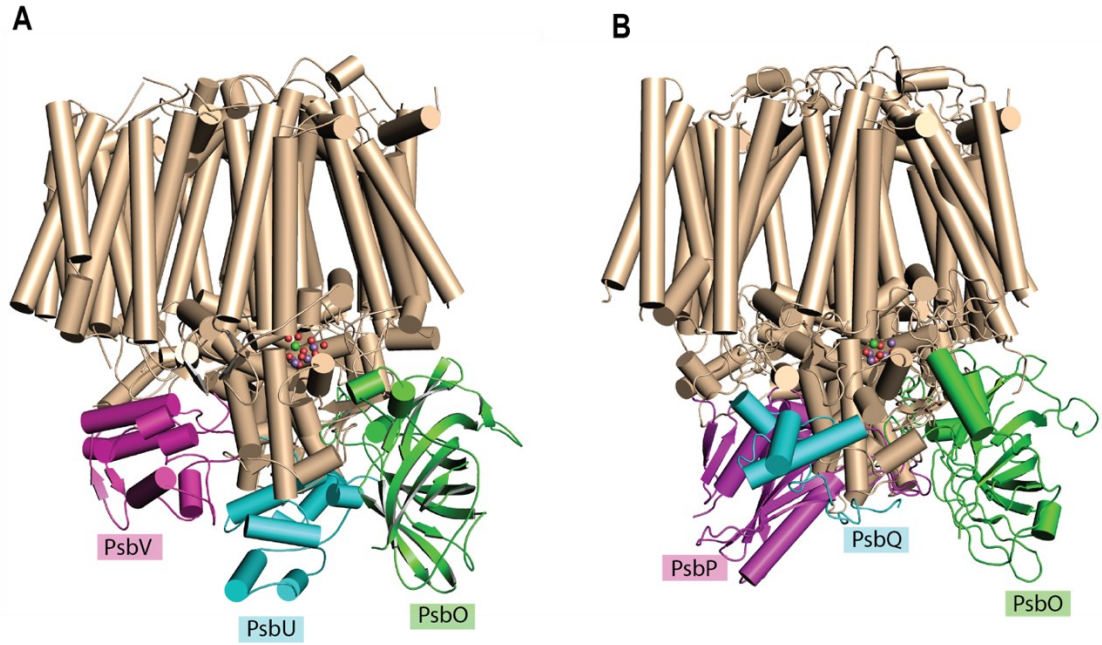

Figure 9 Extrinsic subunits in cyanobacteria and plants. *(A) Side View of the monomeric PSIIcc along the transmembrane plane according to dark state RT crystal structure (PDB ID: 7RF2) at resolution 2.08 Å. All the subunits are in cylinder cartoons. All intrinsic subunits are in wheat color. Extrinsic subunits are color by chain (PsbO (green), PsbU (cyan), and PsbV (magenta). (B) Side View of the monomeric PSIIcc along the transmembrane plane according to plant PSII cryo-EM structure (PDB ID: 3JCU) at resolution 3.2 Å. All the subunits are in cylinder cartoons. All intrinsic subunits are in wheat color. Extrinsic subunits are color by chain (PsbO (green), PsbQ (cyan), and PsbP (magenta).*

All the three extrinsic subunits (PsbO, PsbU and PsbV) (Figure 9A) face the lumenal side of the PSII. They are playing a significant role in stabilizing and protecting the catalytic Mn cluster. In addition, they control the accessibility of the channels that are connecting the Mn cluster to the lumenal side. These channels could supply the Mn cluster with the water substrate or act as an exit channel for protons and molecular oxygen[58-60]. PsbO subunit forms the only β-barrel structure of PSII. It stabilizes the Mn cluster and plays a critical role in maintaining the calcium concentration crucial for the Mn cluster. Furthermore, it is believed to play a role in ejecting the proton away from the Mn cluster towards the lumen[58, 61-66]. Mutating the expression of the PsbO subunit in cyanobacteria was found to result in significantly reducing the oxygen evolution[67], whereas in green algae and higher plants leads to complete loss of oxygen evolution[68]. The PsbU subunit also plays a crucial role in maintaining protein activity. Lacking PsbU was found to impair the energy transfer from the phycobilisomes to the PSII[69]. The PsbV subunit is also known as cytochrome c-550, and it is a heme-binding protein. Like PsbO and PsbU, PsbV plays a role in stabilizing and protecting the PSII [65]. Albeit the long distance between PsbV and the OEC, ~ 22 Å, it is suggested to have a role in the electron transfer reaction because of it's high redox potential, +200 mV[70, 71].

I.3.2. The redox-active co-factors in PSII

The redox-active co-factors are present at subunits D1 and D2 that form the reaction center RC of PSII. They are arranged in a pseudo-*C2* symmetry with a rotation axis crossing the non-heme iron. They mainly consist of a dimer of two Chl *a* molecules (P_{D1}, P_{D2}), pair of another accessory Chl *a* molecules (Chl_{D1}, Chl_{D2}), pair of pheophytins ($Pheo_{D1}$, $Pheo_{D2}$), and pair of plastoquinone (PQ, named as Q_A and Q_B). In addition, non-heme iron is located between the plastoquinone (Q_A and Q_B) pair and coordinated by five ligands; two pairs of histidine residues and one non-protein ligand, which is the bicarbonate. At the periphery of RC, another two Chl *a* molecules are present ($Chlz_{D1}$, $Chlz_{D2}$)[41, 72] (Figure 10).

The CP43 and CP47 subunits, which are flanking the RC subunits D1 and D2, carry 29 Chl *a* molecules in total; 13 in CP43 and 16 Chl *a* in CP47. These Chl *a* molecules are considered the antenna that absorbs the solar energy and funnels it to the RC.

Oxygen evolving complex (OEC) is considered the catalytic heart of PSII. It is formed by four Mn ions and one calcium ion and connected via μ-oxo bridges to give the Mn_4CaO_5 cluster(Mn cluster). This inorganic metal cluster is coordinated by four ligand waters and seven ligands formed by conserved amino acid residues belonging to the subunit D1 and subunit CP43[73]. In addition, close by to the OEC and the dimer molecules of Chl *a* (P_{D1}, P_{D2}), there are two redox-active tyrosine residues (Yz or (D1-Y161) and Y_D (D2-Y160))[73, 74].

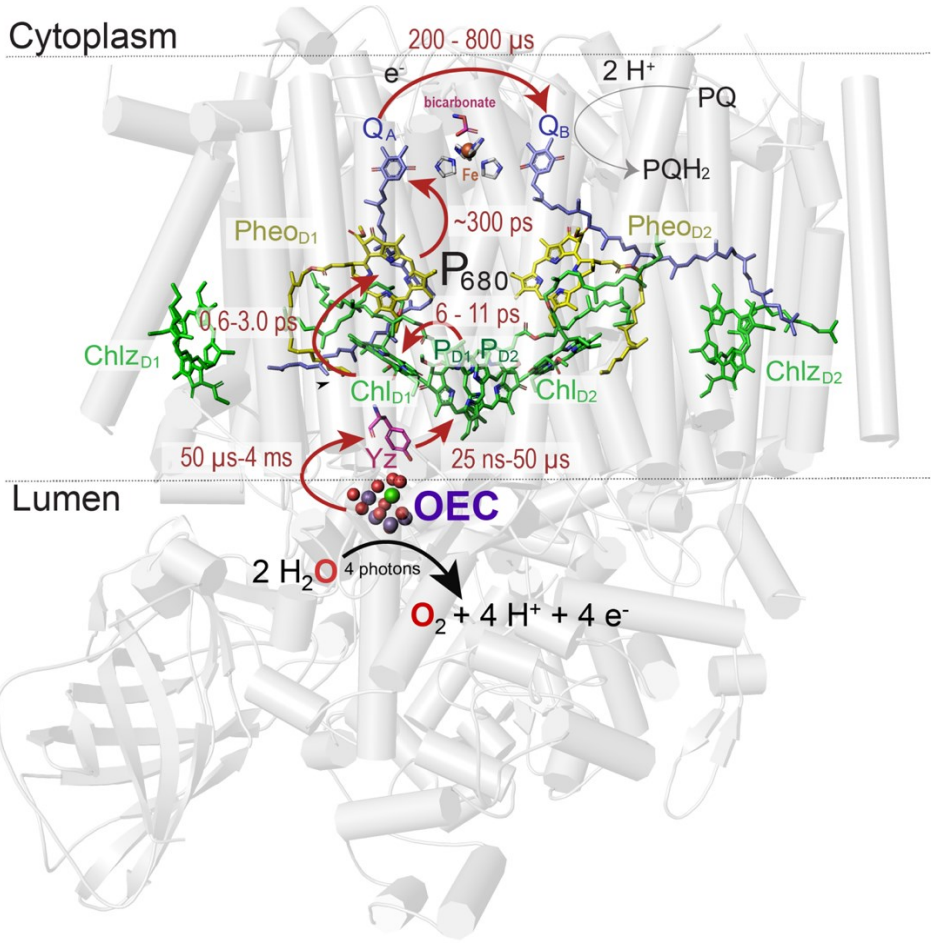

Figure 10 Arrangement of the redox-active co-factors in PSII. *The structure of the monomeric PSII with all the subunits is shown as a cartoon in gray. All the redox-active co-factors involved in charge transfer are shown in color. The electron transfer ET steps are represented by red arrows, along with the time transfer of each step*[75].

I.3.3. Charge separation in PSII

The light absorption occurs through external pigments capable of funneling the excitation energy to the internal Chl *a* molecules in PSII with high transfer quantum efficiency[76]. The energy of excited Chl *a*; Chl *; of the antenna are then transferred by excitonic coupling to the primary electron donor in the RC; P680; resulting in converting it to P680*. The primary electron donor is named P680 due to its maximum absorption wavelength, 680 nm. It is usually defined as the dimeric Chl *a* molecules (P_{D1}, P_{D2}) and the accessory Chl *a* molecules (Chl_{D1}, Chl_{D2}). However, the high-resolution structures of PSII and subsequent computational calculations establish a more accurate definition for the P680. It becomes more evident that several other pigments, i.e., $ChlZ_{D1}$, $ChlZ_{D2}$, contribute to the maximum absorption at 680 nm, not only P_{D1} and P_{D2} (Figure 10).

The light absorption process takes about 40-50 ps, which is considered a relatively slow process because of the considerable distance between the inner antenna and the RC [77, 78].

After exciting the P680, the charge separation process in the RC starts. It is considered a fast process as it takes few picoseconds. The excited electron from P680* is transferred to the primary electron acceptor pheophytin (Pheo), leading to the radical pair $P680^{\bullet+}$ $Pheo_{D1}^{\bullet-}$[79].

$$Chl^{*}_{antenna} + P680 \rightarrow Chl_{antenna} + P680^{*} \quad (10)$$

$$P680^{*} + Pheo_{D1} \rightarrow P680^{\bullet+} + Pheo_{D1}^{\bullet-} \quad (11)$$

One electron transfers from $Pheo_{D1}^{\bullet-}$ to reduce the primary plastoquinone molecule Q_A forming $Q_A^{\bullet-}$. The reduced $Q_A^{\bullet-}$ is later getting oxidized by the second plastoquinone molecule Q_B leads to form $Q_B^{\bullet-}$. After the second light-induced chemical turnover, $Q_B^{\bullet-}$ becomes fully reduced and protonated to form the plastoquinol PQH_2. The plastoquinol PQH_2 leaves the Q_B binding site and gets replacement by a new plastoquinone molecule from plastoquinone molecules present in the thylakoid membranes. The PQH_2 is subsequently getting oxidized again by the Cyt *b6f* complex[31].

$$Pheo_{D1}^{\bullet-} + Q_A \rightarrow Pheo + Q_A^{\bullet-} \quad (12)$$

$$Q_A^{\bullet-} + Q_B \rightarrow Q_A + Q_B^{\bullet-} \quad (13)$$

$$Q_A^{\bullet-} + Q_B^{\bullet-} + 2H^{+}_{cytosol} \rightarrow Q_A + Q_BH_2 \quad (14)$$

$$Q_BH_2 + PQ \rightarrow Q_B + PQH_2 \quad (15)$$

The formed cation radical $P680^{\bullet+}$ has a highly oxidizing potential of around 1.25eV[80]. It oxidizes the OEC by oxidizing the redox-active tyrosine Yz (Tyr 161) that is located near the Mn cluster and acts as an intermediate proton couple electron carrier between P680 and the OEC. The Histidine residue (His 190), which is located in subunit D1, accepts the proton released from the Yz after being oxidized by $P680^{\bullet+}$ to act as the base results in the formation of $Yz^{\bullet}$. The oxidation process of Yz takes place in the ns–µs time scale. However, the reduction of $Yz^{\bullet}$ by the OEC happened in the µs- ms time scale[81]. After four successive oxidations of the OEC, two water molecules are oxidized resulted in releasing one dioxygen molecule and four protons [82].

I.3.4. Oxidation of the OEC

Four successive accumulations of oxidizing equivalents on the OEC are required to split two water molecules and release the molecular oxygen. In 1969, Joliot and co-workers[83] managed to show that the oxygen evolution from dark-adapted algae or chloroplasts after being illuminated by short saturating flashes exhibited oscillations in

periodicity of four. Their study showed that no dioxygen is evolved after the first flash. However, the maximum dioxygen release happens after the third flash. In addition, after four to six periods, the oscillations are completely diminished (Figure 11).

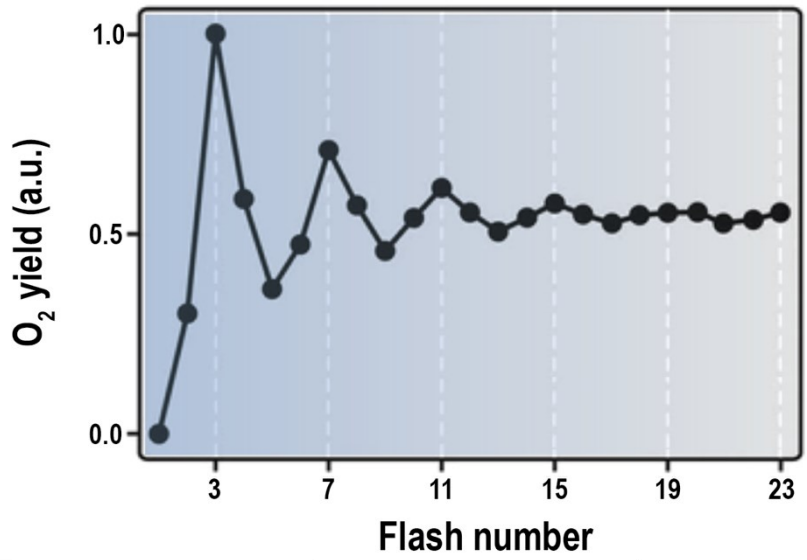

Figure 11 The flash-induced oxygen evolution pattern (FIOP) of a dark-adapted chloroplast from spinach as obtained by[83]. *Measurements were performed at pH 7.9 and 20 °C with a series of single saturating light flashes separated with a dark time of 300 ms. The figure is adapted from[84].*

Based on the study of Joliot et al., 1969, Kok and his co-worker in 1970[85] suggested a model for the charge accumulations that happened on the OEC during light activation. The model suggests a cycle of four states known as S_i (where i represents the number of stored oxidizing equivalents (i= 0, 1, 2, 3, and 4)) (Figure 12). The meta-stable states are S_0, S_1, S_2, and S_3, whereas the S_4 state is considered an intermediate state. Each state transition from S_0 to S_4 is companied by a one-electron transfer. Dioxygen is released during the S_3 to S_0 transition. Whereas, for proton release, a typical stoichiometry of 1:0:1:2 during $S_0 \rightarrow S_1 \rightarrow S_2 \rightarrow S_3 \rightarrow S_0$ transitions respectively is observed[86]. Due to that S_0 state is considered the most reduced metastable state. It consists of 3 Mn^{+3} and 1 Mn^{+4}. In contrast, the S_3 is the most oxidized meta-stable state and consists of 4 Mn^{+4}. As the S_0 state decays back in the dark to S_1, the S_1 state (2 Mn^{+3} 2 Mn^{+4}) is considered the dark stable state. During the transition from S_0 to S_1, one electron is transferred to the oxidized redox-active Y_D (D2-Tyr 160) (the symmetrical residue to the redox-active Yz located in D1)[87-90]. In comparison to Yz (Tyr 161), Y_D (D2-Tyr 160) is not playing a role in the fast electron transfer. However, it can act as a reductant during the decay of S_2 and S_3 states to the dark stable S_1 state[81, 89, 90]. Moreover, two water molecules are split during the Kok cycle. The first one is most likely between the S_2 to S_3 state[51, 91]. The second

water molecule is oxidized between the S_4 to S_0 state, although this event is still unclear (see P1.4.3).

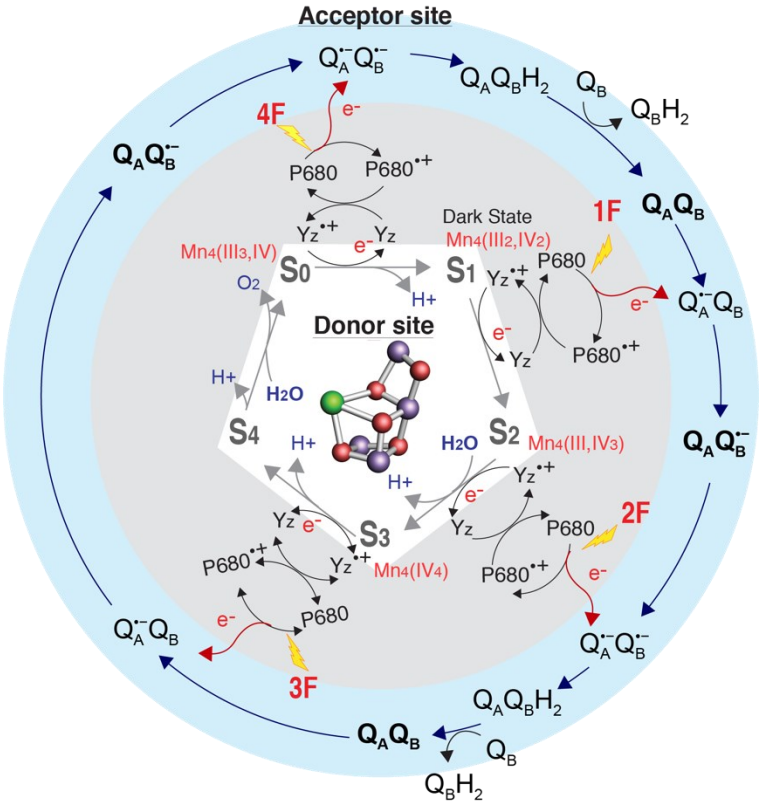

Figure 12 Kok's cycle of the oxygen evolution that takes place at the OEC of the PSII. *It shows the steps of the water oxidation reaction that is triggered by the absorption of photons shown as four light flashes(1F to 4F) by the antenna and the primary electron donor P680, with details of the Si states (S_0-S_4). The white and gray areas represent the electron donor site showing the redox changes of the OEC starting from the dark state S_1 till reaching the S_0 state and the chemical change to Yz and P680. The outer blue circle shows the accompanied electron acceptor side chemistry of the quinones. The figure was modified and adapted from*[91].

I.3.5. Structure of the OEC and its coordinates

In 2011, Umena and co-workers successfully collected a static crystal structure of PSII at a resolution of 1.9 Å for the dark state S_1[73]. This data was collected using synchrotron X-ray diffraction (XRD) at cryogenic conditions. It provides for the first time detailed information about the structure of the Mn_4CaO_5 cluster. The study shows the cluster as a distorted chair composed of four Mn ions, one calcium ion, and five oxygen (Figure 13). Three Mn ions (Mn1, Mn2, and Mn3) and the calcium ion are connected by-μ-oxo bridges through O1, O2, O3, and O5 to form a cubane-like base. The fourth Mn (Mn4) ion is located outside the cubane and is connected to it by di-μ-oxo bridges (O4, O5) to form the back of the chair, and due to that, Mn4 is called the dangler Mn. In addition, the study showed the presence of four water ligands in the Mn-cluster. Two of them (W1, W2) are ligands to Mn4, and the other two are ligands to the Ca ion (W3, W4)

(Figure 14). The interatomic distances provided by these studies showed some differences. They were more elongated in comparison to the distances calculated based on the Extended X-ray Absorption Fine Structure (EXAFS) data[92-94] (Table 2). These differences are due to the radiation damage that happens to the Mn-cluster during data collection. Several radiation damage studies using EXAFS show that the synchrotron's applied X-ray dose resulted in a photoreduction of $Mn^{+3/+4}$ ions to Mn^{+2} [95, 96]. The percentage of reduction was estimated to be around 25% of Mn ions under similar cryogenic conditions[95]. The work of Tanaka *et al.,* recently showed two crystal structures of PSII at a resolution of 1.87 Å and 1.85 Å. These data were collected using synchrotron XRD and at cryogenic temperature but using very low X-ray doses of 0.03 MGy and 0.12 MGy, respectively. The study showed that the photoreduction effect was minimal when using an X-ray dose below 0.12 MGy[97]. These results suggested careful consideration to the data collected using a high X-ray dose and necessary to re-evaluate if it genuinely represents the dark-stable S_1 state. Recently, several studies showed a crystal structure for the dark-stable S_1 state and the other meta-stable states using X-ray free-electron laser (XFEL)[47, 48, 50-52, 91]. This technique enables us to collect radiation damage free crystal structures and under more physiological conditions[98, 99].

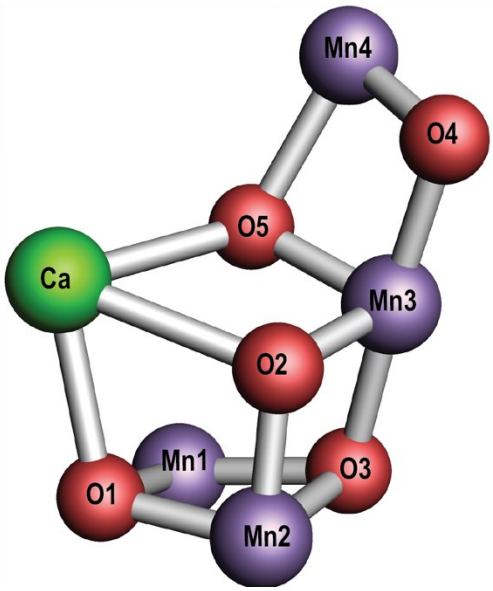

Figure 13 The structure of OEC. *The Mn-cluster according to dark state (S1) RT crystal structure (PDB ID: 7RF2) at resolution 2.08 Å. It appears as a distorted chair consisting of four Mn ions, one Ca ion, and five oxygen atoms.*

The Mn-Cluster has seven ligands of amino acids residues (Figure 14 and Table 1). Six of them belong to subunit D1 (Glu189, His332, Asp342, Ala344, Glu333, and Asp170), and only one residue (Glu354) belongs to subunit CP43. Most ligands have negative side chains (D1-Asp342, D1-Glu333, D1-Asp170, CP43-Glu354), are bidentate, ligating Mn1–Mn2, Mn3–Mn4, Ca-Mn4, and Mn2-Mn3 respectively, except D1-Glu189, which is only monodentate to Mn1. The only positive amino acid side chain, His332, forms a bridge to Mn1. While the carboxylate group C-terminal of D1-Ala344 forms bridges to Ca and Mn2. These amino acid residues and the four ligand waters (W1, W2, W3, and W4) form the ligand environment for the OEC. In addition to the primary ligand of the OEC discussed above, several hydrogen bonds are present between the oxygens of OEC and the surrounding amino acid residues (Figure 14).

The structure of the OEC and its ligand environments and hydrogen bonding are the main reasons beyond the distortion shape of the Mn_4CaO_5 cluster.

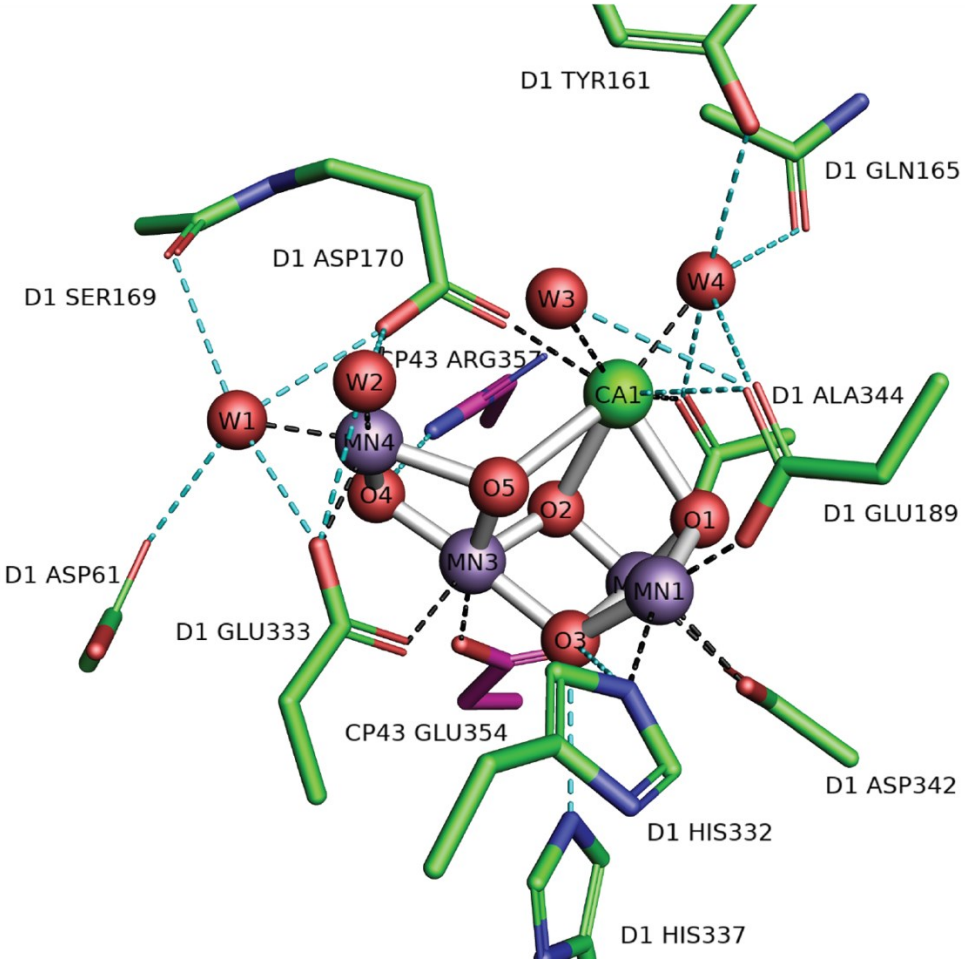

Figure 14 The ligand and hydrogen bonding environment of the Mn-cluster.
The ligand and hydrogen bond environment of the Mn-cluster is shown according to the dark state crystal structure (PDB ID: 7RF2) at resolution 2.08 Å. Residues belonging to

chain A (subunit D1) and chain C (subunit CP43) are depicted in green and pink, respectively. The hydrogen bonding is depicted as dashed lines in cyan, and the ligand interactions to the Mn cluster are depicted as dashed lines in black.

Table 1 The ligand environment of the Mn-cluster of the PSII.

Mn1	Mn2	Mn3	Mn4	Ca
D1-Glu189	D1-Asp342	D1-Glu333	W1	W3
D1-His332	D1-Ala344	CP43-Glu354	W2	W4
D1-Asp342	CP43-Glu354		D1-Asp170	D1-Asp170
			D1-Glu333	D1-Ala344

Table 2 Comparison shows the interatomic distances(Å)between the Mn-ions of the Mn-cluster based on the EXAFS measurements[92, 100], the 1.9 Å resolution SR-XRD crystal structure[73], the 2.44 Å resolution SR-crystal structure[44] and the 2.08 Å resolution XFEL-RT crystal structure[91].

	EXAFS	SR-XRD (PDB: 3WU2)	SR-XRD (PDB:4PJ0)	XFEL-XRD (PDB: 7RF2)
Mn4–Mn3	2.7–2.8	2.8–3.0	2.8–3.0	2.7-2.9
Mn3–Mn2				
Mn2–Mn1				
Mn3–Mn1	3.3	3.3	3.3	3.3

I.4. **Water and proton-transfer channel**

The water-splitting reaction is mediated by PSII protein upon activated by light. In this reaction, the OEC incorporates two water substrates and releases four protons towards the luminal side[91, 100, 101]. Therefore, an efficient catalytic cycle requires an efficient mechanism to transport the water substrates and release the protons.

Transferring water substrate and releasing water from the OEC require the presence of tunnels/channels, which are well connected to the bulk[43, 102-105]. These channels should exhibit specific properties to serve as water-transfer or proton transfer channels. The water transfer- and the proton transfer channel should be filled with water molecules. However, in the case of the water-transfer channel, the channel is filled with mobile water molecules (Figure 15A). Whereas in the proton-transfer channel, water molecules require to be rigidly fixed in position and surrounded by hydrophilic residues[106] (Figure 15B).

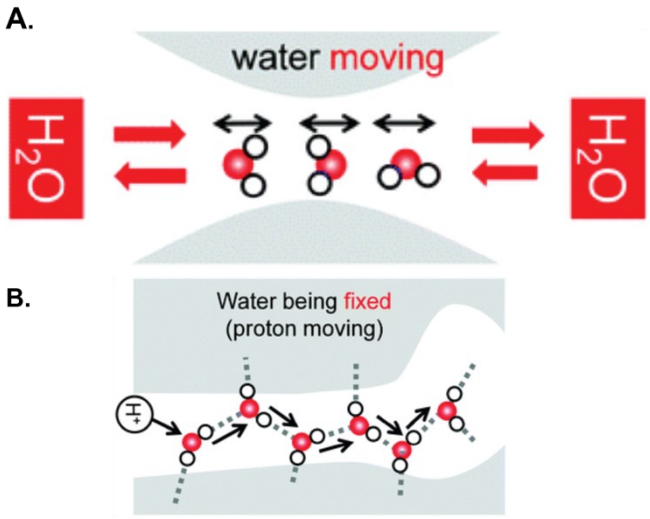

Figure 15 Scheme shows the difference between water transfer channel (A) and proton transfer channel(B). *The figure is taken from[106]. The copyright lies with the authors; original work can be found here: 10.1039/D0CP00295J*

Proton transfer in protein over a long distance requires the presence of a hydrogen bond wire between the donor and the acceptor sites. So the proton transfer can conduct through the protonable residues connected by water molecules[107]. The types of H-bond between the donor and the acceptor moieties are classified based on their p*K*a values (refers to the affinity of the proton toward the donor/acceptor groups)(Figure 16A). The moieties which have the higher p*K*a serve as the H-bond donor. Whereas the moieties which have the lower p*K*a serve as the H-bond acceptor (Figure 16A). Calculating the energy barrier needed to transfer the proton between the donor/acceptor moieties requires determining their p*K*a values[108]. When there is a difference in p*K*a between the donor/acceptor moieties, asymmetric H-bond becomes possible with a distance higher than 2.6 Å. On the other hand, when p*K*a values between the donor/acceptor moieties are closely matched, low barrier H-bond (LBHB) or single well H-bond become possible (Figure 16A). The typical distance between O-O in the LBHB is in the range of 2.5 -2.6 Å, whereas in the single well H-bond, the distance is less than 2.5 Å[109]. Noteworthy, in the case of LBHB and the single well H-bond, the proton coupling between the two moieties is the maximum resulting in decreasing the energy barrier needed for proton transfer. Hence, proton transfers are energetically favorable, unlike the uphill transfer from lower potential energy to high (Figure 16B)[110, 111].

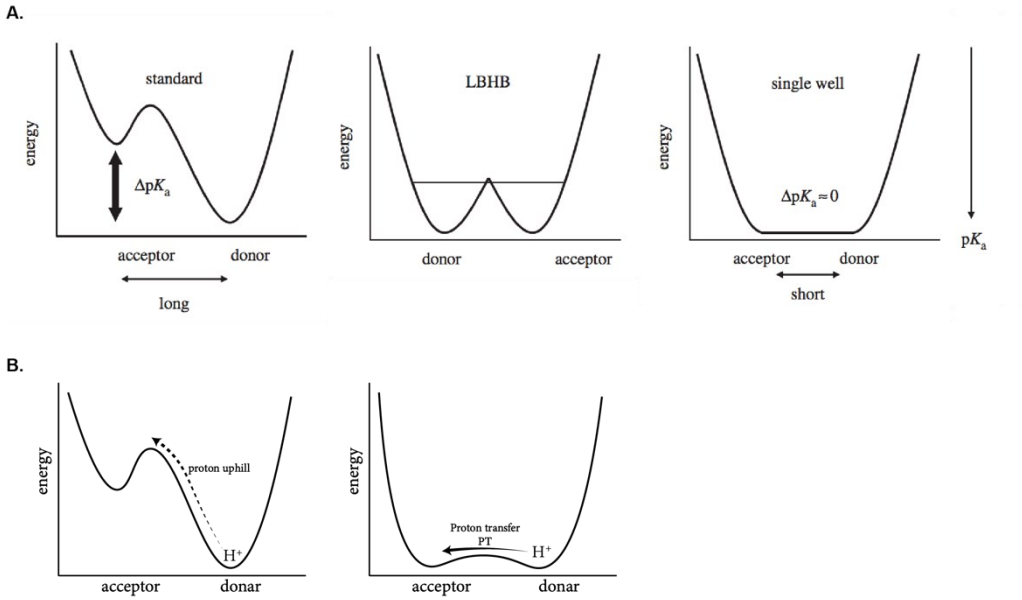

Figure 16 A. Different types of hydrogen bonds with their potential energy profile. *The figure shows the standard H-bond (top right), LBHB (top middle), and the single-well type (top left). The figure is adapted and taken from [110]. The copyright lies with the authors; original work can be found here: https://doi.org/10.1098/rsif.2013.0518*. **B.Overview of the typical proton transfer energetics.** In the bottom left, proton transfer is uphill (energetically unfavoured: from low potential energy to high potential one). Whereas in the bottom right, proton transfer is energetically favored and can occur.

As it is mentioned above, the proton transfer is conducted through the protonable residues. Asparagine sidechain is unlikely to be involved in proton transfer; however, in 2015, Nakamura *et al.* reported tautomerization of an asparagine residue in cellulase protein *Pc*CeI45A[112]. Tatumerization of the aspargine shuffles the side chain between the amide acid form (O=C(R)–NH_2) and imidic acid form (HO–C(R)=NH) (Figure 17), which enables proton relay transfer[112].

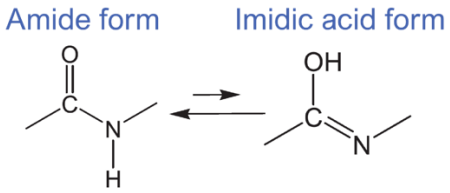

Figure 17 chemical structure of the Amide form and the imidic acid form

Rapid proton transfer through the rigidly fixed water molecules connected by H-bonds can be achieved via the Grotthuss-like mechanism (also known as proton jumping/hopping). Through that, water molecules mediate the proton transfer sequentially. For a proton transfer, a covalent bond between an O-H is cleaved and exchanged with a H-bond with the adjacent water[110, 113]. This event coincides with new O-H covalent bond formation (Figure 18). Proton transfer over a water chain via this mechanism leads to changing the H-bond pattern from pre-PT to post-PT (Figure 18).

After the proton is successfully transferred, the H-bond pattern needs to be organized back to its original pattern (pre-PT) to avoid the back transfer of the proton[110].

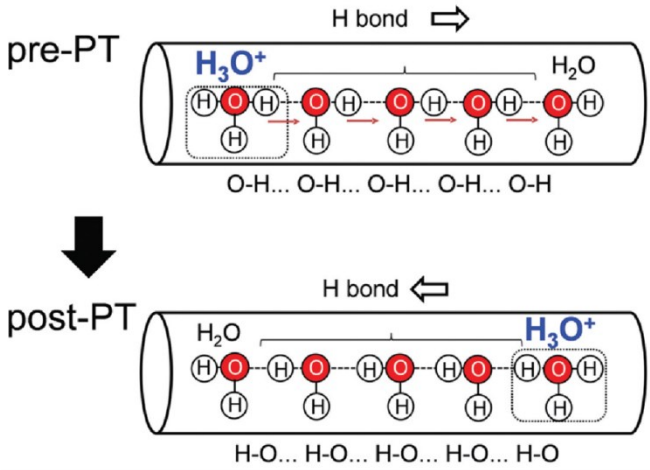

Figure 18 Scheme shows the hydrogen bond patterns before (pre-PT) and after (post-PT) proton transfer via the Grotthuss mechanism. *The figure is taken from[106]. The copyright lies with the authors; original work can be found here: 10.1039/D0CP00295J*

I.4.1. Water channels in PSII

As the Mn_4CaO_5 cluster is buried inside the protein close to the lumenal side, it was postulated early on that adequate water channels and proton exit pathways might present within the complex to ensure proper water substrate delivery and removal of reaction products (in this case, protons and dioxygen) (Figure 15). Initial work was performed based on searches for cavities and channels in the lower resolution crystal structures that did not contain waters within the model[43, 102-104]. Several groups used MD simulations, e.g., to identify new channels, characterize water permeation energetics[103, 105], and study water diffusion from the bulk[114]. These channels match some channels identified in the earlier crystal structures (Table 3).

The most complete report on water channels and protons pathways so far is probably the work done by Vassiliev et al. that combined an MD approach with the water injection method[105]. This approach showed new channels and identified bottlenecks with their corresponding activation energy (Table 4). The study also demonstrated that waters could not permeate from one side of the OEC to the other (i.e., from Ca to Mn4). Still, it did not exclude the possibility of water migrating from one binding site to another. Namely, the environment around W1-4 (binding to Mn4 ion and Ca ion and potential substrate molecules) is restricted and only allows concerted water movements (Figure 15B). Another insight of this study is that none of the channels allow unrestricted water access to the OEC. This explains the difficulty of identifying channels in PSII with static

methods. The potential channels currently proposed from several studies are summarized below, and their corresponding names are shown in Table 4. However, determining which water channels supply the water substrate and which act as the proton exit pathway in each state transition is still elusive.

Table 3 Channel nomenclature in literature. The table summarizes the other names used for identifying the water and proton channels in PSII.

	Ho and Styring [115]	Murray and Barber [116]	Gabdulkhakov et al. [117]	Umena et al. [73]	Vassiliev et al. [118]	Ogata et al. [119]	Sakashita et al. [120]	Weisz et al. [121]
Method	Surface contact calculation	-	Xe	H-bond network analysis	MD simulation			ROS
PDB ID	2AXT	-	3BZ1	3ARC (2WU2)	3ARC (2WU2)	3ARC (2WU2)	3ARC (2WU2)	-
Resolution	3.00 Å	-	2.90 Å	1.90 Å	1.90 Å	1.90 Å	1.90 Å	-
O1 Channel A	large	*channel ii*	B1	-	4.A	-	O1-water chain	Arm 2
O1 Channel B	large	*channel ii*	B2	-	4B	-		Arm 2
O4 Channel	narrow	NA	E, F	4.c	2	Path 3	O4-water chain	-
-	-	-	D	-	Channel X	-	-	Arm 3
Cl1 Channel A	broad	-	G	4.b	1	-	E65/E312 channel	-
Cl1 Channel B	-	*channel iii*	C, D	-	3	Path 2	-	Arm 1
Cl2 network	-	-	-	4.c	-	-	-	-
-	back	*channel i*	A1, A2	3.b	5	Path 1	-	Arm 3

Table 4 Channels description with length, origin at the protein surface, bottleneck (residues involved and activation energy).

	Cl1 channel	*O4 channel*	*O1 channel*	*ref*

Alternative name	*channel 1 channel 3*		*Channel 2*	*Channel 4*		*105*
	"broad"		*"narrow"*	*"large"*		*122*
Length (Å)	*24Å- 43.5Å*		*32.6 Å*	*30Å -35Å*		*105*
Bottleneck close to the OEC	*D1-D61, -E333, -I60 and D2-K317 (Cl^- binding site)*		*from OEC O4 to Mn4, D-D61*	*CP43-V410, -T412, and D1-E329, D1-D342*		*105*
Activation energy of the 1st bottleneck	*7 kcal/mol*		*5 kcal/mol*	*10 kcal/mol*		*105*
	A	*B*	*--*	*A*	*B*	
2nd bottleneck	*D1-E65, -P66, -V67 and D2-E312 (D1-R334)*	*D2-T316, -L319, -L320, PsbO-P159 -K160*	*D1-N338, D2-N350 and CP43-P334, -L334*	*CP43-V410, -E413, PsbV:K47 D1-L341*	*PsbV-G132, -G133, -K134, D2-R348*	*105*
Activation energy of the 2nd bottleneck	*12 kcal/mol*	*12 kcal/mol*	*9 kcal/mol*	*5 kcal/mol*	*6 kcal/mol*	*105*
Surface residues	*PsbO-D224 D2-E310*	*CP47-K423 PsbO-E179*	*PsbU-D96 PsbO-N155*	*CP43-N418, -K79, PsbV-Q34*	*D2-E343*	*105*

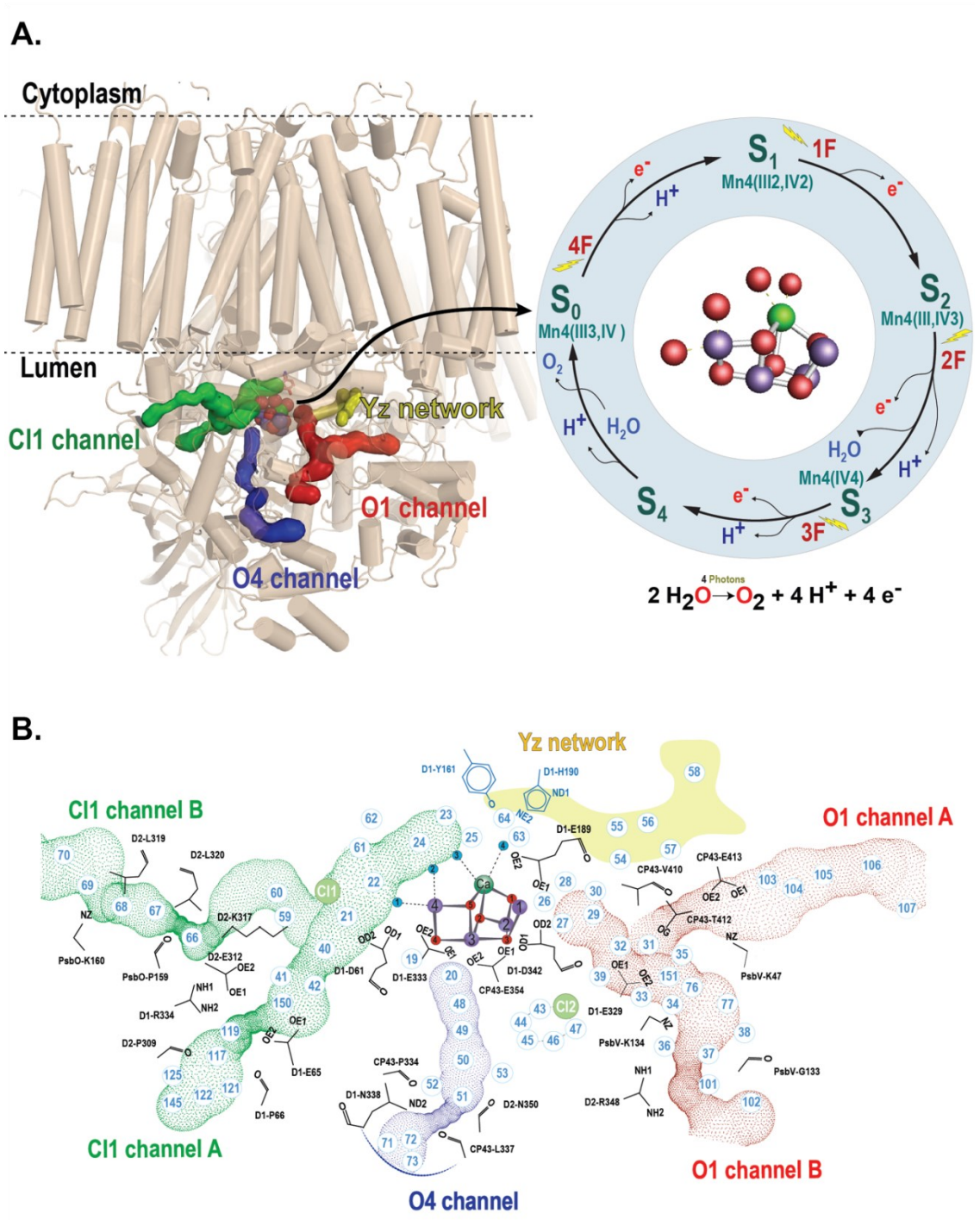

Figure 19 Overview of the main water channels in Photosystem II. *A: (Left) The structure of PSIIcc shows the intrinsic and extrinsic subunits in beige. The Mn cluster, the water channels, and the Yz network are shown in color (O1 Channel (red), O4 Channel (blue), Cl1 Channel (green), and Yz network (yellow). The right side shows Kok's cycle of the water oxidation reaction that is triggered by the absorption of photons and highlights the events of water insertions and proton releasing. B: A schematic view of the water channels connecting the cluster to the bulk. The scheme shows the waters within each channel (O1 Channel dotted in red, O4 Channel dotted in blue, and Cl1 Channel dotted in green). The Yz network is highlighted in yellow. Residues that form bottlenecks of the channels are shown in black.*

The O1-Channel (Figure 19), which is also known as "large channel"[103] or channel 4[105] (Table 3), starts from the Ca side of the cluster and reaches the lumen at the interface of subunits D1, CP43, and PsbV. Close to the cluster, the O1 channel is connected to Yz via a conserved network of five waters (W26-27-28-29-30).

Interestingly, in a recent study on PSII by MD simulation[114], it was found that these five waters do not behave equally; W26 and W28 were identified as exchangeable with the bulk solvent, while W27, W29, and W30 were not. The first bottleneck of this channel is at the residues CP43-V410, -T412, and D1-E329, D2-D342, located 13 Å away from the OEC (Figure 19). After the first bottleneck, the channel splits into two perpendicular branches, branch "A" continues along the PsbV and CP43 interface, and branch "B" extends until a cavity between PsbU, PsbV, D2, and CP47 is opening to the bulk solvent. Both branches have bottlenecks before reaching the bulk solvent but with a relatively low activation energy barrier (5 and 6 kcal/mol) (Table1).

Another well-described channel is the Cl1-Channel (Figure 19). This channel starts from the Mn4 side of the cluster through D1, D2, and PsbO domains for branch A, also known as "broad channel" or "channel 3"[105], and D2 and PsbO for branch B, also known as "channel 1"[105]. It involves one of the chlorides located near the OEC (Cl-1) and D2-K317 and D1-E61 residues that act as gatekeepers[123]. The first segment of this channel, from OEC to the first bottleneck (D2-K317 and D1-E61), contains a stable H-bond network. MD simulations were able to reproduce the diamond shape (W23-24-25 and W3) water network connected to Yz[114].

The O4 channel extends from O4 (close to Mn4 ion in the cluster) toward the lumen through D1-D2 and CP43 subunits before extending to PsbO and PsbU (Figure 19). It is also known as the narrow channel[105]. This 30 Å long channel has a well-identified bottleneck, including residues D1-N338, D2-N350, and CP43-P334, -L334. MD simulation study has described the waters as non-exchangeable with the bulk except W19 and W20, and these waters are delivered through Cl1 channel[114], while another study calculated the energy of water permeation and showed it to be lower than channel Cl[105].

In addition to the above water channels, there is a water network named Yz network. The Yz network is formed via a group of water in the vicinity of the Tyr161-His190-Asn298. Although, unlike the other water channels, the Yz network is not directly extended to the lumen; it connects the OEC with the PsbV subunit near the lumenal side (Figure 19). The Yz network is discussed as a part of the proton release pathway or at least involved in a proton relocation concomitant to the Yz oxidation[73, 124-127], not as a substrate water delivery, as it is not connected to the lumen.

Identifying the water-transfer channel and the proton-transfer channel will shed light on identifying the water substrates and uncovering the proton release mechanism during the water oxidation process. Therefore, investigating the structural changes along the

water channels is crucial for that purpose towards building a complete understanding of the mechanism.

I.5. **Structural change of the OEC during the Kok's cycle**

Despite the vast literature to understand the water oxidation process, the water oxidation mechanism is still elusive. The dynamic process of the water splitting has been vastly investigated using different methodologies; spectroscopical methods, i.e., electron paramagnetic resonance (EPR)[128-135], Fourier transform IR spectroscopy (FTIR)[136-139], and extended X-ray absorption fine structure (EXAFS)[92, 100, 140-146], and theoretical calculations[147-151]. Several structural changes occur during each Kok's cycle transition (Figure 12)[82]. For a long time, the structural data collected by Synchrotron XRD did not agree with the spectroscopical and theoretical ones due to the radiation damage during the XRD data collection. However, the XFEL technique helped overcome such obstacles, and it was possible to collect damage-free XRD data (See part P1.5.2)[48, 50-52].

I.5.1. S_1–S_2 transition

During the S_1-S_2 transition, one Mn^{3+} ion gets oxidized to Mn^{+4} (Figure 20) without releasing any proton from the OEC to the lumen side. Recently, simultaneous XRD and XES measurements using XFEL radiation by Kern et al. 2018 reported interesting isomorphous difference map features after forming the S_2 state, which can be explained by the oxidation of the dangler Mn4 of the OEC (Figure 21)[51]. According to this study[51], no noticeable structural changes were observed at the OEC (Figure 22). The OEC geometry at S_2 state is consistent with the EXAFS data[100] and with the open cubane geometry suggested by the EPR ground spin state of S=1/2 (g= 2.0) in which Mn4 oxidation state is +4[152] without further support the closed cubane structure proposed by EPR ground spin state of S=5/2 (g= 4.1)[153] (Figure 23).

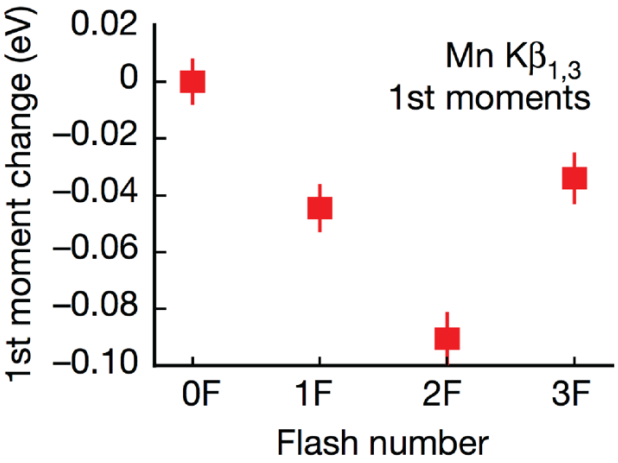

Figure 20 First moment change of the Mn Kβ$_{1,3}$ XES spectra of PSII crystals upon illuminations with laser flashes (527 nm) to probe different S-states; S$_1$, S$_2$, S$_3$, S$_0$ corresponding to 0F, 1F, 2F, and 3F respectively. *The figure is taken from*[51].

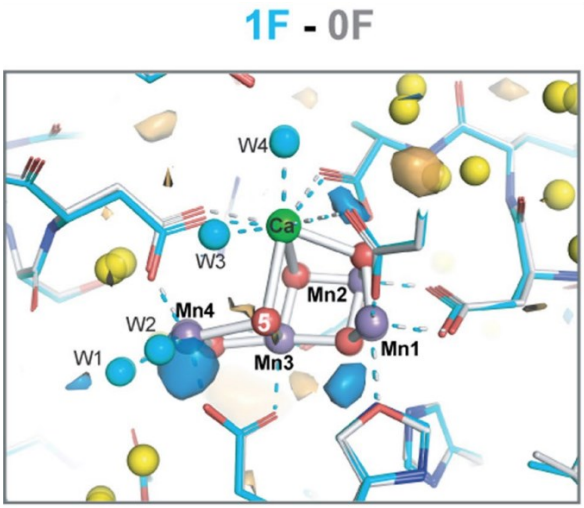

Figure 21 Isomorphous difference map (F$_{obs}$ − F$_{obs}$) at the site of the OEC between the 1F and the 0F data are contoured at +3σ (blue) and −3σ (orange). *The model for the 0F is shown in light grey, whereas the model for the 1F is shown in cyan. The high positive density that appears near the Mn4 site results from the displacement of Mn4 due to oxidation. The figure is taken from*[51].

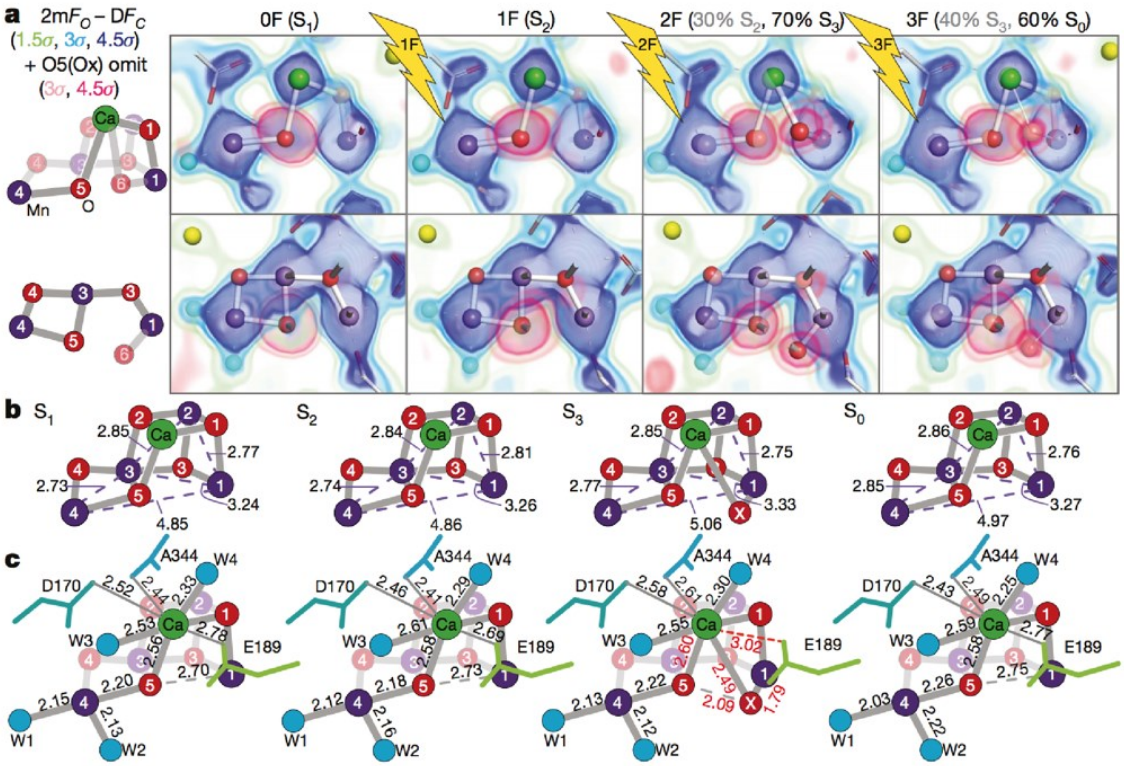

Figure 22 Structural changes near the OEC side at different illumination states. *a, 2Fo − Fc density (green, cyan, blue) and O5/Ox omit map density (pink) shown as the overlay of two contour levels (3 and 4.5 σ) for the two views of the OEC in different S-states. b, c, Atomic distances (in Ångström) in the OEC between metal-metal and metal-ligand distances respectively in each S state. The figure is taken from*[51].

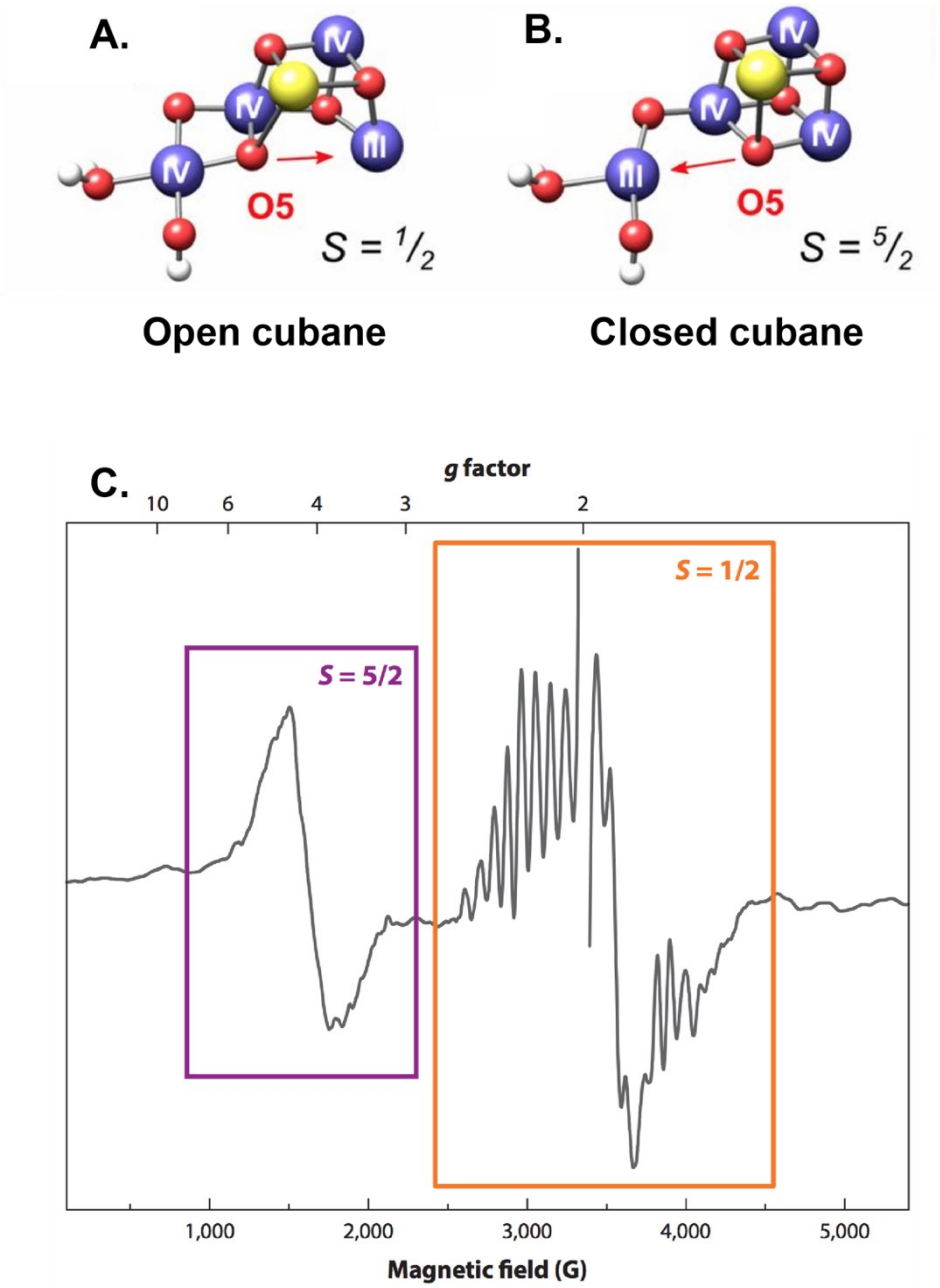

Figure 23 The structure of two S_2 state forms. *The open cubane form (A) and the closed cubane form (B) of the OEC at the S_2 state. Figure (A&B) were modified and adapted from[154]. C) X-band electron paramagnetic resonance spectrum (EPR) of PSII from higher-plant at the S_2 state. The orange box shows the multiline signals centered at g = 2 with a ground spin state of S = 1/2. Whereas the purple box shows a broad signal centered at g = 4.1 with a ground spin state of S = 5/2. The figure is taken with kind permission to reproduce from[101].*

At the acceptor side, after a first flash (S_2 state) on the PSII crystals, clear evidence of the Q_B^- formation was reported (Figure 24a)[51]. After two flashes (Figure 24b), the 2F − 0F isomorphous difference map matched the replacement of the fully reduced quinol with another quinone at the original position. In figure 24c, the 3F − 0F difference map, showing again structural changes similar to the 1F − 0F map, indicating the formation of

the semiquinone. These results indicate that in each S-state transition, one electron was successfully transferred from the OEC to the acceptor side of PSII in the crystals.

Another important observation that was reported by the XFEL investigations is the dislodging of W20, the next water to O4 of the Mn cluster, and it was detected again at 3F data (S_0-rich state) (Figure 25)[51, 52]. This dislodging of W20 disconnects the hydrogen bonding network of the O4 channel from the OEC in the S_2 and S_3-states. Therefore it is unlikely that the O4 channel can act as a proton egress pathway during the S_2 to S_3 transition and the S_3 to S_0 transition.

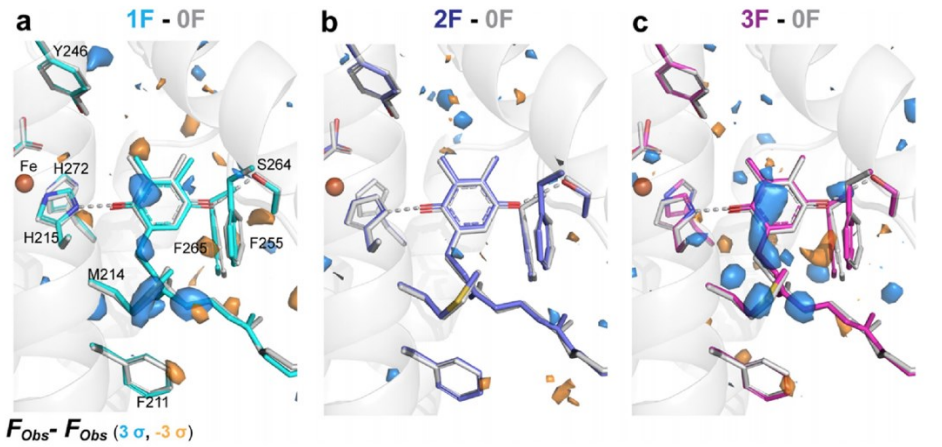

Figure 24 Isomorphous difference maps (Fo-Fo) at the site of Q_B contoured at 3σ. *a) The 1F − 0F difference map shows the effect of the plastoquinone reduction to a semiquinone at 1F, and slight geometry change observed. b) the 2F − 0F difference map shows the replacement of the reduced quinol with another non-reduced quinone. c) The 3F − 0F difference map shows a similar effect observed at the 1F − 0F difference map due to plastoquinone reduction to a semiquinone. The figure is taken from*[51].

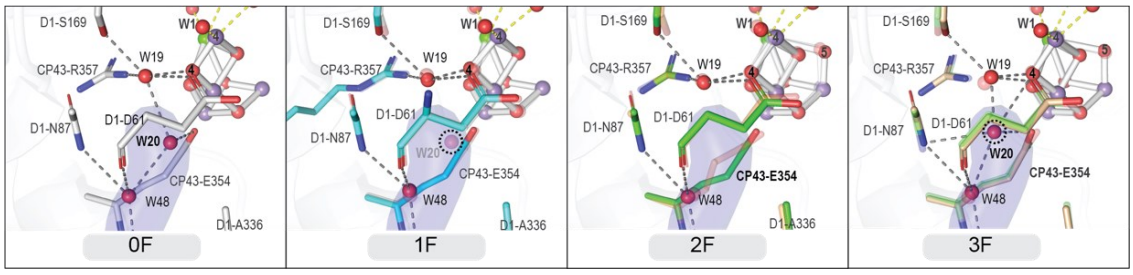

Figure 25 Changes near O4 of the Mn cluster and beginning of O4 water channel at different states. *W20 was not observed only at 1F and 2F data, resulting in disturbing the water H-bond chain at these states. Interaction distances between atoms are shown in gray dashed line and up to 3.2 Å. Structure at 0F is (S_1 state) at 2.08 Å (PDB ID: 7RF2), after 1F (S_2 state) at 2.26 Å (PDB ID: 7RF3), after 2F (200 μs) (S_3 state) at 2.09 Å (PDB ID: 7RF8), after 3F (S_0 state) at 2.04 Å (PDB ID: 6DHP)*[51].

I.5.2. S_2–S_3 transition

Unlike the S_1–S_2 transition, EXAFS data of the S_2–S_3 transition indicate elongation in the Mn–Mn distances at the S_3-state formation[92, 140, 143, 155]. The elongation of Mn-Mn distances suggests that this transition involves a proton-coupled-electron transfer and likely water coordination[156, 157]. Furthermore, the recent XFEL studies showed that Mn1-Mn4 distance increases significantly during this transition by ~0.5Å and clear indications of binding of the first substrate water (Ox/6) to the OEC[51, 52] (Figure 22). Thus, in agreement with the proposed mechanism by Siegbahn and co-workers[158]. In this mechanism, a new water substrate coordinates to Mn1 after the S_2–S_3 transition that involves oxidation of the Mn1 from +3 to +4[158]. In addition, the XFEL study by Kern et al. 2018 also reported strong evidence of the Q_B^{-2} formation and replacement (Figure 24b). Therefore, the S_2–S_3 transition is a crucial step in the water oxidation process and needs further investigation to better understand the mechanism of the water insertion into the OEC and investigate the possible pathway of the water substrate. Also, the protonation states of the different water/hydroxyl ligands and the oxo/hydroxo μ-bridges are of equal importance. Hence, investigating the possible proton release pathways is crucial too.

I.5.3. S_3–S_0 transition

During this transition, the cluster is transforming from the most oxidized state (S_3) to the most reduced state (S_0)[100]. Shortening in the Mn–Mn distances was reported by EXAFS studies[159]. Finally, the cluster transforms back to the open cubane form as in S_1 and S_2 like states, explaining the shortening of the Mn1-Mn4 distance (Figure 22)[100]. The recent XFEL studies also showed a decrease in the Ox/6 density after the S_0-state formation (Figure 22a). The XFEL date from the S_0-state shows that the dislodged water (W20) during the S_2–S_3 transition is back to its position[51, 52] (Figure 21).

I.5.4. S_0–S_1 transition

The EPR/ENDOR data suggest the following manganese oxidation states III, III, IV, IV in the S_1-state instead of III, III, III, IV in the S_0-state[134, 160]. In addition, the EXAFS experiments showed a slight shortening in the Mn–Mn distances upon the S_0–S_1 transition, suggesting oxidation of one Mn ion during this transition[159]. In addition, the last proton release during a complete Kok'cycle takes place also during this transition. Unlike the slow protons release during the S_2–S_3 and S_3–S_0, the proton release in the S_0–S_1 transition is considered a non-rate-limiting process and rapidly conducted[86, 106, 161].

W20 appears again in the S_0 data (Figure 25), which raises the possibility that this channel is a proton release channel during the S_0 to S_1 transition[162].

I.6. Methods for tackling the structure of PSII

Applying serial XFEL protein crystallography can help us uncover the pathways of water substrate insertion and proton egress upon light activation. In addition, Neutron diffraction will define the protonation states of the OEC and the surrounding environment. Applying both techniques requires a deep understanding of the crystallization procedures and using servals crystallization techniques to produce different sizes of dPSIIcc crystal, ranging from a few μm to a few mm, depending on the nature of the technique. Furthermore, PSII protein is a membrane protein, and understanding the protein-detergent complex is crucial to enhance the protein crystallization and improve the crystal diffraction quality. The Small-angle Neutron scattering (SANS) and Small-angle X-ray scattering (SAXS) tool can provide answers to the detergent belt structure and characteristics. Moreover, SAXS and the Dynamic Light Scattering (DLS) allow us to gain information about the monodispersity of the protein in solution prior to crystallization. In this section, an introduction to these techniques is provided.

I.6.1. Protein crystallization

Protein crystallization is considered one of the most experimental techniques used to obtain a detailed structure of large macromolecules by collecting the diffraction patterns mainly of X-rays or Neutron at atomic resolution. However, uncovering the structure of a protein by crystallization requires fulfilling two main parameters, which are considered the bottlenecks of this technique. The first one is to obtain a highly purified monodispersed protein sample, which is critical to fulfilling the second parameter by getting high-quality protein crystals.

The protein crystallization process transforms the protein molecules present in the solution in a disordered state into a highly ordered solid state, the crystalline state. The crystals through this process are formed through three main phases. The first one is the nucleation phase, in which a thermodynamically stable aggregate, also known as the critical nuclei, is formed in a well-ordered format in three-dimension from a few protein molecules. To reach this phase is very important to overcome the kinetic barrier of the state transition required to form the protein crystals (Figure 26). Once the formed nuclei

are becoming above the critical size, which is having the high energy intermediate, they will grow further in the second phase, the growth phase, by incorporating further molecules from the solution into the surface of the crystal. The crystals will continue growing until reaching the last phase, the end of crystal growth, which is happened when the protein molecules in the solution decrease significantly or other impurities present in the solution diffuse to the surface of the crystals[163, 164].

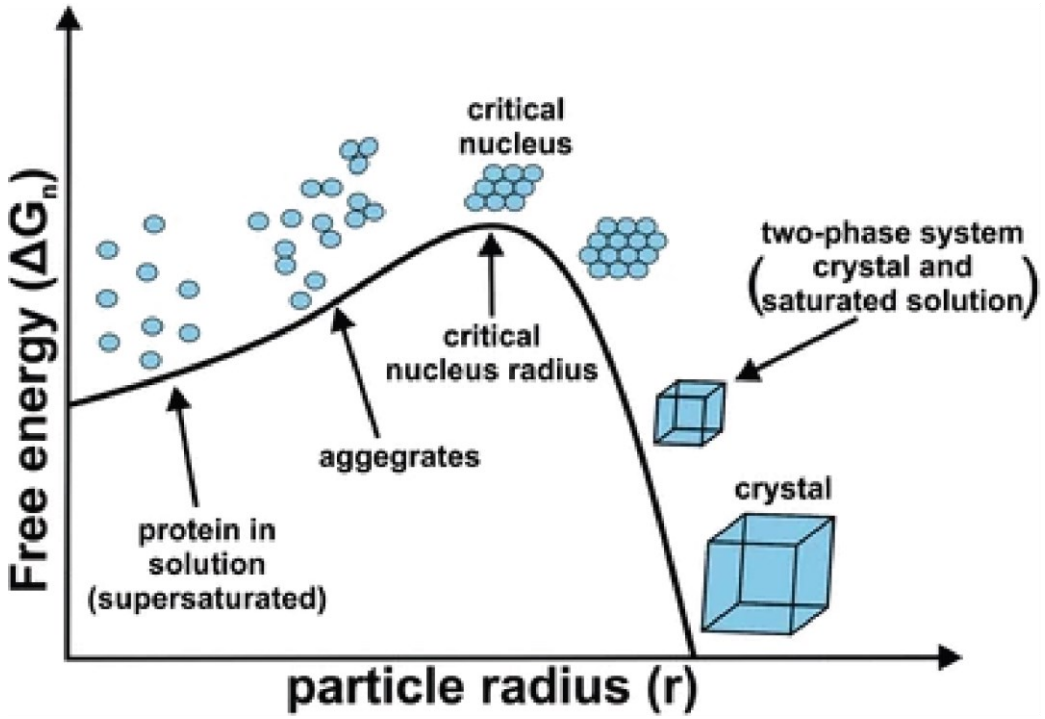

***Figure 26** The relation between the change in Gibbs free energy (ΔG_n) and the crystal nucleus formation with radius r. The figure is modified from[163].*

Inducing protein crystal formation requires bringing the protein solution gradually from the undersaturation condition to the supersaturation conditions using a precipitant. With gradually increasing the saturation level of the solution, the solution becomes supersaturated. This supersaturation region is subdivided into three different zones based on the level of saturations; metastable zone, nucleation/labile zone, and precipitation zone, as represented in the phase diagram (Figure 27). At a low supersaturation level in the labile zone, the critical nuclei form and become stable. Pushing the conditions towards an even lower supersaturation level to the so-called metastable zone leads to further growth of the crystals. However, this zone is a suitable zone for crystal growth; the formation of critical nuclei cannot take place in it. On the other hand, under a high supersaturation level in the precipitation zone, the molecules in the solutions self-aggregating in a disordered arrangement forming amorphous precipitate[163-165].

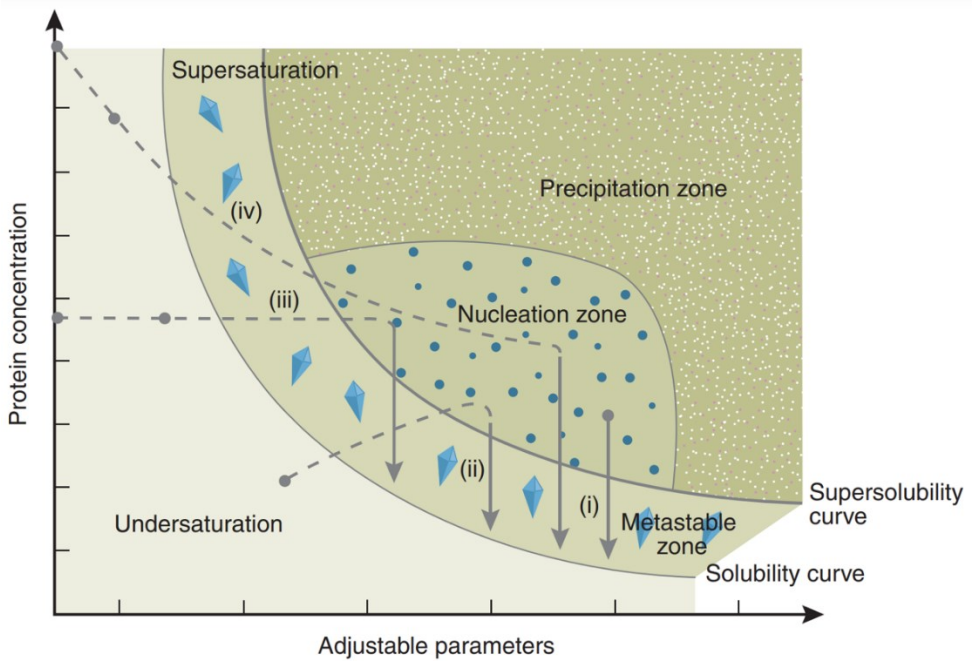

Figure 27 Illustration shows the phase diagram of protein crystallization. *The adjustable parameters in the x-axis can include additive concentration or pH or temperature, or the precipitant concentration. The solubility curve divides the diagram into an undersaturated and supersaturated zone. The protein molecules stay in the solution in the undersaturated zone. With increasing the precipitant concentration, the solubility line is crossed, and the solution starts to become supersaturated. The metastable zone represents the crystal growth zone. Once the nucleation zone is reached, the critical nuclei can reach a critical size and become stable. Formed crystals need to reach the crystal growth zone again so they can continue to grow. At too high supersaturation, precipitation of the protein takes place amorphously. The crystallization paths of reaching the nucleation and metastable zones are shown for the main crystallization methods: (i) microbatch, (ii) vapor diffusion, (iii) dialysis, and (iv) Free interface diffusion (FID) (The x-axis, in this case, is the precipitant concentration). The starting points for these methods are represented by a gray circle. Only in the case of FID and Dialysis methods, two starting points are shown since the protein sample can/ not be mixed with a precipitant in a low concentration. The figure is taken with kind permission from*[166].

Crystal formation depends on several factors and parameters, including sample purity, sample concentration, detergent, buffer system, additives, pH, temperature, and the precipitant[167]. Screening and fine-tuning each of these parameters are necessary to get a high-quality crystal. That means getting a protein crystal that is packed efficiently in an array of several identical unit cells, the building block of the crystal (Figure 28). Protein purity and homogeneity are essential factors for crystal growth and for getting high-quality crystals. For membrane proteins, it is necessary to use an amphiphilic detergent that helps in mimicking the lipid bilayer present in the natural environment through its hydrophobic group, so the protein molecules maintain the native structural conformation and are soluble in the solution because of the hydrophilic group of the detergent. Generally, detergents are subcategorized based on the properties of their hydrophilic groups, so-called headgroups, into three groups ionic, nonionic, and zwitterionic detergent. So for membrane protein crystallization, it is crucial to choose the appropriate

detergent since it can interact and contribute to the crystal contacts and be divided into types I and II based on the packing type (Figure 29)[168, 169]. In addition, choosing the right buffer system is also crucial to avoid the change in the pH, which can affect protein stability and activity as well. Screening for small molecule additives could help to improve crystallization[170, 171] by providing favorable interactions between protein molecules in the crystal. Precipitants are the main crystallizing agents that are usually categorized into four categories salts, polymers, nonvolatile, and volatile organic solvents[171].

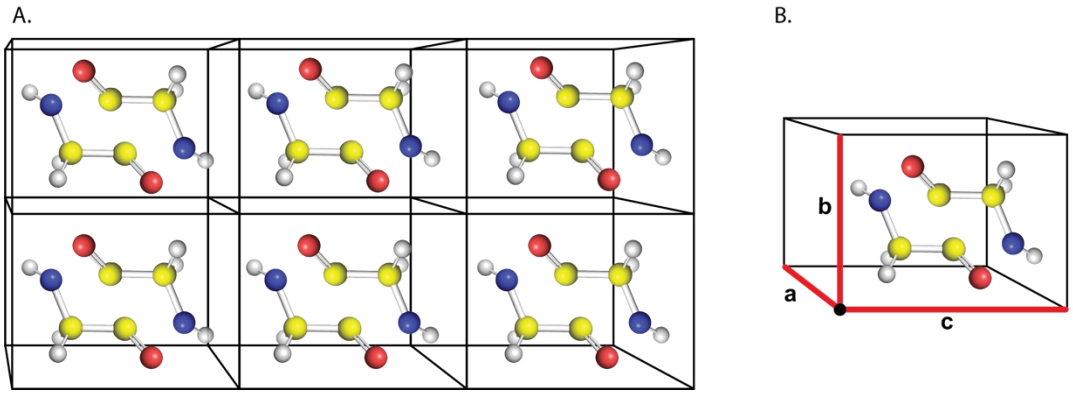

Figure 28 An example of a crystalline lattice consists of six unit cells. *Each unit cell contains two molecules of glycine. B shows the unite cell dimension (a, b, c) highlighted in red. The figure is modified and adapted from*[167].

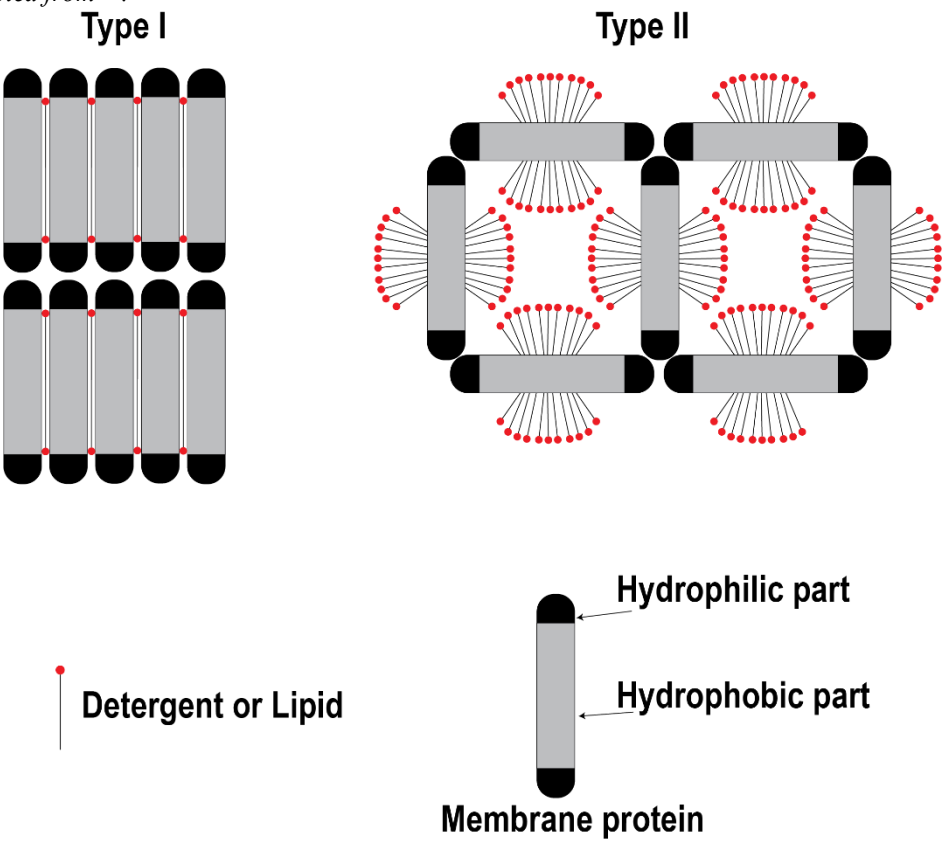

Figure 29 Crystal packing types of membrane protein crystals. *Crystallization of membrane protein solubilized in detergents usually generates type II crystals growing in 3D dimension connected through polar interactions. 3D Type I crystals connected through hydrophobic interactions usually grow using large amounts of detergent or lipid. The figure is modified and adapted from*[168].

Crystal seeding techniques

Crystal seeding is one of the powerful techniques in crystallography that is widely used to optimize crystallization conditions and improve crystal quality[172, 173]. In this process, homogenous or heterogenous crystal seeds are used under proper crystallizing conditions to promote crystal nucleation and/or crystal growth. The technique depends on separating the nucleation and the growth events and hence controlling the crystallization process. As mentioned before, nucleation usually takes place at a higher level of supersaturations, while the growth of ordered crystals happens at a lower level of supersaturations in the metastable zone. So, inserting a crystal seed and/or seeds in the optimal condition for the crystal growth represented in the metastable zone will avoid unnecessary nucleation and help control crystal size, quality, and polymorphism. Moreover, the reproducibility of getting the favored crystals will be guaranteed by developing a seeding protocol[172, 174].

Controlling the size of the crystals by seeding can be achieved by either applying microseeding or macroseeding techniques. In the microseeding (Figure 30), submicroscopic seeds, usually from smashed crystals, are transferred to the optimal condition for the metastable zone, producing crystals in the micro to the medium size range. While in macroseeding (Figure 30), a single crystal of medium size (50-100 μm), after being washed several times, is transferred to the metastable zone, producing a single large crystal in the macro size range[171, 172].

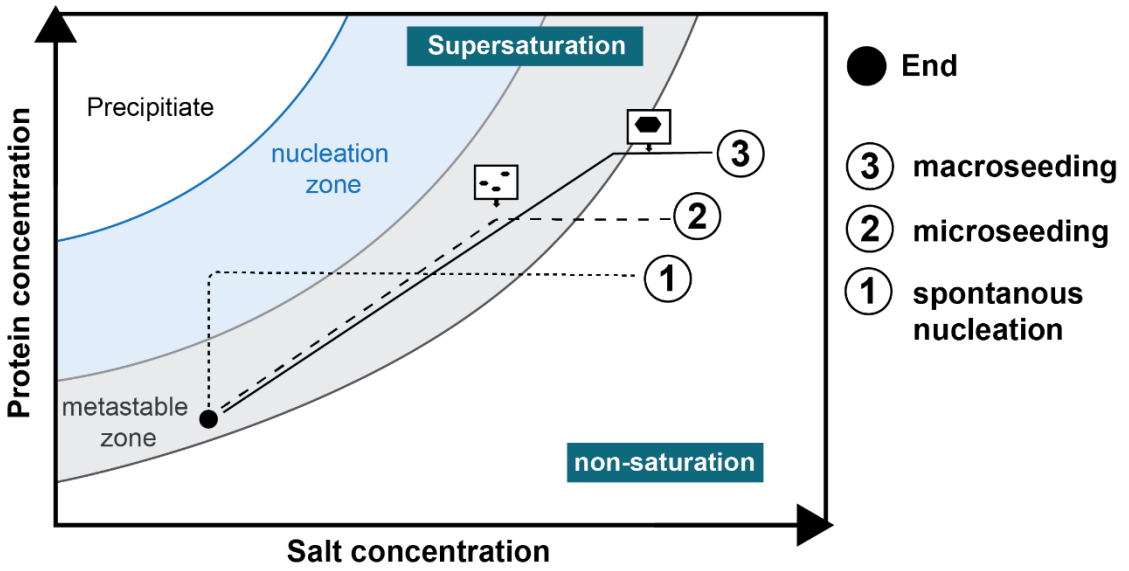

Figure 30 Schematic illustration showing the crystallization phase diagram for trimeric photosystem from Thermosynechococcus elongatus. *The scheme shows the crystallization routes for reaching the metastable zone through applying three different crystallization techniques: spontaneous nucleation, microseeding, and macroseeding against low salt concentration. All the techniques are done by dialysis. The figure is adapted from*[175].

Several factors affect the seeding techniques and are critical to consider, including seed handling, seed size, seed surface, and well-defined metastable zone width. In microseeding, previous nucleated crystals in a stabilizing crystallization buffer are smashed in several ways, including sonication or seeds beads or homogenizers to give the seed stock. Serial dilutions from the seed stock are prepared afterward to provide us with a gradient of seed numbers to be capable of experimentally testing and controlling the size and distribution of the produced crystals. The diluted seeds are transferred later to a pre-equilibrated drop of protein in the metastable zone through pipetting or streaking. In the other seeding technique, macroseeding, seed handling, and loading are considered quite intensive tasks. In this technique, only a single parent crystal is selected and transferred very carefully to a pre-equilibrated drop of protein in the metastable zone. This crystal must be washed multiple times using a buffer in the undersaturation condition to remove the external layer nuclei and give the crystal a fresh surface. In both techniques, selecting high-quality crystals as the source of the seeds to avoid accumulating defects during the growth must be considered and carefully studying the phase diagram of the crystallization condition to define the width of the metastable zone. Following these factors will guarantee a reproducible protocol that can be applied on most of the purified batches and over time and through which the crystal size can be controlled, distribution, quality, and crystallization timing[171, 172, 174].

I.6.2. Serial femtosecond X-ray crystallography

Understanding the mechanism of the water oxidation by the OEC in the PSII requires obtaining high-resolution atomic models for the different S-states as well for time points during each transition. The high-resolution structural models of the meta-stable S-states provide key information to interpret more precisely the results of many other techniques, *i.e.,* Extended X-ray absorption fine structure (EXAFS), Electron Paramagnetic Resonance Spectroscopy (EPR), Nuclear Magnetic Resonance (NMR), X-ray emission spectroscopy (XES), X-ray absorption spectroscopy (XAS). Furthermore, accumulating enough snapshots during each transition can provide the scenes to an atomic movie of the enzyme in action. Synchrotron radiation provided the chance to obtain the structural model of the dark-stable (S_1) state of PSII at cryogenic temperature. Albeit the conventional Synchrotron X-ray sources expose the metalloenzymes, including the PSII, to severe radiation damage, despite collecting data at a cryogenic temperature[176-184].

The very short X-ray (< 50 fs) micro-focused pulses of the X-ray free-electron lasers (XFEL) with high brilliance and coherence beams provide an opportunity for a new era of crystallography [185]. XFEL paved the road for radiation damage-free diffraction data collection at room temperature (RT) and provided new approaches for time-resolved (TR) serial femtosecond crystallography (SFX) experiments[186]. TR-SFX requires nano/microcrystals, which potentially have lower disorder[187]; hence it increases the probability of collecting high-resolution diffraction data. Due to the high brilliance of the XFEL beam and the micro focusing, high-resolution diffraction data can be observed[187]. The approach has been demonstrated by Kern *et al.* using PSII microcrystals at Linac Coherent Light Source (LCLS) (SLAC, USA). An electrospun liquid microjet was used to probe different intermediate states of the Kok's cycle in PSII[46, 188, 189]. Several challenges face the collection of TR-SFX data collection at room temperature. As establishing a reproducible microcrystallization protocol that produces a homogenous microcrystal suspension with a monodisperse crystal size distribution[190], the presence of a reasonable microcrystal delivery system that enables accurate microcrystals pumping and propping with reasonable hit rate and stable running time. An electrospun liquid microjet was used to probe different intermediate states of the Kok's cycle in PSII[46, 188, 189] and recently using Drop-on-demand sample delivery method[51, 191]. Also, Kupitz et al. reported RT diffraction data collection of PSII using microcrystals in a gas-focused liquid jet system[192]. In addition, Suga et al. reported the dark-adapted S_1-state crystal structure using XFEL shots taken from a fixed target large crystals at a cryogenic temperature[47].

Overall, the resolution quality of the XFEL data of PSII has continuously improved up ~2.0 Å, and Hussein *et al.* has pushed it further to 1.89 Å resolution (Figure 31)[193].

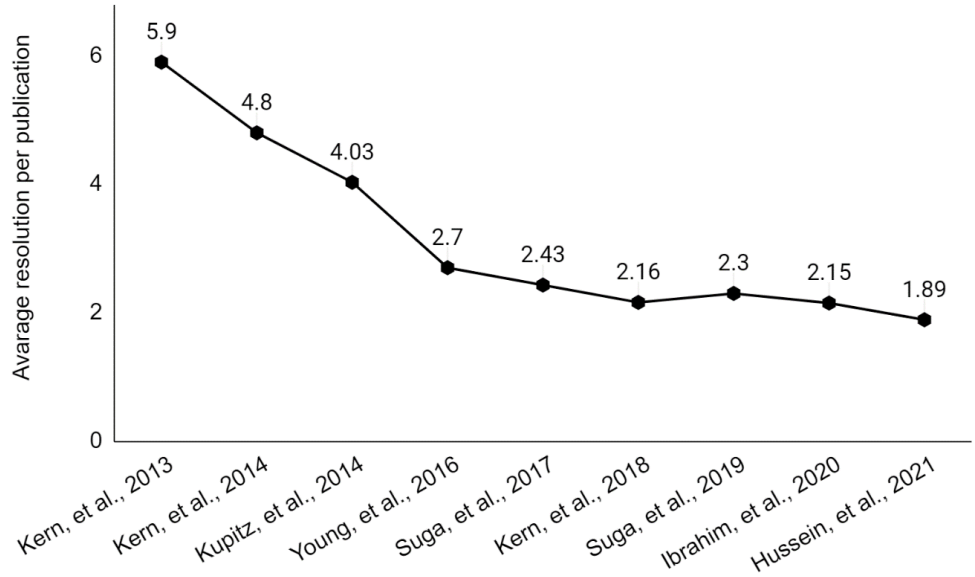

Figure 31 Quality improvement of dPSIIcc microcrystals up to September 2021.

I.6.3. Neutron diffraction studies

Neutron crystallography is a powerful tool in determining the exact location of the hydrogen atoms (H) in the crystal structure[194-196]. Such information is crucial in assigning the protonation state of the catalytic active amino acid residues, defining the hydrogen (H) bonds, and understanding how the H is transferred between residues and solvents. Using X-ray crystallography, collecting diffraction data at a resolution < 1.0 Å is required to locate the hydrogen atoms, and at a resolution of ≤ 0.83 Å will lead to hydrogen bond length that agrees with the neutron data[197, 198]. Since such high atomic resolution is extremely hard to achieve, especially for large membrane proteins as PSII, Neutron crystallography is considered a complementary tool to X-ray crystallography, which can provide precise coordinates for the H atoms at a moderate resolution of around 2.0 Å[199]. Furthermore, Neutron crystallography has other advantages, including the ability to collect diffraction data at room temperature relevant to the functional temperature without any radiation damage.

On the other hand, Neutron crystallography has some disadvantages and complications[165, 194, 195, 200]. The major one is the weakness of the neutron beam flux that is much weaker by many orders of magnitude in comparison to the synchrotron X-ray beam. To overcome this bottleneck, very long data acquisition times and large crystals

(~1 mm^3) are required. Another one is that the H atoms have a very high incoherent scattering cross-section (Table 5 and figure 32), leading to a low signal to noise and a high incoherent scattering background since the H atoms contribute by almost half of the atoms in macromolecules. Moreover, the coherent scattering length of the H atoms is in the negative (-3.741 fm), while the coherent scattering length of other heavier atoms like carbon (C), nitrogen (N), and oxygen (O) are positive (Table 5 and figure 32). These differences result in canceling density in the generated Fourier maps, leading to wrong modeling for the molecules and atoms. Owing to that, it is necessary to replace the H atoms with the hydrogen isotope deuterium (D). The advantages of this replacement are that the D atoms have a significantly lower incoherent scattering cross section than the H atoms. In addition, the D atoms have a positive coherent scattering length (6.671 fm) similar to C, O, and N. Therefore replacing the H atoms with D atoms will help in enhancing the signal to noise ratio, dramatically decreasing the incoherent scattering background and contributing with obvious positive peaks in the Fourier maps, and hence improving the data interpretation and analysis. Besides that, D atoms are facilely visible to be assigned using neutron diffraction data at 2.5 Å or better as they have higher average reflection intensities. In comparison, the H atom is more visible at a higher resolution of around 2.0 Å or better. Partial deuteration/ pre-deuteration to substitute the waters and the titratable H atoms, which represent nearly 25% of all the H atoms present in any protein, can be achieved either by growing the crystals using crystallization buffer prepared using D_2O, which will require further optimization for the crystallization conditions or by soaking the crystals in the deuterated mother liquor. Substituting the remaining non-titratable H atoms will require optimizing the growth of organisms expressing the protein in a deuterated media. However, despite the complications of achieving this step, several advantages and benefits can be gained, including the ability to collect data from relatively smaller size crystals around 0.5 mm^3 or less and reduce the data collection time.

Table 5 Values of X-ray scattering lengths, Neutron scattering lengths, and incoherent cross sections for the most common atom present in proteins

Isotope	Z	X-ray scattering length (fm)	Neuton scattering length (fm)	Incoherent cross section (10^{-15} fm^2)
^1H	1	0.282	-3.74	80.27

$^{2}H(D)$	1	0.282	6.67	2.05
^{12}C	6	1.69	6.65	0
^{14}N	7	1.97	9.37	0.5
^{16}O	8	2.16	5.8	0
^{32}S	16	4.51	2.8	0

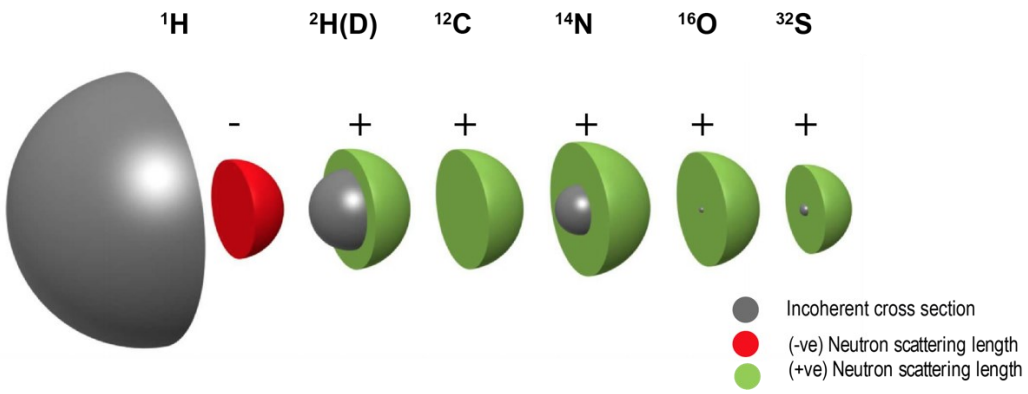

Figure 32 Relative Neutron scattering lengths and incoherent cross sections for the most common atoms present in proteins. *The figure is modified and adapted from*[195].

Several neutron facilities that offer neutron crystallography are present across the world. The neutron beams in these facilities are generated either in nuclear reactor sources through the nuclear fission process of the ^{235}U isotope or in spallation neutron sources through bombarding a target such as liquid mercury with pulsed protons[201, 202]. The neutron diffraction methods in the nuclear reactor sources are either the monochromatic diffraction method, also known as Bragg method, or Laue diffraction method (Figure 33). In the monochromatic method, the incident neutron beam is monochromatic, and the crystal must rotate to allow collecting diffraction frames covering the total range of rotation to ensure completeness of the data. This method enhances the signal-to-noise ratio of the data[196, 200]. On the other hand, the incident neutron beam in the Laue diffraction is not monochromatic but consists of a full spectrum of different wavelengths; due to that, it's also called white beam or polychromatic beam, and the crystal, in this case, stays stationary. Each wavelength will lead to diffraction from different crystal

planes that have to be collected, making the analysis a bit complicated[196]. The neutron diffraction at the spallation neutron source is applying time-of-flight (TOF). Laue methods determine the wavelength of the reflected beams reaching the detector and improve the signal to noise of the data collected[194, 196].

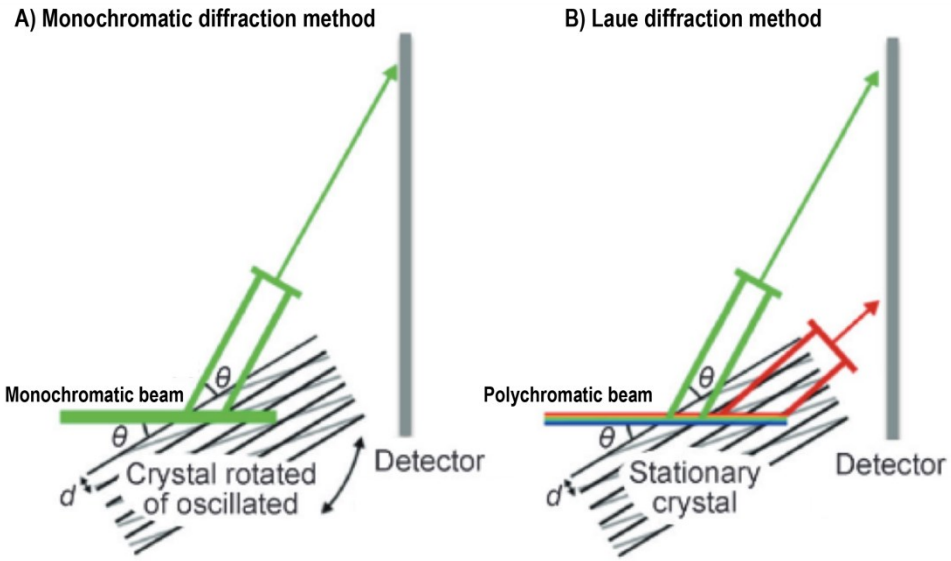

Figure 33 Monochromatic (A) and Laue (B) single-crystal diffraction method. *The space between the crystal planes is represented by d. θ represents the angle between the incident beam and the scattered plane. The figure is modified from*[203].

The Spallation Neutron Source (SNS) located at Oak Ridge National Laboratory (ORNL) in Oak Ridge, Tennessee, has a Macromolecular Neutron Diffractometer (MaNDi) applying time-of-flight (TOF) Laue neutron method with 2.15 Å or 4.3 Å wavelength bandwidth selected from 1 to 10 Å. The detector is spherical to completely cover the crystal sample with a distance to the sample that varies between 39- 45 cm max. It is supported by 40 SNS Anger cameras, providing the detector with 4.1 sr coverage. MaNDi is one of the spallation sources that allows diffraction data collections from crystals with large unit cells up to 300 Å[204]. This advantage makes collecting neutron diffraction data for PSII crystal is feasible.

I.6.4. Small-Angle Scattering

Small-Angle Scattering (SAS) is an efficacious tool to study the structural properties of a broad range of molecular sizes of particles, including biological macromolecules ranging from 1 nm to several hundreds of nm at low resolution[205]. The measurements are conducted under soluble conditions, using small amounts of materials in solution. Apply this technique allow us to study the structure of the protein molecules

and give us information about the overall shape and interactions between complexes in solution and under functional conditions[206]. Since PSII is a membrane complex protein, it needs to be solubilized using detergent molecules. As a result, the hydrophobic core of the isolated protein is always surrounded by a detergent belt in a solution. Understanding the structure of the dPSIIcc-detergent complex in solution is very crucial to determine how the detergent belt is formed around the protein molecule and if it is stable or not. Noteworthy, the detergent molecules form micelles at the critical micelle concentration (CMC). Whereas, at the critical solubilization concentration (CSC), a stable detergent belt around the protein is formed in an aqueous solution[207, 208]. Prior to protein crystallization, it is important to have a stable protein-detergent complex with almost no free micelles in the solution, which is assumed to be achieved if we are right above the CSC[208]. Defining these conditions can help in having well-ordered crystals. Therefore, using the SAS technique is extremely suitable to investigate PSIIcc-detergent complex in solution.

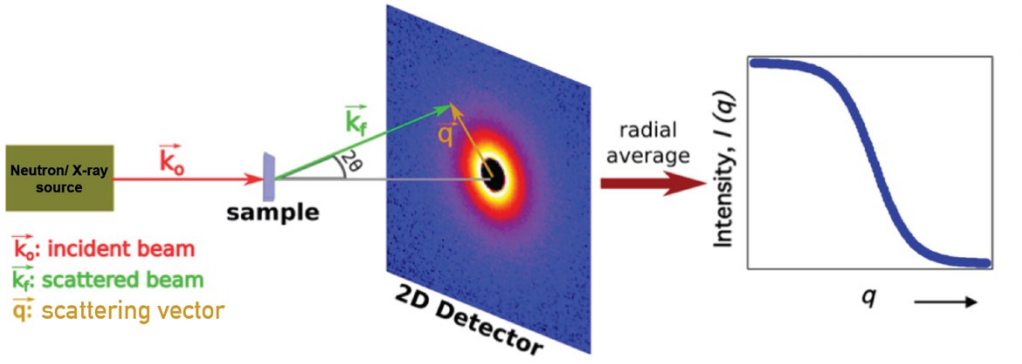

Figure 34 Schematic illustration of a small angle scattering experiment. The figure is modified from[209].

SAS can be performed using a monochromatic beam of X-ray (Small-angle X-ray scattering, (SAXS)) or Neutron (Small-angle Neutron scattering, (SANS)) radiation. The aim is to measure the scattering intensities produced at small angles by the sample interacted with the beam versus the scattering vector (q) (Figure 34)[210]. The scattering vector (q) is defined as:

$$q = \frac{4\pi}{\lambda} \sin\theta, \qquad (16)$$

where λ is the wavelength of the incident beam and θ is half of the scattering angle. The analysis of the collected data can be achieved using the classical Guinier approximation, assuming having monodispersed samples. The classical Guinier approximation can provide us with information about the radius of gyration (R_g), which is defined as the average distance from the mass-weighted point of a molecule[211]. Therefore, it is also

helping verify the aggregation and the monodispersity of the tested sample in solution. The relation between the measured intensity I(q) and the R_g is defined accordingly:

$$I(q) = I(0) \exp\left(-q^2 \frac{R_g^2}{3}\right), \quad (17)$$

where I(0) is the forward scattering and R_g is the radius of gyration.

Furthermore, the measured intensity I(q) is related to the pair-distance distribution function, P(r)[211]. Based on the P(r), the overall shape of the molecule can be modeled using several software programs[212-214].

SAXS is like crystallography; both are based on elastic scattering. If a monochromatic wave interacts with a particle, the electrons of its atoms become sources of secondary waves. Unlike crystallography, where the secondary waves are coming from identically oriented molecules. In SAXS, the secondary waves are coming from randomly oriented and freely moving particles in solution. Therefore, the orientation information is lost; however, the interatomic distances can be obtained, and the overall structural parameters as well the low-resolution shape[215]. The scattering intensity is proportional to the number of electrons, the higher the number, the stronger the scattering intensity. On the other hand, in SANS, the neutrons interact with the nuclei of the particle atoms, and the correlation between the scattering length and the number of the neutrons is somewhat irregular. Albeit, the scattering length of the hydrogens is tremendously different from that of deuterium (Table 5)[215], which makes SANS able to study the structure of a multi-protein complex and dissect its components independently by varying the H_2O/D_2O ratio to achieve different contrasts (Figure 35). Using the contrast variation via solvent exchange (H_2O/D_2O) and combining both techniques, SANS and SAXS, provide a powerful tool to study the detergent belt surrounding the PSII particles, as well as investigate the presence of an excess of free micelles.

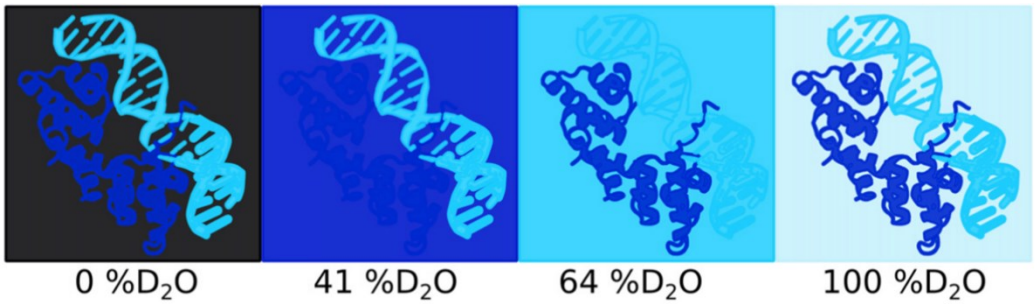

Figure 35 Schematic illustration showing the contrast variation effect in the SANS experiment for protein-DNA complex (PDB ID :1LMB) by varying the H_2O/D_2O ratio. *The figure is taken from[209]. The copyright lies with the authors; original work can be found here: https://doi.org/10.1016/j.csbj.2016.12.004*

I.6.5. Dynamic Light Scattering

Dynamic Light Scattering (DLS) is a powerful technique to determine the particle size by tracking the fluctuation in the intensity of the light that is scattered by particles in the solution after being exposed to a monochromatic laser light over time. This leads to measuring the velocity of the Brownian motion of the scattered particles and hence correlate that with particles size, e.g., small particles will diffuse faster. The Autocorrelation Function (ACF) is used to correlate the change in the light intensity signal over time and calculate the translational diffusion coefficient (D_z). The hydrodynamic radii (R_H), which is defined as the radius of the sphere that diffuses at the same as the particles in the suspension, are then calculated using the Stokes-Einstein equation[216](18).

$$D_z = \frac{K_B T}{6\pi\eta R_H}, \quad (18)$$

where K_B = Boltzmann constant, T = absolute temperature and η = solvent viscosity.

All the purified dPSIIcc samples in the following studies were tested by DLS to investigate the monodispersity and the aggregation behavior prior to crystallization or prior to performing the SANS/SAXS experiment. However, it is noteworthy that measuring the excess of free micelles in the protein solution by DLS is not possible.

I.7. The scope and the aims of the work

The main goals of this work are to decipher the pathway of water insertion and proton release and to pave the way for tracking the change in the protonation state at the active catalytic site towards a better understanding of the mechanism of the water oxidation reaction in PSII. Therefore, three approaches were pursued: a) developing a new protocol for producing a single large crystal of the dimeric PSII core complex (dPSIIcc), b) Investigating the structure of the detergent-protein complex of βDM-dPSIIcc, and c) tracking the structural dynamics in the water channels connecting the OEC to the lumen during the $S_2 \rightarrow S_3$ transition in the Kok cycle.

A better comprehension of the protonation states and well-defining the hydrogen bonds can be achieved through applying Neutron diffraction measurements on PSII macrocrystals. To overcome the large crystal volume prerequisite to collect structural

data using Neutron diffraction, the intention in the first study (P2.1) is to deeply understand the crystallization procedures and to accommodate servals crystallization techniques to develop a crystallization protocol to reproducibly grow different sizes of PSII crystal, ranging from a few µm to a few mm.

PSII protein is a huge membrane protein complex and understanding the protein-detergent complex is crucial to enhance the protein crystallization and improve the crystal diffraction quality. For this purpose, in the second study (P2.2), SANS and SAXS were performed on homogeneous βDM-dPSIIcc solution samples prior to crystallization to analyze the structure of the PSII-detergent complex under functional conditions, including the presence of excess free micelles. The homogeneity of all protein samples used in this study was analyzed by DLS.

Elucidating the structural changes in the OEC upon light-activation and defining the accurate location of the water molecules, as well as understanding the H-bond networking, will improve our understanding of the water oxidation mechanism. During the $S_2 \rightarrow S_3$ transition, the first water substrate binds to the OEC between the Ca and Mn1. This event is accompanied by a proton release from the OEC towards the bulk. Therefore, in the third study (P1.3), the structural dynamics in the water channels connecting the OEC to the lumen during the $S_2 \rightarrow S_3$ transition were investigated by applying serial protein crystallography using XFEL at RT under the functional conditions. The aim was to uncover the pathways of the first substrate insertion and the proton egress.

II. Results

II.1. Optimizing Crystal Size of Photosystem II by Macroseeding: Towards Neutron Protein Crystallography

Authors: Rana Hussein, Mohamed Ibrahim, Ruchira Chatterjee, Leighton Coates, Frank Müh, Vittal K. Yachandra, Junko Yano, Jan Kern, Holger Dobbek, Athina Zouni

Reprinted with permission from Hussein, R., Ibrahim, M., Chatterjee, R., Coates, L., Müh, F., Yachandra, V. K., Yano, J., Kern, J., Dobbek, H., & Zouni, A. (2017). Optimizing Crystal Size of Photosystem II by Macroseeding: Toward Neutron Protein Crystallography. In Crystal Growth & Design (Vol. 18, Issue 1, pp. 85–94). Copyright 2017 American Chemical Society (ACS). Final published version: https://doi.org/10.1021/acs.cgd.7b00878.

Abstract

Photosystem II (PSII) catalyzes the photo-oxidation of water to molecular oxygen and protons. The water splitting reaction occurs inside the oxygen evolving complex (OEC) via a Mn_4CaO_5 cluster. To elucidate the reaction mechanism, detailed structural information for each intermediate state of the OEC is required. Despite the current high-resolution crystal structure of PSII at 1.85 Å and other efforts to follow the structural changes of the Mn_4CaO_5 cluster using X-ray free electron laser (XFEL) crystallography in addition to spectroscopic methods, many details about the reaction mechanism and conformational changes in the catalytic site during water oxidation still remain elusive. In this study, we present a rarely found successful application of the conventional

macroseeding method to a large membrane complex protein like the dimeric PSII core complex (dPSIIcc). Combining microseeding with macroseeding crystallization techniques allowed us to reproducibly grow large dPSIIcc crystals with a size of ~ 3 mm. These large crystals will help improve the data collected from spectroscopic methods like polarized extended X-ray absorption fine structure (EXAFS) and single crystal electron paramagnetic resonance (EPR) techniques and are a prerequisite for determining a 3D structure using neutron diffraction.

Introduction

Oxygenic photosynthesis is considered the basis for aerobic life on earth. It provides us with food and the oxygen present in our atmosphere. The light reactions of oxygenic photosynthesis take place mainly in two major protein complexes; photosystem II (PSII) and photosystem I (PSI). PSII and PSI have a unique capability to utilize light energy through performing light–induced charge separation and convert it into molecular oxygen and the stored chemical energy used to build up carbohydrates[28, 217].

PSII is a large multi-subunit protein complex located in the thylakoid membranes of cyanobacteria, green algae and higher plants. It acts as water-plastoquinone-oxidoreductase, catalyzing the electron extraction from water molecules[100, 218] coupled with the reduction of its final electron acceptor, a plastoquinone[75]. In cyanobacteria, the photosystem II core complex (PSIIcc) is typically homo-dimeric[219-221]. Each monomer has a molecular mass of 350 kDa and consists of a total of 20 subunits; of which 17 are membrane-intrinsic and 3 are membrane-extrinsic located at the lumenal side[28, 43, 222]. The PSII reaction center core consists of a heterodimer of the transmembrane subunits D1 (PsbA) and D2 (PsbD), harboring all of the redox-active cofactors necessary for the electron transfer and water splitting reactions, and is flanked by the two other large subunits CP47 (PsbB) and CP43 (PsbC). Central to water splitting in PSII is the oxygen-evolving complex (OEC) located at the lumenal side and ligated by carboxylate and histidine ligands of the D1 and CP43 subunits. The OEC consists of a cluster having four manganese (Mn) ions and one Calcium (Ca) ion connected by μ-oxo bridges (Mn_4CaO_5 cluster) [28, 73]. This metal complex cycles through five different intermediate states, known as S states (S0, S1, S2, S3, and S4), to facilitate the extraction of four electrons and four protons from two water molecules to form one dioxygen molecule[85, 223, 224].

Elucidating how the electronic and geometric structures change in the OEC during catalysis at each S state will pave the way for a better understanding of the mechanism of

water splitting and the formation of the O-O bond. The occurrence of structural changes during water oxidation have been demonstrated by several biochemical and biophysical techniques; including X-ray crystallography[39-44, 46-50, 73, 225], Fourier transform IR spectroscopy (FTIR) [136-139], extended X-ray absorption fine structure (EXAFS) [92, 100, 140-146] and electron paramagnetic resonance (EPR) [128-135]. The atomic resolution crystal structure of dPSIIcc in the dark stable S1 state from *Thermosynechococcus (T.) vulcanus* at 1.9 Å showed that the core of the metal cluster has the overall shape of a distorted chair [73, 222]. This distorted chair is formed by three Mn ions (Mn1-Mn3), four oxygen atoms (O1-O3 and O5) and one calcium ion, whereas the fourth Mn ion is located outside and is connected via μ-oxo-bridges through O4 and O5. Additionally, two water molecules are assigned to coordinate Mn4 (W1 and W2) and another two water molecules coordinate the calcium ion (W3, W4) [73]. The geometry of the Mn_4CaO_5 cluster revealed by the X-ray crystal structures[47, 73, 225] is an important step on the way to fathom the water splitting mechanism. EXAFS data collected from protein solutions, oriented membranes and single crystals provided precise information about metal-to-metal distances (Mn-Mn and Mn-Ca) and metal-to-ligand distances (Mn-O) with less reduction by X-ray radiation than the X-ray diffraction data [100]. In addition, EPR data gave insights into the electronic structure for the different intermediates of the metal cluster [133, 156, 226, 227]. But despite all the improvements in understanding the structure of the OEC using several approaches, the dynamic mechanism of water oxidization by PSII still remains elusive. In addition to the accurate location of the Mn - ions, Ca^{2+}, bridging oxygen, and the water molecules, we also need to resolve the protonation pattern surrounding the OEC.

In this study, macroseeding in a combination with microseeding is introduced under “PEG-out conditions” to produce large single crystals of dPSIIcc. These large crystals are ideal samples to improve the quality of the data obtained from various orientation dependent spectroscopic techniques that require highly concentrated protein sample like polarized EXAFS[228] and single crystal EPR[229, 230]. Using these crystals will help to enhance the signal-to-noise ratio (S/N) and to provide accurate measurements for each orientation. Therefore, having these large crystals will be very useful to extend the spectroscopic investigation of PSII. Furthermore, these dPSIIcc macrocrystals will help to overcome one of the main obstacles in applying neutron diffraction crystallography. Neutron diffraction studies are complementary to X-ray diffraction analysis. However, they require very large crystals (> 1 mm^3) in order to compensate for the weak beam flux of the available neutron sources [194, 231]. Through applying neutron diffraction on PSII,

radiation damage that usually happens through using synchrotron X-ray sources [184] will be completely avoided. In addition, neutron diffraction has the ability to visualize protons and can therefore help in mapping out water transport channels and revealing details of the hydrogen-bonding network surrounding the OEC, which is difficult to reveal using X-ray diffraction [194, 195, 232-234]. We note that the quality of trimeric Photosystem I (tPSI) crystals was improved by using a protocol based on the combination of micro- and macroseeding techniques under "reverse salting-in" conditions that was developed in 1998 by Fromme and Witt[235]. The improved tPSI crystals obtained by this protocol have been applied in both X-ray structure analysis[236] and electron spin resonance spectroscopy[237].

We developed a fast and reproducible macroseeding protocol, which results in the formation of dPSIIcc crystals of ~1.8 mm length in the long axis within ~ 2 to 3 days. Utilizing repeated seeding, we also produced larger dPSIIcc crystals of ~ 3 mm along the long axis and the details of the developed protocol are discussed in detail in this study. The starting point for this protocol are medium size crystals within the size range of 100 µm that are used as seeds after being washed in a pre-equilibrated drop containing dPSIIcc solution. The growth of too many crystals in the initial step of the crystal growth, which is known to be a general problem of macroseeding techniques [172, 238], was overcome by widening the metastable zone. Hanging drop plates were used to avoid crystals adhering to the wall of the plates and further possible mechanical damage that may happen when trying to transfer these large crystals. The generated dPSIIcc macrocrystals were examined by means of X-ray diffraction measurements at the Synchrotron (BESSY II, Berlin). Furthermore, the first neutron diffraction measurements on hydrogen / deuterium exchanged dPSIIcc macrocrystals were performed at the MaNDi instrument at the Spallation Neutron Source at Oak Ridge National Laboratory (ORNL, USA).

EXPERIMENTAL PROCEDURES

Cell Growth and Protein Purification

Cells of *Thermosynechococcus elongatus* BP-1 were grown and thylakoid membranes were prepared according to Kern et al. [220]. Dimeric PSIIcc (dPSIIcc) and trimeric PSI (tPSI) was extracted from the thylakoid membranes using n-dodecyl-β-D-

maltoside (βDM) as a detergent but with a concentration of 2 % instead of 0.55 %. PSIIcc and the trimeric PSI were separated chromatographically using a weak anion exchanger column (ToyoPearl DEAE; see Figure S1A). The higher concentration of 2 % βDM for the extraction results in a dramatic increase of the amount of extracted tPSI: It increased by a factor of three compared to using 0.55 % βDM (Figure S1). Interestingly, this is accompanied by a significant increase of the amount of the dPSIIcc compared to the monomeric form (mPSIIcc; Figure S2); usually a 1:1 ratio of PSIIcc monomer to dimer after purifying by DEAE column chromatography was obtained using 0.55 % βDM during extraction. In comparison, using 2 % βDM during extraction gave almost pure dPSIIcc and the monomeric form was rarely detected. These results are consistent with the results reported by Watanabe et al.[239] showing that the amount of dPSIIcc extracted relative to mPSIIcc increases with increasing the concentration of βDM from 0.5 % to 2 %. After the chromatography step, the fraction containing dPSIIcc was concentrated using Vivaspin ultrafiltration spin columns (Sartorious, Germany) with a cut-off of 100 kDa. The protein samples were washed twice with 100 mM PIPES (1,4-piperazinediethanesulfonic acid), pH 7.0, 5 mM $CaCl_2$, 5 % glycerol and 0.02 % βDM. Monodispersity and the homogeneity of dPSIIcc were enhanced by pre-crystallization at 0.75 mM chlorophyll (Chl) *a* concentration (equivalent to 8 mg/ml protein) for 12 hours at 4 ºC [220]. The microcrystals of dPSIIcc (Figure S3) were collected and re-solubilized followed by washing and concentrating to 4 mM Chl *a* (equivalent to 42.8 mg/ml protein). Then the sample was directly frozen and stored in liquid nitrogen. This pre-crystallization step was repeated twice and monitored by dynamic light scattering (DLS Wyatt Dynapro with 787 nm laser wavelength). These two pre-crystallization steps decrease the polydispersity of dPSIIcc from ~24 % to ~12 % (see Figure S4).

dPSIIcc Protein Concentrations Via Chl *a* Concentrations

Chl *a* concentration of dPSIIcc samples were determined as usual by extraction in 80 % aqueous acetone and using the extinction coefficient $\varepsilon_{(663nm)} = 74.000\ M^{-1}\ cm^{-1}$. As each dPSIIcc contains 70 Chl *a* pigment molecules, the dPSIIcc concentration is given by

$$\text{dPSIIcc conc. in g/L} = \frac{\text{Chl } a \text{ conc. in mol/L}}{70} \times 750.000$$

where 750.000 g/mol is the molecular mass of dPSIIcc.

Oxygen-Evolving Activity

Oxygen evolution activity of the purified dPSIIcc was assessed at room temperature (RT) using a Clark-type electrode (OxyLab, Hansatech instruments). All the measurements were performed under saturating light conditions to guarantee independence of light intensity. The dPSIIcc samples were diluted to a final concentration of 2 to 5 µM Chl *a* (equivalent to 21.4 – 53.5 mg. ml^{-1} protein concentration) using MCM buffer (20 mM MES/NaOH, pH 6.5, 20 mM $CaCl_2$, 10 mM $MgCl_2$). The artificial electron acceptor DCPQ (2,5-dichloro-p-benzoquinone) was added to the protein mixture at a final concentration of 3 µM. The Clark electrode was calibrated against air-saturated water and nitrogen-saturated water at atmospheric pressure at RT. The final dPSIIcc samples used for crystallization showed oxygen evolution activity rates ranging from 2900 to 4500 µmol O_2 (mg Chl *a* h)$^{-1}$.

Protein Crystallization and Studying the Phase Diagram

The phase diagram of the dPSIIcc/PEG 2000 system (Figure 1) was determined using a range of protein concentrations from 1 mM to 5 mM Chl *a* (equivalent to 10.7 – 53.5 mg/ml protein). The dPSIIcc protein dissolved in a buffer containing 100 mM PIPES, pH 7.0, 5 mM $CaCl_2$, 5 % glycerol and 0.03 % βDM was crystallized by mixing 1:1 with the crystallization buffer containing 100 mM PIPES, pH 7.0, 5 mM $CaCl_2$, 5 % glycerol and 5 – 10 % (w/v) of polyethylene glycol (PEG) 2000 as precipitant. Sitting drop crystallization plates (Hampton Research, USA) were used, and 1 ml of the crystallization buffer was added to the reservoir. All crystallization steps were done at 20 °C. Wells that did not show any crystal growth after 24 h incubation time were seeded with a single microcrystal (~ 50 µm) to differentiate between the unsaturated and the metastable zones.

Increasing the Width of the Metastable Zone

The unsaturated, the metastable and the labile zones of the dPSIIcc were identified at a Chl *a* concentration of 2 mM (final concentration after mixing with the crystallization buffer). The crystallization buffers contained different concentrations of $CaCl_2$ (5 mM, 10 mM, 20 mM, 40 mM) and PEG 2000 (5 % to 7.6 %; see Figure 2). Sitting drop crystallization plates (Hampton Research, USA) were used. 2 µl of the protein solution

at 4 mM Chl *a* (equivalent to 42.8 mg/ml protein) was mixed with the crystallization buffer in a ratio of 1:1, and 1 ml of the crystallization buffer was added to the reservoir.

Controlling the Concentration of PEG 2000 in the Crystallization Buffer

Precise PEG 2000 concentrations in the crystallization buffer were determined by measuring the refractive index (RI) using an Abbe refractometer (KRÜSS, model: AR2008). The standard curve was recorded at RT (20 °C) for a wide range of different PEG 2000 concentrations (0 – 10 %) in the crystallization buffer (see Figure S5 and Table S1). 5 µl from each buffer prepared were used to measure the RI and the corresponding concentration of PEG 2000 was calculated from the standard curve. The error in the concentration was approximately ± 0.15 %.

Macrocrystals Preparation

Microseeds Preparation

The dPSIIcc microseeding stock was prepared as described by Ibrahim et al. [190]. A group of dPSIIcc crystals (around 5 to 7 crystals in the size range of 400 µm) was transferred to an Eppendorf tube and filled up to 500 µl with the crystallization buffer containing 6 % PEG 2000 and 0.03 % βDM. A seed tool kit (Hampton research, USA) was used to crush the crystals by vortexing for a few minutes. The protein was mixed with the seed stock at a ratio of 1:4, respectively. Crystals were grown using hanging or sitting drop plates (Hampton research, USA). 1 ml of the crystallization buffer containing 6 % PEG 2000 was added to the reservoir (Figure 3). Medium size dPSIIcc crystals were produced at 20 °C within 4 to 5 hours (Figure 4).

Steps of Macroseeding

Day one (protein equilibration): The dPSIIcc protein at a concentration of 2 mM Chl *a* (equivalent to 21.4 mg/ml protein) was equilibrated in the metastable zone with crystallization buffer containing 20 mM $CaCl_2$ and 6.5 to 6.8 % PEG 2000. Drops were

equilibrated by vapor diffusion for one day at 20 °C in sitting drop plates (Hampton research, USA).

Day two: Each crystal prepared by microseeding (see section 2.7.1) with a size of 100 to 150 µm was washed in several steps going from high to low concentration of PEG 2000 (from 8 % to 4 %) in the crystallization buffer. This washing step aimed at removing the extraneous nuclei from crystals. The washed crystal was then transferred to 4 µl of the equilibrated dPSIIcc drop with a total concentration of 8 mM Chl *a* (equivalent to 85.6 mg/ml protein) per drop. The equilibrated drop having the washed crystal was then transferred quickly to the silicone greased cover slip (Marienfeld, Germany) and sealed above the hanging drop well (Hampton, USA) having 1 ml of the crystallization buffer with the same concentration of PEG 2000 that had been used during protein equilibration (Figure 5). The dPSIIcc seed crystals in the equilibrated dPSIIcc solution were gown slowly within 2 – 3 days at 20 °C.

Crystallographic Data Collection

The large crystals obtained were partially dehydrated by placing 1 ml of a buffer containing 100 mM PIPES, pH 7.0, 20 mM $CaCl_2$, 25 % PEG 2000, 30 % glycerol in the reservoir of the hanging drop plate for one day. Finally, the crystals were incubated in that buffer for 30 minutes and afterwards directly flash-cooled in a nitrogen gas stream at 100 K. XRD measurement were performed under cryogenic conditions at beamline 14.1 operated by the Helmholtz-Zentrum Berlin (HZB) at the BESSY II electron storage ring (Berlin, Germany)[240]. The data set was collected at 0.91841 Å X-ray wavelength and integrated and scaled with XDS[241] and XDSAPP[240].

Procedure of Hydrogen / Deuterium Exchange in dPSIIcc Macrocrystals and Neutron Diffraction Measurement

The dPSIIcc macrocrystals were grown in hanging drop plates (Hampton, USA) until they reached a size of approximately 2 mm as described in section 2.7.2. The buffer in the reservoir was exchanged with a buffer completely prepared using D_2O (100 mM PIPES, pD 7.0, 20 mM $CaCl_2$, 10 % PEG 2000). After two days, the crystals were partially dehydrated by gradual increasing the PEG 2000 concentration in the deuterated buffer until reaching 30 %. All crystals were left for another two days followed by being mounted and sealed in fused-silica capillaries with an inner diameter of 2 mm (Vitrocom,

USA) along with a drop of the deuterated buffer. The crystals were then transported to the Spallation Neutron Source (SNS) at Oak Ridge National Laboratory (ORNL in Tennessee, USA) to test them at the Macromolecular Neutron Diffractometer (MaNDI) instrument [242, 243]. The Laue neutron beam used in the experiment consisted of neutrons between 2.5 and 4.5 Å. Diffraction was detected using 40 SNS Anger cameras with a crystal to detector distance of 450 mm. MaNDi uses time-of-flight techniques[194] to separate Bragg reflections from a Laue experiment into wavelength-resolved monochromatic data slices. This technique reduces spatial overlap of reflections, which is vital for separating Bragg reflections from unit cells sizes above 150 Å[243] while also decreasing background and thus improving the signal to noise ratio for each reflection. A single ω angle was chosen for data collection and the crystal remained static during the 24 hour exposure time at room temperature (295 K).

RESULTS AND DISCUSSION

Phase Diagram and Macrocrystallization of dPSIIcc

Understanding and identifying the phase diagram of dPSIIcc provides us with the necessary data for controlling the growth of dPSIIcc crystals. A phase diagram of dPSIIcc protein using the crystallization buffer containing 100 mM PIPES, pH 7.0, 5 % glycerol, 5 mM $CaCl_2$ against PEG 2000 as a precipitant (see Figure 1) was determined using vapor diffusion as a crystallization technique, which was also used for macroseeding. The metastable zone (the saturation region), where the crystal growth is supported and no spontaneous nucleation is observed, was identified at different dPSIIcc concentrations between 0.5 and 2.5 mM Chl *a*. The width of this zone was within 1.46 % of PEG 2000 on average for those particular protein concentrations (0.5 to 2.5 mM Chl *a*). The width of this zone is increasing with decreasing protein concentration reaching its maximum at a protein concentration of 0.5 mM Chl *a*. However, transferring a single crystal with size ~100 µm into an equilibrated dPSIIcc solution in the metastable zone at low protein concentration (0.5 mM Chl *a*) did not result in any visible growth of the crystal. After many trials of inserting a crystal to equilibrated drops with different protein concentrations (0.5 mM Chl *a* to 2 mM Chl *a*), dPSIIcc with 2 mM Chl *a* proved to be the most stable and reproducible concentration for crystal growth. The borders between the metastable zone and either the undersaturation region or the labile zone, where

nucleation takes place, were identified to be below 5.3 % of PEG 2000 and higher than 6.6 %, respectively, for a protein concentration of 2 mM Chl *a*.

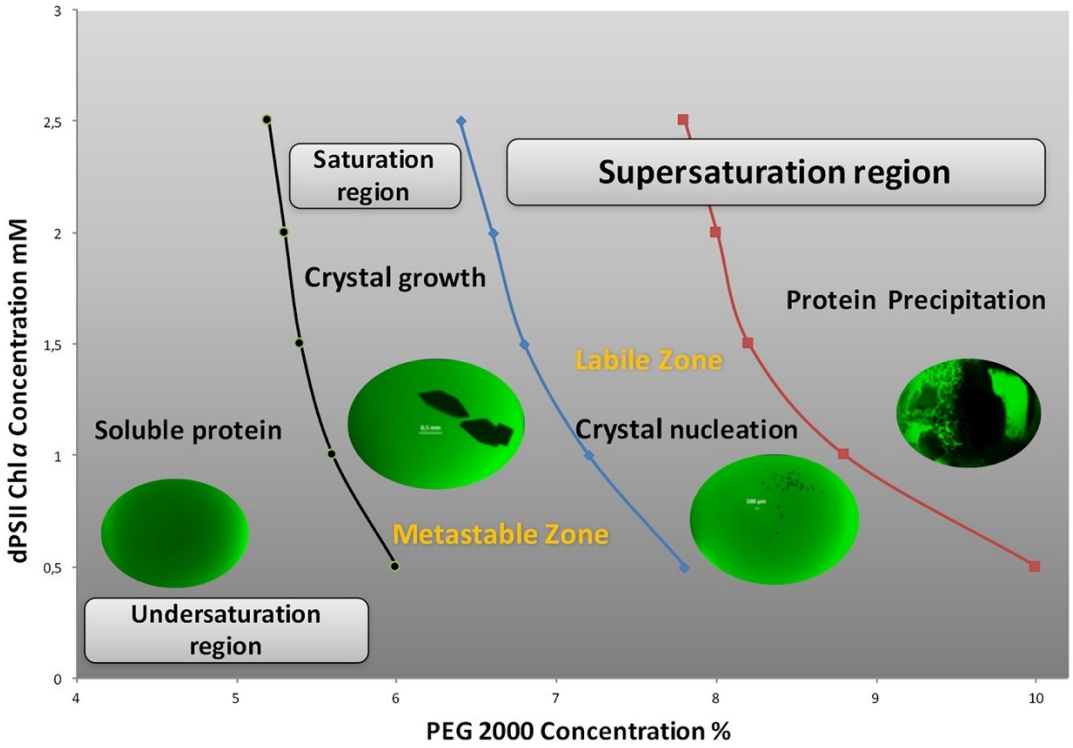

Figure 1 Schematic phase diagram for dPSIIcc (concentration in mM Chl a) against PEG 2000 as a precipitant.

Effect of $CaCl_2$ in Increasing the Metastable Zone Width for Macroseeding

The phase diagram determined in this study revealed the presence of a narrow metastable zone at different protein concentrations (see Figure 1). The metastable zone width varied between 1.2 % and 1.8 % of PEG 2000 for the dPSIIcc protein with 2.5 mM and 0.5 mM Chl *a*, respectively. Applying macroseeding steps at a dPSII concentration of 2 mM Chl *a* resulted in either dissolution of the inserted crystal in the equilibrated drop or in growth of too many small crystals in the drop, and rarely yielded a single large macrocrystal. Previous work [244, 245] has shown that salts like sodium chloride, potassium chloride and calcium chloride can increase or decrease the width of the metastable zone. The effect can vary from buffer to buffer and from crystal type to crystal type. We studied the effect of $CaCl_2$ present in our crystallization buffer on the metastable zone by varying it´s concentration (5 mM, 10 mM, 20 mM and 40 mM). As seen in Figure 2, the width of the metastable zone increases with increasing $CaCl_2$ concentrations. Consequently, increasing the $CaCl_2$ concentration also shifted the nucleation zone to a higher PEG 2000 concentration with little or no effect on the edge of the solubility border. The nucleation

phase is shifted by 0.8 % of PEG 2000 when using 40 mM instead of 5 mM $CaCl_2$, whereas the border between undersaturation and saturation zone is only shifted by 0.2 % of PEG 2000.

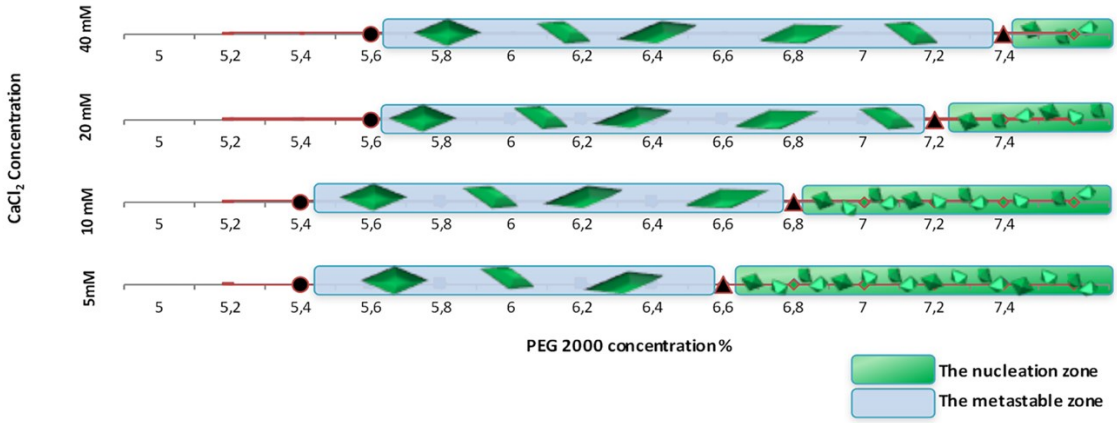

Figure 2 Schematic diagram showing the borders between the metastable zone and either the undersaturation or the labile zone of dPSIIcc with 2 mM Chl a against PEG 2000 at different CaCl2 concentrations. *Black circles represent the PEG 2000 concentration (%) where crystals start to dissolve, whereas black triangles represent the PEG 2000 concentration at which nucleation occurs and microcrystals start growing.*

Macrocrystallizations and Double Macrocrystallization of dPSIIcc

Crystal seeds for macroseeding act as a template on which further molecules of the protein will grow and assemble[238]. Homogeneity in the size and the quality of the crystal seed were achieved by applying the microseeding protocol developed by Ibrahim et al. [190] in which a group of well-shaped crystals suspended in the crystallization buffer having 6 % PEG 2000 was smashed with the use of the seed bead (Figure 3) to prepare the seeding stock. The number of seeds in the crystallization buffer was optimized by several dilution steps for the seeding stock until reaching the optimal concentration. This procedure enables controlling the crystal size distribution resulting in growing medium size crystals with a uniformed size of ~ 100 µm within a few hours (Figure 4) from mixing the seeding stock with the protein. The solubility of these crystals was determined. It was found that the crystallization buffer containing 4 % PEG 2000 represents the lowest concentration at which the crystals were stable for 15 to 20 minutes. Based on that, the extraneous layer of each single crystal was removed by transferring it into a series of four drops (500 µl each) containing the crystallization buffer with gradual decreasing the concentration of PEG 2000 from 8 %, where the dPSIIcc crystal is completely stable, to 4 %, where the crystal can melt completely. Each single crystal was incubated about one

minute in each drop and then transferred directly to 4 µl of an equilibrated dPSIIcc solution in the metastable zone. The crystal was left to grow for 2 to 3 days (Figure 5). On average, 60 % to 70 % of the seeded equilibrated drops yielded large macrocrystals with a size of ~1.8 mm along the long axis (Figure 6).

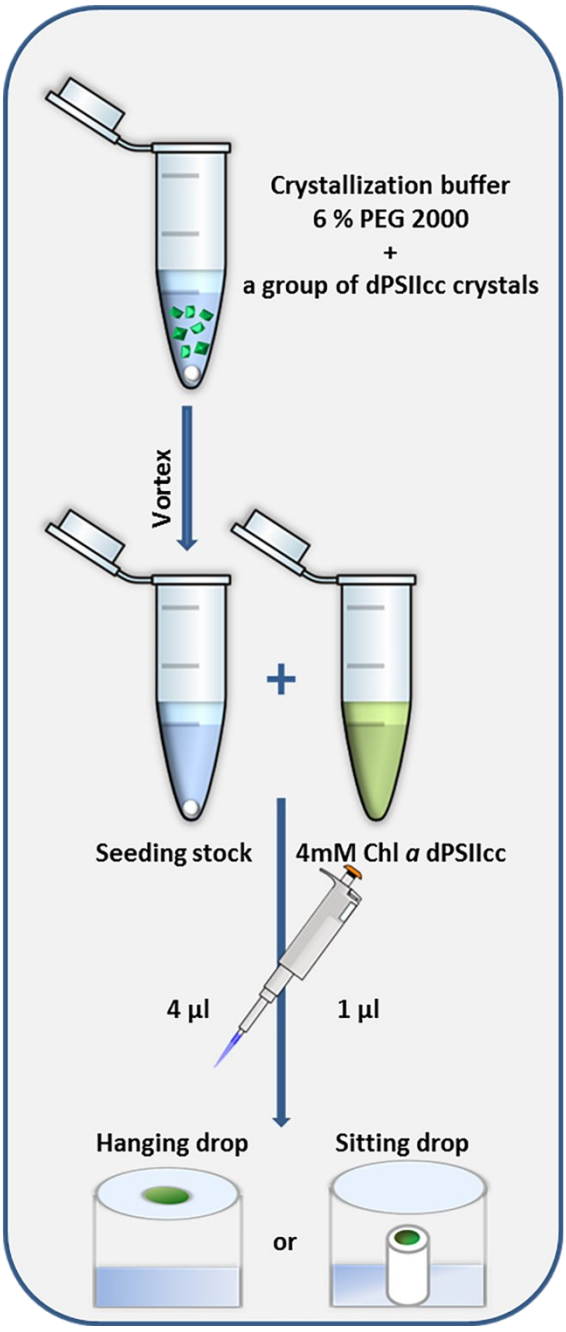

Figure 3 Schematic illustration showing the microseeding steps. *First the seeding stock is prepared by vigorously vortexing a group of crystals in the crystallization buffer containing 6 % PEG 2000 using a seeding bead. Then 4 µl of the seeding stock solution were mixed with 1 µl of the 4 mM Chl a dPSIIcc solution on the coverslip of the hanging drop plate or on the vessel of the sitting drop plate. The plates were left for a couple of hours to allow undisturbed crystal growth.*

Figure 4 Medium size crystals of dimeric PSIIcc obtained by microseeding.

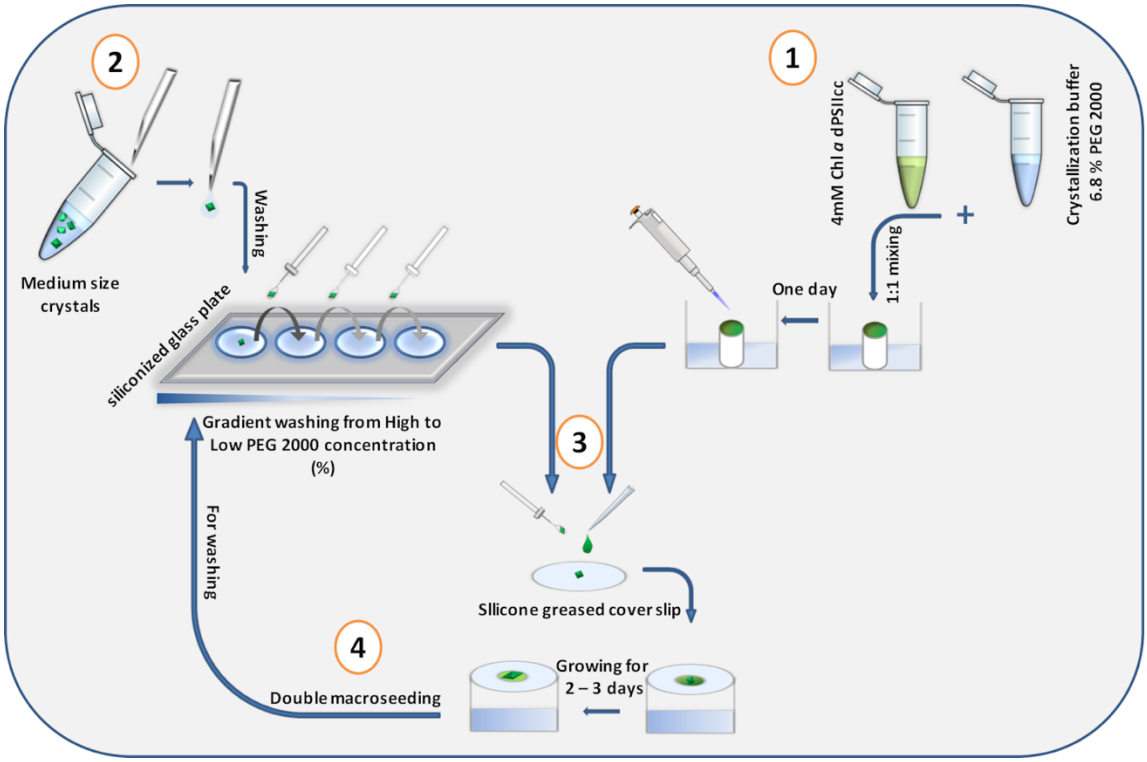

Figure 5 Schematic representation for the macroseeding and double macroseeding method. *At step one; dimeric PSIIcc was mixed 1:1 with the crystallization buffer containing 6.8 % PEG 2000 in a sitting drop plate. The plate was sealed and left for one day to equilibrate. At the second day (step 2), each single crystal was gently transferred for washing in 4 steps from high to low PEG 2000. In step 3, the crystal was first washed and then transferred to a silicone greased cover slip, where it was mixed with 4 µl of the equilibrated drop of dPSIIcc. The cover slip was quickly inverted on the hanging drop well containing 1 ml of 6.8 % PEG 2000 and was left to grow for one week. For double macroseeding (step 4), the large crystal obtained was transferred for serial washing with repeating step 1 and 3.*

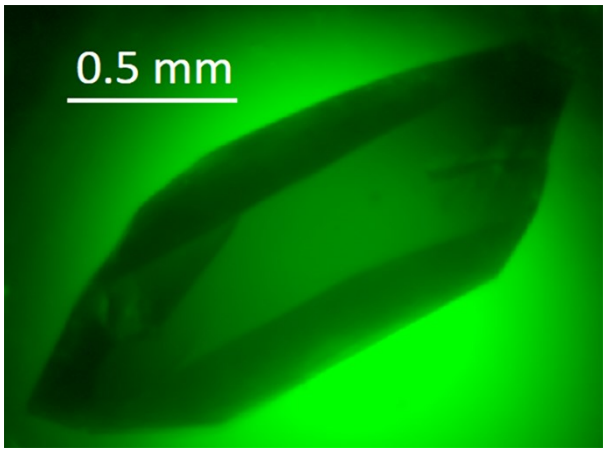

Figure 6 Single macrocrystal of dimeric PSIIcc obtained by macroseeding.

Crystallization buffers with different PEG 2000 concentrations have different refractive indices. Therefore, the refractive index (RI) was utilized to test each preparation of the crystallization buffer used for the protein equilibration in the metastable zone. In this way, the amount of dPSIIcc protein sample and time needed per setup was minimized. Also, we tried to maintain the shape of the drop on the coverslip to be as spherical as possible. As the equilibrated drop of dPSIIcc always contains 0.015 % of βDM, it was challenging to keep the droplet shape uniform and well-structured, especially as all macroseeding steps needed to be carried out as quickly as possible. Different kinds of siliconized cover slips as well as silicon oil were tested. Unfortunately, none of these treatments gave stable reproducible results. Finally, greasing the glass cover slip with silicone grease resulted in the formation of uniformly stable, spherical droplets (Figure 7).

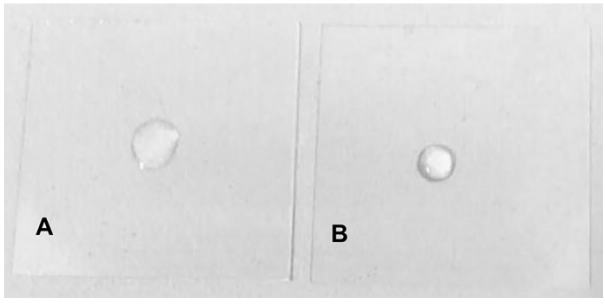

Figure 7 Siliconized cover slip versus silicone greased cover slip. *(A) Siliconized cover slip 22 mm × 0.22 mm (Hampton, USA) with 4 µl of the crystallization buffer containing 0.015 % βDM. (B) Glass cover slip 22 mm × 0.16 mm (Marienfeld, Germany) with a thin layer of silicon grease.*

In the double macroseeding protocol, the crystals resulting from the macroseeding with an average size of 1.5 to 2.0 mm were used as a seed in the next step. After being

washed carefully, the crystals were transferred to a 10 µl equilibrated drop of dPSIIcc solution. The success rate in the double macroseeding was around 30 % and the crystals grew up to ~ 3.0 mm (Figure 8). The small success rate is due to difficult handling and transferring of the large crystals without inducing stress to them. Such stress and the handling often leads to contamination of the equilibrated drops with other tiny seeds resulting in growth of multiple crystals in the same drop.

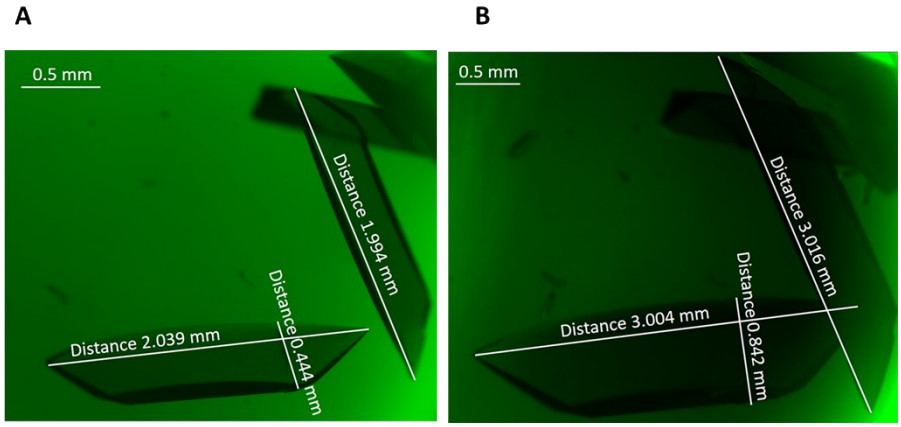

Figure 8 Macroseeding and double macroseeding crystals of dPSIIcc*. (A) Macrocrystals of dPSIIcc obtained after the first round of macroseeding and (B) the same macrocrystals after being washed and incubated with an equilibrated amount of dPSIIcc in the metastable zone.*

Results of the X-Ray diffraction studies

A rectangular-shaped single dPSIIcc crystal with the dimensions ≈ 2 × 0.60 × 0.40 mm^3 was used for collecting a diffraction data set. The dataset was processed to 4.11 Å resolution with a completeness of 88.9 % (Table 1). The crystal belonged to the same space group as the unseeded βDM-dPSIIcc crystals [39, 41, 43]; having the orthorhombic space group $P2_12_12_1$ with unit cell constants a = 126.59 Å, b = 223.15 Å, c = 305.46 Å. The diffraction pattern revealed clear diffraction spots without signs of twinning or the presence of polycrystals. It also showed an anisotropic diffuse background near the highest resolution shell (see Figure 9). The same is observed with the unseeded βDM dPSIIcc crystals [220]. This result indicates no significant difference between the unseeded and the seeded dPSIIcc crystals in terms of diffraction resolution.

Further improvements of the diffraction quality of the macrocrystals are currently planned by applying the macroseeding techniques developed in this work for the generation of dPSIIcc macrocrystals with the detergent $C_{12}E_8$ instead of βDM with subsequent postcrystallization treatment as described in the work of Hellmich et al. [44] which reproducibly improves the resolution of our diffraction data sets [44, 48].

Table1. XRD data statistics

Data collection	
Wavelength (Å)	0.918409
Space group	$P\,2_1\,2_1\,2_1$
Unit cell parameters	
a (Å)	126.59
b (Å)	223.15
c (Å)	305.46
a = β = γ (°)	90
Resolution limit (Å)	49.11-4.11 (4.36-4.11)[a]
Measured reflections	867591
Unique reflections	66764
Multiplicity	12.99
Completeness (%)	97.9 (88.9)
Mean I/sigma(I)	6.99 (1.07)
R-meas (%)	34.1 (237.5)
Wilson B-factor	140.12
Mosaicity (°)	0.254
$CC_{1/2}$	99.4 (64.6)
ISa	11.86

[a] Data in the highest resolution shell

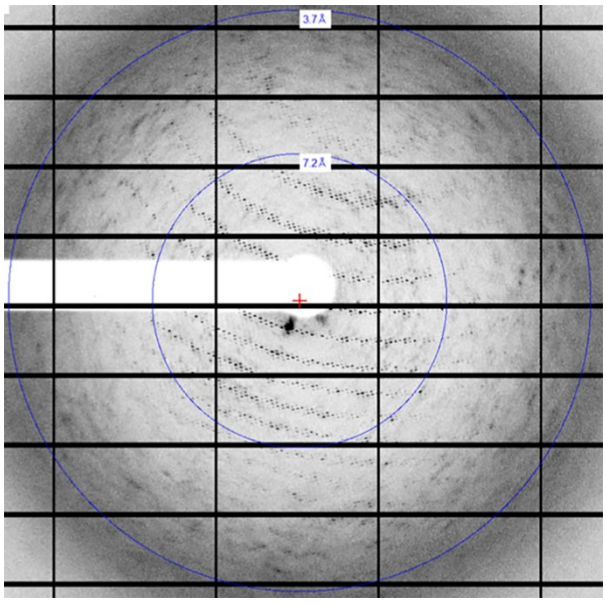

Figure 9 XRD diffraction pattern of a dPSIIcc microcrystal

Results of Initial Neutron Diffraction Tests

A large single dPSIIcc crystal of ~ 2.0 × 0.8 × 0.3 mm^3 generated using the macroseeding procedure was incubated in D_2O containing buffer (see section 2.9) to achieve partial D/H exchange and measured at the MaNDi instrument of the SNS at

ORNL. Upon exposure for 24 h at room temperature weak diffraction with a maximum resolution of ~ 8.0 Å was observed (Figure 10). These limited resolutions of 8 – 10 Å were due to non-optimal deuteration for the crystals as well as limited crystal volume given the large unit cell size of the dPSIIcc crystals. Further improvements in the neutron diffraction quality could be achieved by a more complete D/H exchange, including a complete exchange of the PEG and detergent against deuterated versions. These efforts are currently underway.

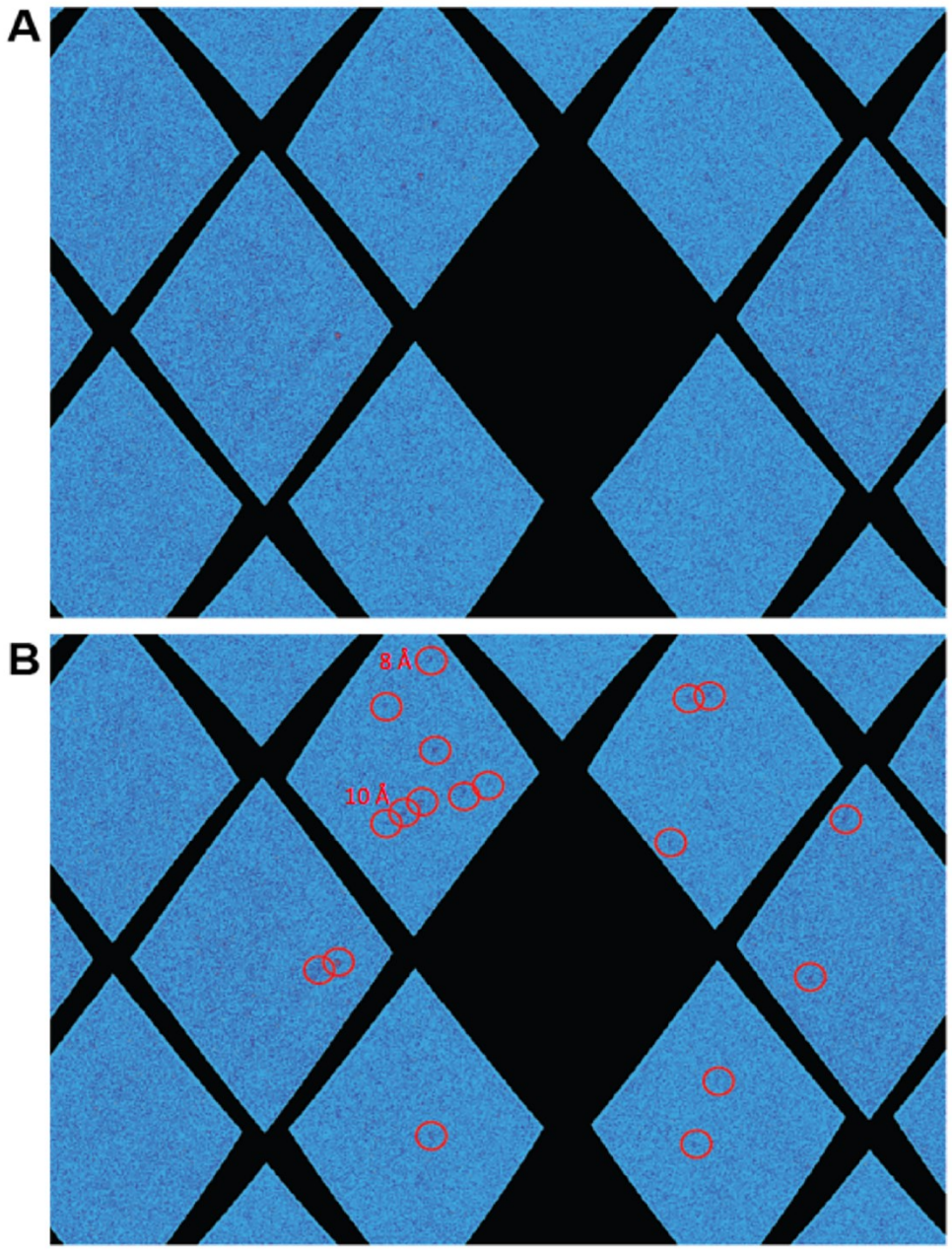

Figure 10 Neutron diffraction pattern of a dPSIIcc macrocrystal. *(A) Time-of-flight range corresponding to neutrons with wavelengths between 3.5 and 3.6 Å. For clarity, only a subset of the 40 SNS Anger cameras on MaNDi is shown. (B) Individual reflections are highlighted for better visibility, based on the wavelength and the diffraction angle of the Bragg reflections. The maximum estimated resolution of the Bragg peaks observed is 8 Å*

CONCLUSION

Highly purified and monodisperse dPSIIcc solutions were prepared from the cyanobacterium *T. elongatus* BP-1 by solubilizing the thylakoid membrane with an approximately 4-fold higher concentration of detergent (βDM) compared to the standard procedure [220]. Using that monodisperse dPSIIcc sample with a combination of microseeding and macroseeding crystallization techniques, we were able to generate dPSIIcc macrocrystals. In this study, all the steps from both techniques were discussed in detail, demonstrating the ability of producing relatively fast growing macrocrystals. The width of the metastable zone was increased by increasing the concentration of calcium chloride, which provided us with a quite wide window for transferring the crystals into the pre-equilibrated drop of the protein and avoiding the growth of too many crystals in the beginning of the growth phase. The quality of the macro-sized crystals was tested using XRD. We collected an X-ray diffraction data set from a βDM-dPSIIcc macrocrystal at 4.11 Å resolution. These large crystals will enhance the potential of collecting high-quality data from polarized spectroscopy techniques that require single crystals of PSII. They also represent another step towards obtaining a more detailed picture of the water environment surrounding the OEC using neutron diffraction.

ACKNOWLEDGMENTS

We acknowledge access to beamlines of the BESSY II storage ring (Berlin, Germany) via the Joint Berlin MX-Laboratory sponsored by the Helmholtz Zentrum Berlin für Materialien und Energie, the Freie Universität Berlin, the Humboldt-Universität zu Berlin, the Max-Delbrück-Centrum and the Leibniz-Institut für Molekulare Pharmakologie. We thank Dr. Martin Bommer for his support at BESSY and for helping in structure analyses, Ina Seuffert for technical assistance. We thank also the support stuff at beamline 14.1 at the BESSY II and at MaNDi instrument at ORNL.

Supporting information

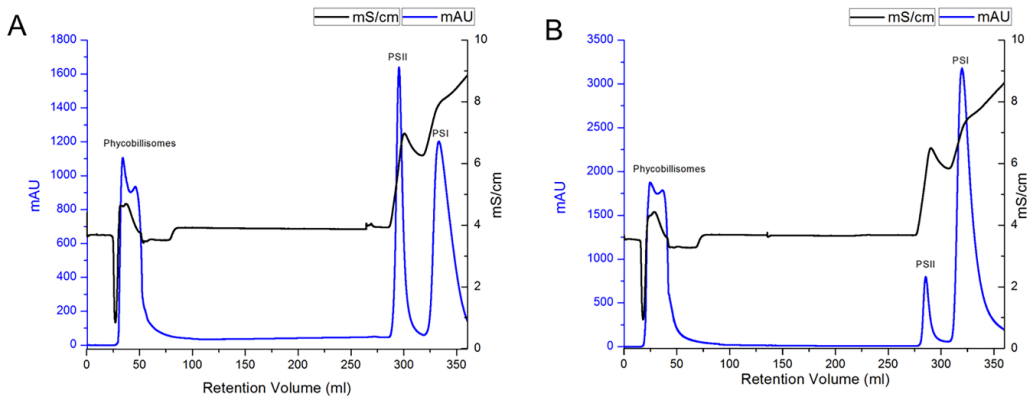

Figure S1 DEAE anion exchange column chromatography to purify the crude extract with 0.55 % βDM (A) and 2 % βDM (B). *Blue lines represent the absorbance at 280 nm in mAU and black lines the conductivity in mS/cm.*

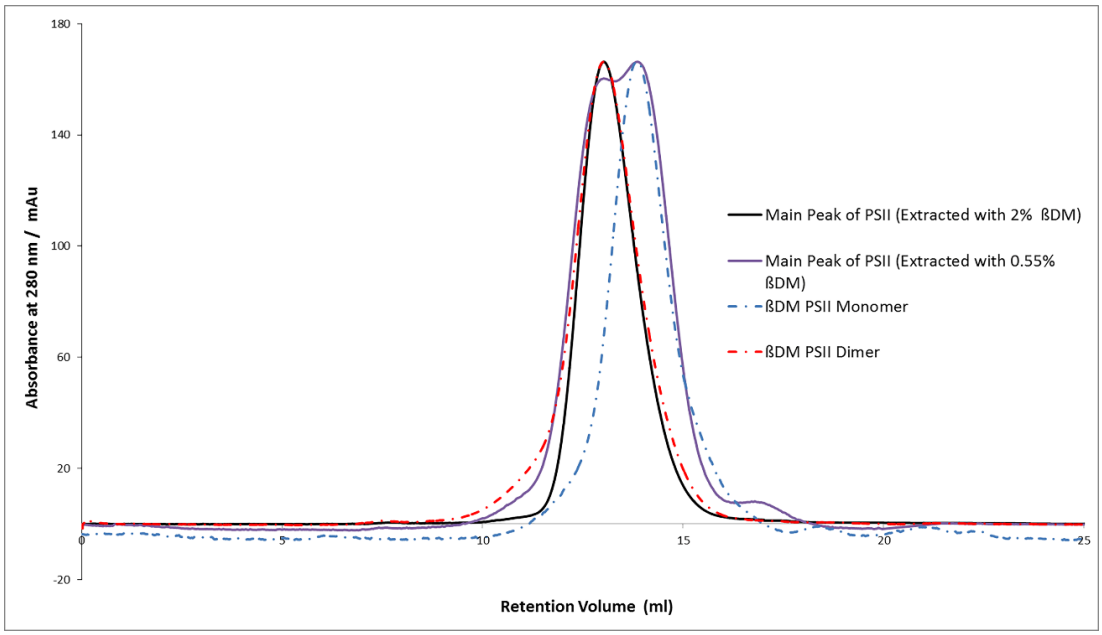

Figure S2 Gel filtration chromatography of dPSIIcc. Peak of PSIIcc as obtained from extraction of the thylakoid membrane with 2 % βDM (solid black line) and with 0.55 % βDM (solid violet line). *After eluting the samples from the DEAE column, they were loaded onto a Superose 6 column (GE health care) and ran individually. Separate controls were run with purified βDM-PSIIcc monomer (blue dotted line) and purified βDM-PSII dimer (red dotted line). UV-Absorption was detected at 280 nm.*

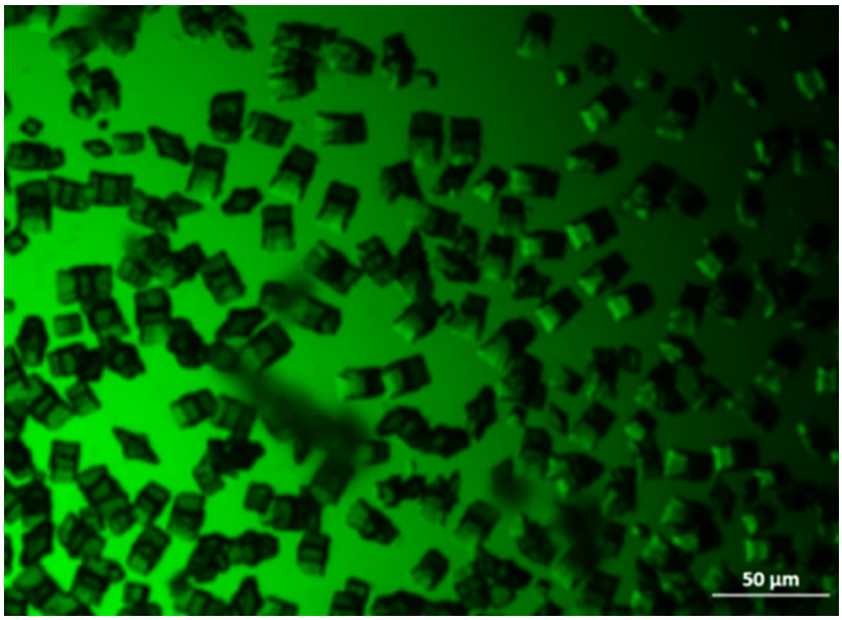

Figure S3 Microcrystals of dPSIIcc obtained from pre-crystallization.

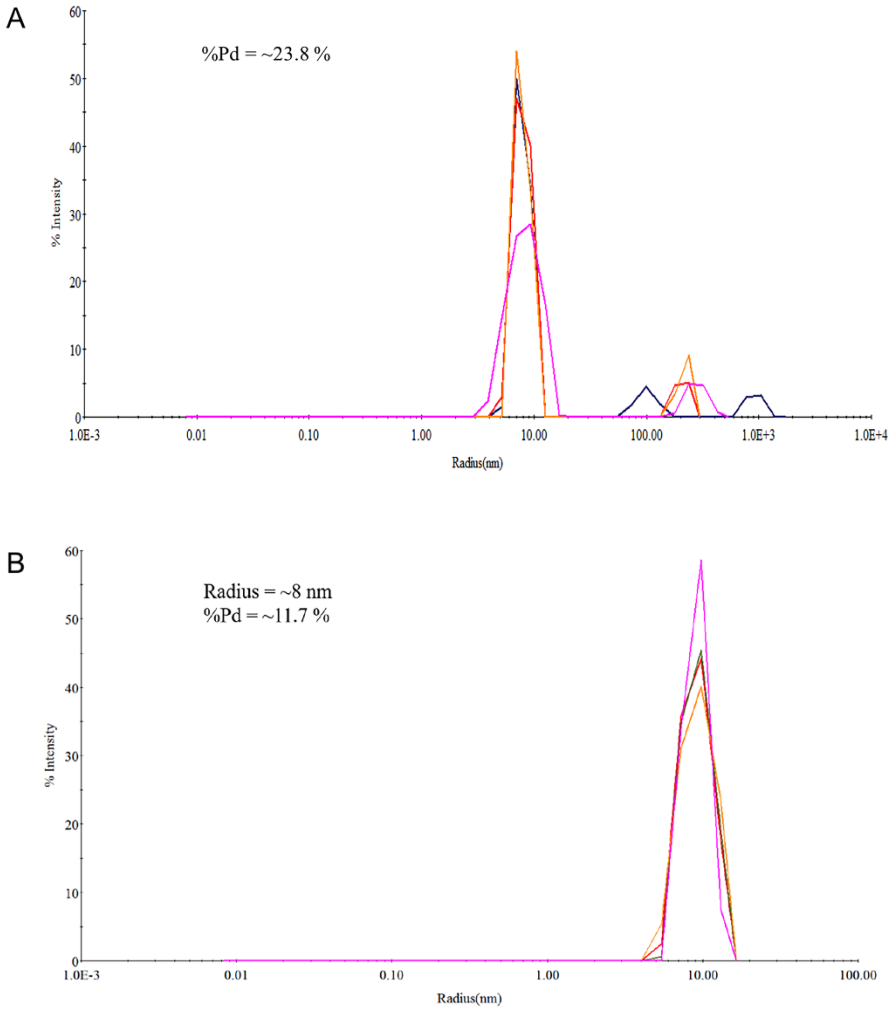

Figure S4 Size distribution of the dPSIIcc solution obtained from DLS. The dPSIIcc sample were measured before (A) and after (B) pre-crystallization steps. *Different line colors represent the reading from four independent measurements.*

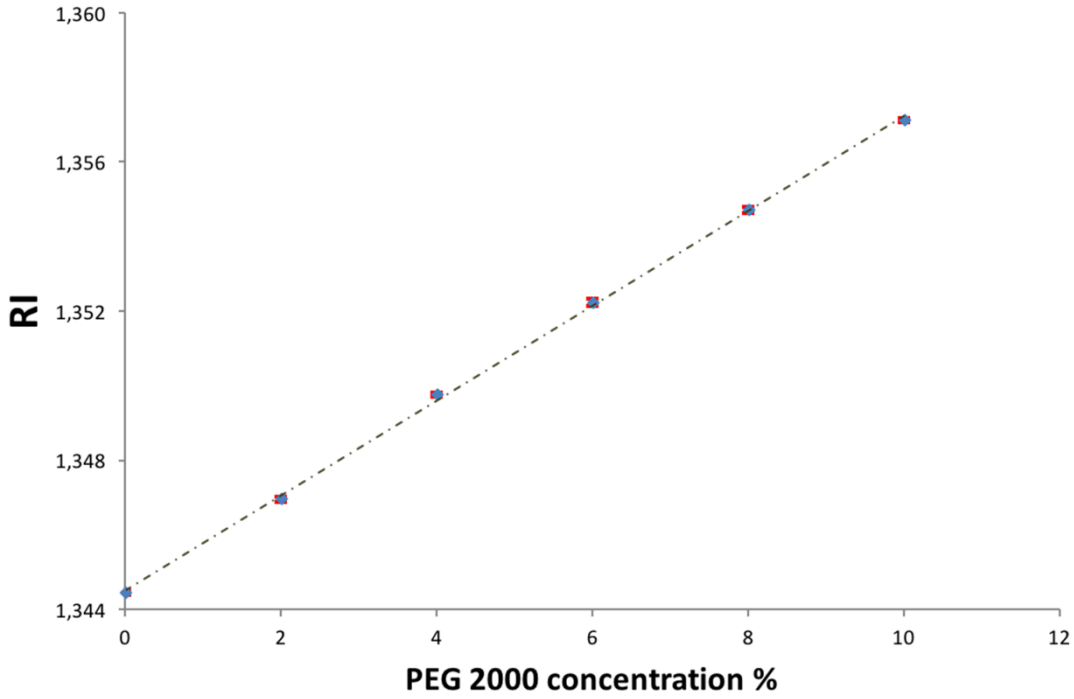

Figure S5 Refractive index of the crystallization buffer as a function of PEG 2000 concentration (standard curve). *Error bars (in red color) represent the standard error derived from four technical repeated measurements.*

Table S1. An example of using RI in measuring the PEG 2000 Concentration.

Calculated Concentration of PEG 2000 %	RI	Prepared Concentration of PEG 2000 %
1,9	1,347	2
3,1	1,349	3
4,0	1,350	4
5,2	1,351	5
5,9	1,352	6

II.2. Solution Structure of the Detergent-Photosystem II Core Complex investigated by Small Angle Scattering Techniques

Authors: M. Golub[a], R. Hussein[a], M. Ibrahim, M. Hecht, D.C.F. Wieland, A. Martel, B. M. Machado, A. Zouni, and J. Pieper

[a]Equal contributions as a co-first author

Reprinted with permission from Golub, M., Hussein, R., Ibrahim, M., Hecht, M., Wieland, D. C. F., Martel, A., Machado, B., Zouni, A., & Pieper, J. (2020). Solution Structure of the Detergent–Photosystem II Core Complex Investigated by Small-Angle Scattering Techniques. In The Journal of Physical Chemistry B (Vol. 124, Issue 39, pp. 8583–8592). Copyright 2020 American Chemical Society (ACS). Final published version: https://doi.org/10.1021/acs.jpcb.0c07169

Abstract

Albeit achieving the X-ray diffraction structure of dimeric photosystem II core complexes (dPSIIcc) at atomic resolution, the nature of the detergent belt surrounding dPSIIcc remains ambiguous. Therefore, the solution structure of the whole detergent-protein complex of dPSIIcc of *Thermosynechococcus elongatus* (*T. elongatus*) solubilized in n-dodecyl-ß-D-maltoside (βDM) was investigated by a combination of small-angle X-ray and neutron scattering (SAXS and SANS) with contrast variation. First, the structure of dPSIIcc was studied separately in SANS experiments using a contrast of 5% D_2O. A Guinier analysis reveals that the dPSIIcc solution is monodisperse, virtually free of aggregation in the studied concentration range of 2-10 mg/ml dPSIIcc, and characterized by a radius of gyration of 62 Å. A structure reconstitution shows that dPSIIcc in buffer solution widely retains the crystal structure known from X-ray free electron laser (XFEL) studies at room temperature with a slight expansion of the entire protein. Additional SANS experiments on dPSIIcc samples in a buffer solution containing 75% D_2O deliver information about the size and shape of the whole detergent-dPSIIcc. The radius of gyration increases to 76 Å, i.e. it is about 14 Å larger than that of dPSIIcc only thus indicating the presence of an additional structure consistent with the length of about one βDM molecule. Thus, it can be concluded that dPSIIcc is surrounded by a

monomolecular belt of detergent molecules under appropriate solubilization conditions. The homogeneity of the βDM-dPSIIcc solutions was also verified using the dynamic light scattering method. Complementary SAXS experiments indicate the presence of unbound detergent micelles by a separate peak consistent with a spherical shape possessing a radius of about 40 Å. The latter structure also contributes to the SANS data, but rather broadens the SANS curve artificially. Without a simultaneous inspection of SANS and SAXS data, this effect may lead to an apparent underestimation of the size of the PSII-detergent complex. The formation of larger unbound detergent aggregates in solution prior to crystallization may have a significant effect on crystal formation or quality of the βDM-dPSIIcc.

Introduction

Photosynthesis has shaped the atmosphere by massive O_2-formation from water and the biosphere by facilitating the large-scale production of primary biomass and energy-rich carbohydrates[28, 217]. This process is initiated by photosystem II (PSII), a multisubunit pigment-protein complex located in the thylakoid membrane of cyanobacteria, algae, and plants. By using solar energy, PSII acts as a water: plastoquinone oxidoreductase, catalyzing the electron extraction from water molecules[100, 246] coupled with the reduction of the final electron acceptor, a plastoquinone molecule[247]. Thereby, water is split into dioxygen (O_2), protons and bound electrons through a series of successive reactions. PSII is a homodimeric core complex (dPSIIcc) with a molecular weight of about 750 kDa [53] consisting of 20 different protein subunits, 17 of which are membrane-intrinsic (PsbA to PsbF, PsbH to PsbM, PsbT, PsbX to PsbZ, and ycf12) and 3 membrane-extrinsic (PsbO, U, and V) located at the lumenal side[28, 43, 222]. Each monomer of PSII harbors nearly 100 cofactors. Light-excitation of the reaction center (RC) of PSII formed by subunits PsbA (D1) and PsbD (D2) results in the oxidation of a chlorophyll (P_{D1}) and the reduction of a plastoquinone (Q_B) and affords reducing equivalents (plastoquinol, Q_BH_2) [247]. The cryogenic crystal structure of dPSIIcc from the thermophilic cyanobacterium *Thermosynechococcus vulcanus* at 1.9 Å resolution revealed the oxygen-evolving complex (OEC), which contains a heteronuclear, oxo-bridged Mn_4CaO_5 cluster located at the lumenal side of PSII[73]. Electrons are extracted from the OEC by oxidized P_{D1} via a redox-active tyrosine of PsbA (Y_Z, A-Tyr161) hydrogen bonded to A-His190. By repeated excitation of the RC, the OEC cycles through five successive oxidation states, called S_i-states (i = 0 - 4), leading to the oxidation of two water molecules to dioxygen, four protons, and four electrons [248-251].

In the cryogenic dPSIIcc crystal structure the longest dimensions of the membrane integral part is 190 Å x 100 Å, which is 40 Å thick and extends from the stromal side of the membrane by no more than 10 Å, whereas the luminal side of each monomer has prominent protrusions up to 55 Å from the membrane[39, 41, 252]. Recently, structural data close to 2.0 Å resolution for all four (meta)stable intermediate S-states of the Kok cycle under physiological conditions using the femtosecond (fs) serial crystallography at the XFEL were published [51]. In difference to the cryo X-ray structure, an expansion of dPSIIcc by ca. ~0.5 Å in all directions within the integral part was observed [48]. It adds to the complexity that the conformational flexibility of PSII increases drastically above 240 K and was shown to depend strongly on temperature and hydration [253, 254]. However, structural information of a stable detergent-dPSII core complex in a buffer solution under physiological conditions is still missing due to the inherent structural heterogeneity of the detergent belt.

During the last 19 years, cryo-X-ray structures of dPSIIcc were obtained based on measurements of detergent-protein crystals[39, 41, 43, 47, 73, 252]. In most cases, dPSIIcc from a thermophilic cyanobacterium is isolated, purified and crystallized using the mild and non-ionic detergent n-dodecyl-ß-D-maltoside (βDM), whereby the protein retains its full oxygen activity[220, 255]. This detergent, which is in the focus of the present study, is of high interest as it is frequently used for isolation of membrane proteins being an appropriate choice in many solubilization and crystallization studies, as well as in reconstitution experiments[256].

PSII is embedded in the thylakoid membrane, a lipid bilayer with a hydrophobic core, and can be dissolved out of the membrane due to the amphiphilic nature of βDM. At the critical micelle concentration (CMC), the monomer detergent molecules self-assemble into globular micelles. In a similar concentration range, referred to as critical solubilization concentration (CSC), a stable detergent-protein complex (DPC) is formed in aqueous solution[208, 257]. The CSC of the DPC plays a decisive role in the crystallization of βDM-dPSIIcc, although a detailed understanding of this role is still missing[208]. It is assumed that right above the CSC, all protein molecules are ideally surrounded by a detergent belt and almost no free micelles are present in the solution. Well above the CSC, the concentration of DPCs remains essentially constant, but the concentration of (protein-free) micelles may further increase. The formation of free micelles negatively influences the crystallization of βDM-dPSIIcc, as they reduce protein-protein interactions and weak

detergent-detergent interactions[208]. In the cryo-X-ray structures, type-II crystals of βDM-dPSIIcc contain a fully developed detergent belt[41, 43, 44].

Small-angle neutron and X-ray scattering (SANS and SAXS, respectively) experiments are perfectly suitable to give access to unique structural information on the shape, domain organization and interactions of biomolecules in solution [258, 259] . While SANS and SAXS are widely complementary, the difference in the scattering length densities of deuterium and hydrogen in SANS experiments allows highlighting individual components of the protein-detergent system by varying the ratio of H_2O and D_2O in the solvent [260-263]. In addition, a combination of the SAXS- and SANS techniques is widely used to study large, flexible, and glycosylated proteins. SANS and SAXS have also been successfully employed in photosynthesis research [264, 265], e.g. for neutron studies of the structural arrangement of cyanobacterial and plant thylakoid membranes [266-269], but also to investigate state transitions in *Chlamydomonas reinhardtii* [264]. SANS is also powerful experimental tool for determining solution structures of assemblies of pigment-protein complexes [270, 271] or of complexes undergoing structural changes upon external triggers [272]. Furthermore, solution structures of the major light-harvesting complex LHCII of green plants [273], the PsbO from cyanobacterial photosystem II [274], the bacterial light-harvesting complex LH2 at physiological temperatures [275] and PS I trimers [276, 277] were also determined by SANS- and SAXS measurements. The advantage of both methods is also that free micelles in the βDM-dPSIIcc solution can be determined before crystallization. This allows conclusions about the quality of the formed crystals for X-ray measurements.

Here, we report the detailed study of the solution structure of isolated βDM-dPSIIcc from the cyanobacterium *T. elongatus*. We use a combined approach of the two complementary small-angle scattering techniques SANS and SAXS. In particular, SANS is used along with contrast variation to selectively highlight the solution structure of dPSIIcc and of the detergent organization within the solubilized protein-detergent complex, respectively. The homogeneity of the detergent-protein complex is also verified by dynamic light scattering (DLS) at different protein concentrations (0.5-10 mg/ml) at a constant βDM concentration (0.02%). Using SANS/SAXS measurements we investigate different dPSIIcc solutions (2-10 mg/ml) at constant βDM concentration (0.02%) to probe a possible formation of free micelles. The information gathered also bears a particular relevance for crystallization of dPSIIcc, since the quality of type-II βDM-dPSIIcc crystals

for X-ray diffraction depends on the βDM concentration as a function of the dPSIIcc concentration and on the presence of free detergent micelles.

Materials and Methods

Sample Preparation: The isolated PSII core complex (PSIIcc) was obtained from the thermophilic cyanobacterium *T. elongatus* in the form of a homodimer, using the detergent βDM as described by Kern et al., 2005. The dPSIIcc samples were redissolved with a buffer containing 0.1 M PIPES-NaOH (1,4-piperazinediethanesulfonic acid), pH 7.0, 5 mM $CaCl_2$, 5% glycerol and 0.02% βDM. A prerequisite for using SANS/SAXS measurements on the βDM-dPSIIcc samples is their monodispersity and homogeneity. Therefore, the monodispersity and homogeneity of these samples were increased by a double precrystallization procedure. Each pre-crystallization step was done at 0.75 mM chlorophyll (Chl) *a* concentration which is equivalent to 8 mg/ml protein and left overnight at 4°C[220, 255]. The collected crystals were resolubilized followed by washing in a buffer containing 0.1 M PIPES-NaOH, pH 7.0, 10 mM $CaCl_2$, 5% glycerol and 0.02% βDM at final concentration of 1 mM chlorophyll concentration (equivalent to 10.7 mg/ml protein). For SANS measurements, the dPSIIcc samples were rewashed with a buffer containing 0.1 M PIPES-NaOH, pH 7.0, 10 mM $CaCl_2$, and 0.02% βDM with different content concentrations of D_2O (5%, 75%, and 100%).

The activity of all prepared samples was assessed at room temperature using the measurement of steady-state O_2 evolution rate under continuous illumination via a Clarke-type electrode (OxyLab, Hansatech instruments). The dPSIIcc samples show O_2 evolution rates of ~2500 μmol O_2/(mg Chl *a* h) as measured in buffer containing 20 mM MES/NaOH, pH 6.5, 20 mM $CaCl_2$, 10 mM $MgCl_2$ and 3 μM DCBQ (2,5-dichloro-p-benzoquinone) as an artificial electron acceptor.

Dynamic light scattering Experiment: Dynamic light scattering (DLS) was applied using DLS Wyatt Dynapro Nanostar with 787 nm laser wavelength to measure the monodispersity and the homogeneity for the purified dimeric βDM-PSIIcc samples used for the SAXS/SANS measurements. The measurements were performed at different protein concentrations ranging from 0.5 mg/ml to 10 mg/ml in a buffer containing (0.1 M PIPES-NaOH, pH 7.0, 5 mM $CaCl_2$, 5% glycerol and 0.02% βDM). Three successive DLS measurements with 15 acquisitions each, at 20 °C were performed per sample. DLS was used to obtain directly the diffusion coefficient (*Dz*) of protein particles. The translational diffusion coefficient is determined by the autocorrelation

function of the scattered light. It permits the calculation of the hydrodynamic radius (R_H) of the protein particles by using of the Stokes–Einstein equation,

$$R_h = \frac{k_B T}{6\pi\eta D_Z}$$

where k_B is Boltzmann coefficient, T is an absolute temperature, η is the viscosity of the solvent and D_Z is the diffusion coefficient.

The refractive index of the buffer at 589 nm was determined using the Abbe refractometer (AR008) (KRÜSS, Germany) to be equal to 1.341. The kinematic viscosity was determined using a capillary viscosimeter (type cannon fenske routine, size 100, Q Glass Company Inc., USA), whereas the density of the solvent was obtained using a digital densitometer DA-100 (KEM, Japan) to be 1.018 g/cm^3. The dynamic viscosity of the buffer was calculated to be equal to 1.151 cP. All the measurements were done at 20 °C.

SANS experiments: The SANS measurements were carried out at the D33 massive dynamic q-range small-angle scattering instrument (ILL, Grenoble, France). Two wavelengths of 6 and 12 Å at sample-detector distances of 5.3 and 12.3 m, respectively, were used to cover the q-range from 0.05 to 0.45 Å^{-1}. The temperature of the sample cells was set to 10 °C during the measurement. A detailed description of the D33 SANS instrument can be found elsewhere [278].

In order to independently investigate the protein and the detergent structures, two different D_2O/H_2O contrast match points were used. The topological shape of dPSIIcc was determined from the SANS data collected at 5% D_2O contrast, which was considered as a match point of the hydrophobic tails of the detergent molecules. The structural information about the βDM-dPSIIcc core complex was obtained from SANS data measured at a contrast of 75% D_2O. In each SANS measurement, three protein concentrations of 2, 5 and 10 mg/ml, respectively, were investigated. The measurement of a concentration series allowed extrapolating to infinite dilution approximation, so that possible interactions between the protein molecules can be neglected [279, 280].

SAXS Experiment: The complementary SAXS experiments were carried out at the BM29 Bio-SAXS beam line (ESRF, Grenoble, France) [281]. The current of the incident beam was 200 mA. The scattering curves were collected in the q-range of 0.025 – 5 nm^{-1} by a 2D detector (Pilatus 1M). Each measured SAXS curve was recorded as 10 frames (one second per frame) in the flow mode to counter damage of the samples by the x-ray beam. Data collection, processing and analysis were performed in an automated manner using the dedicated beam line software BsxCuBE. SAXS measurements were

performed using samples of both contrast of 5 and 75 % D_2O and at three protein concentrations of 2, 5 and 10 mg/ml, respectively.

Theoretical Background: The simplest model independent analysis of small angle scattering data can be achieved following the classical Guinier approximation, which is valid for diluted solutions of monodisperse particles:

$$I(q) = I(0)\exp\left(-q^2\frac{R_g^2}{3}\right), \tag{1}$$

where q is the scattering vector, R_g is the radius of gyration of a monodisperse particle in solution and I(0) is the forward scattering, which is a shape-independent function of the total scattering power of the sample. The Guinier approximation is valid for small q values according to the relation $qR_g<3$ and can provide the mass wheighted size of a particle in the case of a monodisperse solution. It is an appropriate tool to verify monodispersity as well as presence of aggregation in the sample solution.

The structure of a single particle can be characterized by the so-called correlation function γ(r) introduced by Porod in 1951, where r is the distance between pairs of atoms in the sample. Multiplying by r^2 we obtain the distance distribution function P(r)

$$P(r) = \gamma(r)r^2. \tag{2}$$

The square of the radius of gyration is half the normalized second moment of the latter function according to

$$R_g^2 = \frac{\int P(r)r^2dr}{2\int P(r)dr} \tag{3}$$

Furthermore, the scattering intensity at zero angle is a constant related to P(r) by

$$I(0) = 4\pi\int P(r)dr. \tag{4}$$

In the case of monodisperse macromolecular solutions, the scattering is proportional to the scattering of a single particle averaged over all orientations. While, the relation between the scattering intensity and the properties of the single particle is given by the Fourier transformation following

$$I(q) = 4\pi\int_0^{D_{\max}} P(r)\frac{\sin(qr)}{qr}dr, \tag{5}$$

where P(r) is non-zero only in the range from 0 to D_{max}, D_{max} corresponds to the maximum distance in the particle. The scattering vector is given by

$$q = \frac{4\pi}{\lambda_0}\sin(\theta), \quad (6)$$

where λ_0 is the wavelength of the monochromatic radiation and θ is the scattering angle.

Specific model shapes can be applied to fit the small angle scattering data within the approximation of an ideally dilute solution of monodisperse particles based on the master equation[258, 259]:

$$\frac{d\sigma(q)}{d\Omega(q)} = n\Delta\rho^2 V^2 P(q)S(q), \quad (7)$$

where n is the number particles, Δρ is the difference in scattering length density (SLD) between the particles and the solvent, and V is the volume of the particles. P(q) is the form factor, which is a function of the averaged shape and size of the scattering particles. The effective structure factor is given in the formula as S(q), which, however, is identical to unity in dilute solutions.

The SANS data were fitted using the NSNR SANS software developed at NIST [282]. One model used within this study is the form factor of the elliptical cylinder averaged over all its possible orientations, which is defined according to[283]

$$P_{cylinder}(q) = \frac{S_{cylinder}}{V_{cyl}}\int_0^1 \Psi_{ec}\left(q, a\sqrt{1-x^2}\right) j_0^2\left(\frac{qLx}{2}\right)dx, \quad (8)$$

where $S_{cylinder}$ is a scaling factor, V_{cyl} is the particle volume, α is the minor radius of the elliptical cross section and L is the length of the elliptical cylinder. The zero order Bessel function is equal to $j_0 = \frac{\sin(t)}{t}$. The function Ψ_{ec} (q,a) is given by

$$\Psi_{ec}(q,a) = \frac{1}{\pi}\int_0^\pi \Lambda_1^2\left[qa\left(\frac{1+\nu^2}{2} + \frac{1-\nu^2}{2}\cos(y)\right)^{1/2}\right]dy, \quad (9)$$

where ν is the ratio between major and minor radius of the elliptical cross section. The function Λ_1 is defined as $\frac{2j_1(t)}{t}$, where j_1 is the first order Bessel function $j_1 = \frac{\sin(t) - t\cos(t)}{t^2}$.

In order to analyze the SAXS data and SANS data collected at 75% D_2O, the two contributions of the protein-detergent complex and free micelles have to be taken into account. Therefore, it was necessary to perform a global fitting of the SAXS and SANS data assuming a linear superposition of two contributions and treating the SLD values as the only independent fitting parameters:

$$I_{total}(q) = A * I_{cylinder}(q) + B * I_{core\_shell}(q) . \quad (10)$$

Here, A and B are prefactors related to the number of the protein-detergent complexes and free micelles, respectively. $I_{cylinder}$ is the scattering contribution from the elliptical cylinder associated with dPSIIcc. At the same time, I_{core_shell} is the intensity profile of the free detergent micelles calculated by applying the spherical core shell model, which is based on previous investigations of βDM micelles[256].

The form factor of a spherical core shell is given by [284]:

$$P_{core\_shell}(q) = \frac{s_{sphere}}{V_{sphere}} \left[\frac{3V_{core}(\rho_{core} - \rho_{shell}) j_1(qr_{core})}{qr_{core}} + \frac{3V_{shell}(\rho_{shell} - \rho_{solv}) j_1(qr_{sphere})}{qr_{sphere}} \right], \quad (11)$$

where S_{sphere} is a scaling factor, V_{sphere} is the total volume of the spherical core shell with the radius r_{sphere}, r_{core} is defined as the radius of the core inside the sphere; ρ_{shell}, ρ_{core} and ρ_{solv} are scattering length densities of the shell, core, and solvent, respectively.

In addition to the model dependent analysis, the small angle data can also be analyzed in terms of the distance distribution function P(r), see above. In this case, the P(r) function and the particle maximum dimension D_{max} can be determined using the Inverse Fourier transform (IFT) method employing the software routine GNOM [285]. For the IFT analysis, we used the limited q-range up to 0.1 $Å^{-1}$, where the scattering contribution of βDM micelles can be neglected.

The software routines CRYSOL and CRYSON[286] were used to calculate theoretical SANS and SAXS curves based on the pdb structure of dPSIIcc protein and compare them with the experimental small angle data.

Further modeling on the basis of an ab-initio approach was carried out using the software routines DAMMIF/DAMMIN. The overall model structure of dPSIIcc core complex is obtained from the small angle scattering data using DAMMIF developed by the group of D. Svergun[212]. All modeled structures on the basis of the dummy bead model were averaged over 20 iterations; for each iteration it was taken into account that dPSIIcc possesses an oblate form and has a P2 symmetry. We used Pymol (2006 DeLano

Scientific LLC) to compare the result of the DAMMIF analysis with the known PDB structure of dPSIIcc.

Results and Discussion

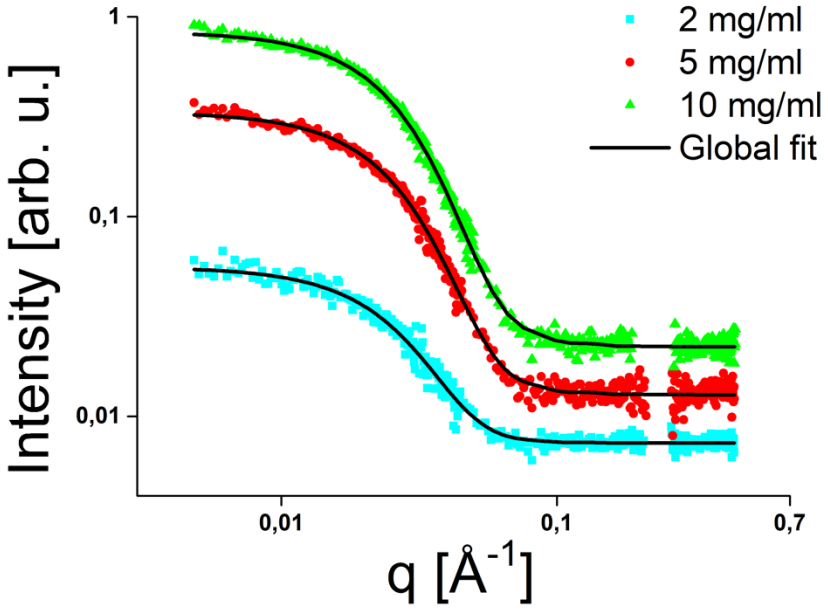

Figure 1 SANS data of PSII core complexes collected at a contrast of 5% D_2O and at protein concentrations of 10 mg/ml (green triangles), 5 mg/ml (red dots), and 2 mg/ml (cyan squares), respectively. *The full lines are fits using the elliptical cylinder model, see text.*

The dPSIIcc solution structure: In order to investigate the solution structure of dPSIIcc selectively, we first performed SANS measurements using 5% D_2O content in the buffer solution, which is the theoretical contrast match point for the hydrophobic tail of βDM detergent molecules. This means that the detergent tails have nearly the same SLD as the solvent and, as a result, cannot be distinguished from the solvent by SANS. On the other hand, a contrast remains between the protein and the buffer/detergent tail, thus highlighting the protein contribution selectively. Although the contrast of 5% D_2O does not match the βDM head group region, the latter contribution is further altered by D_2O molecules absorbed in the head group region, so that the average contrast for the head group region is not strong enough to become visible in the scattering profile.

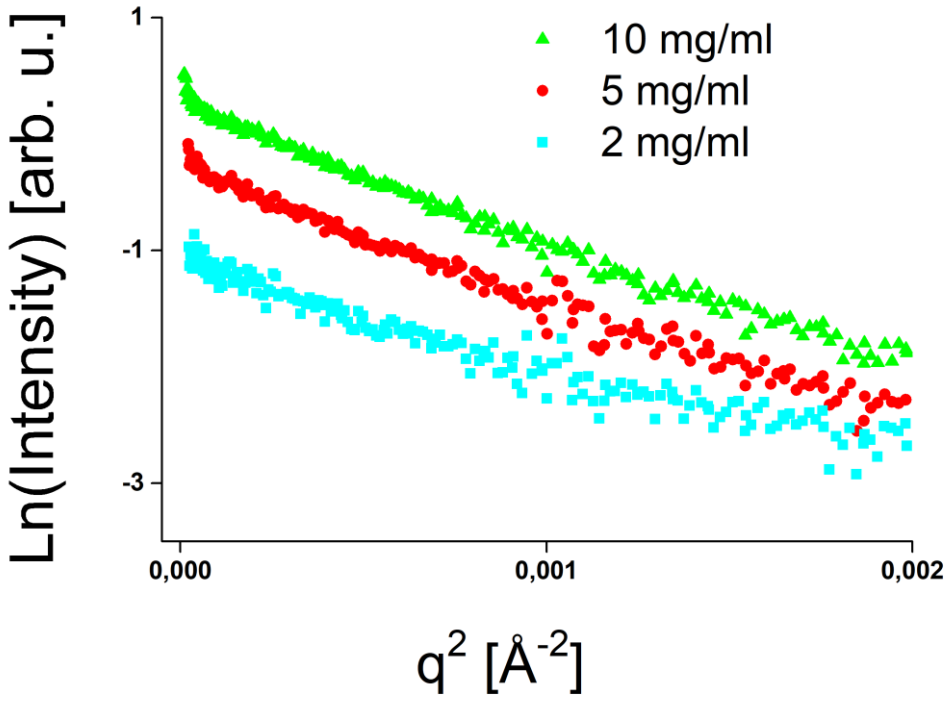

Figure 2 Guinier plots of the SANS data of PSII core complexes shown in Fig. 1, which are collected at a contrast of 5% D_2O and at protein concentrations of 10 mg/ml (green triangles), 5 mg/ml (red circles), and 2 mg/ml (cyan squares), respectively.

The SANS data of dPSIIcc obtained at a contrast of 5% D_2O are shown in Figure 1 for three different protein concentrations. Guinier plots of the same data sets are presented in Figure 2. An inspection of this plot reveals that the SANS data exhibit the expected linear behavior over almost all the Guinier region except for a slight upturn at the smallest q-values of the higher concentrations. This indicates that the dPSIIcc samples under study are diluted monodisperse solutions and widely free of aggregation at all investigated protein concentrations. This is also supported by DLS measurements (see Figure 3) showing that the βDM-dPSIIcc samples exhibit an average polydispersity of 13.2 ± 1.5 % within the measured range of protein concentrations. A sample is considered to be monodisperse, when the percentage of polydispersity is less than 15 %. This finding is important as aggregation is known to affect the spectroscopic properties of pigment-protein complexes[287, 288]. The hydrodynamic radius (R_H) of dPSIIcc measured using DLS will be discussed below, because it applies to the whole dPSIIcc-detergent complex.

Furthermore, a radius of gyration R_g of about 62 Å can be obtained from the Guinier plots shown in Figure 2, which is roughly 4 Å larger than the R_g value calculated from the crystal structure of the PSII core complex (pdb code 3WU2[73]) using the

CRYSON routine. This small deviation between the experimental and theoretical value for the radius of gyration is indicating a slight increase of the molecule size of dPSIIcc in buffer solution at physiological temperature.

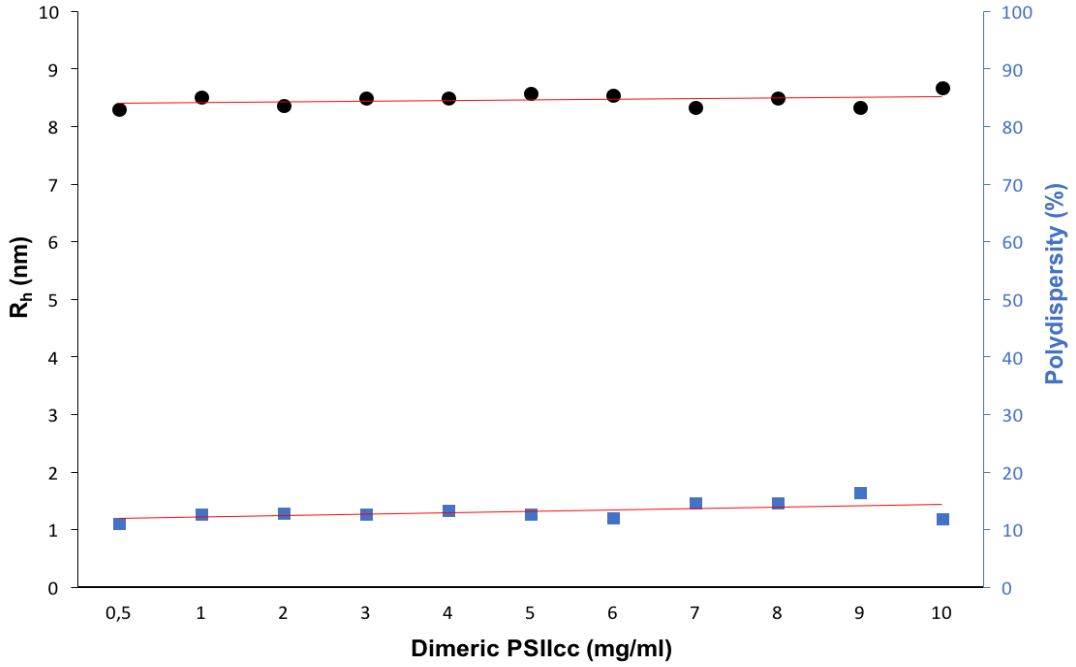

Figure 3 Hydrodynamic radius R_H (black dots) of ßDM-dPSIIcc as a function of the protein concentration derived from DLS measurements. *Blue squares show the polydispersity (in %) of the sample representing the degree of homogeneity. The ßDM-dPSIIcc samples were monodisperse within the measured range of protein concentrations with an average hydrodynamic radius of 8.4 ± 0.1 nm and polydispersity of 13.2 ± 1.5 %.*

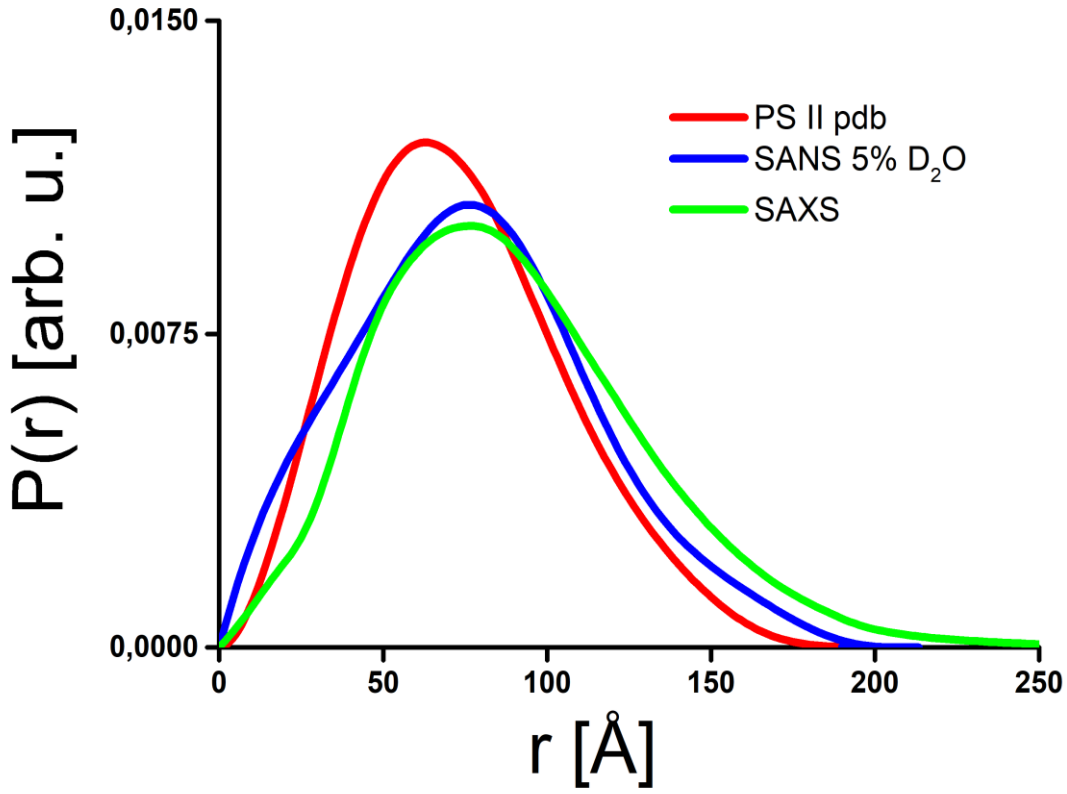

Figure 4 Comparison of P(r) functions calculated from SAXS data (green line) and SANS data measured in 5% D_2O contrast (blue line) of PSII core complexes at a protein concentration of 2 mg/ml using the IFT method.*The red line corresponds to the crystal structure of PSII (pdb code 3WU2[73])*

The distance distribution function P(r) was calculated from the dPSIIcc SANS data set collected at a contrast of 5% D_2O via the IFT method using the GNOM routine. This function illustrates size and shape of the protein molecule in more detail than the simple approximation of the radius of gyration. As shown in Figure 4, the P(r) function calculated from the SANS data is characterized by an asymmetric peak indicating a cylinder-like shape of the particles in the buffer solution (see blue line in Figure 4). The peak position is found at 76 Å, while the tail of the P(r) function extends is up to a D_{max} value of 220 Å. For comparison, the theoretical P(r) function calculated on the basis of the known PSII crystal structure is also shown as a red line in Figure 4. It has a very similar general shape to the experimental one, although it appears to be generally shifted to smaller distances indicating an expansion of the PSII structure in solution at physiological temperatures. Although P(r)-functions are individual properties of each protein, the general shape observed here is similar to previously reported P(r) functions for other membrane proteins [264, 273, 276, 289, 290]. An expansion of proteins in solution has also been observed for different membrane proteins[291].

Table 1. SANS/SAXS fitting parameters defined in the equations (3), (4) and (6) for the dimeric PSII core complex solubilized using the detergent βDM.

	SAXS	SANS (75% D_2O)	SANS (5% D_2O)
Ellipt. Cylinder Scale			
a (Å)	41 ± 2	41 ± 2	39 ± 2
ν	2.87 ± 0.05	2.87 ± 0.05	2.6 ± 0.05
L (Å)	116 ± 4	116±4	116 ± 4
$\rho_{cylinder}$ (10^{-6} Å^{-2})	9.59e-06	2.2e-06	2.2e-06
ρ_{sovent} (10^{-6} Å^{-2})	9.46e-06	4.6e-06	-2.2e-07
Core_Shell Scale			
r_{core} (Å)	11 ± 3	14 ± 3	
r_{sphere} - r_{core} (Å)	26.5 ± 3	22.5 ± 3	
ρ_{core} (10^{-6} Å^{-2})	7.5e-06	-2.53e-07	
ρ_{shell} (10^{-6} Å^{-2})	9.55e-06	3.97e-06	
ρ_{sovent} (10^{-6} Å^{-2})	9.46e-06	4.6e-06	

In a next step, we performed a model-dependent analysis of the SANS data of PSII obtained at a contrast of 5% D_2O. Guided by the asymmetric shape of the P(r) function we applied the elliptical cylinder model to fit the data (see full lines in Figure 1). The fit parameters are summarized in Table 1 and correlate very well with expected values from the known pdb structure of PSII (pdb 3WU2[73]). For example, the length of the model cylinder is found to be equal to 116 ± 4 Å matching the combined lateral size of the extrinsic and intrinsic parts of dPSIIcc. Furthermore, the fit shows that the elliptical diameters equal to 202 ± 4 Å and 82 ± 4 Å, respectively, coinciding well with the dimensions of the membrane integral part of the dPSIIcc crystal structure[39]. It is also most remarkable that all three data sets obtained at different protein concentrations can be fitted with the same set of parameters indicating once more that the PSII preparation used is widely monodisperse and aggregation is virtually absent over the whole range of concentrations probed in the present study.

Finally, the overall structure of dPSIIcc in buffer solution was modeled based on the SANS data shown in Figure 1 using the ATSAS routine. The result of the reconstruction is shown by grey spheres in Figure 5. A comparison with the crystal structure of dPSIIcc (pdb code 3WU2[73]) reveals a high consistency with the solution structure derived in this work, which is remarkable considering the complexity of dPSIIcc as a whole. Nevertheless, the modeled structure appears to be slightly larger than the crystal structure, which is especially visible in the region of the membrane-extrinsic PSII proteins. This is an additional indication for a slight expansion of dPSIIcc in buffer solution. Since the latter expansion concerns largely the membrane-extrinsic parts of PSII, it may also be caused by a larger conformational flexibility in this region of dPSIIcc [254, 292, 293].

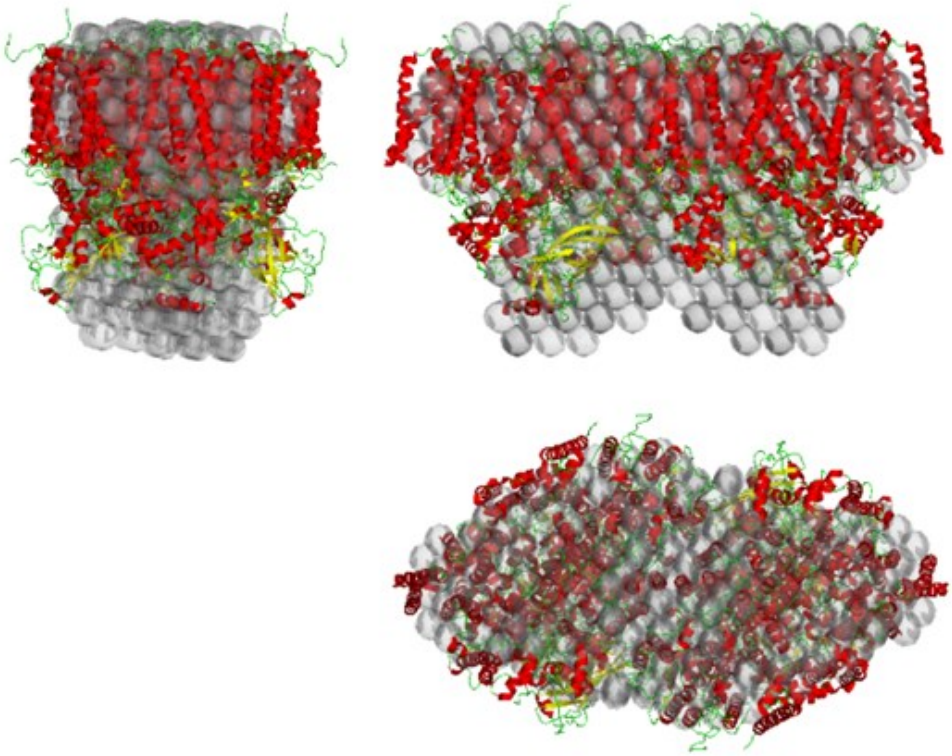

Figure 5 Comparison of the low-resolution solution structure of PSII core complexes (grey spheres) obtained from the SANS data shown in Fig. 1 using the DAMMIN software tool and a dimeric high-resolution structure (red and yellow ribbons) pdb 3WU2[73].

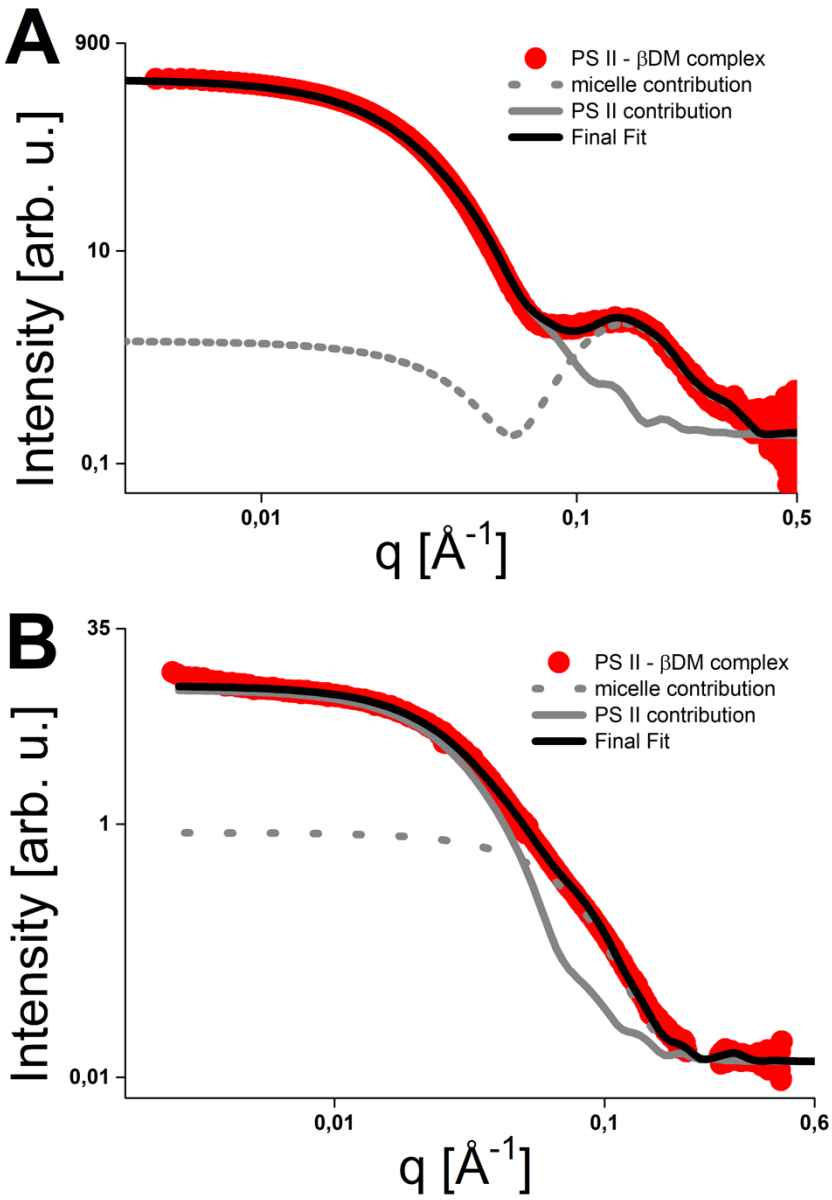

Figure 6 SAXS (A) and SANS (B) curves of the PSII-βDM complex in 75% D_2O and at a protein concentration of 2 mg/ml*. The red dots correspond to the experimental data. The fit function (black line) consists of contributions from the PSII-βDM complex (solid grey line) and from free detergent micelles (dotted grey line).*

The Interaction of dPSIIcc with Detergent Molecules: The overall solution structure of the dPSIIcc-detergent complex was probed using complementary SAXS and SANS experiments using a buffer solution containing 75% D_2O. Under the latter conditions, no specific contrast match is achieved in SANS experiments so that the results of SANS and SAXS are expected to be qualitatively similar, but to differ due to the method-specific SLD values of the components of the dPSIIcc-detergent complex. The respective SANS and SAXS curves of the dPSIIcc-detergent complex are shown in Figure 6.

A model independent analysis of the SANS curves measured in 75% D_2O solution in terms of the Guinier approximation (see above for the general approach) yields a value for the radius of gyration R_g of 68 Å, which is larger than that of dPSIIcc only determined at a contrast of 5% D_2O above. The IFT analysis of the corresponding SAXS data also gives the peak position of distance distribution function P(r) at 76 Å (see Figure 4). This is the same peak position as for P(r) function calculated from SANS data set at 5% D_2O contrast above. However, the P(r) function obtained from the SAXS data has a longer tail towards higher q-values, which extends up to 250-260 Å. We assume that the R_g and D_{max}-values are increased due to presence of a detergent belt, which is located at the hydrophobic part of dPSIIcc in buffer solution.

The hydrodynamic radius (R_H) of the detergent-dPSIIcc was measured using DLS at 11 different concentrations (see Figure 3). The average R_H value was found to be 84 ± 10 Å. This leads to a ratio R_g/R_H of 0.81, which is significantly higher than the value of 0.77 expected for a spherical protein. This deviation is consistent with an ellipsoidal shape as employed in the model-dependent simulations below.

A close inspection of the SANS and SAXS data sets of the PSII-detergent complex shown in Figure 6 reveals that they possess qualitatively different shapes with the SAXS data displaying a distinct peak at about 0.17 $Å^{-1}$. The latter peak is at least not separately visible in the SANS data of the same sample, which appears to be a seeming contradiction. Such a peak is indicative of a small particle with average size of only about 35-40 Å. Therefore, it cannot be identified with the protein-detergent complex itself, but may rather suggest the presence of free detergent micelles in the buffer solution. This has led us to perform a simultaneous fit of both SANS and SAXS data sets of the dPSIIcc-detergent complex using the same model function defined as the linear superposition of two components: 1) an elliptical cylinder according to Eq. 8 corresponding to the protein-detergent complex and 2) a spherical core shell applied to take into account the contribution of free micelles to the scattering profile. The result of the global fitting of the SANS and SAXS data is shown in Figure 6. The corresponding parameters are listed in Table 1. The parameters of the core shell model corresponding to free micelles are in a good agreement with literature values for spherical βDM micelles, which are formed in aqueous solution at concentrations higher than the CMC and have a radius of about 32 Å [294, 295]. The major radius of the elliptical cylinder representing the dPSIIcc-detergent complex is about of 117 Å for SAXS/SANS data measured using 75% D_2O contrast, while the major radius for SANS data measured in 5% D_2O solution (and solely

representing dPSIIcc under contrast matching conditions) is only about 98 Å (see above). We attribute the difference between the two radii to a belt of detergent molecules associated with the PSII protein.

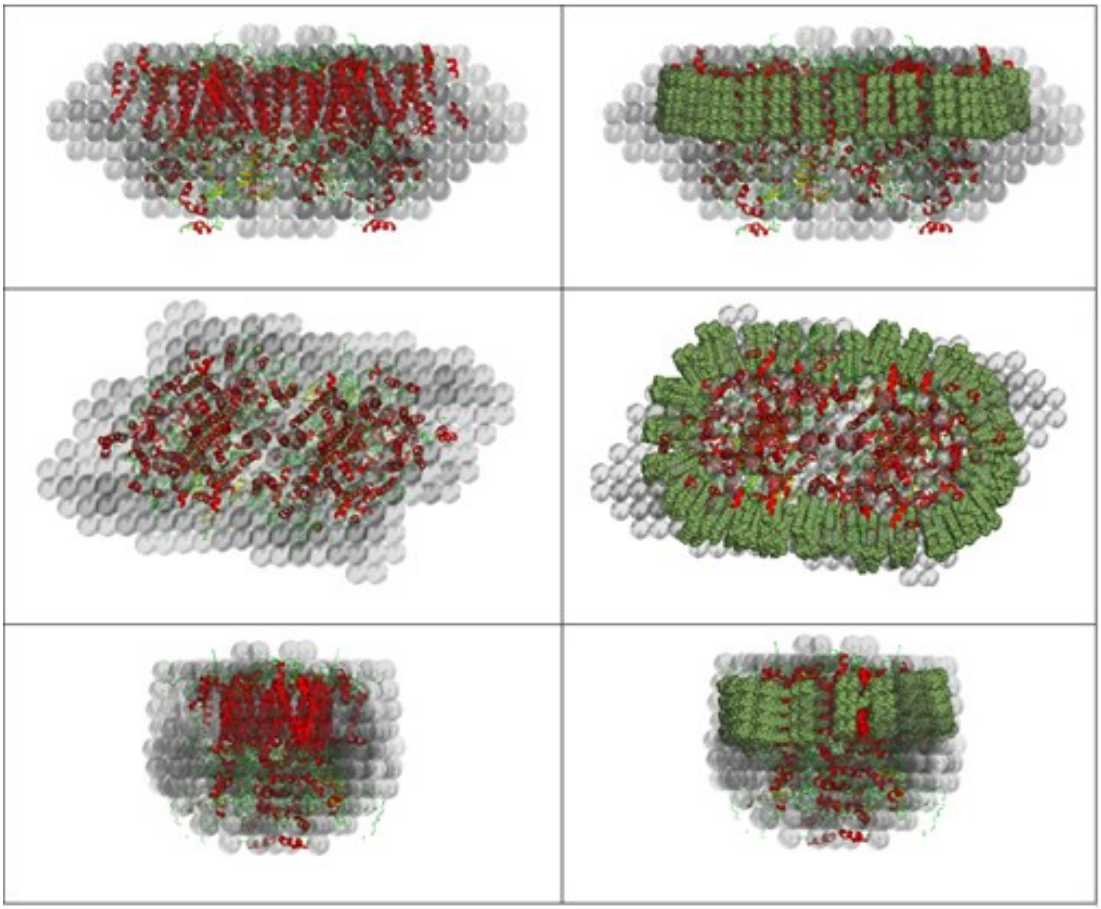

Figure 7 Left panels: Comparison of the modeled solution structure of the PSII -detergent complex (grey spheres) obtained from the SANS data at a contrast of 75% D_2O (see Fig. 5) using the DAMMIN software tool and a dimeric high-resolution structure (red and yellow ribbons) pdb 3WU2[73]. *Right panels: Comparison of the structural model as shown in the left panels (grey spheres) and a dimeric high-resolution PSII crystal structure (red ribbons) surrounded by a monomolecular βDM detergent shell (green dots). To compose the detergent shell, we have used the βDM pdb structure computed by PubChem [296].*

In order to obtain more precise information about size and shape of the protein-detergent complex, we have modeled its solution structure from the SAXS data measured at 75 % D_2O using DAMMIN/DAMMIF. It has to be taken into account that an analysis using DAMMIN/DAMMIF is performed only for q-values smaller than 0.1 $Å^{-1}$, where according to our model dependent analysis the contribution of the free βDM micelles to the experimental scattering data is weak in comparison to the dPSIIcc contribution (see Figure 6A). The solution structure reconstructed using DAMMIN/DAMMIF is compared with the crystal structure of dPSIIcc in Figure 7. A closer inspection of this structure

overlay clearly reveals that there is an additional structure surrounding dPSIIcc, which is mainly located at its hydrophobic surfaces, i.e. at those surfaces in contact with lipid molecules when dPSIIcc is embedded in the thylakoid membrane. The size of this additional structure is in the range of 15-20 Å, which is very close to the length of a single βDM detergent molecule. This finding corroborates the conclusion above that dimeric PSII is surrounded by a monomolecular layer of detergent molecules at its hydrophobic surface. Therefore, we constructed a rather simplistic model detergent belt assuming the closest possible packing of βDM molecules as shown schematically in Figure 7. Based on these assumptions, we arrive at a rough estimate of 432 βDM molecules bound in the dPSIIcc-detergent complex. This further proves that dPSIIcc is properly solubilized in the investigated βDM-containing buffer solution. Our finding is also in agreement with previous studies on membrane protein-detergent interactions, which revealed that a ring-like monomolecular layer is the most likely structure of detergent that is bound to membrane proteins [256, 257, 294, 297]. The assumption of a detergent monolayer of about 20 Å thickness also explains the increase of the total D_{max}-values of the dPSIIcc – βDM complex (75% D_2O contrast) compared with the same parameter determined for dPSIIcc only (5% D_2O contrast, see above).

Finally, we add that SAXS data of PSII samples measured at 5% D_2O and 75% D_2O contrasts, respectively, are virtually identical (not shown) thus proving that H-D-exchange procedures do not affect or disturb the solution structures of dPSIIcc. This can be directly concluded because SAXS is not sensitive to isotope exchange (unlike SANS) so that any difference in SAXS data would indicate a structural difference of the samples in different solutions.

Conclusions

In the present study, we have used SANS with contrast variation to investigate the solution structure of dPSIIcc and the organization of the detergent shell around the solubilized membrane protein in a βDM-containing buffer solution prior to crystallization. The solution structure of dPSIIcc is visible in SANS experiments with a contrast of 5% D_2O without any detergent contribution. The solution structure of dPSIIcc widely resembles its crystal structure at room temperature determined using the XFEL [48, 51]. The protein sample is monodisperse and virtually free of aggregation over the studied concentration range of 2-10 mg/ml PSII at constant βDM concentration as shown by DLS- and SANS-measurements. Additional SANS experiments on dPSIIcc samples at a

contrast of 75% D_2O reveal size and shape of the entire dPSIIcc-detergent complex, whose radius appears to be about 15-20 Å larger than PSII only measured at 5% D_2O contrast, suggesting a monomolecular belt of detergent (βDM) molecules. Complementary SAXS experiments indicate the presence of free detergent micelles by a separate peak consistent with a spherical shape of a radius of about 40 Å. It is thus very likely that the dPSIIcc-detergent samples studied are well above the CSC, leading to the formation of constantly stable PSII detergent complexes, but also to the formation of free micelles. Possibly, the formation of these free micelle aggregates during the crystallization process could have a disturbing effect, reducing the quality of dPSIIcc crystals. In future, further SANS/SAXS measurements on PSII samples prior to crystallization at different βDM concentrations near the CSC will be required to achieve a monomolecular layer of detergent belt around the dPSIIcc avoiding formation of free micelle aggregates [208].

Acknowledgement

Financial support by the Estonian Research Council (Grants PRG 539 and SLOKT 12026 T) is gratefully acknowledged. A.Z., G.B. gratefully acknowledge financial support by the Deutsche Forschungsgemeinschaft (DFG, German Research Foundation) under Germany´s Excellence Strategy – EXC 2008/1 and EXC 314/2–390540038 (Gefördert durch die Deutsche Forschungsgemeinschaft (DFG) im Rahmen der Exzellenzstrategie des Bundes und der Länder – EXC 2008/1 und EXC 314/2 – 390540038) and Sfb1078 (Humboldt Universität Berlin), TP A5 (R.H., M.I., A.Z.). We also gratefully acknowledge the allocation of beamtime by the ILL Grenoble on the instrument D33 and by ESRF on the BM29 BioSAXS beamline.

II.3. **Structural Dynamics in the Water and Proton Channels of Photosystem II During the S_2 to S_3 Transition**

Authors: Rana Hussein[a], Mohamed Ibrahim[a], Asmit Bhowmick[a], Philipp S. Simon[a], Ruchira Chatterjee[a], Louise Lassalle, Margaret Doyle, Isabel Bogacz, In-Sik Kim, Mun Hon Cheah, Sheraz Gul, Casper de Lichtenberg, Petko Chernev, Cindy C. Pham, Iris D. Young, Sergio Carbajo, Franklin D. Fuller, Roberto Alonso-Mori, Alex Batyuk, Kyle D. Sutherlin, Aaron S. Brewster, Robert Bolotovsky, Derek Mendez, James M. Holton, Nigel W. Moriarty, Paul D. Adams, Uwe Bergmann, Nicholas K. Sauter, Holger Dobbek, Johannes Messinger, Athina Zouni, Jan Kern, Vittal K. Yachandra, Junko Yano

[a]Equal contributions as a co-first author

Abstract

Light-driven oxidation of water to molecular oxygen is catalyzed by the oxygen-evolving complex (OEC) in Photosystem II (PSII). This multi-electron, multi-proton catalysis requires the transport of two water molecules to and four protons from the OEC. A high-resolution 1.89 Å structure obtained by averaging all the S states and refining the data at various time points during the S_2 to S_3 transition has provided better visualization of the potential pathways for substrate water insertion and proton release. Our results indicate that the O1 channel is the likely water intake pathway, and the Cl1 channel is the likely proton release pathway based on the structural rearrangements of water molecules and amino acid side chains along these channels. In particular in the Cl1 channel, we

suggest that residue D1-E65 serves as a gate for proton transport by minimizing the back reaction. The results show that the water oxidation reaction at the OEC is well coordinated with the amino acid side chains and the H-bonding network over the entire length of the channels, that is essential in shuttling substrate waters and protons.

Introduction

Water is a necessary ingredient for life on Earth. It is a solvent for all enzymatic reactions and essential for protein folding and activity[298]. In the case of Photosystem II (PSII), which catalyzes the photosynthetic water oxidation reaction in nature, water is also the substrate. The oxidation of water produces most of the O_2 in the atmosphere and shapes the biosphere by facilitating the large-scale production of biomass and energy-rich carbohydrates[217]. PSII is embedded in the thylakoid membranes of cyanobacteria, algae, and plants that oxidizes water to dioxygen using light as follows[23]:

$$2H_2O \xrightarrow{\text{light}} O_2 + 4H^+_{\text{lumen}} + 4e^-$$

The protons (H+), which result from water oxidation, are released into the lumen. PSII carries out this reaction by coupling the one-electron photochemistry occurring at the reaction center with the four-electron oxidation of water at the oxygen-evolving complex (OEC) (Fig. 1A)[100, 101]. The OEC consists of a heteronuclear Mn_4CaO_5 cluster, which cycles through five intermediate S-states (S_0 to S_4) that correspond to the abstraction of four successive electrons from the OEC via a redox-active tyrosine residue (Yz)[85]. Once four oxidizing equivalents accumulate at the OEC (metastable or transient S_4-state), the release of O_2 and the formation of the S_0-state take place spontaneously.

During one cycle of the catalytic reaction, the OEC consumes two water molecules; one is introduced into the cycle during the $S_2 \rightarrow S_3$ transition and the second during the $S_3 \rightarrow S_0$ transition (Fig. 1A)[50, 51, 91, 299-301]. In addition to four electrons, four protons are released from the catalytic reaction in the pattern of 1:0:1:2 for S-state transitions, $S_0 \rightarrow S_1 \rightarrow S_2 \rightarrow S_3 \rightarrow S_0$, respectively[300, 302-306] (Fig. 1A). The spatially controlled transport of substrate (water) and products (protons and dioxygen) between the catalytic center and the lumenal side of the membrane is essential for efficient catalysis, especially, for a multi-electron process like the water oxidation reaction. Therefore, it is crucial to understand the role of water and proton channels and the hydrogen bond network(s) during the reaction process. Several possible water/oxygen/proton channels within PSII have been proposed from computational studies based on structural information obtained

at cryogenic temperature at an intermediate resolution[43, 102, 104, 122, 307], and more recently based on higher resolution data (Fig. 1A,B)[66, 73, 120, 308-310].

As the Mn_4CaO_5 cluster is embedded inside the protein close to the lumenal side of the membrane, it was postulated earlier that water channels and proton exit pathways most likely exist within the complex to ensure proper substrate supply and removal of reaction products (protons and oxygen). Initial work was performed based on the search for cavities and channels using the lower resolution crystal structures, which did not resolve the positions of the waters in the model[102, 104, 122, 307]. A summary of these studies is given in the supplementary material (Supplementary Table 1).

Applying molecular dynamics (MD) simulations gave new insights into, e.g. identifying new channels, characterizing water permeation energetics[122, 310], and investigating water diffusion from the bulk[120]. These channels match with some paths identified in the earlier crystal structures (Supplementary Table 1). Among those, Vassiliev et al. demonstrated the first steered MD simulations of solvated PSII[309, 310]. This approach, which involves accelerating water permeation by continuous water injection near the OEC, revealed new channels and identified the amino acid residues that narrow the channels and form the bottlenecks and determined the corresponding activation energies for opening of these bottlenecks. This study also provided two crucial insights concerning water movement. First, water molecules cannot directly permeate from one side of the OEC to the other (Fig. 1B). However, this finding did not exclude the possibility for water to migrate from one binding site at the OEC to another. Second, none of the channels permit unrestricted access of water to the OEC. This illustrates the difficulty of identifying channels in PSII with static methods (for example, using standard software packages like CAVER or MOLE to map cavities and channels). The potential water channels currently proposed from a series of studies are the O1 channel, the Cl1 channel, and the O4 channel (Fig. 1A,B), and their corresponding names in other studies are summarized in Supplementary Table 1. The O1 channel aka the large channel[122] starts from near the Ca in the active site, and reaches the lumen at the interface of subunits D1, CP43, and PsbV for branch A and PsbU, PsbV, D2 and CP47 for branch B. Despite the absence of PsbU and PsbV in the PSII of higher plants, the O1 channels are found to be conserved (Supplementary Fig. 1)[311]. The Cl1 channel starts from the Mn4 and connects to the lumen through D1, D2, and PsbO domains for branch A(short) and D2 and PsbO for branch B (long). The O4 channel aka narrow channel[122], starts at the O4 side toward the lumen via the D1, D2 and CP43 subunits, before extending to PsbO and PsbU. Similar

to the O1 channel, the O4 channel is also conserved in plant PSII[311]. The bottlenecks along each channel that may gate the entrance of the water molecules are shown in Fig. 1B.

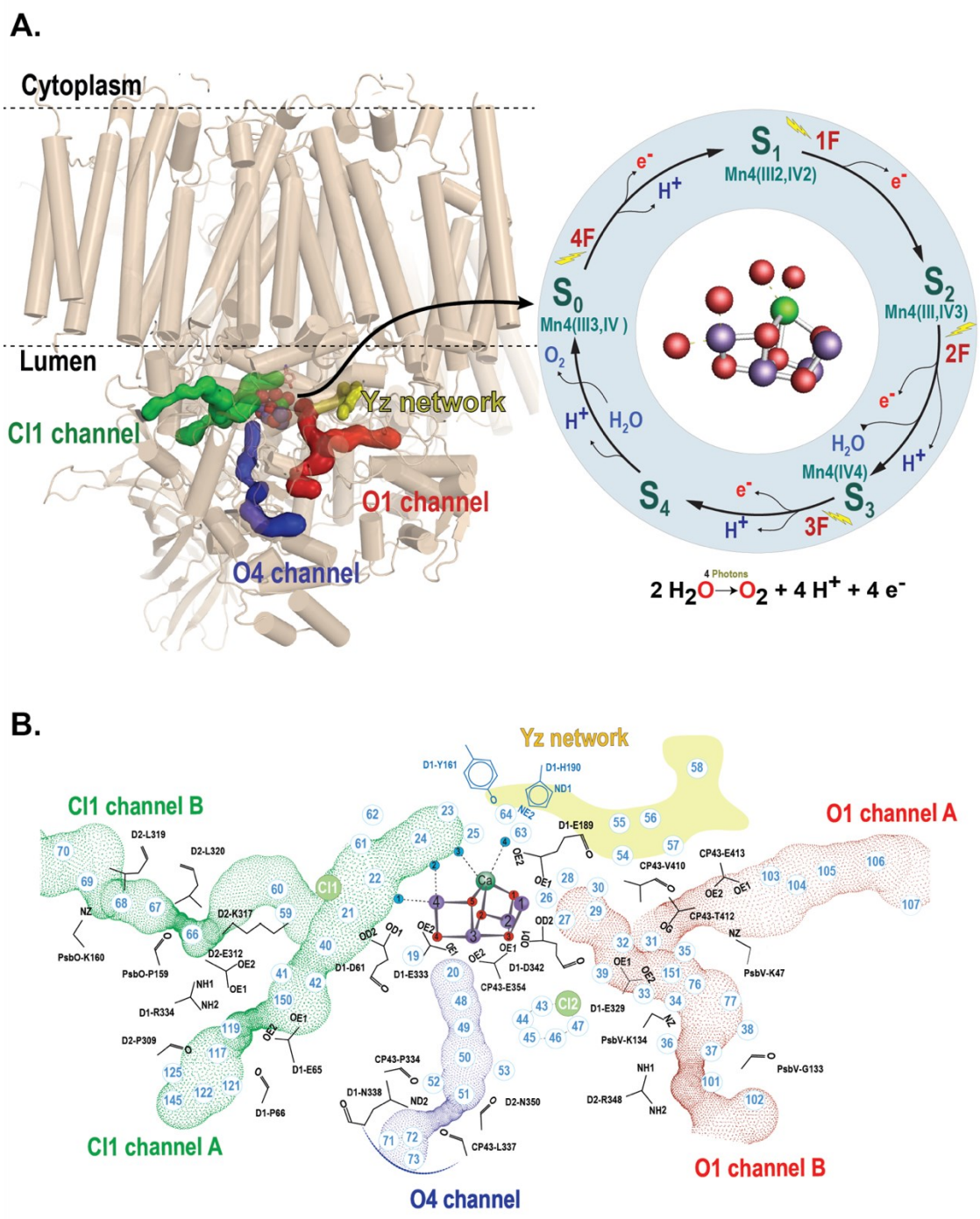

Figure 1 An overview of Photosystem II and the main water channels and networks from the OEC to the lumenal side. *A: (Left) The structure of PSII showing the membrane-embedded helices and the extrinsic subunits in beige. The OEC and the water channels, in addition to the Yz network, are shown in color. The Kok cycle of the water oxidation reaction that is triggered by the absorption of photons is shown on the right and highlighted with a blue circle. B: A detailed view of the water channels showing the waters within each channel (O1 Channel red dotted, O4 Channel blue dotted, and Cl1 Channel green dotted). The region highlighted with solid yellow represents the Yz network. Residues involved in forming bottlenecks in the channels are shown in black.*

Recent advances in X-ray free-electron laser (XFEL)-based room temperature (RT) crystallography enabled us to study the dynamics of the structure of the water network under functional conditions[48, 50, 51, 312]. The ability to take snapshots of the structure at the various time points at RT during the reaction allows for the investigation of water movements and changes in hydrogen bonding networks in proteins[51]. These studies can provide new insights into the reaction mechanism in PSII by potentially identifying water and proton pathways. They also provide starting models for MD simulations, using RT structures that are the catalytically relevant and functional states, along a reaction trajectory.

In an earlier study by Ibrahim et al.[91], we showed the RT structural changes of PSII together with the kinetics of the Mn oxidation in the OEC during the S_2 to S_3 transition (at time points 50 μs, 150 μs, 250 μs, 400 μs, and 200 ms after the 2nd flash) under functional conditions, and discussed the major sequence of structural events. We also reported that the OEC remains in the open-cubane configuration, seen in the S_1 and S_2 states, throughout the $S_2 \rightarrow S_3$ transition[51, 91]. There was no indication of the suggested rearrangement of the cluster between an "open-cubane" and a "closed-cubane" structure[152].

In the present study, we focus on the question of mobility of the waters surrounding the OEC. We do that by combing the large data set we have previously acquired throughout the Kok cycle to obtain a high-resolution structure at 1.89 Å. Regions with more mobility will show a more disordered electron density, whereas regions of less mobility will be more distinct. With this approach we also identified more waters than previously within the channels described above. These waters were also present in the difference density maps (Fo-Fc) of the individual datasets, but at low sigma level ≤3.0 σ, and hence they were not initially modeled. The presence of these waters in the high-resolution data enabled us to model them into the structure. Introducing these waters into the models for the S_2 to S_3 time point data and re-refining them led to improved electron density maps and the identification of additional waters.

The S_2 to S_3 transition is a critical step as it is coupled with the first water binding to the Mn_4CaO_5 cluster and the release of one proton. In light of the newly provided information, we investigated the changes in the positions of the amino acid sidechains and the water network(s) that lead to the insertion of water into the open coordination site of Mn (Mn1)[50, 51, 91], and the release of protons to identify the possible substrate intake

and proton release pathway(s) in relation to previous computational and spectroscopic studies[126, 127, 162, 300, 301, 313-318]. We also investigated the structure of the water channels and the hydrogen bonding network through a comparison of the cryogenic and RT crystallographic studies obtained using an XFEL.

Results

Mobility of water in the channels during the $S_2 \rightarrow S_3$ transition using high-resolution structural data

A high-resolution data set was generated by merging more than one hundred thousand high-quality diffraction images collected at RT from PSII crystals in various illumination states and a structure was refined to a resolution of 1.89 Å (Supplementary Table 2). In this high-resolution structure, the waters in the O1 channel have higher B-factor values than waters within the O4 and Cl1 channels (Fig. 2A and Supplementary Fig. 2, see Supplementary Table 3 for water numbering). The average B-factor values for the waters up to approximately 15 Å from the OEC in the O1 channel, O4 channel and the Cl1 channel are around 38, 31 and 27 $Å^2$ respectively. Note that B-factors, or atomic displacement parameters, are directly proportional to the mean square displacement of atoms around their equilibrium position[319]. The waters with high B-factor in the O1 channel are distributed through the entire channel, starting from the bulk waters (lumen side) to the waters close to the OEC. On the other hand, the waters within the Cl1 have high B-factor values only near the bulk at the lumen side (~33 $Å^2$ on average) (Supplementary Fig. 2). The different B-factor values in the channels could be due to the crystal contacts. To check for such potential effects, we compared the B-factors of waters in both monomers, with fixed occupancy during the refinement, as they have different crystal contacts. We show in Supplementary Fig. 3 that in both monomers, the waters in the O1 channel have higher B-factors than those in the Cl1 or O4 channel. See also Supplementary Table 4 and 5 for omit density peak heights and B-factors of waters in the individual datasets.

Furthermore, several Fo-Fc (difference density map) peaks in the high-resolution data set likely imply partial occupancy of highly mobile waters in the channels. Therefore, the Fo-Fc peaks ($\geq$+3σ) were mapped within all the proposed channels (Fig. 2A). In the O1 channel, the Fo-Fc peaks are distributed through the entire channel, starting from the bulk waters (lumen side) to the waters close to O1 of the OEC. By contrast, the Fo-Fc peaks in the Cl1 and O4 channels appear only near the bulk water on the lumen side.

Besides analyzing the high-resolution data set, we investigated the change in the normalized B-factor (see SI Methods) of each water within the channels in the dark-adapted state S_1, and illuminated states S_2, S_3, and the four transient time points (50, 150, 250, and 400 μs after the second flash) (Supplementary Fig. 4). The deviation of water positions from the S_2-state was also investigated in these time point data (Supplementary Fig. 5).

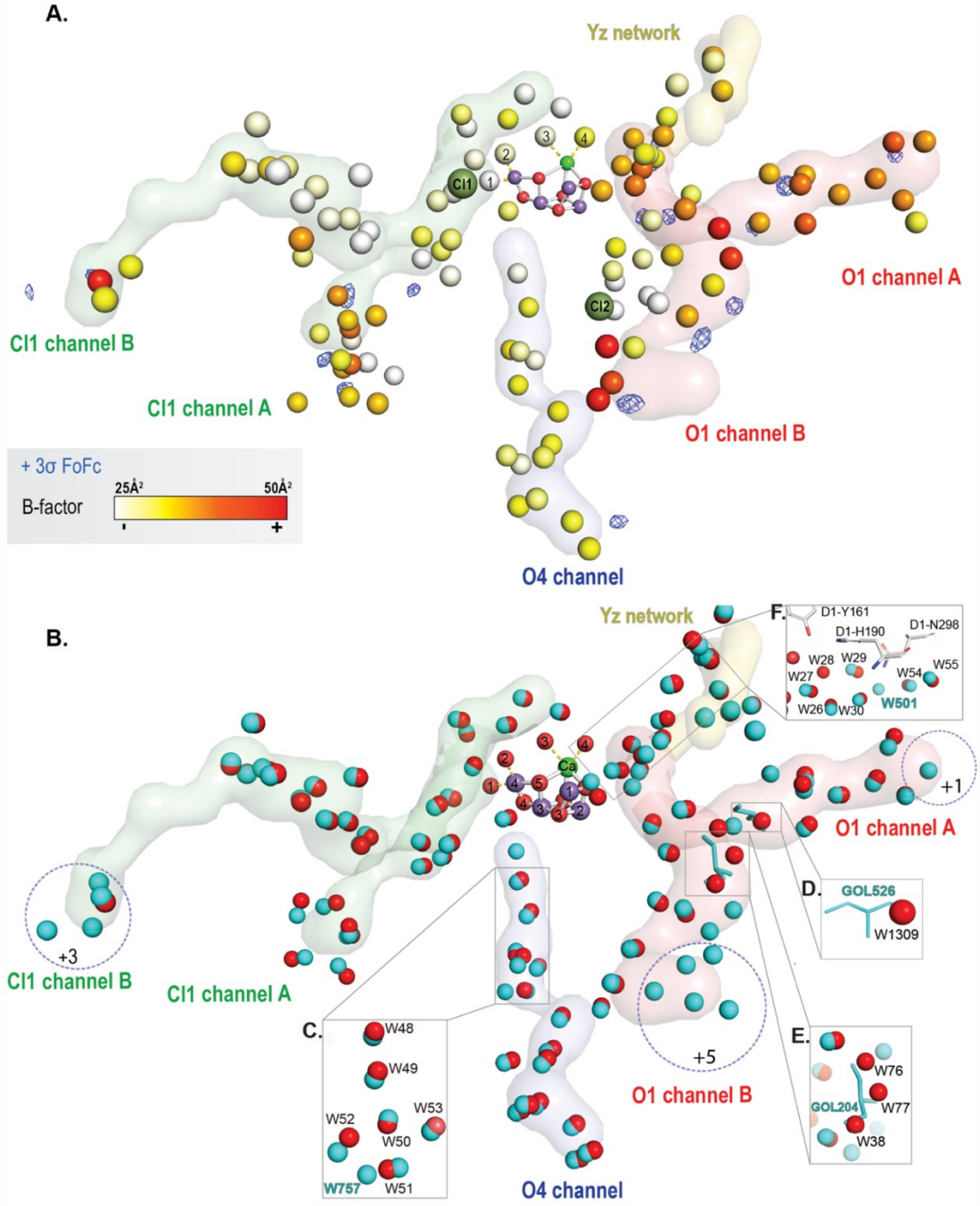

Figure 2 Water channels in the 1.89 Å resolution RT structure. *A: Fo-Fc, electron density omit map, contoured at ≥ +3σ in blue for all the proposed water channels. The water molecules are represented using a color gradient scale, representing the B-factor of each water (white color for B-factor 25 to red color for B-factor 50). The channels and the network, O1 Channel in red, O4 Channel in blue, Cl1 Channel in green, and Yz network in yellow.* ***B****: Comparison between water channels in the RT and cryo structures. The water*

*molecules detected within 3.5 Å from the water channels in red for the 1.89 Å RT structure (PDB ID: 7RF1) and cyan for the 1.95 Å cryo structure (PDB ID: 4UB6). Extra water molecules in the 1.95 Å cryo structure (PDB ID: 4UB6) detected within 5 Å away from the bulk are in the yellow circle. A comparison of the structural differences present in the O4 channel, O1 channel A and O1 channel B between the 1.89 Å RT structure (colored in red and labeled in black) and the 1.95 Å cryo structure (PDB ID: 4UB6) (colored in cyan and labeled in cyan) are shown in (**C**), (**D**) and (**E**), respectively. **F**: Structural differences in waters of the Yz network between 1.89 Å RT structure (colored in red and labeled in black) and the cryo structure with PDB ID: 6JLJ (colored and labeled in cyan).*

Differences in the water network in the cryo and RT structures

Analyzing the water molecules within the potential channels in the combined high-resolution RT structure and the high-resolution cryo (< 2.0 Å) structures[45, 47], shows that the numbers of the waters detected in the channels are comparable at cryo and RT conditions (Fig. 2B and Supplementary Table 6). Our analysis showed that only near the bulk region (up to ~5 Å from the lumen), more waters are observed in the cryo structures, and the most significant difference is observed in the O1 channel B (Fig. 2B).

However, the water networks are different in several locations between the RT and cryo structures. Small non-native molecules, i.e., glycerol or dimethyl sulfoxide (DMSO), are observed in several crystal structures, Supplementary Table 7, in both the A and B branches of the O1 channel (Fig. 2E, D). These molecules are used as a cryoprotectant[45, 47, 52, 307], or as an additive during crystallization[50, 320]. This implies that small molecules like cryoprotectants can pass through the cavity of the O1 channel. The presence of these molecules in the channel leads to changes in the water network due to their different hydrogen bonding geometry. For example, a glycerol molecule disturbs the water positions, W38, W76, and W77 of the branch B in the O1 channel (See Fig. 2E).

Unlike the O1 channel, the waters in the much narrower O4 and Cl1 channels are less mobile, as discussed above and also shown by Ibrahim et al.[91]. A small difference in the cryo and RT structures is observed in the O4 channel, where four waters (W50-53) are connected with charged residues and located right before the bottleneck formed by the residues D1-N338, D2-N350, and CP43-P334, -L334 (Fig. 1B). In our RT data, throughout the different illumination states, W50 is connected to three waters (W51-53), creating a "star shape" at the end of the branch (Fig. 1B, Fig. 2C and Supplementary Fig. 6), but it is different from what was observed at cryo temperature (Fig. 2C and Supplementary Fig. 6)[47, 50, 52]. It was found that one extra water, W603 (PDB ID: 6JLJ)[52] or W757 (PDB ID: 4UB6)[47], is only detected under cryogenic conditions, affecting the hydrogen-bonding water network around W50 (Supplementary Fig. 6).

Differences in the dark S_1-state between the cryo and RT structures are also observed in the hydrogen-bonding network around the redox-active Y_Z (D1-Y161) that mediates electron transfer between the Mn_4CaO_5 cluster and the primary electron donor P_{D1}^+ (Fig. 2F and Supplementary Fig. 7). At cryogenic temperature, a water (W501 (PDB ID: 6JLJ)[52]/ W1117 (PDB ID: 3WU2)[73]) was located close to D1-N298 (Fig. 2F and Supplementary Fig. 7) but it is absent at RT. Hence, D1-N298 is the only connection between the penta-cluster waters W26-27-28-29-30 via W29 and a chain of waters (W54-55-56) on the other side of D1-N298, which in turn are connected to a hydrogen-bonding network to the lumen.

Structural changes of the waters and sidechains within the channels

In the next step, we evaluate the motion of waters and amino acid residues along the channels using the RT crystallography data collected for the S_2 (200 ms after one flash (1F)) and the S_3 state (200 ms after the 2nd flash (2F)), and four time points (50, 150, 250, and 400 μs after the 2nd flash) during the S_2 to S_3 transition (Supplementary Table 2), where both a proton release and water insertion occur. Extra waters which are well identified in the combined high-resolution data and also present in the difference density maps (Fo-Fc) of the individual datasets are included in the models of these time points. Structural refinement, allowing water occupancy changes, results in improving the electron density maps and identifying new features. Figs. 3, 4 and 5 show the structural changes in the channels O1, O4, and Cl1 at various time points during the S_2 to S_3 transition.

O1 channel

The mobility of waters in the O1 channel is higher than those in the Cl1 or O4 channels as shown above (Fig. 2A**)**. Prior to the insertion of Ox, the D1-E189 sidechain, which is ligated to Mn1 and Ca in the S_2-state, moves away from Ca in the S_3-state[51], and Ox becomes a new bridging oxygen between Ca and Mn1. Ibrahim et al.[91] reported that this movement starts within 50μs after the 2nd flash, and by 150μs, the D1-E189 residue is no longer ligated to Ca. This sidechain motion at 2F(50μs) is accompanied by a drop of electron density of two waters, W25 and W30, that are hydrogen-bonded to D1-E189 (Fig. 3B,C). W25 is additionally H-bonded to Y_Z and W3.

Among the waters in the O1 channel, the position of waters that are in close proximity to the OEC (W26, W27, W28 and W39), change the most during the S_2 to S_3 transition (Fig. 3A). A significant decrease in electron density and occupancy of W27 were observed at 2F(150μs) and the W39 electron density increases to reach its maximum at

this time point (Fig. 3B,C). This decrease and increase of the electron density at W27 and W39 coincide with the starting of the Ox density build-up at the open coordination site of Mn1. Among the four ligand waters (W1-4), the B-factor of W4 relative to W1 – W3 increases during the S_2 to S_3 transition (Supplementary Fig. 8).

In addition, we observe changes at distal waters, >15 Å from the OEC, in the later time points. For example, W76 and W77, located at ~15 Å from the OEC, along the channel before the bottleneck formed by residues PsbV-G132, -G133, -K134, D2-R348, show significant movements (Fig. 3A) as seen by the electron density fluctuations (Fig. 3C). At 2F(400µs), new electron density appears near the D1-E329 residue close to W34. This density indicates a new water at this position (W151) (Fig. 3A,C). In the 2F(200ms) data (i.e. S_3), its electron density drops significantly.

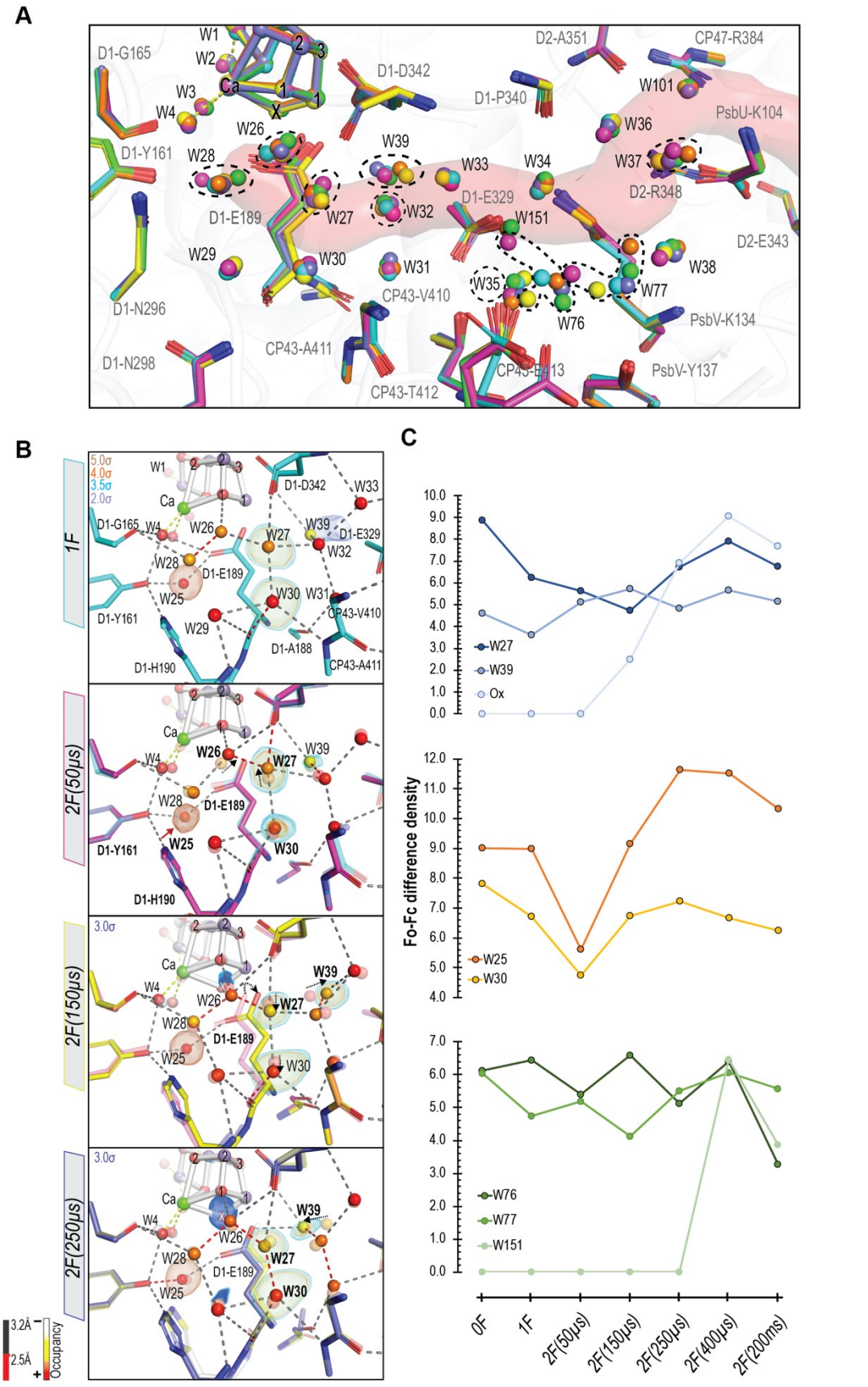

Figure 3 Structural changes in the O1 channel during the $S_2 \rightarrow S_3$ transition. *A: The structural changes in the O1 channel are shown for all time points in the $S_2 \rightarrow S_3$ transition (1F (teal, PDB: 7RF3) and 2F time points (50 µs: magenta, PDB: 7RF4; 150 µs: yellow, PDB: 7RF5; 250 µs: slate, PDB: 7RF6; 400 µs: orange, PDB: 7RF7; 200 ms: green, PDB: 7RF8)). O1 channel is in red. Waters that show significant movement during the $S_2 \rightarrow S_3$ transition are marked with a black dashed circle.* ***B****: Structural changes in*

the beginning of the O1 channel during the transition at different time points: (1F (teal) and 2F time points (50 µs: magenta; 150 µs: yellow; 250 µs: slate)). Each model overlaid with the model of the earlier time point, shown in a transparent color. The waters are colored based on their occupancies, represented by a color gradient from white to red as shown at the bottom left. The positions for certain waters are confirmed by Fo-Fc omit maps contoured at different σ levels (3.5σ, 4σ) with the exception of W30 at 1F and Ox omit maps contoured at 2σ and 3σ, respectively. The H-bond length is color-coded, as described at the bottom left. Movements of W26, W27, W39 and D1-E189 are marked with black dashed arrows. ***C****: Difference density heights from the Fo-Fc omit maps for selected waters in the O1 channel and Cl1 channel.*

O4 channel

A H-bonded water network in the O4 channel starts from O4 of the OEC and extends through the subunit CP43 until reaching the cavity before the bottleneck formed by D1-N338, D2-N350, CP43-P334 and CP43-L334 (Fig. 1B). It then extends further to the lumen side through the PsbO and PsbU subunits. The RT structural data reported earlier by Young et al.[48] shows the disappearance of W20, the 2nd water from the OEC in this channel, during the S_1 to S_2 transition (Supplementary Fig. 9). The same observation was reported by Kern et al.[51], and Suga et al. (W20 named as W699)[52]. This disappearance is due to either W20 moving away from its position in the channel or having an increased mobility after the 1st flash. In both scenarios, the hydrogen-bonding network along the O4 channel becomes disconnected from the OEC in the S_2-state and is restored only in the S_0-state. In addition, the positional changes of waters W19, W49, and W50 (Supplementary Fig. 9) along this channel, also result in keeping the hydrogen-bonding network disrupted during the S_2 to S_3 transition. We also observed changes at the beginning of the channel, in the O4 - W19 – D1-S169 - W1 network, during the S_2 to S_3 transition (Fig. 4). As the changes in this area are also related to the changes in the Cl1 channel, we discuss them together in the next section.

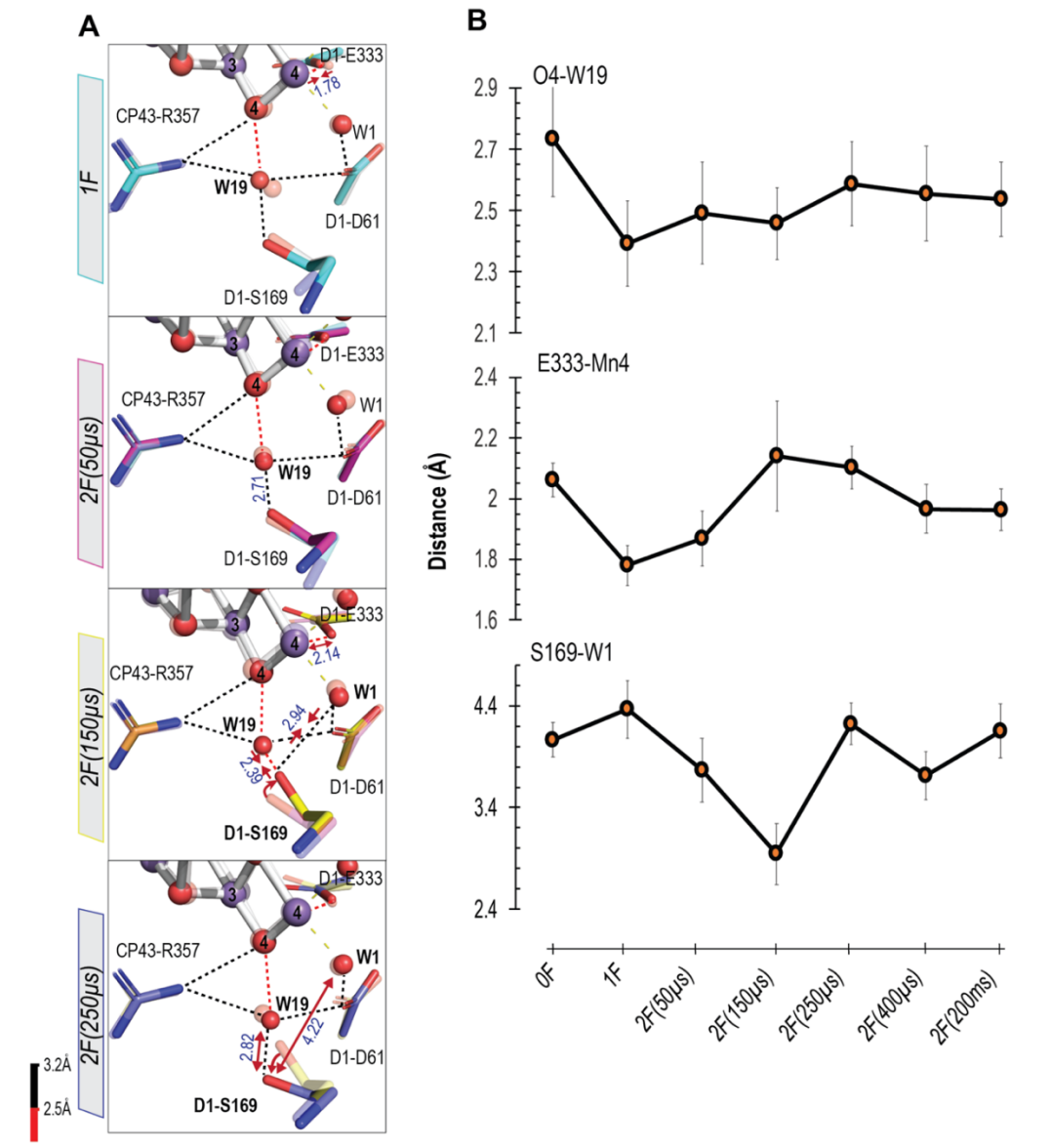

Figure 4 Changes near W1 and O4 environment during the $S_2 \rightarrow S_3$ transition. ***A***: *Structural change in the region of W1 and O4. The structures at different time points are indicated in the left margin, each in solid colors overlaid with the earlier time point, which is in a transparent color scheme (0F (white, PDB: 7RF2), 1F (teal, PDB: 7RF3) and 2F time points (50 µs: magenta, PDB: 7RF4; 150 µs: yellow, PDB: 7RF5; 250 µs: slate, PDB: 7RF6)). The H-bond length is color-coded, as described at the bottom left. Red arrows indicate elongation/ shortening of the interatomic distances. The interatomic distances (Å) are shown in blue. 2F(150 µs) structural data shows rotation in the D1-S169 sidechain affecting the H-bonding network.* ***B***: *Distance changes for selected bond lengths within the W1 and O4 environment during the $S_1 \rightarrow S_2$ and $S_2 \rightarrow S_3$ transitions. Error bars represent the standard deviation calculated by generating 100 randomly perturbed datasets and re-refining, as described in SI Methods.*

Cl1 Channel

The Cl1 channel that starts from the Mn4 side of the OEC involves one of the chlorides (Cl1) near the OEC and D2-K317 and D1-D61 residues that form a bottleneck

(Fig. 1B). Through D1-D61, the Cl1 channel is connected to W19, which is also the first water in the O4 channel. Along the Cl1 channel, we observed sequential changes during the S_2 to S_3 transition along branch A around the bottleneck that is formed by D1-E65, D1-P66, D1-V67 and D2-E312, and in the area of O4, W19, D1-S169 and W1 (shown in Figs. 5 and 4**,** respectively).

After the 1st flash, the Mn4-$O_{D1\text{-}E333}$ distance is shortened from 2.06 to 1.78 Å, which is accompanied by the shortening of the O4-W19 distance by 0.34 Å with standard deviation of 0.14 (2.73 Å → 2.39 Å) (Fig. 4A,B). This could be due to the oxidation of Mn4 (from III to IV) after the 1st flash, which likely influences the Mn4-O4 oxo-bridge. By 150 µs after the 2nd flash (2F(150µs)), the sidechain of D1-S169 moves significantly (Fig. 4A), decreasing the distance between S169 and W1. Concomitantly, the D1-E65 sidechain, a pivotal contributor to the bottleneck, rotates ~50°, which results in a drastic rearrangement of the H-bond network in this area (Fig. 5A,B). The rotation of D1-E65 disturbs its hydrogen-bonding interaction[321] to D1-N335 (2.70 Å → 3.35 Å). This also weakens the interaction between D1-E65 and D2-E312 (2.65 Å → 2.72 Å), while strengthening the interactions to D1-R334 (3.18 Å → 2.54 Å). The rotation of D1-E65 alters the interaction to W119 (3.47 Å → 2.49 Å), and W42 (3.46 Å → 3.03 Å) (Fig. 5). The analysis of the radius of this bottleneck of Cl1 channel during the S_2 to S_3 transition showed that the D1-E65 rotation, at 150 µs after the 2nd flash, reduces the radius of the bottleneck (Supplementary Fig. 10). We note that this channel appears too narrow for water transport, but that transient openings occurring, at any studied time point, only in small fractions of the centers cannot be excluded.

By 250 µs into the S_2 to S_3 transition (2F(250µs)), the D1-E65 side chain rotates back to its original position, and concomitantly a new water (W150) with ~55 % occupancy appears in hydrogen-bonding distance to D1-E65 and within close distance to W40 (~2.1 Å). This is accompanied by shortening of the distance between D1-E65 and D2-E312 from 2.72 to 2.46 Å and a decrease in the electron density of W119 (Figs. 4 and 5) and its occupancy from ~80% at 2F(150 µs) to ~53% at 2F(250 µs). However, the omit densities of W119 fluctuates during the S_2 to S_3 transition (Fig. 5A).

In addition to the side chain motions described above, we observed the appearance/disappearance of some additional waters along the Cl1 channel. In the region after the bottleneck, W117 observed in the S_1-state is not present in 1F (S_2), but present at 2F(50 µs) (Fig. 5 and Supplementary Fig. 11). W121 is not observed in the 2F(50 µs)

data, while extra electron density near PsbO-D224 modeled as W145 was observed. In 2F(150μs), these changes are reversed, i.e., the W117 and W121 densities reappeared, together with the disappearance of W145.

By 400 μs into the S_2 to S_3 transition (2F(400 μs)), the Cl1-channel environment is rearranged back to one being similar to the S_1-state (Fig. 5), and no significant changes are observed between the S_1 and the fully evolved S_3-state (2F(200 ms)) (Supplementary Fig. 11).

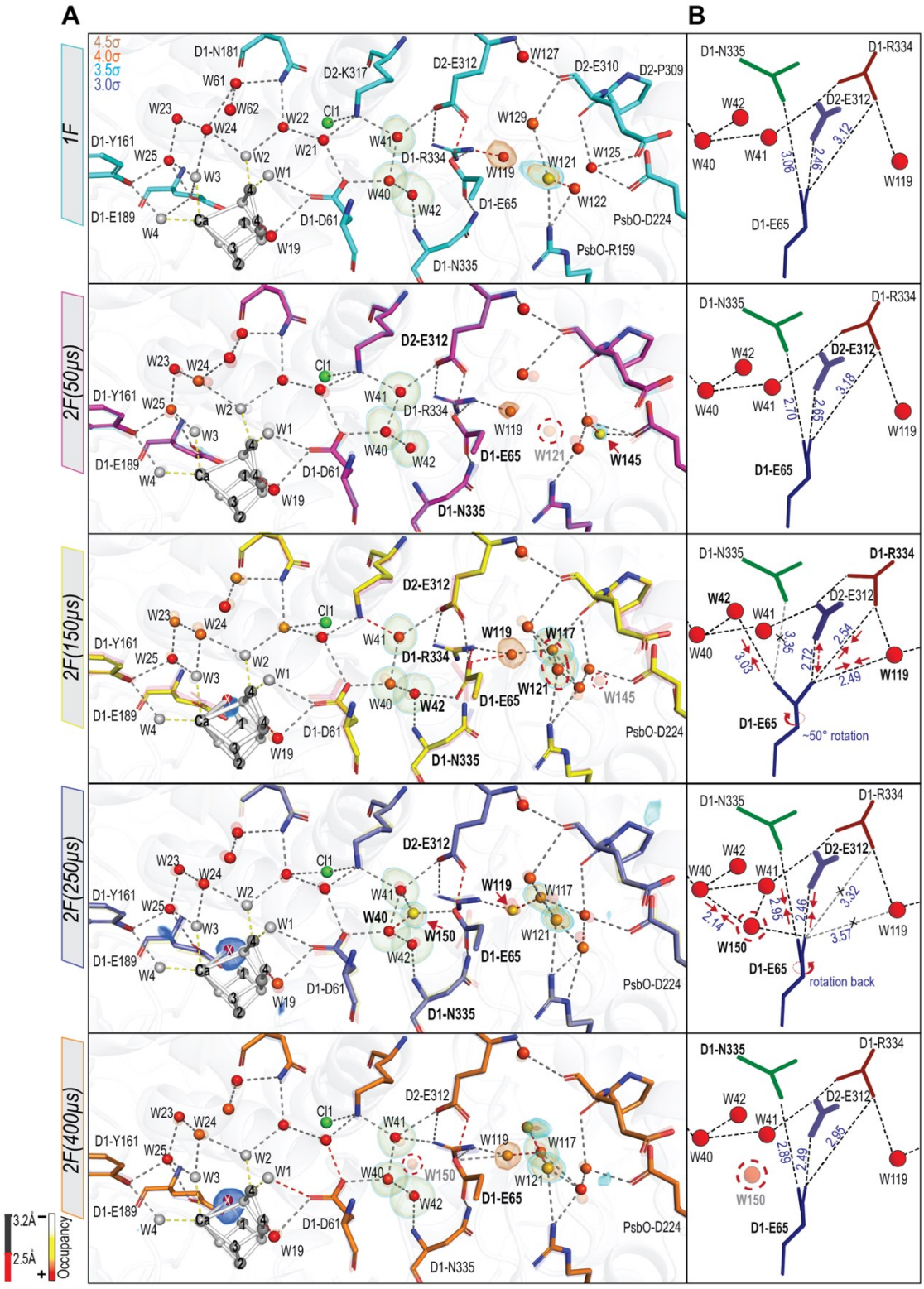

Figure 5 Structural changes in the Cl1 water channel during the $S_2 \rightarrow S_3$ transition. ***A***: *Structural changes in the protein and water molecules during the transition at different time points: (1F (teal, PDB: 7RF3) and 2F time points (50 µs: magenta, PDB: 7RF4; 150 µs: yellow, PDB: 7RF5; 250 µs: slate, PDB: 7RF6; 400 µs: orange, PDB: 7RF7)). Each model overlaid with the model of the earlier time point, shown in a transparent color. The waters are colored based on their occupancies, represented by a color gradient from white to red as shown at the bottom left. The positions for certain waters are confirmed by Fo-Fc omit maps contoured at different σ levels (3.5σ, 4σ) with the exception for W25, W119 and Ox omit maps contoured at (5σ, 4.4σ and 3σ respectively). The H-bond length is color-coded, as described at the bottom left. Appearance and disappearance of W121, W117, W121, W145 and W150 at different time points are marked with a red dashed circle.* ***B***: *Model of the structural changes around D1-E65, D2-E312 and D1-R334. The H-bonds are shown in dashed black line and up to 3.2 Å. Red arrows indicate elongation/ shortening of the*

interatomic distances. The interatomic distances (Å) are shown in blue. The rotation of the D1-E65 at 2F (150 µs) is marked by a red circle arrow. Appearance and disappearance of W150 at 2F (250 µs) and at 2F (400 µs), respectively, are marked with a red dashed circle.

Discussion

Our study investigates the motion of waters and surrounding amino acid residues using snapshots of the RT crystal structures of PSII to identify substrate water and proton release channels. We focus on the S_2 to S_3 transition step, where one electron and one proton are released, and one water molecule comes into the OEC to the open coordination site of Mn1 as a bridging oxo or hydroxo ligand between Mn1 and Ca[50, 51, 91]. The water positions are largely preserved between the RT and cryogenic structures in the dark-adapted state, suggesting that most of the waters along the potential channels are highly structured, except at the exit of each channel into the bulk. There are, however, some differences, which likely have important implications for the interpretation of the proton relay (Fig. 2B). We have also observed sequential changes of several water positions at RT along the course of the S_2 to S_3 transition after the 2nd flash (Supplementary Fig. 5). Based on the above observations, we discuss the likely channels for proton release and water intake.

For substrate intake pathways, the O1, O4 and Cl1 channels have been proposed based on theoretical studies[120, 122, 153, 309, 310, 322, 323]. Therefore, determining the substrate channel will help reducing possible substrate insertion pathways in the OEC that lead to Ox in the S_3 state. The combined 1.89 Å high-resolution structure of PSII in this study helped model partially occupied waters in the crystal structures of the individual timepoint data. Previously these water densities were visible in the timepoint data but were not included in the model due to the uncertainty[51, 91]. In addition, the high-resolution data shows several Fo-Fc peaks (Fig. 2A), that are spread along the O1 channel, but not in the Cl1 or O4 channel. This is most likely due to waters occupying different positions at different time points or the presence of new partially occupied waters included in the combined data, implying more mobile waters in the O1 channel (Fig. 2A). Besides, the combined high-resolution structure shows that the waters in the O1 channel have significantly higher B-factors than those in the Cl1 channel or O4 channel (Fig. 2 and Supplementary Figs. 2 and 3). Along the same line, deviations in the positions and the high fluctuations in the normalized B-factors of the waters in the O1 channel at the different time points during the $S_2 \rightarrow S_3$ transition confirm the higher mobility of water in the O1 channel in comparison to Cl1 and O4 channels (Supplementary Figs. 4 and 5).

Moreover, in the crystal structures with glycerol or DMSO present in the crystallization process[47, 50, 52, 73], these molecules were visible in the O1 channel, but not in the Cl1 or O4 channel. The FTIR data by Kato et al. reported that the S-state turnover efficiency of crystals (with glycerol) is slightly lower than that of the solution sample (without glycerol) in the S_2 to S_3 and S_3 to S_0 transitions, the steps where the substrate water insertion is involved[313, 324]. We hypothesize that such a decrease may be caused by the slightly altered water network in the O1 channel in the presence of small additives that influence the access or mobility of waters. We, however, note that the effect of such small additives in the O1 channel is minor and does not block the water oxidation reaction.

The new water near D1-E329 detected in the 2F(400μs) data after the completion of the Ox insertion at the Mn1 site may also support the O1 channel being the water intake channel from the lumenal side of the membrane. However, we cannot determine whether branch A, or B, or both serve as a pathway. Regarding the possibility of the Cl1 channel being the water intake pathway, we think this is unlikely due to the following observations: First, the mobility of waters in the channel is lower than that of the O1 channel. Second, no structural changes were observed along branch B. Third, the structural changes observed at the bottleneck region in branch A do not allow a water to pass through. While D1-E65 rotated by ~50º, this flipping motion does not open up the Cl1 channel (Supplementary Fig. 10). We think that the reversible motion of D1-E65 and the presence of less mobile waters makes the Cl1 channel more suitable to serve as a proton pathway (Fig. 6). This hypothesis is also supported by a study of oxidative modifications in PSII by Weisz et al., where the authors identified the O1 channel as one of the possible pathways for water intake, but not the Cl1 branch A[325]. Nevertheless, branch B of the Cl1 channel was also found to be oxidized by ROS formed at the OEC.

Building upon the hypothesis of the O1 channel being the water intake pathway, we explore the question of how the water in the O1 channel ends at the open coordination site of Mn1 as a bridging ligand, Ox (oxo or hydroxo), to Mn1 and Ca during the S_2 to S_3 transition[50, 51, 91]. Prior to the Ox insertion, our timepoint data showed the changes of the interaction between the redox-active Y_Z and H190, due to the oxidation of Y_Z by the primary electron donor P_{D1}^+ following charge separation[91]. A detailed description of the structural changes within this region was reported in Ibrahim et al.[91]. The main change is the tilting of the histidine side chain and the backbone, providing the driving force for the D1-E189 to move away from Ca[91]. While the motion of E189, ligated to Mn1 and located

close to the O1 channel, changes its position, there is not enough space for the direct insertion of water from the O1 channel to occur.

An alternative route for the Ox insertion is via W3, which is a ligand of Ca[91]. Ugur et al. suggested that W3 moves to the open coordination site of Mn1[326], which was later supported by FTIR[327] and other theoretical studies[315]. If W3 is the entrance of substrate water to the Ox from the O1 channel, it likely needs to come via W4 first, which is refilled from the water wheel-like ring (penta cluster) of W26, 27, 28, 29, and 30 (Fig. 7). In this case, Ca likely plays a pivotal role to shuffle water from W4, W3, and then to Ox. Our data show that the B-factor of W4 relative to W1 – W3 is higher during the transition (2F(50 μs), 2F(150 μs), and 2F(400 μs) (Supplementary Fig. 8). Among the O1 channel waters proximal to the OEC, W28 is found in a suitable geometry to refill W4, and W28 could be refilled by W26/W27 (Fig. 3).

Another possibility is that W25 replaces W3, as W25 is located close to D1-E189 and W3. W25 shows reduced electron density at 50 μs after the 2nd flash (Fig. 3). This drop of the electron density is likely related to the loss or weakening of the H-bond to Y_Z due to Yz oxidation, thereby weakening the H-bond between W25 and the side chain of E189, possibly priming it for replacing W3.

Accompanied by electron transfer and the intake of a water, the egress of a proton is also required during the $S_2 \rightarrow S_3$ transition. The Cl1 and O4 channels as well as the Yz network, have been proposed in the literature as a proton release pathway[111, 126, 127, 317, 318, 328, 329]. The current structural study provides several indications of the Cl1 channel being the proton exit pathway in the S_2 to S_3 transition. Below we discuss the possibility of proton transfer for all three pathways and provide support for the hypothesis of the Cl1 channel being the proton pathway in the S_2 to S_3 transition.

Recently the O4 channel was discussed as a possibility for the egress of a proton during the $S_0 \rightarrow S_1$ transition[162]. Theoretical studies suggested that the water chain in the O4 channel provides a downhill proton transfer[317, 330]. In the S_1 to S_2 transition (Fig. 3B), the disappearance of W20 was observed near the OEC at the beginning of the channel near O4[48, 51, 52]. The dislodging of W20 disconnects the hydrogen bonding network of the O4 channel from the OEC in the S_2-state, and therefore it is unlikely that the O4 channel can serve as a proton release pathway during the S_2 to S_3 transition. This channel has been proposed as a proton release channel during the S_0 to S_1 transition[106, 162, 317, 330]. If the proton release during the $S_0 \rightarrow S_1$ transition is via the O4 channel[162], the current

observation raises the possibility that the proton release pathway may differ in each S-state transition.

The Y_Z network, which was postulated to connect Y_Z to the lumen via D1-N298, has been suggested to be involved in a proton pathway based on the nature of the [YzO···H···Nε-His] H-bond[73, 124, 125] and the water positions in the cryogenic structure[126, 127]. In the RT structural data, however, one water (W501), which could be essential for proton transfer via this network (Supplementary Fig. 7), is missing. If this water does not exist or is highly mobile, the Y_Z network would require a proton transfer through an asparagine (D1-N298)[120, 127] residue that is not generally considered suitable for proton relay. The Yz network ending at the lumen surface residue PsbV-K129 is also rich in other asparagine residues (D1-N301-303-322), and these require tautomerization or amide rotations to allow proton transferring through them[126]. In our current crystal structures, we do not observe any structural changes of these residues during the $S_2 \rightarrow S_3$ transition (Supplementary Fig. 12). An alternative proton pathway that involves waters would require an interaction between W57 and W58. These two waters, however, are separated by 6.4 Å in the S_2-state and do not show any substantial distance changes in all the timepoint models. Therefore, we concluded that the Yz network, based on the RT structural data, is unlikely to be a proton release pathway.

The Cl1 channel has been proposed as a proton release pathway during the S_2 to S_3 transition in many studies in the literature[66, 111, 328, 331], and our current structural observation prefers this assignment. We observe structural changes around D1-E65, D2-E312 and D1-R334 at 150 µs after the 2nd flash, which are reversed by 250 µs. We hypothesize this motion might be triggered by the excess positive charge after Yz oxidation, and slower protonation and H-bonding rearrangements, and is related to the opening of the channel to proton transfer and release as illustrated in Fig. 6 and described in the following. In the S_2-state, D1-E65 and D2-E312 share a proton as indicated by the short H-bonding distance of around 2.5 Å and confirmed by simulations[111]. This suggests that in the S_2-state and up to 50 µs after the 2nd flash (2F(50µs)), the Cl1 channel is in a 'closed state' for proton egress, since D1-E65 is H-bonded to D1-N335, which is inert to a Grotthuss proton hopping mechanism, and D1-R334 is H-bonded to W119, functioning with its positive charge as a directional barrier (Figs. 5B and 6). At 150 µs after the 2nd flash, however, we observe a new conformation of D1-E65 that rearranges the E65/E312 region and hydrogen bonds to W119 (Figs. 5B and 6). This rearrangement forms an 'open state' for an effective proton transfer to the other side of the bottleneck. The proton

transfer from the protonated D1-D61 to a deprotonated D1-E65 or E312 was recently reported to be exothermic via one or two waters[111]. This implies that E65-E312 can accept a proton from the OEC only after releasing a proton towards the bulk (Fig. 6). This conformation is stabilized by a newly formed H-bond between E65 and R334, preventing the released proton to return. A proton could now be transferred from D61 to E65 via at least two possible water chains involving W40/42 or the alternative water position of W150. The newly arrived proton will be repelled by R334 and attracted by E312, so that by 250 µs the D1-E65 side chain rotates back to its original position. At 400 µs, W150 is not present anymore, and with it the last indication of a fraction of open states.

With the current data, however, we cannot conclude when exactly the proton is released to the bulk from the Cl1 channel. Early changes (50 µs after the 2nd flash) are observed around the water network at the PsbO-D2 interface (Fig. 5A), which may indicate a fast, long-range electrostatically triggered proton release of surface carboxylates as found in PSII membrane particles from plants[303, 332]. The short H-bonding interaction of E65 and R334 in the open state of the gate at 150 µs may indicate that a proton is already released from the gate in line with a suggested fast refilling of the earlier deprotonated site[332]. Alternatively, the gate may stay open until the proton is released in an apparent single proton hopping event occurring with Mn oxidation[329]. This is supported by the observation that at 150 µs the averaged distance between E65 and E312 is still ~2.7 Å, indicating that in some centers a proton is still shared between both residues and the proton release cannot be terminated, yet. In any case, the gate opening and closing can directly explain the involvement of multiple protonatable side chains as observed in pH dependent oxygen activity[333] and the reported pH dependency of the proton-coupled electron transfer (PCET) of Mn oxidation in the S_2 to S_3 transition[329, 334]: In the open state (Fig. 6), when the proton is still located at the gate, a low pH at the proximal bulk may prevent it from releasing its proton. This will slow down the deprotonation of D61 and also the deprotonation of the newly inserted substrate water (Ox).

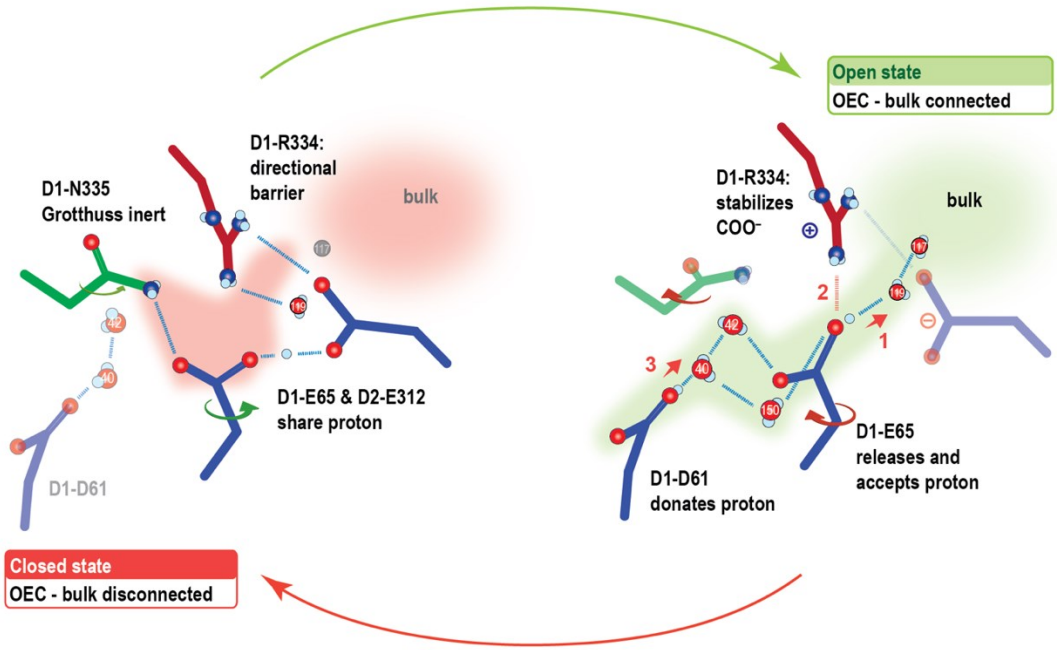

Figure 6 The proposed proton gate around D1-E65, D2-E312 and D1-R334 in the open and closed state. *In the closed state, the H-bonding network connecting the OEC to the bulk is disrupted by D1-N335 and D1-R334, while in the open state, the OEC is connected via D1-E65 and waters to the bulk. The opening of the gate by the rotation of D1-E65 could be caused by the protonation of D1-D61 and the subsequent rearrangement of the H-bonding network. We hypothesized that the proton released towards the bulk was shared between D1-E65 and D2-E312 before. The deprotonated D1-E65 can then be stabilized by approaching D1-R334. Rotation of D1-E65 back to the original position and closing of the gate may be caused by proton transfer from D1-D61 to D1-E65 and the subsequent repulsion and attraction of the newly arrived proton by D1-R334 and D2-E312, respectively.*

In Fig. 7, we summarize the structural sequence of events during the S_2 to S_3 transition, based on our current observation of the structural changes starting from the S_2 formation; we integrated the proposed proton release and water insertion process with the O1 channel as a water intake, and the Cl1 channel as a proton release pathway. Upon the S_2-state formation (Fig. 7A to 7B), Mn4 is oxidized, which is indicated by the shortening of the Mn4-O_{E333} distance, as reported previously[91]. This redox change may trigger the structural changes around the area; the W19-O4 distance is shortened, likely due to equal sharing of the proton between them, leading to the weakening of the hydrogen-bond between W19 and W20. The W20 density is not visible in the S_2-state, only reappearing in the S_0-state. As a consequence, the hydrogen-bond network from the OEC to the O4 channel is disconnected during the S_2 to S_3 and S_3 to S_0 transitions.

Upon the 2nd flash, Yz oxidation triggers the movement of the Y_Z-His190-E189 region, that shifts D1-E189 away from Ca and the elongation of Mn1-Mn4 is observed by 150 µs after the 2nd flash (Fig. 7C). In the same timescale, D1-S169 rotates to be in H-bond distance to W1 (Figs. 4 and 7C). One plausible explanation for this motion is that

W1 releases a proton via D1-D61 and becomes an OH^-, that interacts with S169. The low barrier proton release of W1 via D1-D61 was suggested from the DFT calculations for the S_2 to S_3 transition[335]. Also, the role of D1-E65 and D1-D61 in the proton release has been widely discussed[43, 111, 120, 123, 124, 314, 321, 328, 336-338]. The new conformation of D1-E65/E312 with W119 forms an 'open state' for proton release towards the bulk by 150 µs (Fig. 7C). By 250 µs (Fig. 7D), the changes in the E65/E312 and D1-S169-W1 region are reversed, after D1-E65 gets protonated from D1-D61 via W40 and W150/W42, and the proton gate is closed. As indicated by the increased distance of D1-S169 to W1, the OH^- (W1) ligand becomes protonated again. Proton motions most likely correlate with the PCET reaction that involves the Mn1 oxidation and the Ox insertion from the O1 channel. Since the water is easier to be deprotonated when bound to a metal like Mn or Ca, we propose water is first bound to Ca or Mn prior to being inserted at the open coordination site of Mn1, possibly via W3. The time constant of the Mn1 oxidation we observed by Mn $K\beta_{1,3}$ XES is around 350 µs[91]. Therefore, the reprotonation of W1 can proceed from the newly inserted Ox. By 400 µs, all the movement around the OEC is complete, and no major changes are observed in the channel regions between 2F(400 µs) and the S_3-state (2F(200 ms), Fig. 7D.

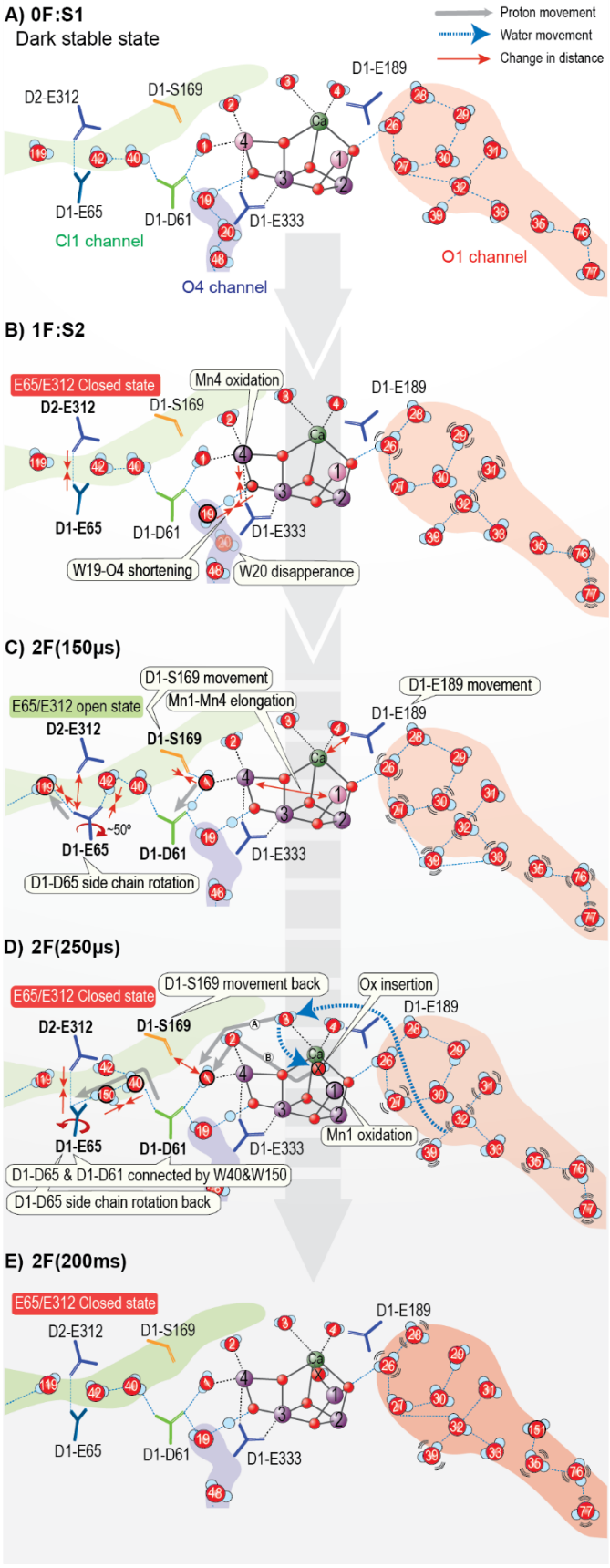

Figure 7 Schematic summarizing the structural changes in the O1, Cl1, and O4 channels leading to the first water insertion and proton release during the $S_2 \rightarrow S_3$ transition. *Mn1 and Mn4 oxidations from (III) to (IV) are shown as a color change from pink to purple. The gray arrow represents the possible proton pathway, while the blue dashed arrow represents the potential stepwise water insertion pathway.*

In summary, we investigated the water and proton channels that connect the OEC to the lumenal bulk water. Based on the RT structures, we propose that the O1 channel with mobile waters is suitable for water intake from the bulk to the OEC, while the more rigid network of the Cl1 channel branch A, formed with amino acids and waters extending through W1, D1-D61, to D1-E65, is suitable for proton relay during the S_2 to S_3 transition. Based on the observed structural changes, we hypothesize that D1-E65, D2-E312 and D1-R334 form a proton gate by minimizing the back reaction, thus regulating proton release from the OEC to the bulk. We also note that different proton release pathways may be used during different S-state transitions. The current study is a first step showing how the coordinated motion of amino acid residues and the water network is key to spatially control substrate and proton transport required for a multi-electron/proton process like the water oxidation reaction.

Code availability: The open source programs *dials.stills_process*, the *cctbx.xfel* GUI and *cxi.merge* are distributed with *DIALS* packages available at http://dials.github.io, with further documentation available at http://cci.lbl.gov/xfel.

Data availability: The atomic coordinates and structure factors have been deposited in the Protein Data Bank, www.pdb.org (PDB ID code 7RF1 for the combined data , 7RF2 for the 0F, 7RF3 for the 1F, 7RF4 for the 2F(50 μs), 7RF5 for the 2F(150 μs), 7RF6 for the 2F(250 μs), 7RF7 for the 2F(400 μs), and 7RF8 for the 2F(200ms) data).

Acknowledgments

This work was supported by the Director, Office of Science, Office of Basic Energy Sciences (OBES), Division of Chemical Sciences, Geosciences, and Biosciences (CSGB) of the Department of Energy (DOE) (J.Y., V.K.Y., J.K.) for X-ray spectroscopy and crystallography data collection and analysis, and methods development for photosynthetic systems, by the National Institutes of Health (NIH) Grants GM055302 (V.K.Y.) for PSII biochemistry, GM110501 (J.Y.) and GM126289 (J.K.) for instrumentation development for XFEL experiments, GM117126 (N.K.S.) for development of computational protocols for XFEL data. The NIH grants GM124149 and GM124169 (J.M.H.), and Germany`s Excellence Strategy (Project EXC 2008/1-390540038 (A.Z., H.D.) coordinated by T.U. Berlin and by the German Research Foundaton (DFG) via the Collaborative Research Center SFB1078 (Humboldt Universität zu Berlin), TP A5 (A.Z., H.D., M.I., R.H.), Carolina von Humboldt-

Stipendium (R.H) and Vetenskapsrådet 2016-05183 (J.M.), 2020-03809 (J.M.) and 2017-00356 (T.F.) are acknowledged for support. This research used resources of NERSC, a User Facility supported by the Office of Science, DOE, under Contract No. DE-AC02-05CH11231. XFEL data was collected at LCLS/SLAC, Stanford. Testing of crystals and various parts of the setup was carried out at synchrotron facilities that were provided by the ALS in Berkeley and SSRL in Stanford, funded by DOE OBES, and PL14 at BESSY, Berlin. The SSRL Structural Molecular Biology Program is supported by the DOE OBER, and by the NIH (P41GM103393). Use of the LCLS and SSRL, SLAC National Accelerator Laboratory, is supported by the U.S. DOE, Office of Science, OBES under Contract No. DE-AC02-76SF00515. We thank the support staff at LCLS/SLAC, SSRL (BL 6-2, 7-3) and ALS (BL 5.01, 5.0.2, 8.2.1, 8.3.1).

Methods

Sample Preparation: Crystals ranging in size from 20-60 μm were obtained from PSII dimers of *T. elongatus*[44, 190] and were used for XRD measurements in 0.1 M MES, pH 6.5, 0.1 M ammonium chloride and 35% (w/v) PEG 5000. PSII crystals are highly active in O_2 evolution show no Mn(II) contamination[339], and turnover parameters and S-state populations under our experimental conditions were determined by membrane inlet mass spectroscopy [340] as described previously[190].

Analysis of O1 channel in cyanobacteria and higher plants: The O1 channel was mapped by Caver 3.0 Pymol plugin[341] using the RT crystal structural of cyanobacterial PSII (PDB: 7RF2) and the Cryo-EM structure of plant PSII (PDB: 3JCU). The channels start near the Ca side and extend through the D1 subunit (Supplementary Figure 1). The termini of the channels in cyanobacteria were found to be between subunits CP43 and PsbV, crossponding to O1 channel A (Supplementary Figure 1A), or between subunits D2, CP47, PsbV and PsbU, corresponding to O1 channel B (Supplementary Figure 1C). The termini of the channels in plant were found to be either between subunits CP43 and PsbP (Supplementary Figure 1B) or between subunits D2, CP47, PsbP and PsbQ (Supplementary Figure 1D). Our results showed that the cyanobacterial O1 channel A and O1 channel B are structurally conserved in plants as they correspond well with the channel detected in PSII of plants that proceeds along subunits CP43 and PsbP and subunits D2, CP47, PsbP and PsbQ, respectively.

X-ray data collection: The crystallography data were collected at the MFX instrument of LCLS at the SLAC National Accelerator Laboratory, Stanford[342, 343]. XRD and XES

of PSII crystals was measured using X-ray pulses of ~40 fs length, at 9.5 keV, with pulse energies of 2-4 mJ, and with an X-ray spot size at the sample of ~3 μm in diameter. XRD data were collected using a Rayonix 340 detector, operating in the 3-by-3 binning mode, at a frame rate of 20 Hz. Sample was delivered to the X-ray interaction region using the previously described Drop-on-Tape setup[191]. Illumination conditions for populating different S-states are described in the following references from[51,190].

X-ray diffraction data processing: From the data collected at LCLS for different illumination states, as described previously[190], a total of 262,254 integrated lattices were obtained using *dials.stills_process*, with a target unit cell of a=117.0 Å, b=221.0 Å, c=309.0 Å, $\alpha=\beta=\gamma=90°$, and the space group $P2_12_12_1$. Signal was integrated to the edges of the detector and subsequently a per-image resolution cutoff was used during the merging step. Integrated intensities were corrected for absorption by the kapton conveyor belt to match the position of the belt and crystals relative to the X-ray beam[191]. Ensemble refinement of the crystal and detector parameters was then performed on the data using *cctbx.xfel.stripe_experiment* and improved the unit cell distribution and final isomorphous difference maps. After ensemble refinement and filtering out 32,428 lattices that belonged to a different crystal isoform, a total of 229,810 integrated lattices was obtained with an average unit cell of a=117.0 Å, b=221.7 Å, c=307.6 Å, $\alpha=\beta=\gamma=90°$ and the space group $P2_12_12_1$.

Image sets were also culled to include only images extending past 3 Å, as we have done previously for PSII datasets to improve statistics by removing contamination due to low-quality images[51]. The remaining integrated images were merged using *cxi.merge* as described previously [51, 190]. A combined dataset at 1.89 Å, containing images from all illumination states was first obtained using a previously obtained reference model with no restrictions on the unit cell parameters. The combined dataset was obtained by merging reflections from all the images in the experiment, which had reflections extending beyond 3 Å. This included all the stable intermediate states of the Kok cycle (S_1, S_2, S_3, and S_0) as well as the timepoints between those intermediates. In total, 111,922 images were merged to yield a combined dataset cut at 1.89 Å by using the criterion of monotonic falloff of the $CC_{1/2}$ and the resolution where the average multiplicity falls below 10. The R_{merge} for the dataset is 11.7% (91.4% in the highest resolution shell, 1.922-1.890 Å). This combined mtz file was used to generate a refined pdb model of the combined dataset as described below, and this pdb model was used as the reference model for merging the separate illumination states. The unit cell outlier rejection option in *cxi.merge* was used

to remove images with a unit cell that differed by more than 1% from the reference model, so a pre-filtering step was not necessary.

Final merged datasets were acquired for the combined dataset, 0F, 1F, 2F(50 µs), 2F(150 µs), 2F(250 µs), 2F(400 µs), and 2F states to resolutions between 2.27 and 1.89 Å, containing between 4464 and 111,922 images (Supplementary Table 1). Please note that the merged data sets for the individual illumination conditions are the same as those used in ref. 2.

Model building and map calculation: About 112,000 diffraction images, collected at room temperature from PSII crystals in various illumination states and falling within a 1% unit cell tolerance cutoff, were merged, which resulted in a high-resolution data set. Initial structure refinement against this combined dataset at 1.89 Å was carried out starting from a previously acquired high-resolution PSII structure in the same unit cell (PDB ID: 5TIS)[48] using *phenix.refine*[344, 345]. The R_{free} set was 0.89% of the total reflections and was created by extending the resolution of the R_{free} set used for the refinement of the individual datasets. As a result, the R_{free} reflections for the combined dataset contain all the R_{free} reflections used for the individual datasets. B-factors were reset to a value of 30 and waters were removed. After an initial rigid body refinement step, *xyz* coordinates and isotropic B-factors were refined for tens of cycles with automatic water placement enabled. Custom bonding restraints were used for the OEC (with large σ values, to reduce the effect of the strain at the OEC on the coordinate refinement), chlorophyll-*a* (CLA, to allow correct placement of the Mg relative to the plane of the porphyrin ring), and unknown lipid-like ligands (STE). Custom coordination restraints overrode van der Waals repulsion for coordinated chlorophyll Mg atoms, the non-heme iron, and the OEC. Following real space refinement in *Coot*[346] of selected individual sidechains and the PsbO loop region and placement of additional water molecules, the model was refined for several additional cycles with occupancy refinement enabled, then as before without automatic water placement, and then as before with hydrogen atoms. NHQ flips and automatic linking were disabled throughout. A final 'combined' dataset model was obtained with R_{work}/R_{free} of 17.2%/21.7%.

In the final steps of refinement, Phenix-Auto-water-placement was used to model the waters. The water positions were manually inspected in COOT. The waters positioned within the discussed channels were moved to a different chain and renamed OOO. A

bonding restraint CIF dictionary for OOO, identical to that for HOH, was supplied to Phenix.

With reset B-factors to 30 and removed waters, the above model was subsequently refined against the illuminated datasets with the lattermost refinement settings and different OEC bonding restraints. Using the 1.89 Å-model improved some important electron-density features. These features were visible initially at a lower sigma level (<3), but after improving the model they mostly were present at higher sigma level (>4); i.e., W150, W151. OEC bonding restraints for the 0F dataset prevented large deviations from the high-resolution dark state OEC structure reported by Suga *et al.* (PDB ID: 4UB6[47]). Bonding restraints for the other datasets loosely restrained the models to metal-metal distances matching spectroscopic data and metal-oxygen distances matching the most likely proposed models[347-351]. A number of ordered water positions were excluded from subsequent automatic water placement rounds by renaming the residue names to OOO and the waters coordinating the OEC were incorporated into the OEC restraint CIF file directly. Density for an additional oxygen present in the S_3 state, O_X as reported previously[51, 190], was visible in the 2F(150µs) and later time point data and the Ox atom was included in the model and in the OEC CIF restraints in the final refinement for these four states. After 12-15 of cycles of refinement in this manner, individual illuminated states at various resolutions were obtained ranging in R_{work}/R_{free} from 17.95%/22.70% to 18.48%/23.92% (Supplementary Table 1).

As described before[190] to best approximate the contributions of dimers that did not advance to the next S-state due to illumination misses, for the 2F(150µs), 2F(250µs), 2F(400µs), and 2F datasets, the models were split into A and B alternate conformers in regions of chains A/a, C/c and D/d surrounding (and including) the OEC. The main conformer was set at 0.3 (2F (150us)), 0.5 (2F (250us)), 0.7 (2F (400us)), and 0.75 (2F) occupancy and the minor conformer was set to give a total occupancy of 1. The major conformer was allowed to refine as usual, while the minor conformer was fixed during refinement and set to match the S_2 state obtained from the refined 1F structure.

Estimated positional precision: To estimate the positional precision of the OEC atoms, we used *END/RAPID* to perturb the structure factors, in an approach similar to one we previously employed[190, 352]. Depending on resolution and the fraction of S_3 present, metal-metal distances at the OEC had standard deviations between 0.07 and 0.27 Å across these

trials, while distances between OEC metals and coordinating ligands were found to have standard deviations between 0.09 and 0.25 Å (for details see[190]).

Modeling of Waters: To ensure the reliability of the modeling of waters in the channels, individual polder omit maps were generated, using *phenix.polder*, and the peak height was calculated, using *ccp4.peakmax*[353, 354]. Peaks above 5 σ were considered to indicate a water molecule in the final models. While peaks between 3 and 5 σ, were only considered if they are present in one of the S states, at least, in the same vicinity, with a peak higher than 5 σ. Waters with peaks below 3 σ were rejected, i.e. W39 in some data sets (Supplementary Table 5).

B-factors of the waters: To investigate the B-factors of waters in the 1.89 Å-model, the occupancies were set to 1, then the waters were refined, including B-factor refinement against the data and results for both monomers were evaluated. To investigate the influence of occupancy on the refinement, a parallel refinement in which both occupancy and B-factors were allowed to refine was performed. Both strategies showed similar trends (Data not shown).

Similar strategies were used to track the changes in the water B-factors for the different time-points models. Since we are comparing the B factors from different models at different resolutions, it was necessary to standardize them. First, the water B-factors were extracted from each model. Then, the normalized B-factors (norm B) of each model were calculated by applying a Z-score as described by Carugo et al.[319],

$$norm\ B = \frac{B\ -\ B_{avg}}{B_{std}}$$

$$\text{with } B_{avg} = \frac{\sum B}{n} \text{ and } B_{std} = \sqrt{\frac{\sum (B - B_{avg})^2}{n-1}}$$

FoFc difference omit density: To estimate the peak-height of water omit densities**,** changes in the electron density at the water (W_i) position were obtained from the omit maps of W_i using the *FFT* program from the *CCP4* package[353, 354].

Water numbering convention: We utilized a water numbering scheme for all waters in the vicinity of the OEC that is consistent with the numbering used in refs 2 and 9. Waters are numbered with increasing numbers indicative of their distance to the OEC along the channels starting with W19. As the PDB does not allow to retain identifiers for waters

the numbering in each deposited coordinate file is different. Hence, we are providing a table (Supplementary Table 4) that correlates the numbering used in this work with the numbering in each of the deposited coordinate files.

Supplementary Information

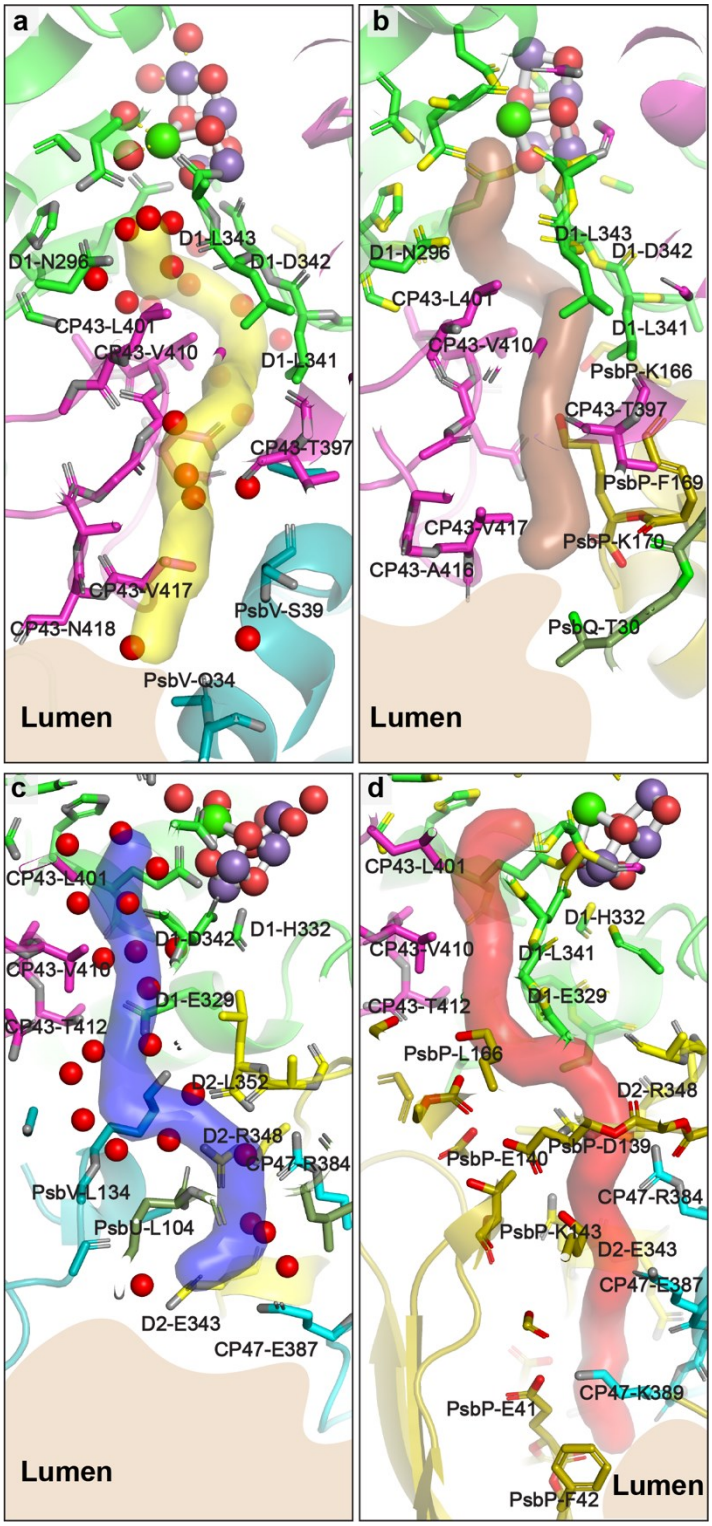

Supplementary Figure 1 Analysis of the O1 channel in cyanobacteria and plants. ***(a**, **c)** represent branches A and B of the O1 channel in the cyanobacterial structure (PDB: 7RF2). **(b**, **d)** show the branches A and B of the O1 channel in the plant PSII structure (PDB: 3JCU). While details at the lumenal termini are different between plants and cyanobacteria due to the different architecture of the lumenal extrinsic part of the complex the region close to the OEC and the general direction and shape are highly conserved for both branches.*

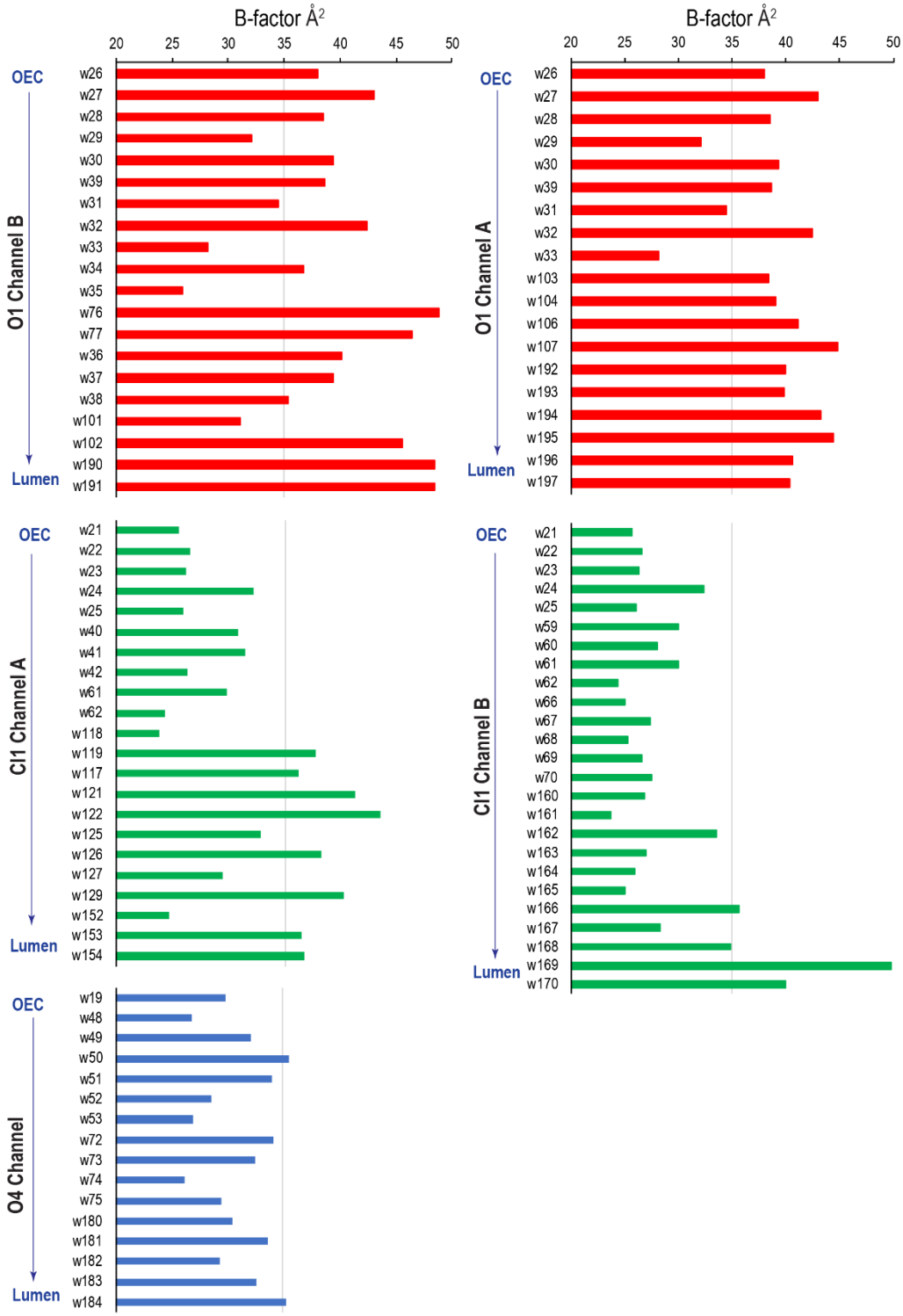

Supplementary Figure 2 The B-factor values of the waters *in the O1 channel A, O1 Channel B, Cl1 channel A, Channel B and O4 channel in the combined data (7RF1). Numbering is according to Supplementary Table 4. Source data are provided as a Source Data file.*

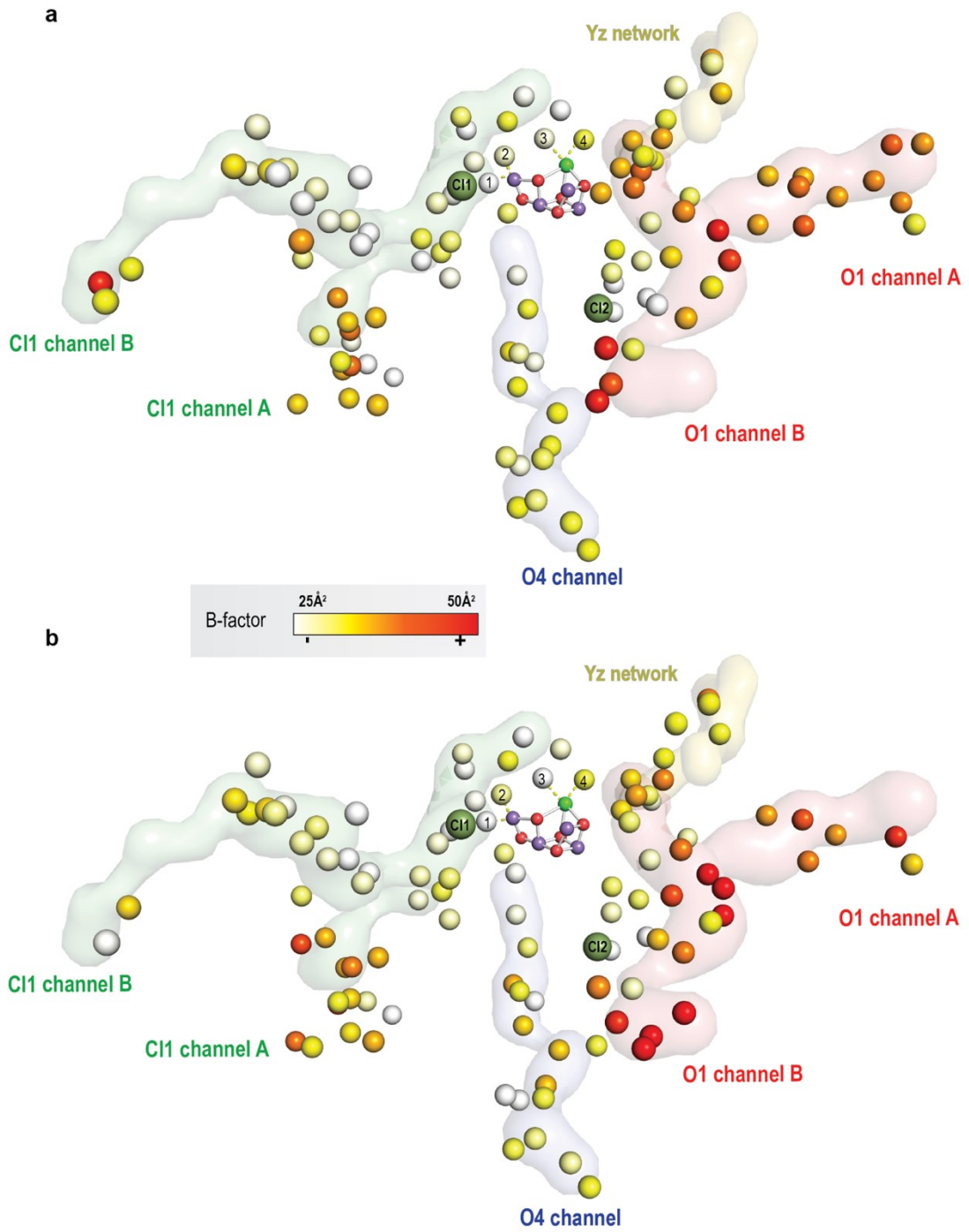

Supplementary Figure 3 Water channels in the 1.89 Å resolution room temperature structure (7RF1) in both monomers m1 (a) and m2 (b). *The water molecules are represented in a color gradient scale, indicating the B factor of each water (white color for B-factor 25 to red color for B-factor 50 Å^2 for both monomers). The channels and the network are indicated by different colors, O1 Channel in red, O4 Channel in blue, Cl1 Channel in green, and Yz network in yellow.*

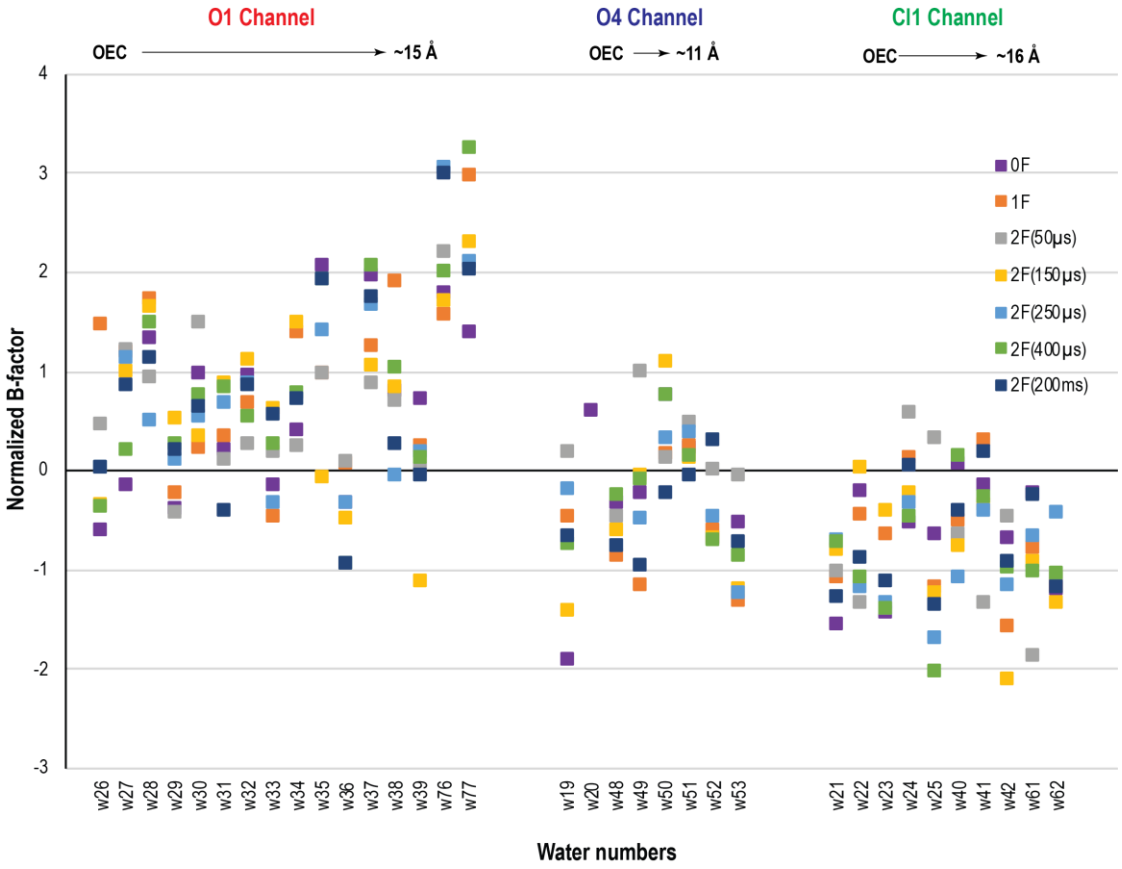

Supplementary Figure 4 Comparison of the normalized B-factors of waters present in the water channels at 0F, 1F, 2F, and the time points between 1F and 2F. *The normalized B factors of the waters are shown as a function of their distance from the Mn cluster within the three discussed channels: O1, O4, and Cl1. Source data are provided as a Source Data file.*

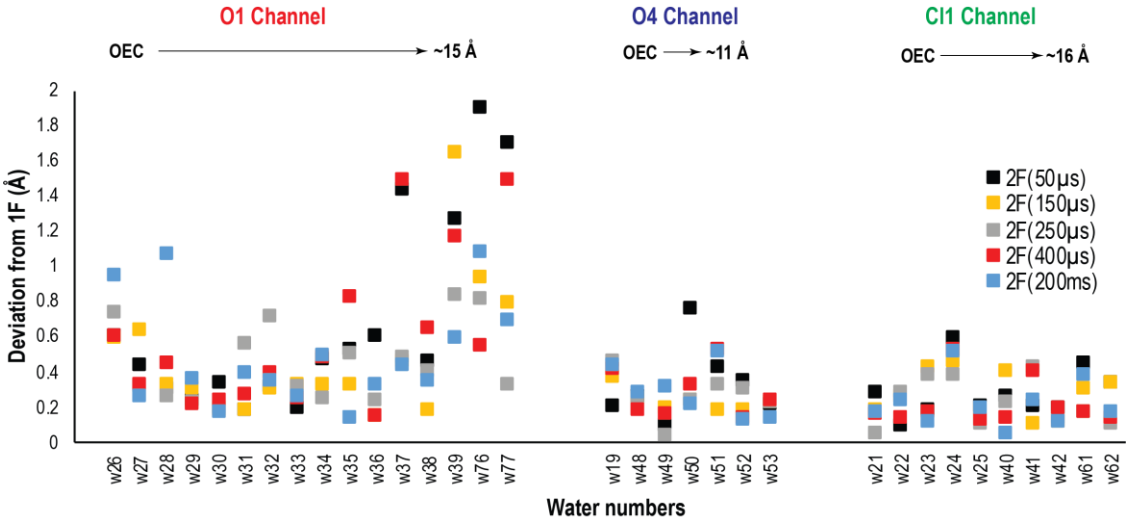

Supplementary Figure 5 The deviation of water positions from the S_2-state (1F) within water channels. *The deviation of the water positions for different time points in the S_2-S_3 transition is shown as a function of their distance from the Mn cluster within the three discussed channels: O1, O4, and Cl1. Source data are provided as a Source Data file.*

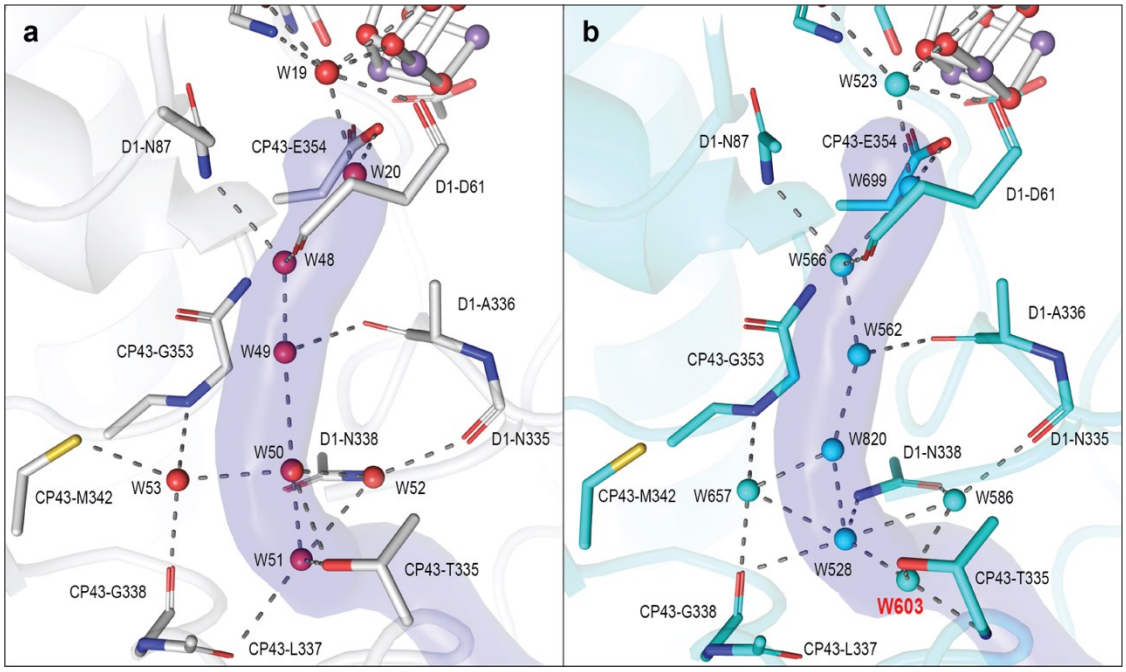

Supplementary Figure 6 Structure of the O4 channel for the dark state at different temperature. *Interaction distance between atoms up to 3.2 Å is shown as gray dashed line. The light blue surface represents the O4 channel. A) structure collected at room temperature (PDB ID:7RF2) ref. B) structure collected at cryo temperature with XFEL at 2.15 Å (PDB ID: 6JLJ) [52]. Extra water (W603) (labeled with red color) is detected only in the dark state in the cryo structure effecting the H-bonding networked of the O4 channel.*

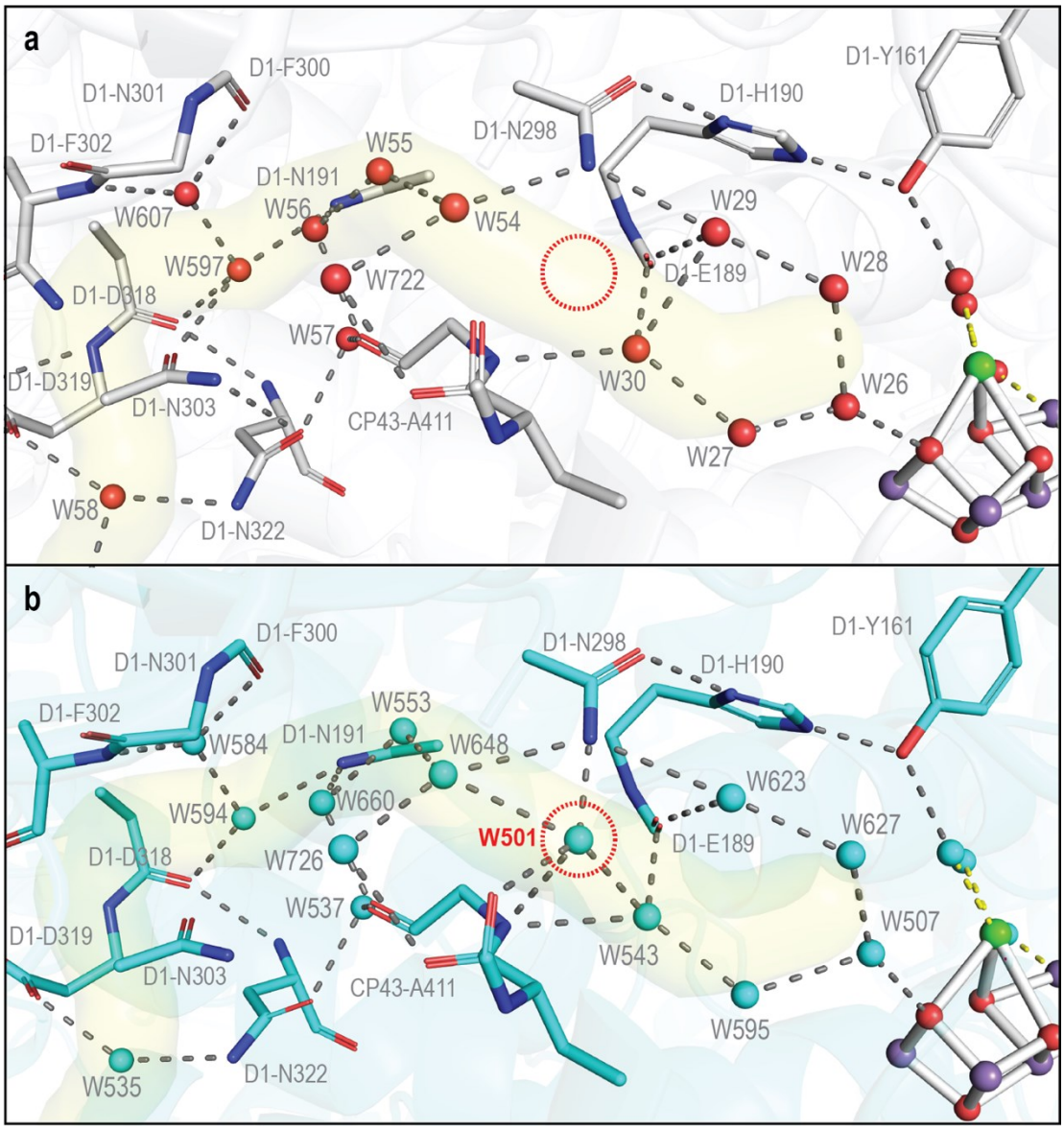

Supplementary Figure 7 Yz network for dark state at different temperatures. *Hydrogen-bond distances connecting the Mn_4CaO_5 cluster and Yz toward the luminal bulk side are shown as gray dashed lines and up to 3.2 Å. A) PSII structure with XFEL at RT (PDB ID 7RF2). B) PSII cryo structure with XFEL at 2.15 Å (PDB ID 6JLJ). Extra water (W501) (highlighted with red dashed circle) detected only at the cryo-structure and not in the RT-structure effecting the possible proton path out to the lumen for each structure. In the RT-structure only D1-N298 connects the penta-cluster waters (26-27-28-29-30) via W29 to W54 that proceed towards the lumen. However, in the cryo-structure, in addition to D1-N298, W501 is also connecting the penta cluster waters to the opposite side of the network that expands towards the lumen.*

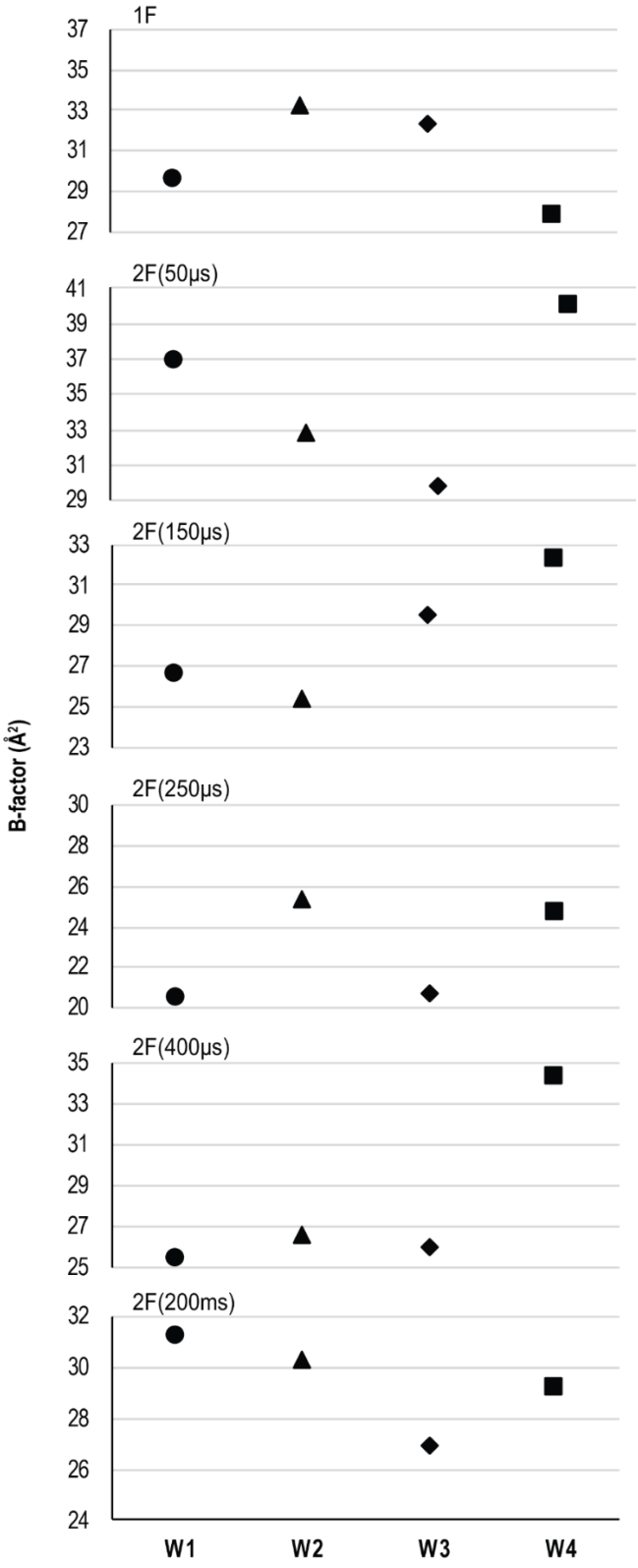

Supplementary Figure 8 B-factors of OEC ligand waters at each time point in the $S_2 \rightarrow S_3$ transition. *W4 shows higher B-factor after the second illumination than the other ligand waters (W1, W2 and W3), in the 2F(50μs) structure (PDB ID: 7RF4), the 2F(150 μs) structure (PDB ID: 7RF5), the 2F(250 μs) structure (PDB ID: 7RF6), and the 2F(400 μs) structure (PDB ID: 7RF7). Source data are provided as a Source Data file.*

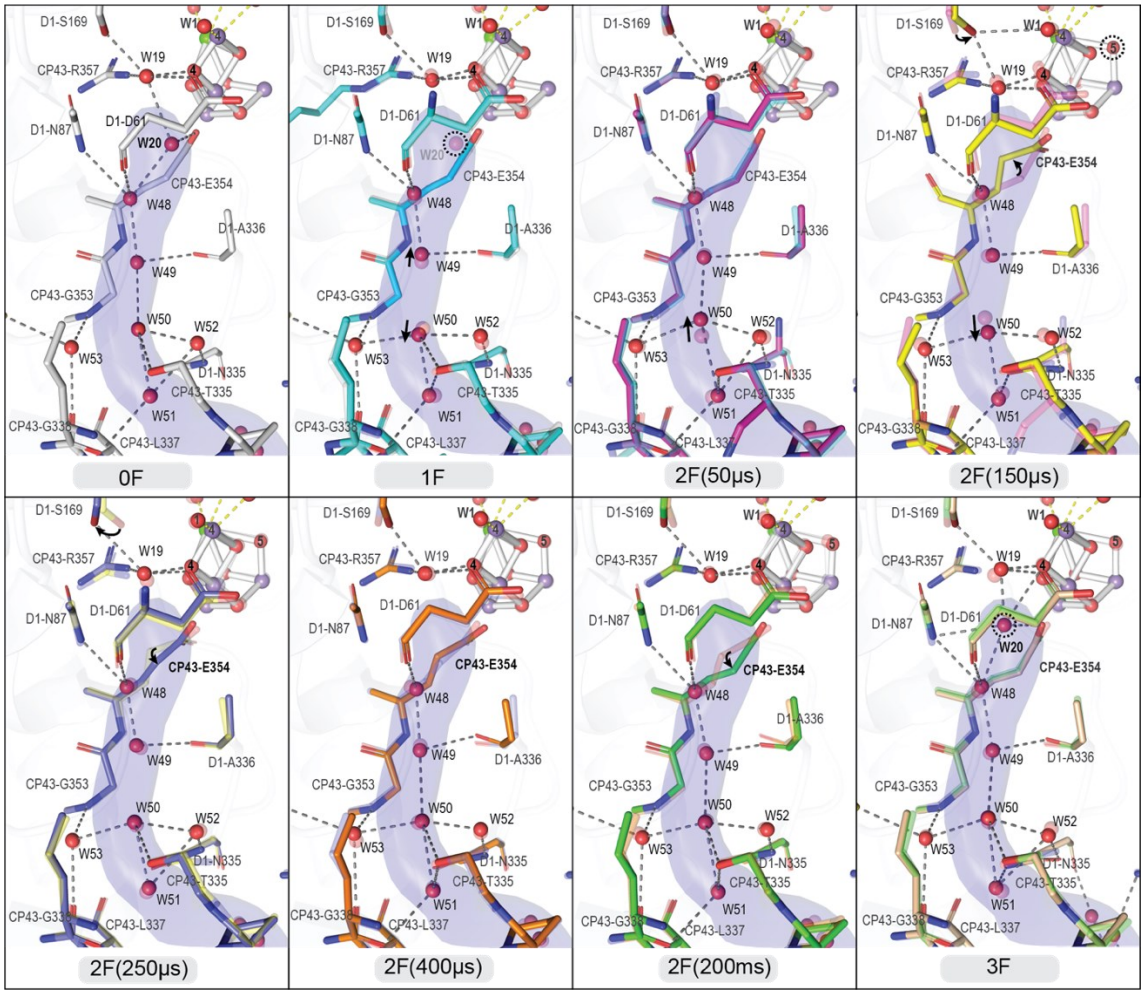

Supplementary Figure 9 Structural changes in the O4 water channel for the different illumination states by XFEL at room temperature. *Interaction distances between atoms are shown in gray dashed line and up to 3.2 Å. Positional shifts of the water molecules (W49 and W50) and a.a residues (CP43-E354 and D1-S169) are indicated by black arrows. Structure at 0F is (S_1 state) at 2.08 Å (PDB ID: 7RF2), after 1F (S_2 state) at 2.26 Å (PDB ID: 7RF3), after 2F(50µs) (50µs after S_2 state) at 2.27 Å (PDB ID: 7RF4), after 2F(150 µs) is (150µs after S_2 state) at 2.23 Å (PDB ID: 7RF5), after 2F(250 µs) (250µs after S_2 state) at 2.01 Å (PDB ID: 7RF6), after 2F(400 µs) (400 µs after S_2 state) at 2.09 Å (PDB ID: 7RF7), after 2F (200 µs) (S_3 state) at 2.09 Å (PDB ID: 7RF8), after 3F (S_0 state) at 2.04 Å (PDB ID: 6DHP)*[51].

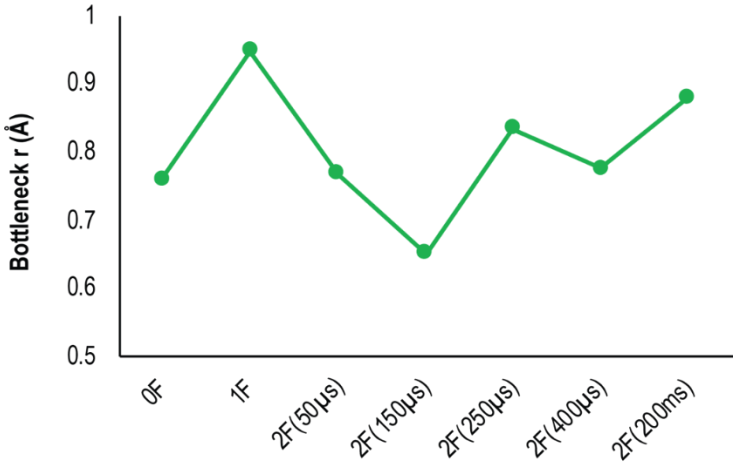

Supplementary Figure 10 Changes in Cl1 channel A bottleneck radius at different time points. *Analysis of the bottleneck radius build by D1-E65, D1-P66, D1-V67 and D2-E312 are performed using caver 3.0 Pymol plugin[341] for 0F model (PDB ID: 7RF2), 1F model (PDB ID: 7RF3), 2F(50µs) model (PDB ID: 7RF4), 2F(150 µs) model (PDB ID: 7RF5), 2F(250 µs) model (PDB ID: 7RF6), 2F(400 µs) model (PDB ID: 7RF7), 2F (200 µs) model (PDB ID: 7RF7). Source data are provided as a Source Data file.*

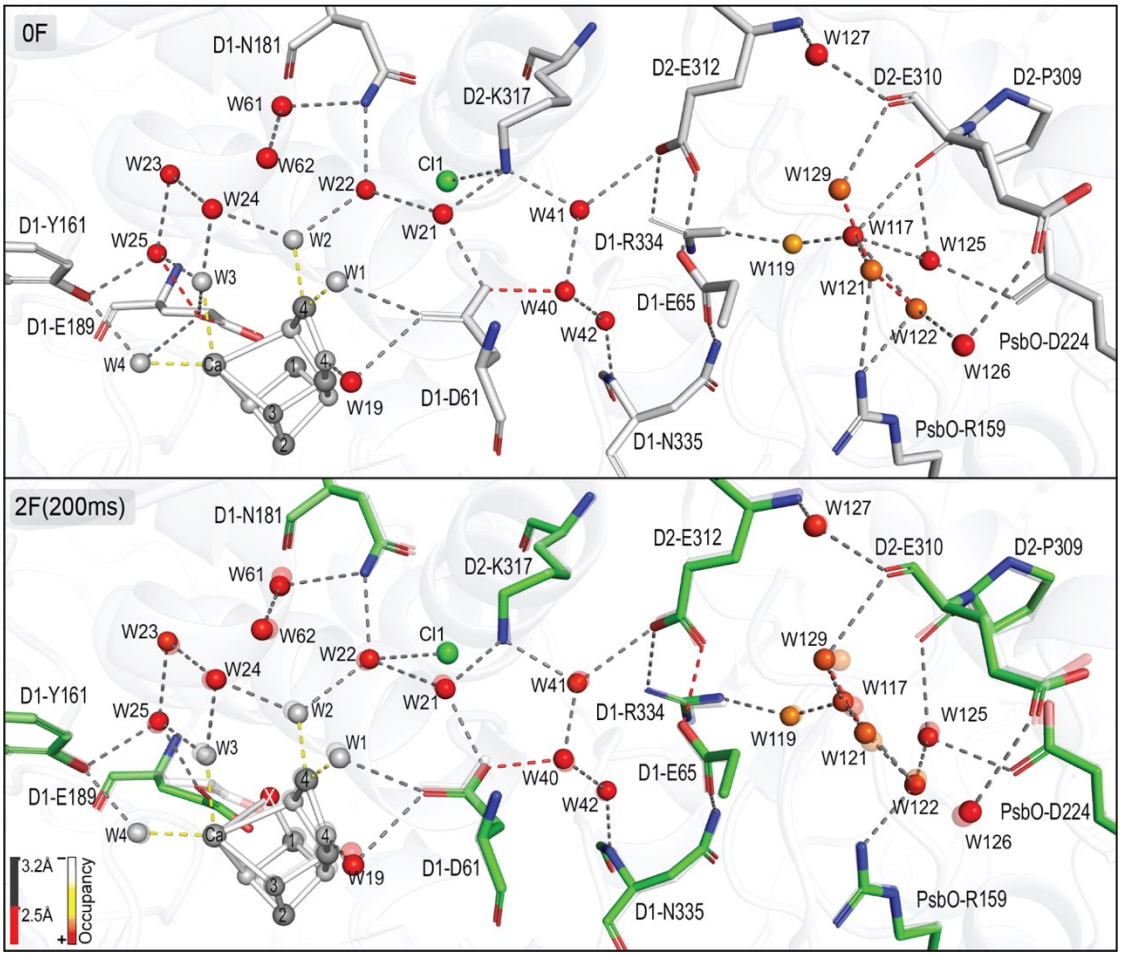

Supplementary Figure 11 Structural changes in the Cl1 water channel detected in the dark state structure (0F, PDB ID: 7RF2) and S3-rich structure (2F (200ms), PDB ID: 7RF8). *0F model is colored with white. 2F (200ms) model is colored with green and overlaid with the 0F model, shown in a transparent color. The waters are colored based on their occupancies, represented by a color gradient from white to red. The H-bond length is color-coded, as described at the bottom left.*

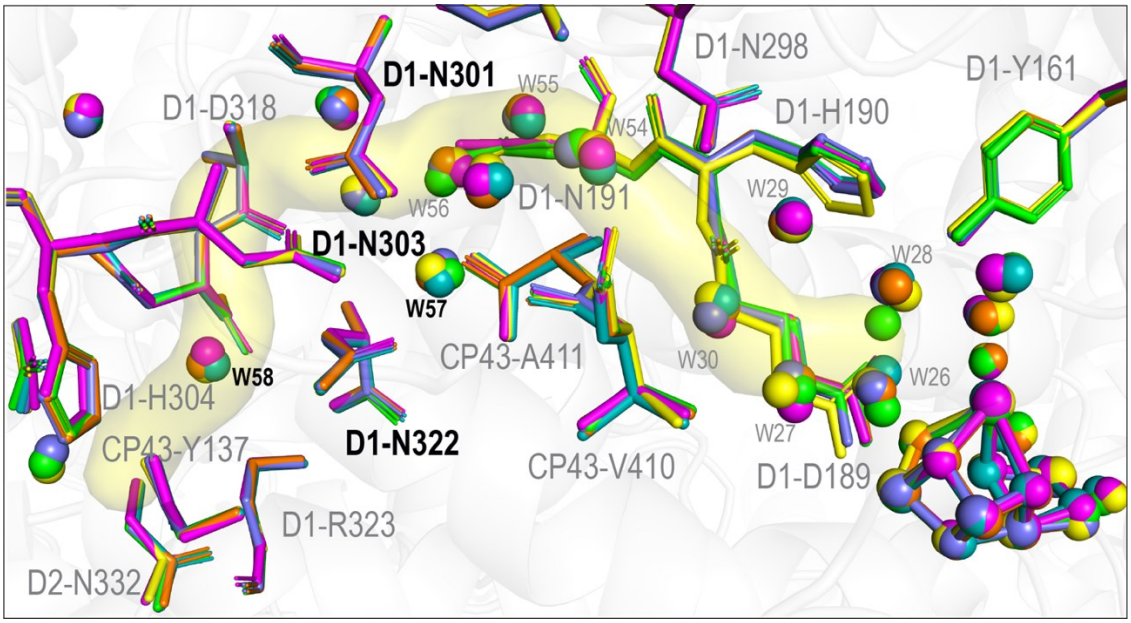

Supplementary Figure 12 Structural changes in the Yz network channel during the $S_2 \rightarrow S_3$ transition.
The structure of the Yz network is shown for all time points in the $S_2 \rightarrow S_3$ transition (1F (teal) and 2F time points (50 µs: magenta; 150 µs: yellow; 250 µs: slate; 400 µs: orange; 200 ms: green)).

Supplementary Table 1: Channel nomenclature in literature. There are multiple names used for identifying the water and proton channels in PSII. The table summarizes their correspondence.

	Ho and Styring [115]	Murray and Barber [116]	Gabdulkhakov et al. [117]	Umena et al. [73]	Vassiliev et al. [118]	Ogata et al. [119]	Sakashita et al. [120]	Weisz et al. [121]
Method	Surface contact calculation		Xe	H-bond network analysis	MD simulation			ROS
PDB ID	2AXT		3BZ1	3ARC (2WU2)	3ARC (2WU2)	3ARC (2WU2)	3ARC (2WU2)	
Resolution	3.00 Å		2.90 Å	1.90 Å	1.90 Å	1.90 Å	1.90 Å	
O1 Channel A	large	*channel ii*	B1		4.A		O1-water chain	Arm 2
O1 Channel B	large	*channel ii*	B2		4B			Arm 2
O4 Channel	narrow	NA	E, F	4.c	2	Path 3	O4-water chain	
			D		Channel X			Arm 3
Cl1 Channel A	broad	-	G	4.b	1		E65/E312 channel	
Cl1 Channel B		*channel iii*	C, D		3	Path 2		Arm 1
Cl2 network				4.c				
	back	*channel i*	A1, A2	3.b	5	Path 1		Arm 3

Supplementary Table 2: Merging and refinement statistics

State	Combined	$0F^+$	$1F^+$	2F (50 µs)$^+$	2F (150 µs)$^+$	2F (250 µs)$^+$	2F (400 µs)$^+$	$2F^+$
PDB ID	7RF1	7RF2	7RF3	7RF4	7RF5	7RF6	7RF7	7RF8
Resolution range refined (Å)	33.670-1.890	33.638 - 2.080	33.545 - 2.260	33.453 - 2.270	33.698 - 2.230	33.588 - 2.010	33.651 - 2.090	33.649 - 2.090
Resolution range upper bin (Å)	1.923-1.890	2.116 - 2.080	2.299 - 2.260	2.309 - 2.270	2.268 - 2.230	2.0345 - 2.010	2.126 - 2.090	2.216 - 2.090
Wavelength (Å)	1.302	1.302	1.302	1.302	1.302	1.303	1.302	1.302
Space group	$P2_12_12_1$	$P2_12_12_1$	$P2_12_12_1$	$P2_12_12_1$	$P2_12_12_1$	$P2_12_12_1$	$P2_12_12_1$	$P2_12_12_1$
Unit cell parameters (Å)	a=117.0 b=221.6 c=307.7	a=116.9 b=221.6 c=307.8	a=117.0 b=221.6 c=307.9	a=117.1 b=222.1 c=308.4	a=117.0 b=221.8 c=308.2	a=117.0 b=221.9 c=308.3	a=117.0 b=221.7 c=308.2	a=117.0 b=221.6 c=307.8
Lattices merged	111922	11734$^+$	4464$^+$	5357$^+$	6195$^+$	8659$^+$	5546$^+$	10043$^+$
Unique reflections	632624	474828	370481	367301	386505	535670	468621	468019
(upper bin)	(31359)	(23014)	(17988)	(17756)	(18749)	(25929)	(22792)	(22666)
Completeness	99.97%	99.77 %	99.60 %	99.61%	99.64%	99.78%	99.72%	99.75 %
(upper bin)	(99.9%)	(97.48 %)	(97.47 %)	(97.06%)	(97.52%)	(97.34%)	(97.60%)	(97.42 %)
$CC_{1/2}$	99.6%	98.0%	96.2%	96.7%	96.5%	97.7%	97.2%	97.9%
(upper bin)	(2.9%)	(5.4%)	(9.1%)	(4.7%)	(5.6%)	(5.1%)	(7.7%)	(4.4%)
$I/\sigma_{Ha14}(I)^\dagger$	31.2	13.2	11.8	11.8	8.0	14.3	12.3	12.8
(upper bin)	(0.4)	(0.6)	(0.9)	(0.6)	(0.5)	(0.6)	(0.7)	(0.6)
Wilson B-factor	30.3	34.4	37.8	41.3	39.1	32.7	34.4	37.6
R-factor	17.09	18.52	17.82	18.18	17.58	18.02	18.56	18.10
R-free	21.41	23.85	23.79	24.43	23.30	22.70	23.92	23.88
Number of atoms	104289	103675	103283	103257	105567	106133	106087	105942
Number non-hydrogen atoms	52524	52138	51715	51603	52802	53366	53322	53252
Ligands	212	187	192	196	198	195	197	192
Waters	1952	1994	1573	1415	1409	1973	1929	1900
Protein residues	5302	5302	5302	5302	5302	5302	5302	5302
RMS (bonds)	0.01	0.01	0.01	0.01	0.01	0.01	0.01	0.01
RMS (angles)	1.52	1.51	1.45	1.50	1.45	1.43	1.43	1.46
Ramachandran favored	97.3%	97.3%	97.2%	96.5%	96.8%	97.4%	97.4%	97.1%
Ramachandran outliers	0.3%	0.2%	0.2%	0.3%	0.3%	0.1%	0.1%	0.2%
Clashscore	5.7	4.4	5.1	5.7	5.2	4.1	5.3	4.8
Average B-factor	39.0	40.6	43.7	47.2	46.0	39.3	40.1	45.5

[+] Note that the merged datasets for the individual time points are the same as used in ref. 2 but refined models are different.
† as defined in ref. [98]

Supplementary Table 3. Water numbering convention used in this work and relation to residue numbers in pdb files (note that numbers are only given for the first monomer in each model, "x" indicates water not present, for W1-W4 only the refined component is given for 2F (150 µs) and later time points).

Numbering in manuscript	Channel	Combined (7RF1)	0F (7RF2)	1F (7RF3)	2F (50 µs) (7RF4)	2F (150 µs) (7RF5)	2F (250 µs) (7RF6)	2F (400 µs) (7RF7)	2F (7RF8)
W1		A/515	A/528	A/516	A/526	A/719	A/712	A/518	A/505
W2		A/555	A/579	A/543	A/557	A/728	A/718	A/533	A/537
W3		A/603	A/612	A/582	A/584	A/789	A/803	A/593	A/602
W4		A/525	A/532	A/522	A/513	A/739	A/728	A/564	A/549
W19	O4	A/519	A/526	A/510	A/517	A/715	A/727	A/515	A/529
W20	O4	x	C/675	x	x	x	x	x	x
W21	Cl1A/B	A/512	A/547	A/536	A/569	A/756	A/726	A/514	A/531
W22	Cl1A/B	A/550	A/571	A/557	A/536	A/752	A/729	A/554	A/555
W23	Cl1A/B	A/575	A/588	A/548	A/559	A/791	A/784	A/574	A/603
W24	Cl1A/B	A/622	A/602	A/613	A/581	A/794	A/817	A/616	A/593
W25	Cl1A/B	A/541	A/507	A/540	A/537	A/734	A/713	A/546	A/538
W26	O1A/B	A/612	A/575	A/604	A/566	A/761	A/732	A/552	A/546
W27	O1A/B	A/505	A/508	A/515	A/502	A/710	A/747	A/535	A/508
W28	O1A/B, YZ	A/619	A/601	A/589	A/604	A/775	A/828	A/615	A/625
W29	O1A/B, YZ	A/576	A/613	A/551	A/575	A/764	A/761	A/582	A/600
W30	O1A/B, YZ	A/506	A/527	A/513	A/533	A/714	A/768	A/513	A/509
W31	O1A/B	A/553	A/550	A/528	A/549	A/731	A/704	A/510	A/518
W32	O1A/B	A/637	A/631	A/616	A/614	A/808	A/838	A/638	A/626
W33	O1A/B	A/608	A/595	A/590	A/608	A/777	A/777	A/617	A/611
W34	O1B	A/524	A/524	V/314	A/525	A/732	A/733	A/521	A/517
W35	O1B	C/669	C/618	C/641	C/612	C/664	C/614	C/609	C/608
W36	O1B	D/575	A/577	D/542	A/551	D/512	A/775	D/555	D/564
W37	O1B	U/221	U/211	U/202	U/224	U/209	U/220	U/219	U/204
W38	O1B	V/356	V/351	V/337	V/343	V/341	V/351	V/344	V/359
W39	O1A/B	A/620	A/617	A/599	A/602	A/803	A/748	A/608	A/621
W40	Cl1A	A/534	A/521	A/519	A/528	A/707	A/714	A/529	A/510
W41	Cl1A	D/567	D/527	D/535	D/532	D/519	D/543	D/521	D/550
W42	Cl1A	A/630	A/599	A/612	A/609	A/798	A/833	A/620	A/614
W43	Cl2	A/616	A/585	A/544	A/577	A/788	A/780	A/588	A/587
W44	Cl2	C/764	A/620	A/608	A/599	A/802	A/830	C/725	A/617
W45	Cl2	C/646	C/653	C/664	C/636	C/676	C/682	C/645	C/626
W46	Cl2	C/710	C/660	C/690	C/676	C/679	C/709	C/690	C/695
W47	Cl2	C/692	C/636	C/673	C/629	C/668	C/701	C/669	C/669
W48	O4	A/535	A/581	A/549	A/563	A/782	A/791	A/559	A/558
W49	O4	A/557	A/589	A/574	A/539	A/724	A/781	A/599	A/569
W50	O4	C/723	C/728	C/686	C/694	C/700	C/731	C/702	C/682
W51	O4	C/753	C/750	C/705	C/681	A/797	C/730	C/708	C/710
W52	O4	A/548	A/574	A/545	A/542	A/740	A/703	A/539	A/522
W53	O4	C/696	C/687	C/679	C/678	C/649	C/677	C/665	C/688
W54	YZ	A/623	A/584	C/650	C/635	A/758	C/743	A/609	A/605
W55	YZ	A/521	A/530	A/517	A/512	A/723	A/710	A/508	A/535
W56	YZ	C/631	C/674	C/637	C/608	C/627	C/626	C/649	C/603
W57	YZ	A/504	A/515	A/503	A/504	A/709	A/738	A/502	A/519
W58	YZ	A/590	A/572	A/588	A/532	A/768	A/763	A/571	A/583
W59	Cl1B	A/592	A/605	A/594	A/598	A/793	A/806	A/600	A/571
W60	Cl1B	D/554	D/590	D/556	D/565	D/562	D/553	D/539	D/583
W61	Cl1A/B	A/617	A/614	A/601	A/558	A/795	A/814	A/590	A/601
W62	Cl1A/B	A/510	A/555	A/563	A/544	A/711	A/724	A/534	A/514
W66	Cl1B	D/548	D/541	D/550	D/553	O/335	D/536	D/543	D/532
W67	Cl1B	D/558	O/344	D/562	O/318	O/333	D/540	O/324	O/322
W68	Cl1B	D/608	D/592	D/581	D/586	D/573	D/579	D/558	D/582
W69	Cl1B	D/579	O/330	D/522	D/535	O/309	D/574	D/529	D/519
W70	Cl1B	D/635	D/630	D/600	D/599	D/596	D/614	D/624	D/622
W71	O4	A/511	A/531	A/530	A/543	A/745	U/218	A/579	A/567
W72	O4	D/611	D/609	D/585	D/591	D/591	D/596	D/600	D/608
W73	O4	U/237	U/241	U/225	U/227	U/219	U/230	U/229	U/226
W74	O4	O/326	C/642	O/326	O/320	O/316	O/322	C/652	C/648
W75	O4	U/218	U/216	U/210	U/214	U/213	U/209	U/209	U/213

Supplementary Table 3 continued

Numbering in manuscript	Channel	Combined (7RF1)	0F (7RF2)	1F (7RF3)	2F (50 µs) (7RF4)	2F (150 µs) (7RF5)	2F (250 µs) (7RF6)	2F (400 µs) (7RF7)	2F (7RF8)
W76	O1B	C/670	C/748	C/717	A/612	C/637	C/675	C/628	C/619
W77	O1B	V/363	V/358	V/322	C/685	V/313	V/349	V/363	V/358
W101	O1B	D/573	U/217	D/546	U/219	D/507	D/520	D/536	D/508
W102	O1B	B/863	B/856	D/817	x	x	x	x	B/853
W103	O1A	C/660	C/703	C/625	x	x	C/667	x	x
W104	O1A	C/770	C/759	C/724	C/691	x	C/747	x	x
W106	O1A	C/772	C/761	C/714	C/632	x	C/742	x	C/721
W107	O1A	C/662	C/649	x	x	C/634	C/679	x	C/685
W117	Cl1A	D/623	D/615	x	x	D/578	D/608	D/615	D/615
W119	Cl1A	A/577	A/558	A/504	A/587	A/726	A/757	A/543	A/573
W120	Cl1A	x	x	x	x	x	x	x	x
W121	Cl1A	O/384	O/366	O/353	x	O/357	O/373	O/372	O/382
W122	Cl1A	O/339	O/335	O/337	O/335	O/354	O/318	O/334	O/348
W125	Cl1A	O/348	O/332	O/316	O/333	O/322	O/326	O/332	D/595
W126	Cl1A	O/399	D/617	D/580	D/592	O/364	O/382	D/608	D/605
W127	Cl1A	A/595	D/558	D/528	D/551	D/569	A/794	D/595	D/586
W129	Cl1A	A/556	A/586	A/553	A/592	D/589	A/821	A/613	A/599
W145	Cl1A	x	x	x	O/323	x	x	x	x
W150	Cl1A	x	x	x	x	x	A/786	x	x
W151	O1B	x	x	x	x	x	x	A/516	C/732
152	Cl1A	A/539	A/551	A/552	A/573	A/730	A/754	A/558	A/544
153	Cl1A	O/325	O/349	O/344	x	O/324	O/347	O/329	O/329
154	Cl1A	O/357	O/352	x	x	O/353	O/353	O/354	O/367
160	Cl1B	B/740	B/753	B/771	B/802	B/764	B/740	B/758	B/808
161	Cl1B	D/518	D/534	D/536	D/514	D/527	D/516	D/559	D/522
162	Cl1B	B/769	B/779	B/786	B/807	x	B/796	B/829	B/728
163	Cl1B	D/543	D/545	O/329	O/324	D/523	D/514	D/532	O/331
164	Cl1B	O/336	O/324	x	O/312	O/329	O/314	O/326	O/315
165	Cl1B	B/785	B/746	B/733	B/757	B/762	B/766	B/780	B/764
166	Cl1B	B/821	B/770	B/748	x	B/724	B/752	B/804	B/767
167	Cl1B	D/615	D/598	D/587	D/566	D/590	D/601	D/582	D/585
168	Cl1B	O/319	B/826	O/335	x	B/768	O/325	O/328	O/332
169	Cl1B	B/774	x	x	x	x	x	x	x
170	Cl1B	O/369	x	x	x	O/318	x	x	O/364
180	O4	O/327	O/337	O/330	O/316	O/306	O/312	O/321	O/317
181	O4	U/211	U/220	U/208	U/207	U/204	U/216	U/218	U/208
182	O4	O/404	O/387	O/379	U/229	U/231	O/389	O/379	O/395
183	O4	U/243	U/236	U/232	U/228	U/224	U/239	U/230	U229
184	O4	U/232	U/231	U/223	U/221	U/215	U/225	U/227	U/225
190	O1B	D/528	D/593	x	x	D/517	D/580	D/538	x
191	O1B	D/633	D/628	D/599	x	x	D/613	x	D/626
192	O1A	C/628	x	x	x	x	C/648	x	C/709
193	O1A	C/643	x	C/675	x	x	x	x	C/655
194	O1A	C/625	C/741	C/684	C/649	x	x	C/616	C/720
195	O1A	C/714	C/713	x	V/312	x	x	x	V/311
196	O1A	C/762	x	x	x	x	x	x	C/721
197	O1A	C/728	C/708	x	C/638	x	C/686	C/678	C/687

Supplementary Table 4. The peak heights of individually generated polder-omit maps for waters present in the water channels and up to approximately 15 Å from the OEC at 0F, 1F, 2F and the time points between 1F and 2F in both monomers (m1) and (m2). The waters with 3-5 σ are depicted in bold.

m1

W	0F	1F	2F50	2F150	2F250	2F400	2F
19	12.02	9.9	8.26	10.2	9.83	10.51	9.02
20	7.67	--	--	--	--	--	--
21	10.83	10.56	8.6	8.75	11.49	10.11	10.24
22	9.58	9.21	9.3	7.45	10.78	10.55	8.91
23	10.79	9.9	10.01	8.49	10.84	10.06	9.26
24	9.49	8.92	7.44	7.97	9.12	8.55	8.76
25	9.00	8.98	5.61	9.15	11.63	11.5	10.31
26	9.5	6.9	6.95	7.62	8.17	7.45	7.44
27	8.85	6.24	5.63	4.73	6.73	7.91	6.75
28	7.61	7.21	6.6	6.74	8.47	6.69	6.89
29	9.5	10.01	8.22	7.91	9.23	8.42	8.16
30	7.8	6.71	4.74	6.73	7.21	6.65	6.23
31	7.88	7.66	7.34	6.88	6.58	6.34	7.76
32	6.85	7.77	7.2	6.48	6.28	6.65	6.25
33	9.1	8.56	8.33	7.58	9.2	8.07	7.67
34	8.03	6.55	6.75	5.78	7.58	7.1	7.09
35	6.46	6.98	6.76	7.48	5.8	6.72	6.67
36	9.53	8.63	7.87	9.05	8.6	9.87	9.86
37	6.63	6.81	6.33	7.57	6.25	5.66	6.49
38	7.05	6.36	6.49	6.97	8.23	6.41	7.23
39	4.59	**3.61**	5.1	5.71	4.82	5.67	5.13
40	9.08	8.19	8.13	8.19	10.4	8.37	8.64
41	9.47	8.04	9.36	7.94	8.94	8.93	8.46
42	9.69	11.02	9.26	10.08	11.1	10.59	9.85
43	10.15	9.32	9.74	8.5	10.6	8.47	10.4
44	8.79	7.84	7.68	6.72	9.17	8.12	8.36
45	9.3	9.9	11.08	10.32	10.62	10.29	9.99
46	10.36	9.98	8.04	10.79	10.65	9.7	10.11
47	10.41	11.41	8.55	9.77	11.03	10.86	10.57
48	10.13	10.44	8.45	9.35	10.77	9.23	9.42
49	8.89	9	5.8	7.78	8.5	7.97	9.18
50	8.05	8.28	7.11	7.41	7.84	7.6	8.17
51	8.13	8.99	7.18	8.29	8.32	8.71	8
52	9.28	9.07	7.67	8.77	9.75	9.94	8.64
53	8.81	9.96	7.57	9.9	10.48	9.61	8.9
54	9.46	8.07	8.09	8.85	8.96	9.3	8.38
55	7.57	7.73	7.03	7.71	8.39	8.86	9.07
56	6.59	7.67	6.68	7.28	8.81	7.79	7.67
57	8.67	6.73	7.78	6.09	8.94	7.8	7.14
58	8.81	8.99	9.26	9.34	11.45	9.06	9.19
59	8.85	8.85	8.99	7.57	9.83	9.28	8.12
60	8.48	8.22	8.02	9.72	9.47	9.6	8.31
61	9.35	9.29	9.59	8.81	10.58	10.34	9.48
62	10.29	10.43	8.37	9.64	9.73	9.25	9.38
63	9.88	8.61	6.77	7.93	10.01	6.94	9.55
64	8.65	9.03	6.78	8.82	9.5	8.16	8.61
65	8.3	7.66	7.54	7.3	6.99	8.02	7.61
66	10.96	10.78	10.61	10.23	11.88	10.95	10.11
67	11.36	9.45	9.29	11.45	10.98	10.79	10.68
68	10.71	10.92	9.59	9.73	11.07	10	10.74
69	10.82	10.65	10	9.22	11.96	11.77	10.39
70	10.49	8.9	8.2	10.68	12.31	10.65	10.21
71	7.01	7.34	5.9	7.02	9.01	8.15	8.22
72	8.1	9.06	5.37	8.7	8.73	8.72	7.55
73	10.24	9.4	8.89	9.32	10.35	10.21	9.3
74	10.29	10.05	10.63	10.67	11.61	10.09	10.41
75	10.29	9.84	8.87	8.95	11.52	10.03	8.51
76	6.12	6.44	5.4	6.6	5.13	6.41	**3.28**
77	6.05	**4.74**	5.19	**4.13**	5.5	6.06	5.58

m2

W	0F	1F	2F50	2F150	2F250	2F400	2F
19	10.61	8.06	7.8	8.7	9.68	9.27	9.17
20	6.75	--	--	--	--	--	--
21	9.78	10.81	10.35	9.96	10.83	10.61	10.72
22	9.23	10.23	10.41	9.19	10.06	10.64	10.62
23	9.77	8.97	7.23	8.75	9.8	9.5	9.12
24	9.89	9.88	8.74	9	9.32	9.17	9.66
25	8.79	9.23	8.95	9.53	10.17	10.32	9.01
26	8.86	8.56	8.12	8.99	8.96	8.26	7.29
27	6.82	5.6	7.12	4.08	5.03	4.2	6.14
28	7.77	7.24	6.8	9.11	8.71	7.98	6.85
29	8.97	8.42	8.23	8.48	8.56	9.15	9.14
30	7.74	7.6	8.45	7.26	7.19	7.14	8.22
31	6.5	6.85	5.93	6.32	7.85	6.84	7.61
32	7.68	8.35	6.28	6.47	8.37	6.25	6.28
33	9.8	8.29	9.13	9.82	9.17	8.55	9.9
34	6.34	7.66	5.71	7.52	7.07	7.5	7.89
35	7.84	8.24	7.06	7.96	6.42	6.94	6.96
36	8	7.95	6.64	8.78	9.04	8.32	7.52
37	5.62	6.67	5.32	6.02	7.76	7.82	6.1
38	8.7	7.88	6.64	9.01	9.58	8.73	7.44
39	--	--	--	**4.34**	--	**4.16**	5.33
40	9.79	8.83	6.83	7.34	8.87	9.14	8.85
41	8.85	10.99	8.46	8.44	10.32	10.39	10.07
42	8	8.82	8.69	8.44	9.27	9.3	9.19
43	8.33	6.85	7.06	8.54	8.82	8.52	9.49
44	8.95	7.09	8.78	7.7	8.5	7.72	8.16
45	8.47	9.32	10.34	10.13	9.76	9.09	9.84
46	11.07	9.17	9.64	10.39	11.44	10.32	10.77
47	8.94	9.93	9.07	9.59	10.85	10.73	9.95
48	11.83	9.7	10.66	10.29	9.84	10.24	10.09
49	9.37	10	8.22	9	9.33	9.72	8.33
50	9.28	8.01	7.98	9.33	8.7	7.51	7.42
51	7.92	8.42	8.35	7.7	8.14	8.51	7.42
52	8.91	7.87	7.96	9.49	9.93	8.65	8.62
53	9.24	9.5	9.2	10.46	9.72	10.87	9.97
54	8.78	8.88	9.68	9.42	9.71	8.65	8.84
55	8.84	7.85	8.2	8.61	8.35	7.72	7.84
56	7.55	8.63	9.08	8.34	9.31	8.54	9.02
57	8.99	7.74	8.11	7.84	8.22	8.05	8.77
58	10.1	8.27	7.63	8.66	9.25	8.51	9
59	9.49	9.62	7.72	8.57	8.54	7.47	9.73
60	10.21	10.56	9.03	10.4	9.43	9.58	10.64
61	9.96	8.63	6.34	8.56	8.85	9.74	10.18
62	10.25	8.58	9.39	9.37	10.81	11.76	10.5
63	8.6	9.31	8.08	8.82	10.06	10.49	10.07
64	9.23	8.42	7.76	9.06	10.24	9.07	9.37
65	8.57	8.01	7.87	7.67	8.52	8.75	7.72
66	10.96	11.4	9.36	10.06	12.25	11.8	11.7
67	10.48	10.51	9.28	9.51	11.21	10.95	11.22
68	9.01	9.51	8.17	9.08	10.97	9.23	9.49
69	9.14	8.72	7.84	9.79	10.3	10.15	9.17
70	9.76	8.55	9.02	9.58	10.18	9.9	10.32
71	8.24	10.13	7.47	7.47	9.02	8.08	9.59
72	7.06	8.4	7.23	8.08	9.23	8.23	8.7
73	8.37	8.56	6.96	9.04	8.26	8.18	8.24
74	8.56	9.04	8.1	8.91	9.19	8.47	9.85
75	9.67	10.22	8.33	9.34	10.81	8.76	9.2
76	**4.72**	6.42	5.65	5.86	**4.77**	5.33	6.43
77	5.11	6.64	5.38	5.51	5.16	5.64	5.34

Supplementary Table 5. The B-factor (Å^2) of waters present in the water channels and up to approximately 15 Å from the OEC at 0F, 1F, 2F and the time points between 1F and 2F in both monomers (m1) and (m2).

m1								m2							
W	0F	1F	2F50	2F150	2F250	2F400	2F	W	0F	1F	2F50	2F150	2F250	2F400	2F
19	19.9	32.5	41.0	28.7	26.8	27.0	37.5	19.0	21.9	33.9	32.0	30.1	22.6	27.9	25.8
20	33.0	--	--	--	--	--	--	20.0	27.2	--	--	--	--	--	--
21	22.9	27.5	32.4	33.7	26.3	30.9	34.4	21.0	21.9	24.2	26.9	30.0	21.9	24.8	24.7
22	29.2	30.2	30.4	28.9	25.6	26.0	31.6	22.0	29.4	26.5	26.6	32.4	25.9	25.0	27.3
23	26.9	32.7	33.7	32.3	25.3	25.1	33.7	23.0	22.7	26.2	32.6	32.6	24.7	24.9	24.7
24	30.4	35.8	36.4	31.9	28.1	27.6	31.6	24.0	26.2	27.5	40.6	35.1	29.4	27.0	31.9
25	60.5	28.7	36.5	30.7	22.5	21.8	27.1	25.0	29.3	28.1	33.9	31.5	22.3	29.0	34.6
26	30.2	36.8	40.0	32.4	26.6	27.5	29.4	26.0	33.1	35.8	35.3	30.3	25.5	30.5	32.5
27	31.9	37.1	39.3	32.1	29.6	30.3	34.3	27.0	34.0	34.6	39.4	34.3	31.4	33.5	34.1
28	36.6	32.6	41.1	34.0	27.1	31.8	38.4	28.0	35.6	34.2	37.5	32.3	26.1	28.3	34.2
29	32.0	32.9	38.2	37.2	31.5	33.2	39.4	29.0	34.9	37.5	37.7	35.7	27.8	30.1	35.3
30	36.1	39.0	48.5	39.4	33.8	34.2	40.0	30.0	40.9	37.3	41.0	39.5	32.3	33.2	43.0
31	37.8	39.6	40.4	37.3	32.2	32.9	37.5	31.0	39.7	37.0	39.9	37.1	30.3	36.1	36.9
32	37.3	40.3	38.1	36.2	32.7	31.3	37.9	32.0	36.8	36.1	42.4	40.9	29.1	33.4	38.1
33	29.9	35.6	38.1	39.3	29.5	35.5	38.8	33.0	29.0	36.2	31.8	33.3	34.0	34.7	35.0
34	32.0	39.3	40.0	42.0	36.8	35.6	39.8	34.0	43.8	43.1	46.7	45.9	42.3	42.0	44.5
35	41.1	39.4	45.2	36.0	36.2	38.3	46.5	35.0	37.5	39.6	41.2	39.1	39.5	38.1	44.5
36	28.7	35.6	40.0	32.5	30.5	29.2	30.7	36.0	33.3	37.8	43.1	36.3	35.3	33.2	36.8
37	37.7	39.4	42.5	38.4	35.9	38.4	42.8	37.0	45.2	41.3	45.2	43.7	39.8	37.4	45.0
38	32.7	39.3	43.0	37.6	29.9	32.0	40.4	38.0	29.2	36.5	42.7	36.6	32.0	33.5	40.7
39	36.8	35.5	36.5	34.9	27.0	31.9	37.1	39.0	--	--	--	32.1	--	30.1	39.4
40	31.9	30.4	36.3	29.4	22.1	34.9	28.9	40.0	24.8	31.0	40.3	34.9	27.1	27.0	31.8
41	28.7	33.7	30.8	30.4	30.0	31.3	32.2	41.0	31.4	26.8	31.9	32.2	25.6	23.6	28.0
42	27.5	24.7	36.9	27.1	25.1	27.8	26.1	42.0	28.7	32.6	28.1	28.3	25.0	27.0	24.2
43	24.8	30.1	30.0	36.9	27.0	31.5	30.7	43.0	27.5	30.9	33.9	29.4	28.1	31.8	28.5
44	30.3	37.3	37.8	36.3	25.5	30.8	37.2	44.0	22.6	29.4	30.0	33.1	20.8	27.2	26.7
45	27.3	25.6	24.6	23.4	25.8	25.9	30.4	45.0	29.9	27.9	25.0	28.1	29.4	29.5	26.3
46	22.2	25.0	32.0	25.8	24.7	25.5	33.1	46.0	16.3	31.2	30.4	26.9	24.3	28.9	23.4
47	20.7	20.2	34.9	29.5	23.5	23.8	27.4	47.0	27.5	26.3	30.2	29.1	25.2	23.3	27.5
48	28.9	29.4	35.5	35.8	27.5	32.2	30.8	48.0	18.7	27.6	23.1	27.3	27.1	28.7	27.4
49	29.9	25.4	38.5	32.8	23.8	28.5	29.4	49.0	23.1	25.0	36.7	31.7	28.1	23.5	31.3
50	36.6	38.0	36.5	38.5	29.5	31.1	37.7	50.0	26.6	33.6	36.0	33.0	28.1	31.9	37.3
51	35.0	36.6	43.2	34.5	32.4	32.5	39.1	51.0	36.9	36.9	35.9	38.4	27.6	31.8	37.2
52	28.2	31.6	38.3	30.0	28.3	30.2	34.8	52.0	34.7	35.0	40.8	33.0	26.5	34.5	36.5
53	29.6	26.7	37.1	31.0	23.8	28.3	32.8	53.0	24.6	32.7	30.0	30.5	26.0	23.6	31.6
54	30.3	41.6	41.4	39.8	34.3	34.8	40.1	54.0	35.2	36.8	33.0	35.6	31.1	35.4	40.2
55	39.3	34.7	38.9	36.0	31.3	32.2	34.0	55.0	39.7	41.8	38.4	39.4	38.0	35.9	44.4
56	34.8	34.2	36.1	29.2	27.2	31.9	35.6	56.0	43.1	39.2	36.4	41.3	37.1	37.7	40.3
57	26.6	28.7	39.5	33.8	25.3	28.4	30.2	57.0	31.5	42.4	39.4	38.8	32.1	35.0	40.1
58	26.5	27.5	29.0	26.7	24.3	26.3	27.5	58.0	27.0	32.9	41.8	31.2	30.1	34.7	32.8
59	32.7	30.2	32.3	31.5	24.4	26.3	35.0	59.0	23.8	30.0	34.6	28.8	27.6	32.7	32.1
60	29.6	31.2	41.2	27.9	24.4	27.1	34.1	60.0	25.9	29.6	31.8	31.3	28.2	30.8	29.4
61	32.1	30.3	28.3	25.2	26.9	26.3	32.4	61.0	25.8	29.4	30.5	30.8	25.8	20.8	23.7
62	25.5	29.4	34.3	28.7	27.5	23.7	29.9	62.0	20.1	31.8	25.2	26.9	24.5	21.9	25.2
63	24.2	36.4	41.9	34.8	22.5	30.5	30.3	63.0	34.7	31.9	39.8	36.8	31.1	26.5	35.4
64	33.4	30.6	37.8	34.8	29.1	29.5	32.9	64.0	27.6	31.1	37.2	39.2	28.4	32.1	34.3
65	29.9	32.8	34.0	31.2	24.0	25.5	36.1	65.0	31.3	30.6	31.6	34.3	25.0	28.6	32.5
66	22.4	25.9	29.4	29.6	24.0	23.9	27.1	66.0	20.6	25.5	33.6	31.0	21.8	22.2	26.7
67	21.3	30.3	33.8	26.8	24.1	25.5	28.0	67.0	21.9	24.0	25.9	26.5	23.3	24.9	26.2
68	24.3	24.9	33.4	34.2	26.6	27.5	30.0	68.0	29.9	32.5	34.3	27.6	24.6	29.8	30.0
69	27.4	22.8	31.2	36.2	28.6	22.5	30.7	69.0	29.2	31.9	38.2	26.2	27.0	27.0	29.3
70	23.6	27.5	34.0	26.5	22.4	27.5	27.8	70.0	24.5	29.4	31.7	27.7	26.9	25.0	24.5
71	34.8	29.1	30.6	33.0	27.2	26.1	31.9	71.0	30.8	34.4	35.2	33.7	26.7	35.4	35.2
72	30.7	28.6	35.2	30.9	27.0	25.2	35.0	72.0	36.1	40.0	43.5	36.9	32.1	34.3	35.9
73	31.8	34.9	37.8	37.0	33.3	31.7	35.8	73.0	34.6	33.5	39.6	33.0	30.3	33.3	37.7
74	25.8	27.3	25.0	29.2	22.7	28.9	29.0	74.0	30.3	32.1	40.2	29.7	28.8	29.4	35.5
75	27.8	31.7	33.7	35.0	26.7	30.3	33.6	75.0	25.6	24.6	34.4	31.7	24.8	33.2	33.1
76	34.1	44.9	46.9	42.2	39.6	41.5	41.5	76.0	48.6	45.5	49.6	49.5	49.1	43.3	47.0
77	34.2	43.1	53.7	41.2	36.0	38.4	45.5	77.0	43.9	42.8	51.6	45.5	43.3	35.5	44.2

Supplementary Table 6. Comparison between number of water molecules detected in high resolution cryogenic data and RT data. The table shows the total number of water molecules detected in the whole structure and within 3.5 Å of each water channel. Number of water molecules in the channels between cryogenic data and RT data are quite comparable. However, water molecules detected in O1 Channel B are higher in cryogenic data than RT.

	4UB6	5B66	combined data(PDB ID 7RF1)
X-ray source	XFEL	synchrotron	XFEL
Temperature during collection	cryo	cryo	RT
Radiation	Damage free	0.03 MGy	Damage free
State	0F	0F	Combined data (0F-3F)
Resolution	1.95 Å	1.85 Å	1.89 Å
Reference	Suga et al.[47]	Tanaka et al.[355]	Current study
No. of water molecules in the structure	2624	4066	1960
No. of water molecules in O1 Channel A	19	20	20
No. of water molecules in O1 Channel B	23	28	18
No. of water molecules in O4 Channel	20	20	18
No. of water molecules in Cl1 Channel A	16	16	16
No. of water molecules in Cl1 Channel B	26	24	23
No. of water molecules in the channels	104	108	95
No. of water molecules in the channels within 5 Å from the bulk	25	22	16

Supplementary Table 7. Number of cryo-protectant or additive molecules detected in RT and cryo-structure data

PDB (ID)	Reference	State	Sample condition	Cryo-protectant/additives	Numbers of cryo-protectant molecules
6JLJ	Suga et al.[52]	0F	cryo	glycerol	20
4UB6	Suga et al.[47]	0F	cryo	glycerol	39
5WS5	Suga et al.[50]	0F	RT	glycerol	5
5B5E	Tanaka et al.[355]	0F	cryo	DMSO	112
5B66	Tanaka et al.[355]	0F	cryo	DMSO	97
3WU2	Umena et al.[73]	0F	cryo	glycerol	36

III. Discussion

In this chapter, the main objectives and the result parts (PII.1-PII.3) will be overviewed, discussed, and compared with other studies as well with the following order:

III.1. Optimizing crystal size of Photosystem II by macroseeding: an early step toward neutron protein crystallography (related to PII.1)

III.2. Solution structure of the detergent-photosystem II core complex investigated by small-angle scattering techniques (related to PII.2)

III.3. Structural Dynamics in the Water and Proton Channels of Photosystem II During the S_2 to S_3 Transition (related to PII.3)

III.1. Optimizing crystal size of Photosystem II by macroseeding: an early step toward neutron protein crystallography (PII.1)

PSII catalyzes the water oxidation upon light exposure to molecular oxygen and protons. Albeit the progress in improving crystal structure resolution and tracking the dynamic in the Mn-cluster using XFEL crystallography and several spectroscopic methods, the reaction mechanism remains elusive. Several conformational changes occur at the catalytic site during the water oxidation process inside the oxygen-evolving complex (OEC). Elucidating the protonation state changes at the active catalytic site and in the surrounding side chains during catalysis at each S-state and the electronic and geometric changes of the OEC are essential to enhance our understanding of the mechanism of water oxidation. Neutron crystallography is a crucial complementary tool to X-ray crystallography, which enables directly locating the hydrogen atoms, assigning the protonation state, defining the hydrogen bonds, and understanding how the proton is transferred between residues and solvents[194-196]. In addition, polarized extended X-ray

absorption fine structure (EXAFS) and electron paramagnetic resonance (EPR) data collected from single macrocrystals able to provide the precise distances for metal to metal like (Mn-Mn and Mn-Ca) and metal to ligand like (Mn-O)[100], and to provide insights into the electronic structure of OEC[133, 156, 226, 227] respectively.

In this study (PII.1), a macroseeding protocol for the dimeric PSII core complex (dPSIIcc) has been developed by combining microseeding and macroseeding crystallization techniques. The generated protocol allowed us to quickly and reproducibly grow a large single crystal of the dPSIIcc with a size of ~ 1.8 mm length in the long axis within a couple of days. Moreover, we got larger macro-dPSIIcc crystals of ~ 3mm along the long axis using the generated large crystal as a seed. These large crystals are considered the first step towards fulfilling the prerequisite for collecting structural data using neutron diffraction. Neutron diffraction data require a considerable huge crystal volume ≥ 1 mm^3 to overcome the weakness of the beam flux of the most available neutron sources[194, 231]. Such a crystal volume would improve the signal-to-noise ratio of the data collected by spectroscopic methods like polarized EXAFS and single-crystal EPR techniques.

III.1.1. Major challenging in dPSIIcc macrocrystallizations

The key two steps in the protocol are to grow crystals within the size range of 100 µm to use them as crystal seeds and identify the metastable zone of the crystallization condition based on "PEG-out conditions" This first step was achieved by applying the micro-seeding technique. This technique is considered one of the powerful crystallization techniques used to optimize crystal growth and improve crystal quality[172] (PII.1. Figure 3). The micro-seeding protocol developed by Ibrahim et al.[190] allowed us to produce crystals with a uniform size of around 100 µm within a few hours (PII.1. Figure 4). Before transferring the crystal seeds to the pre-equilibrated drop of dPSIIcc protein in the metastable zone, crystal seeds were washed by transferring them gradually from high to low concentration of PEG 2000, aiming to dissolve the extraneous nuclei and get a fresh surface (PII.1. Figure 5). Identifying the metastable zone of the crystallization condition was achieved by deeply understanding the phase diagram to be able to promote single crystal growth and avoid unnecessary nucleation (PII.1. Figure 1). In the beginning, we faced a problem because of growing several crystals instead of a single large crystal in the seeded pre-equilibrated drop. This spontaneous nucleation is a general problem of

macroseeding techniques[172, 238] and mainly due to having a narrow width of the metastable zone.

Several studies were shown that some salts like potassium chloride, calcium chloride, and sodium chloride have an effect in controlling the width of the metastable zone[244, 245]. Therefore, the influence of increasing $CaCl_2$ concentration in widening the metastable zone was examined. Screening different concentrations of $CaCl_2$, the already existing salt in our crystallization buffer, showed that the width of the metastable zone increases with increasing $CaCl_2$ concentrations and that by shifting the nucleation phase and rarely affecting the unsaturated zone. If the crystallization buffer contains 40 mM $CaCl_2$, the nucleation phase is shifted by 0.8 % of PEG 2000, whereas the unsaturated zone is only shifted by 0.2 % of PEG 2000, compared to using 5 mM $CaCl_2$ as in the original crystallization buffer (PII.1. Figure 2). Based on this information, the equilibration of dPSIIcc protein in the metastable zone was achieved by mixing the protein at 2 mM Chl *a* and the crystallization buffer containing 20 mM $CaCl_2$ and 6.5−6.8% PEG 2000 for 1 day in sitting drop plates containing 1 ml of the crystallization buffer in the reservoir at 20 °C. Precise measuring and adjusting the PEG 2000 concentration were done using the refractive index (RI), which is a crucial step that helped us to minimize the amount of protein sample and the needed time for testing each batch. Finally, after being washed, each crystal seed was transferred to 4 µL of the equilibrated dPSIIcc in a silicone-greased coverslip and sealed above the hanging drop well containing 1 mL of the crystallization buffer. The crystal growth was left for 2 - 3 days at 20 °C.

Initially, it was challenging to keep the droplet shape on the coverslip uniform and well-structured because dPSIIcc always contains 0.015% of βDM. However, greasing the glass coverslip with silicone grease (PII.1. Figure 7) helped overcome this problem and resulted in uniformly stable, spherical droplets. This fast and reproducible macroseeding protocol provides a single large crystal of dPSIIcc around ~1.8 mm length in the long axis within ~ 2-3 days (PII.1. Figure 6). Moreover, by utilizing these large crystals of dPSIIcc as a crystal seed, we managed to produce even larger dPSIIcc crystals of ~ 3mm along the long axis (PII.1. Figure 8). However, the double macroseeding step has a success rate of around 30 %. That is due to the difficulties of handling and transferring the large crystal seeds without being suffered from physical stress, which can usually lead to growing multiple crystals in the same drop.

III.1.2. Crystal quality by X-ray/Neutron diffraction

The quality of the produced macrocrystals was tested by X-ray diffraction at BESSY (Adlershof, Berlin). The dataset collected from a rectangular-shaped single dPSIIcc crystal with a dimension ≈ 2 x 0.60 x 0.40 mm was processed to a resolution of 4.11 Å and with a completeness of 88.9 %. The results showed that the crystal belonged to the same orthorhombic space group $P2_12_12_1$ with unit cell constants a = 126.59 Å, b = 223.15 Å, c = 305.46 Å (PII.1. Table 1 and PII.1. Figure 9) as the unseeded crystals of the βDM dPSIIcc[39, 41, 43]. Furthermore, the collected diffraction patterns analysis showed clear diffraction spots with no signs of twining. In addition, diffraction patterns reveal an anisotropic diffuse background near the highest resolution shell, similarly to the unseeded βDM dPSIIcc crystals[220, 356]. In terms of crystal quality, these results confirm no significant difference between the unseeded and the seeded dPSIIcc crystals.

In addition to testing the quality of macrocrystals by X-ray diffraction, one of the generated crystals with a dimension of ≈ 2.0 x 0.8 x 0.3 mm was also examined by neutron diffraction. Partial D/H exchange was done by soaking the crystal in D_2O containing buffer followed by dehydrating it by gradually increasing the PEG 2000 concentration in the deuterated buffer until it reached 30 % PEG 2000 and left for two days. The crystal was mounted in fused-silica capillaries then transported to the SNS at ORNL, where the crystal was tested by the Macromolecular Neutron Diffractometer (MaNDI) instrument[242, 243]. Weak diffraction spots were observed after 24 h at room temperature with a maximum resolution of ~ 8.0 Å (PII.1. Figure 10). This limited resolution could be explained by the non-optimal deuteration of the crystals and the necessity for having a complete D/H exchange for the protein, the used PEG, and the detergents.

III.1.3. Summary

The study **PII.1** presents a fast and reproducible protocol to grow a single large crystal of the dPSIIcc. The introduced technique combined the microseeding and macroseeding crystallization techniques to achieve a crystal of ~1.8 mm length in the long axis within ~ 2 to 3 days. Following this, a double macroseeding protocol was introduced to achieve a considerable large crystal of around ~ 3 mm along the long axis. These single large crystals will open the door to collect high-quality data using different polarized spectroscopy techniques. Furthermore, the advantages of the large crystal are enhancing the signal-to-noise ratio and facilitating accurate data collection at each orientation. Therefore, these large crystals will be crucial to extend the spectroscopic studies of PSII.

Furthermore, it represents the first step towards collecting the first complete neutron diffraction dataset from dPSIIcc, as one of the main obstacles in neutron crystallography, which is the large crystal volume (> 1 mm^3) required to compensate for the weakness of neutron fluxes from the available neutron sources[194, 231]. This step is vital for better understanding the water environment and proton pattern surrounding the OEC. However, several optimizations are still needed to improve the neutron diffraction quality of the crystals.

III.2. Solution structure of the βDM-dPSIIcc investigated by small-angle scattering techniques (PII.2)

PSII is a complex protein embedded in the thylakoid membrane. Therefore, its purification requires solubilizing the protein's hydrophobic core from the membrane's lipid bilayer using detergents. Detergents have an amphiphilic character where each detergent molecule has a hydrophilic head and a hydrophobic tail. The monomeric detergent molecules spontaneously form non-covalent aggregates called micelles at the critical micelle concentration (CMC). Therefore, it is crucial to optimize the detergent concentration to be right above the critical solubilization concentration (CSC), where all the protein molecules are surrounded by a detergent belt resulting in having a stable detergent-protein complex (DPC) in an aqueous solution[208, 257] with non-formation of free micelles (without protein). Therefore, understanding the interaction between the detergent and the protein molecule in that complex and how the detergent belt is formed around the protein plays an essential factor in protein crystallization and, ultimately, crystal quality. Therefore, it can be concluded that correct determination of the CSC decreases the chances of having free micelles in the solution, which may influence the protein crystallization and weaken the packing of the protein molecules inside the crystals, resulting in poor crystal quality.

In this study (PII.2), we focused on studying dPSIIcc, which is isolated and solubilized using the non-ionic detergent n-dodecyl-ß-D-maltoside (βDM) by applying Small-angle neutron scattering (SANS) with different contrast and Small-angle X-ray scattering (SAXS). We were very keen to deeply understand this complex because of several factors; First, the purified βDM-dPSIIcc is highly stable and has a high oxygen activity[220, 255]. Second, most of the crystal structures of dPSIIcc were collected from βDM-dPSIIcc crystals[39, 41, 43, 47, 73, 252]. Third, the developed macroseeding protocol to develop single large crystals are based on βDM-dPSIIcc[268]. Our results showed that under

appropriate solubilization conditions, the βDM is forming a monomolecular belt surrounding the dPSIIcc. An expansion in the size of the dPSIIcc in the solution under the functional condition in comparison to the size of the dPSIIcc in the cryogenic crystal structure[73] was observed. Furthermore, the monodispersity of the samples had been investigated by DLS, SANS, and SAXS. Our SAXS data showed a peak corresponding to a spherical shape with a radius of around 40 Å, indicating the presence of free micelles unbound to the protein.

III.2.1. The structure of the βDM-dPSIIcc in solution

By varying the ratio of H_2O and D_2O in the solvent, the SANS data are capable of providing structural information about the individual components of the protein-detergent complex because of the scattering length densities of deuterium and hydrogen are different[260-263]. So first, the structure of dPSIIcc was investigated by SANS using 5% D_2O content in the buffer solution as a contrast match point for the hydrophobic tail of βDM detergent molecules at different protein concentrations range of 2−10 mg/mL dPSIIcc. The SANS data collected (PII.2. Figure 1) and Guinier analysis (PII.2. Figure 2) showed that the dPSIIcc in solution has a radius of gyration of 62 Å. Next, the model-dependent analysis was performed using an elliptical cylinder as a model. The fit parameters of the model were found to be consistent with the dimension values of the crystal structure of PSII (PDB ID: 3WU2)[73] (PII.2. Table 1). In addition, the Guinier analysis and the fit parameters of the models showed that all the analyzed samples at different protein concentrations are free of aggregation. This finding was consistent with the DLS measurements (PII.2. Figure 3) that showed the βDM-dPSIIcc at different protein concentrations of 0.5−10 mg/mL dPSIIcc are monodisperse. This point is crucial not only for optimizing protein crystallization but also for studying the pigment-protein complexes[287, 288] using spectroscopic techniques that are affected by the presence of aggregations.

III.2.2. The overall structure of dPSIIcc-detergent complex

The overall structure of the βDM-dPSIIcc was investigated by SANS using 75% D_2O content in the buffer solution that achieves no specific contrast match, and also by applying SAXS. So that the data collected (PII.2. Figure 6) by both methods should represent the structural data for the dPSIIcc-detergent complex. Guinier analysis from the

SANS measurement of the sample in 75% D_2O showed that the dPSIIcc in solution has R_g of 68 Å, which is higher by around 6 Å in comparison to the R_g of the sample in 5% D_2O. The P(r) functions calculated from SAXS data and from SANS data set at 5% D_2O (PII.2. Figure 4) showed a similar peak position to 76 Å. However, in the case of the SAXS data, the peak has a longer tail extending the particle maximum dimension to 250-260 Å. This increment in the R_g and the particle maximum dimension D_{max} are proposed to be due to the contribution of the detergent belt which surrounds the hydrophobic core of dPSIIcc. In the same direction, the SAXS and SANS data collected using 75% D_2O contrast showed that the radius of the elliptical cylinder of the βDM-dPSIIcc is around 117 Å. While SANS data was collected using 5% D_2O contrast, the radius is only about 98 Å. This difference in the radius is because of the contribution detergent belt. All above confirm that βDM is forming a monomolecular layer around the dPSIIcc. Our modeling showed around 432 β-DM molecules are bound to dPSIIcc to form a monolayer belt with a thickness around 20 Å (PII.2. Figure 7). These results explain the difference in the radius and the increment in the R_g and the particle maximum dimension D_{max}. They are consistent with previous studies showing that the membrane proteins are most likely surrounded by a monolayer ring of the detergent[256, 257, 294, 297].

Interestingly, the SAXS data clearly showed a presence of another peak at about 0.17 $Å^{-1}$ (PII.2. Figure 6), which indicates the presence of small molecules with a size around 35-40 Å. This finding suggests the presence of free detergent micelles unbound to the protein. Furthermore, performing a simultaneous fit of both SANS and SAXS data confirmed that this peak corresponds to a spherical core-shell model representing the βDM micelles (PII.2. Figure 6) with a radius around 32 Å[294, 295].

III.2.3. Comparison between the structures of dPSIIcc in solution and crystal

The Guinier analysis from SANS data collected using 5% D_2O contrast showed that the dPSIIcc in solution has a radius of gyration of 62 Å. While the radius of gyration calculated from a cryogenic crystal structure of dPSIIcc (PDB ID: 3WU2) is around 58 Å. This result support that the size of dPSIIcc in the solution at RT is slightly larger than in the cryogenic crystal. Furthermore, the dPSIIcc model in the solution, which is built based on the SANS data collected using 5% D_2O contrast, showed that the dPSIIcc size was slightly larger than the dPSIIcc from the cryogenic crystal (PDB ID: 3WU2)[73] especially extrinsic subunits of the protein. This observation could be because of the

conformational flexibility of the extrinsic subunits in the solution in comparison to the crystal[254, 292, 293]. The recent crystal structure of dPSIIcc collected under functional conditions at RT using XFEL[48] showed the presence of expansion of the dPSIIcc size by ~ 0.5 Å in all directions within the intrinsic part. It was noticed that the conformational flexibility of the PSII depends on the temperature and the level of hydration, and it was shown to increase significantly above 240 K[253, 254].

III.2.4. Summary

In **PII.2**, we applied SAXS and SANS with different contrast to prob and investigate the structure of the detergent protein complex βDM-dPSIIcc in the solution. The overall structure of dPSIIcc without the detergent contribution is studied by collecting SANS data for protein samples in 5% D_2O content in the buffer solution. In complementary, SANS data collected using 5% D_2O contrast and SAXS data gave the structural information for the overall structure of βDM-dPSIIcc. Our results showed that βDM is forming a monomolecular layer around the dPSIIcc. Furthermore, our results showed the presence of expansion in the size of the dPSIIcc in the solution under the functional condition in comparison to the size of the dPSIIcc in the cryogenic crystal structure[73]. This result is consistent with the recent study by Young *et al.*[48]. This study showed the expansion of the dPSIIcc size by ~ 0.5 Å in all directions within the intrinsic part of the crystal structure of dPSIIcc collected under functional conditions at RT using XFEL[48] compared to the crystal structures of dPSIIcc collected under cryogenic conditions. Our DLS and SANS measurements for protein samples at a concentration range of 2-10 mg/ml PSII showed that all the samples are monodisperse and free from aggregation. However, the SAXS data detected a peak assigned for the free micelles of βDM. This finding suggests that the detergent concentration in the studied protein samples is above the CSC. The presence of these free micelles during crystallization could negatively affect the growth of the crystal and hence the quality of the diffraction. In addition to negatively collecting spectroscopic data, which needs to perform on a free aggregation sample. This overall finding is crucial to optimize the βDM concentrations in the solution to avoid having an excess of free micelle aggregates.

III.3. Structural Dynamics in the Water and Proton Channels of Photosystem II During the S_2 to S_3 Transition (PII.3)

For the water oxidation process, water substrates need to be delivered to the OEC, and protons need to be transferred to the luminal side. Protons egress is a crucial step for advancing the S-state of the OEC[157]. The stoichiometry of deprotonation during the S_1-S_2, S_2-S_3, S_3-S_0, and S_0-S_1 is 0:1:2:1[316, 357, 358]. In earlier crystallographic studies, eight potential water/proton channels were identified, which extend from the Mn_4CaO_5 cluster toward the lumen; three channels have a minimum Van der Waals diameter of ~2.7 Å. In addition, another five narrower channels start from the OEC, with their minimum van der Waals diameter being 1.3 Å[117]. However, using only one static conformation of only one S-state is one of these studies' significant limitations[359]. On the other hand, Vassiliev and co-workers' work on identifying the channels using Molecular Dynamics (M.D.) calculations allowed for conformational changes. It showed only five channels extended from the luminal side to the OEC, including the described here O1 channel, Cl1 channel, and O4 channel, PII.3. Figure1[310].

Previously undetectable conformational changes, which occur during the transition between two consecutive states, can now be investigated by serial femtosecond XFEL. These changes could allow for identifying the water/proton channels. This work (PII.3) investigates the dynamics of the amino acid residues and the waters along the identified water channels using snapshots of the RT crystal structures of PSII to identify the possible channel that delivers the substrate water and the proton release channel. The study mainly focuses on the S_2 to S_3 transition, where one proton is released towards the bulk, and one water molecule binds into the OEC, forming an oxo or hydroxo μ-bridge between Mn1 and Ca[50, 51, 91].

Water positions identified at the RT or the cryogenic structures are mostly identical in the dark-adapted state, indicating that most of the waters are highly structured along the potential channels, except for the waters located at the exit of each channel near the bulk. However, some differences are detected. These position differences affect water connections described before as potential proton channels, PII.3. Figure2B resulting in a significant impact on the potential roles of these channels. Furthermore, sequential changes of several water positions at RT have been observed along the course of the S_2 to S_3 transition after the 2nd flash (PII.3. Supplementary Figure 5), suggesting the likely channels for proton release and water intake.

III.3.1. Identifying the possible Water substrate pathway

Based on theoretical studies[120, 122, 153, 309, 310, 322, 323], the O1, Cl1, and O4 channels have been suggested to act as the intake pathway for the water substrate. Investigating the channels mobility among the proposed candidates may narrow down the possible intake pathways that lead to the Ox binding at the S3 state. Therefore, we investigated the B-factors of the waters along the channels using the combined 1.89Å high-resolution structure. The high resolution of the combined structural data helped model the partially occupied waters, which were not modeled in the individual timepoint structural data because of the uncertainty (Fo-Fc peak < 3σ)[51, 91]. The B-factor can be used to express flexibility, rigidity and/or internal motion[360]. In a structural model, a low B-factor represents a localized electron density, and a high B factor corresponds to diffused electron density[361]. For crystal structures, the higher the resolution, the more accurate the estimated B-factor is. In addition to the B-Factor analysis, we also investigate the presence of Fo-Fc (≥ +3σ) peaks, which represent the partially occupied waters in the combined structural data. Examining the Fo-Fc peaks (≥ +3σ) within the proposed channels in the 1.89Å combined structure shows many peaks spread through the O1 channel but not through the Cl1 or O4 channels. These peaks likely indicate water position changes or new waters coming in the O1 channel (PII.3. Figure 2A). Besides, the O1 channel's waters have B-factor values significantly higher than those in the Cl1 channel or O4 channel (PII.3. Figure 2 and PII.3. Supplementary Figures 2 and 3). Furthermore, analyzing the deviations in the water positions from the 1 Flash (1F) (S_2 data) and the fluctuations in the normalized B-factors of waters at the different time points during the $S_2 \rightarrow S_3$ showed that waters in O1 channels are significantly deviating and highly fluctuating (PII.3. Supplementary Figures 4 and 5). These results agree with what we early reported in Ibrahim *et al.* 2020, where the root mean square deviation (RMSD) analysis of waters during the S_1-S_3 transitions significantly fluctuates within the O1 channel, unlike the other channels. These results confirm that the O1 channel's waters are highly dynamic, showing significant water rearrangement during transitions over the whole channel from the lumenal side to the OEC.

Furthermore, several crystal structures[47, 50, 52, 73] showed the presence of glycerol or Dimethyl-Sulfoxide (DMSO) molecules in the O1 channel but not in Cl1 or O4 channels. That is mainly because of the broadness of the O1 channel that allows accommodating molecules like glycerol or DMSO. The recent FTIR studies[313, 324] showed that the crystals having glycerol molecules have slightly lower efficiency of the S-state turnover during

S_2 to S_3 and S_3 to S_0 transitions compared to the non-containing glycerol solution sample. It is worth to be noted that the S_2 to S_3 and S_3 to S_0 transitions are the steps where the substrate water insertion is involved. Therefore, the decrease in the efficiency could be due to altering the water networking within the O1 channel due to the presence of glycerol molecules, which may restrict the mobility of waters in the channel.

Several structural changes were observed during the analysis of the time point data supporting the role of the O1 channel in delivering the water substrate to the OEC. At 2F(400 µs), a new water (W151) was detected in the O1 channel located near the D1-E329 (PII.3. Figure 3A). This event took place after the complete insertion of Ox into the OEC that happened earlier at 2F(250 µs). Furthermore, a gradual decrease in Fo-Fc difference density of W27, one of the waters located at the beginning of O1 channel from the OEC side, was observed and reached its maximum at 2F(150µs) data (PII.3. Figure 3C) right before the after the complete insertion of Ox. On the other hand, in comparison to other possible channels to act as the water substrate delivery like Cl1 channel, we see that the chances are minimal because of three main reasons: First, the water mobility along the Cl1 channel except for the exit that closes from the bulk is low. Second, no structural modifications were detected in branch B of Cl1. Third, the analysis of the structural changes detected due to the rotation of the D1-E65 side chain at branch A showed that the difference in the radius of the bottleneck formed by D1-E65, D1-P66, D1-V67 and D2-E312 at 2F(150 µs) data do not allow a water to pass through (PII.3. Supplementary Figure 10). These later observations suggest more that the Cl1A channel plays a role in the proton egress from the OEC. O4 Channel also has been proposed to deliver the water substrate to the OEC[151]. This possibility was not supported by a study performed by Weisz et al., aimed to identify the oxidative modifications formed by Reactive Oxygen Species (ROS) at the OEC in PSII[325]. The previous study did not identify oxidized residues involved in the channel O4 and the Cl1 branch but detected a large part of the residues involved in the O1 channel. In addition, the oxidized residues were also detected in branch B of the Cl1 channel.

III.3.2. Possible routes for Ox binding

The possible routes that lead to Ox binding into the OEC, forming an oxo- or hydroxo bridge between Mn1 and Ca[50, 51, 91], are discussed here based on the available possibility that O1 channel is the water channel responsible for the water substrate delivery during the S_2 to S_3 transition. We think that direct and smooth water insertion from O1 channel

to the binding site of Ox at OEC is not possible. The analysis of the timepoint structural data showed structural changes at 2F(50 μs) near the redox-active Y_Z due to the Y_Z oxidation. This event reported in Ibrahim et al.,[91] affected the interaction between Y_Z and H190 and provided the motive for the D1-E189 to move away from Ca, while still being ligated to Mn1. However, the movement of the D1-E189 was significant; it is still not enough to allow direct water delivery from O1 channel.

Based on the above hypothesis, we eliminate the carousel/ pivot mechanism[151]. It has been proposed that in the carousel mechanism, the water molecule is delivered through channel O4. Or through the Cl1 channel based on the recent M.D. simulations that showed waters W19 and 20 from channel O4 get exchanged from the bulk solvent via channel Cl1[120]. This mechanism also requires that the Mn cluster presents in the closed-cubane-like configuration (PI. Figure 23). However, the closed-cubane Mn cluster has not been observed in any reported XFEL study, neither at room temperature nor cryogenic[47, 50-52, 91]. The results in this study suggested alternative routes for Ox insertion. These alternative routes consider the Ox insertion is done via the binding of W3, which is one of the ligand waters to Ca, to the open coordination site of Mn1[91, 326]. Several theoretical studies and FTIR studies[315, 327] support this hypothesis. Therefore, the replacement of W3 could be via W4, which is likely replenished later through the penta-cluster waters (W26, 27, 28, 29, and 30) present at the beginning of the O1 channel (PII.3. Figure 3). The B-factor analysis of the four ligand waters (W1-W4) (PII.3. Supplementary Figure 8) showed that the B-factor of W4 is higher in all the time points data 2F(50 μs), 2F(150 μs), and 2F(400 μs) in comparison to the other ligand waters. The other option of W3 replacement is via W25, which is located near Y_Z and D1-E189 (PII.3. Figure 3). The W25 possible route is supported by the observation at 2F(50 μs) data, where a drop in the electron density of W25 is noted. This reduction in the electron density could be due to the oxidation of Yz, resulting in weakening the H-bond to Y_Z and the side chain of E189, which is likely facilitating the movement of W25 toward W3 position.

III.3.3. Identifying the possible pathway for proton release

During the S_2 - S_3 transition, one proton is released from OEC toward the bulk. Several studies[111, 126, 127, 317, 318, 328, 329] proposed the Cl1channal, O4 channel, or the Yz network to act as the proton release pathway. The current results of this study support more the Cl1 channel to serve as the proton egress pathway during the S_2 - S_3 transition.

The recent FTIR study by Shimizu et al.,[162] discussed the possibility of proton releasing through the O4 channel during the S_0 -S_1 transition. The proton transfer through the O4 channel has been suggested to a downhill proton transfer[317, 330]. However, during the S_1 to S_2 and S_2 to S_3 transition, the structural data[48, 51, 52] showed the disappearance of W20, which is located at the beginning of the O4 channel. This disappearance is either because of moving away or increasing its mobility resulting in disconnecting the hydrogen bonding network of the O4 channel. Therefore, releasing a proton from this side of the OEC during the S_2-S_3 transition would be unlikely to occur using the O4 channel if W20 is not present. However, further structural analysis by Kern et al.[51] demonstrated that W20 reappears again in S_0 state. Therefore, the O4 pathway could be the route for proton release during the S_0-S_1 transition, but not earlier.

The Y_Z network has also been proposed to act as the proton exit pathway[73, 124-127]. This suggestion was based on a well H-bond network connecting the Y_Z to the lumen via D1-N298. Our analysis showed that one of its waters (W501) detected in the cryogenic structure[126, 127] is missing in the RT structural data. This disappearance disconnects the hydrogen network (PII.3. Supplementary Figure 7) and makes the proton transfer is only possible through the D1-N298[120, 127]. Asparagine residues are usually unsuitable for accepting and releasing protons and require tautomerization or amide rotations to allow proton transfer through them[126]. Our current analysis did not show or support any structural changes to D1-N298 or other asparagine residues (D1-N301-303-322) in this network during the S_2-S_3 transition (PII.3. Supplementary Figure 12). Hence, the release of a proton from this network during the S_2-S_3 transition would be unlikely

Several studies have been proposed the Cl1 channel as the proton exit channel during the S_2-S_3 transtion[66, 111, 307, 328, 331]. This study reports apparent structural changes near its bottleneck region formed by D1-E65, -P66, -67, and D2-E312. Significant changes have been observed around D1-E65, D2-E312, and D1-R334 at 2F(150 μs), and reversed at 2F(250 μs). These changes suggest that these residues form a gate that controls the proton release through the channel (PII.3. Figure 6). The distance between D1-E65 and D2-E312 at the S_2-state is around 2.5 Å. This short distance indicates that D1-E65 and D2-E312 share a proton[111]. Furthermore, our analysis showed that D1-E65 is H-bonded to D1-N335, and as we mentioned before, asparagine residues are not considered suitable for proton relay. It is also observed that W119, which is located after the bottleneck, is H-bonded to D1-R334. We suggest that D1-R334 could act as a directional barrier with its positive charge (PII.3. Figures 5B and 6). These observations indicate that the Cl1 channel

is in a 'closed state' for proton egress at the S_2-state. At 2F(150 µs), we observed a rotation in the side chain of the D1-E65. This rotation results in structural rearrangements that destabilize the H-bond between the D1-E65 and D2-E312 and strengthen the H-bond between the D1-E65 and D1-R334 (PII.3. Figures 5B and 6). Concomitantly, W119 forms a strong H bond to D1-E65. These rearrangements switch the Cl1 channel to be open for an effective proton transfer to the other towards the bulk. Recently, it was reported that proton release from the protonated D1-D61 to a deprotonated D1-E65 is exothermic through one or two waters[111]. This indicates that D1-E65 can accept a proton from the OEC only after D1-E65/D2 -E312 releases a proton to the other side of the bottleneck (PII.3. Figure 6). The H-bond between D1-E65 and D1-R334 stabilizes the proton release and prevents the released proton from returning. The deprotonated D1-E65/E312 will attract the proton released from OEC through D1-D61. Hence at 2F(250 µs), the side chain of the D1-E65 rotates back to its original position.

These current observations cannot conclude precisely when the proton is released from the Cl1 channel to the bulk. The interaction between D1-E65 and D1-312 at 2F(150 µs) may indicate that a proton release from the gate already happened, as suggested by the fast refilling of the earlier deprotonated event[332]. Another explanation is that a proton is released from the gate concomitantly with Mn oxidation[329]. In general, these structural changes occur at 150 µs and 250µs after the second flash are most likely corresponding to the presence of multiple protonatable residues as supported by the reported pH dependency of the proton-coupled electron transfer (PCET) of Mn oxidation during the S_2 to S_3 transition[329, 334]. In the later FTIR study, two phases were detected during the S_2 to S_3 transition, only the late phase step (~ 350 µs) was affected by the pH variation, whereas the early phase (~100 µs) was not.[329] This likely indicates that the proton release is taking place during the late phase, concomitantly to the deprotonation of inserted water Ox.

III.3.4. The structural sequence of events during the S_2 to S_3 transition

Upon the S2 state formation after the first flash, shortening of the distance between Mn4 and O_{E333} was reported[91], which indicates Mn4 oxidation (PII.3. Figure 7A to 7B). This oxidation may strengthen the interaction between W19-O4 as the distance between these atoms becomes shortened. The later interaction may weaken the H-bond between W19 and W20, causing W20 to be either highly mobile or being moved far from its

positions. Therefore, the hydrogen network of the O4 channel is disconnected during S_2 -S_3 transition since no electron density for W20 is detected during S_2 -S_3 transition.

With the second flash, Yz oxidation occurs and triggers the significant movement of D1-E189 away from the Ca site. Specifically, at 150 μs after the 2nd flash, elongation in the distance between Mn1 and Mn4 is observed (PII.3. Figure 7C). At the same time, the side chain of D1-S169 rotates to be in a suitable geometry allowing H-bond interaction with W1(PII.3. Figures 4 and 7C). This step maybe because of the following: a proton is released from W1 via D1-D61 and becomes an OH^- and D1-61 becomes protonated. Then D1-S169 stabilizes the proton release and prevents the released proton from returning to W1 by sharing its proton with W1. At the same time scale, the rotation of the D1-E65 side chain occurs, causing structural rearrangements in the residue forming the gate at the Cl1 channel. These rearrangements make an 'open state' for proton release towards the bulk through the Cl1 channel (PII.3. Figure 7C).

By 250 μs after the 2nd flash, the observed changes at the gate are reversed, and D1-S169 moves to its original position. This may indicate that the gate is closed after D1-E65 becomes protonated again via D1-D61 through W40 and W150/W42. Increasing the distance between D1-S169 and W1(OH^-) can be explained by the protonation of W1 again, most probably via the newly inserted water, possibly W3. We assume that the inserted water needs to be bound to a metal ion first like Ca ion or Mn ion to facilitate its deprotonation before being inserted at the open coordination site of Mn1. The reported kinetic analysis combining Mn $K\beta_{1,3}$ XES and the time points crystal structural data[91] showed that the Mn1 oxidation is correlated with the newly inserted water. Hence, the W1(OH^-) protonation can occur from the newly inserted Ox. No significant structural changes are observed upon S_3-state 2F(200 ms) formation (PII.3. Figure 7D).

IV. Summary

The water oxidation catalyzed by the PSII upon light exposure releases electrons, protons, and molecular oxygen. The catalytic activity of PSII requires substrate water delivery and an efficient proton egress mechanism. Deciphering the water substrate pathway and tracking the change in the protonation state at the active catalytic site and the surrounding side chains during catalysis are essential to enhance our understanding of the mechanism. Protons egress is a crucial step for advancing the S-state of the OEC[157]. Proton's egress takes place during the S_1-S_2, S_2-S_3, S_3-S_0, and S_0-S_1 with stoichiometry 0:1:2:1[316, 357, 358]. My Ph.D. thesis aimed to elucidate the pathway of water insertion and proton release during the water oxidation reaction in PSII. For this purpose, three different strategies were pursued.

In the first part of my work (**PII.1**), a macroseeding protocol for the βDM-dPSIIcc has been developed (PII.1), resulting in growing a single large crystal of ~ 3 mm length in the long axis. These crystals pave the way for collecting structural data using neutron diffraction. Neutron crystallography is a powerful tool for directly locating the hydrogen atoms, assigning the protonation state, defining the hydrogen bonds, and understanding how the proton is transferred between residues and solvents[194-196]. For the first time, the neutron diffraction of these dPSIIcc macrocrystals soaked in D_2O was measured at the MaNDi instrument at the Spallation Neutron Source at Oak Ridge National Laboratory (ORNL, USA). The maximum observed resolution was about ~ 8.0 Å.

Improving the quality of these crystals is a crucial step for collecting high-resolution data. Therefore, in the second part, **PII.2**, the structure of the detergent-protein complex of βDM-dPSIIcc has been investigated by applying small-angle neutron scattering (SANS) with different contrast. The results showed that βDM is forming a monomolecular layer around the dPSIIcc. The DLS and SANS measurements for protein samples at a concentration range of 2-10 mg/ml PSII showed that all the measured

samples are monodisperse and free from aggregation. However, the SAXS data detected the presence of peak assigned for the free micelles of βDM, indicating that the detergent concentration in the studied protein samples is above the CSC. The presence of these free micelles during crystallization likely negatively affects the crystal's growth and, hence, the diffraction quality. This finding is crucial to optimize the βDM concentrations in the solution to avoid excess free micelle aggregates.

Finally, in the last study, **PII.3**, the structural dynamics in the water and proton channels connecting the OEC to the lumen during the S_2 to S_3 transition were investigated using serial femtosecond XFEL. A high-resolution data set was generated by combining data collected at RT throughout the Kok cycle to obtain a resolution of 1.89 Å. This high-resolution data enabled the identification of the regions in the channels with more mobility. Furthermore, it allowed modeling new waters within the channels in the S_2 to S_3 time point data. Analyzing the combined data and the individual time points data (2F, 2F 50 μs, 2F 150 μs, 2F 250 μs, and 2F 400 μs and 2F 200 ms) showed that waters occupied the O1 are more mobile than those in the Cl1 or O4 channels. Based on this information, we propose that the substrate water insertion into the open coordination site of Mn1 is delivered through O1channel. On the other hand, the proton release from the OEC to the bulk is likely facilitated via the more structured H-bond network of the Cl1 A channel. The structural changes observed around D1-E65, D2-E312, and D1-R334 at 150 μs after the 2^{nd} flash, suggested that these residues act as a proton gate to regulate releasing the proton through the Cl1 channel during the S_2 to S_3 transition. This work is a fundamental step toward understanding the mechanism of the water oxidation reaction in PSII.

V. Outlook

The work presented here added a milestone in understanding the water oxidation reaction in PSII by elucidating the possible pathway of water insertion and proton release. Nevertheless, a more precise assigning of the protonation states and the hydrogen bonds in the vicinity of the OEC are still required to uncover the exact mechanism of the deprotonation of the substrate waters. Therefore, growing a single large macrocrystal of the βDM-dPSIIcc (result PII.1) was a prerequisite step for collecting structural data using time-resolved neutron diffraction. This method can answer those questions undoubtedly. However, the current resolution achieved by these macrocrystals, 8 - 10 Å, doesn't allow valuable dataset collection by neutron crystallography.

Several factors are discussed here for optimizing the preparation and the crystallization to obtain better-diffracting crystals. The first important factor is substituting all titratable and non-titratable H atoms with D atoms in the protein. In this study, the neutron diffraction measurements were performed by soaking the crystal in D_2O buffer. This partial H/D exchange is known to allow only the substitution of the waters and the titratable H atoms, nearly 25% of all the H atoms present in any protein[362]. The proposed step, however challenging, will help significantly decrease the incoherent scattering background from H atoms and enhance the signal-to-noise ratio. However, approaching this step requires optimizing the growth of cyanobacteria in fully deuterated media. Furthermore, optimization for protein purification and crystallization will also be required. As discussed in PII.2, the structure analysis of the detergent-protein complex of βDM-dPSIIcc by applying SAXS detected the presence of free micelles in the protein solution. This result indicates that the used detergent concentration in the protein samples is above the CSC. In the light of this information, further optimization is required to adjust the detergent concentration of βDM to avoid having such free micelles during crystallization that may negatively affect the growth of the crystal and hence the

diffraction quality. Furthermore, SANS/SAXS measurements will be determined on C12E8-dPSIIcc at different detergent concentrations to verify the presence of free micelles.

The study **PII.3** investigated the structural dynamics in the water and proton channels connecting the OEC to the lumen during the S_2 to S_3 transition using serial femtosecond XFEL. The results suggested the substrate water insertion reaches through O1channel for the substrate water insertion. While the proton release from the OEC is most likely done through the Cl1 A channel. Furthermore, studies using serial femtosecond XFEL are ongoing to investigate the structural dynamics during the S_3 to S_0 transition and S_0 to S_1 transition. Here, deconvoluting the collected structural data of the different S-states is necessary. Still, it is also challenging since the S-state advancement is not perfect, leading to having mixed S-state populations. These studies will provide more and more insights into the mechanism of water oxidation by PSII.

VI. References

1. Bricker, T.; Burnap, R., The extrinsic proteins of photosystem II. *Photosystem II* **2005**, 95-120.
2. Planavsky, N. J.; Asael, D.; Hofmann, A.; Reinhard, C. T.; Lalonde, S. V.; Knudsen, A.; Wang, X.; Ossa, F. O.; Pecoits, E.; Smith, A. J., Evidence for oxygenic photosynthesis half a billion years before the Great Oxidation Event. *Nature Geoscience* **2014,** *7* (4), 283-286.
3. Fischer, W. W.; Hemp, J.; Johnson, J. E., Evolution of oxygenic photosynthesis. *Annual Review of Earth and Planetary Sciences* **2016,** *44*, 647-683.
4. Lubitz, W.; Chrysina, M.; Cox, N., Water oxidation in photosystem II. *Photosynthesis research* **2019,** *142* (1), 105-125.
5. Hamilton, T. L.; Bryant, D. A.; Macalady, J. L., The role of biology in planetary evolution: cyanobacterial primary production in low-oxygen Proterozoic oceans. *Environmental microbiology* **2016,** *18* (2), 325-340.
6. Shevela, D., Adventures with cyanobacteria: a personal perspective. *Frontiers in plant science* **2011,** *2*, 28.
7. Shevela, D.; Pishchalnikov, R. Y.; Eichacker, L. A., *Oxygenic photosynthesis in cyanobacteria*. CRC Press Boca Raton: 2013.
8. Sukenik, A.; Zohary, T.; Padisák, J., Cyanoprokaryota and other prokaryotic algae. **2009**.
9. Ke, B., *Photosynthesis photobiochemistry and photobiophysics*. Springer Science & Business Media: 2001; Vol. 10.
10. Vavilin, D. V.; Vermaas, W. F., Regulation of the tetrapyrrole biosynthetic pathway leading to heme and chlorophyll in plants and cyanobacteria. *Physiologia Plantarum* **2002,** *115* (1), 9-24.
11. Sui, S.-F., Structure of Phycobilisomes. *Annual Review of Biophysics* **2021,** *50*, 53-72.
12. Bryant, D. A., *The molecular biology of cyanobacteria*. Springer Science & Business Media: 2006; Vol. 1.
13. Kirilovsky, D.; Kerfeld, C. A., Cyanobacterial photoprotection by the orange carotenoid protein. *Nature plants* **2016,** *2* (12), 1-7.
14. Green, B. R., What happened to the Phycobilisome? *Biomolecules* **2019,** *9* (11), 748.
15. Kirilovsky, D.; Büchel, C., Evolution and function of light-harvesting antenna in oxygenic photosynthesis. *Advances in Botanical Research* **2019,** *91*, 247-293.
16. Zheng, L.; Zheng, Z.; Li, X.; Wang, G.; Zhang, K.; Wei, P.; Zhao, J.; Gao, N., Structural insight into the mechanism of energy transfer in cyanobacterial phycobilisomes. *Nature communications* **2021,** *12* (1), 1-11.

17. Watanabe, M.; Ikeuchi, M., Phycobilisome: architecture of a light-harvesting supercomplex. *Photosynthesis Research* **2013,** *116* (2-3), 265-276.
18. Frank, H.; Cogdell, R., 8.6 Light Capture in Photosynthesis. **2012**.
19. Goodwin, T. W.; Mercer, E. I., Introduction to plant biochemistry. **1990**.
20. George, D. M.; Vincent, A. S.; Mackey, H. R., An overview of anoxygenic phototrophic bacteria and their applications in environmental biotechnology for sustainable Resource recovery. *Biotechnology Reports* **2020**, e00563.
21. Allen, J. F., Origin of oxygenic photosynthesis from anoxygenic type I and Type II reaction centers. In *The Biophysics of Photosynthesis*, Springer: 2014; pp 433-450.
22. Chotewutmontri, P.; Barkan, A., Light-induced psbA translation in plants is triggered by photosystem II damage via an assembly-linked autoregulatory circuit. *Proceedings of the National Academy of Sciences* **2020,** *117* (35), 21775-21784.
23. Kern, J.; Renger, G., Photosystem II: Structure and mechanism of the water:plastoquinone oxidoreductase. *Photosynthesis Research* **2007,** *94* (2), 183-202.
24. Nugent, J. H., Oxygenic photosynthesis: electron transfer in photosystem I and photosystem II. *European journal of biochemistry* **1996,** *237* (3), 519-531.
25. Wollman, F.-A.; Minai, L.; Nechushtai, R., The biogenesis and assembly of photosynthetic proteins in thylakoid membranes1. *Biochimica Et Biophysica Acta-Bioenergetics* **1999,** *1411* (1), 21-85.
26. Kern, J. Structural and functional investigations of Photosystem II from Thermosynechococcus elongatus. Universitätsbibliothek, 2005.
27. Barber, J.; Iwata, S.; Satoh, K.; Wydrzynski, T., Photosystem II. The light driVen water: plastoquinone oxidoreductase. Satoh, K., Wydrzynski, TJ, Eds: 2005.
28. Satoh, K.; Wydrzynski, T. J., Introduction to photosystem II. In *Photosystem Ii*, Springer: 2005; pp 11-22.
29. Taiz, L.; Zeiger, E., *Plant Physiology*. Sinauer Associates: 2010.
30. Messinger, J.; Renger, G., Photosynthetic water splitting. *Primary processes of photosynthesis, Part* **2008,** *2*, 291-351.
31. Molina-Heredia, F. P.; Wastl, J.; Navarro, J. A.; Bendall, D. S.; Hervás, M.; Howe, C. J.; Miguel, A., A new function for an old cytochrome? *Nature* **2003,** *424* (6944), 33-34.
32. Cramer, W. A.; Hasan, S. S.; Yamashita, E., The Q cycle of cytochrome bc complexes: a structure perspective. *Biochimica et Biophysica Acta (BBA)-Bioenergetics* **2011,** *1807* (7), 788-802.
33. Grotjohann, I.; Fromme, P., Photosystem I. In *Encyclopedia of Biological Chemistry: Second Edition*, Elsevier Inc.: 2013; pp 503-507.
34. Wayne, R. O., *Plant cell biology: from astronomy to zoology*. Academic Press: 2009.
35. Caspy, I.; Borovikova-Sheinker, A.; Klaiman, D.; Shkolnisky, Y.; Nelson, N., The structure of a triple complex of plant photosystem I with ferredoxin and plastocyanin. *Nature plants* **2020,** *6* (10), 1300-1305.
36. Junge, W.; Nelson, N., ATP synthase. *Annual review of biochemistry* **2015,** *84*, 631-657.
37. Bassham, J. A.; Calvin, M., The path of carbon in photosynthesis. In *Die CO2-Assimilation/The Assimilation of Carbon Dioxide*, Springer: 1960; pp 884-922.
38. Lopez, F.; Barclay, G., Plant anatomy and physiology. In *Pharmacognosy*, Elsevier: 2017; pp 45-60.
39. Zouni, A.; Witt, H.-T.; Kern, J.; Fromme, P.; Krauss, N.; Saenger, W.; Orth, P., Crystal structure of photosystem II from Synechococcus elongatus at 3.8 Å resolution. *Nature* **2001,** *409* (6821), 739-743.

40. Kamiya, N.; Shen, J.-R., Crystal structure of oxygen-evolving photosystem II from Thermosynechococcus vulcanus at 3.7-Å resolution. *Proceedings of the National Academy of Sciences* **2003,** *100* (1), 98-103.
41. Loll, B.; Kern, J.; Saenger, W.; Zouni, A.; Biesiadka, J., Towards complete cofactor arrangement in the 3.0 Å resolution structure of photosystem II. *Nature* **2005,** *438* (7070), 1040-1044.
42. Kawakami, K.; Umena, Y.; Kamiya, N.; Shen, J.-R., Location of chloride and its possible functions in oxygen-evolving photosystem II revealed by X-ray crystallography. *Proceedings of the National Academy of Sciences* **2009,** *106* (21), 8567-8572.
43. Guskov, A.; Kern, J.; Gabdulkhakov, A.; Broser, M.; Zouni, A.; Saenger, W., Cyanobacterial photosystem II at 2.9-Å resolution and the role of quinones, lipids, channels and chloride. *Nature structural & molecular biology* **2009,** *16* (3), 334-342.
44. Hellmich, J.; Bommer, M.; Burkhardt, A.; Ibrahim, M.; Kern, J.; Meents, A.; Müh, F.; Dobbek, H.; Zouni, A., Native-like photosystem II superstructure at 2.44 Å resolution through detergent extraction from the protein crystal. *Structure* **2014,** *22* (11), 1607-1615.
45. Tanaka, A.; Fukushima, Y.; Kamiya, N., Two Different Structures of the Oxygen-Evolving Complex in the Same Polypeptide Frameworks of Photosystem II. *J Am Chem Soc* **2017,** *139* (5), 1718-1721.
46. Kern, J.; Tran, R.; Alonso-Mori, R.; Koroidov, S.; Echols, N.; Hattne, J.; Ibrahim, M.; Gul, S.; Laksmono, H.; Sierra, R. G.; Gildea, G. H.; Hellmich, J.; Lassalle-Kaiser, B.; Chatterjee, R.; Brewster, A. S.; Stan, C. A.; Glöckner, C.; Lampe, A.; DiFiore, D.; Milathianaki, D.; Fry, A. R.; Seibert, M. M.; Koglin, J. E.; Gallo, E.; Uhlig, J.; Sokaras, D.; Weng, T.-C.; Zwart, P. H.; Skinner, D. E.; Bogan, M. J.; Messerschmidt, M.; Glatzel, p.; Williams, G. J.; Boutet, S.; Adams, P. D.; Zouni, A.; Messinger, J.; K. Sauter, N.; Bergmann, U.; Yano, J.; Yachandra , V. K., Taking snapshots of photosynthetic water oxidation using femtosecond X-ray diffraction and spectroscopy. *Nature communications* **2014,** *5* (1), 1-11.
47. Suga, M.; Akita, F.; Hirata, K.; Ueno, G.; Murakami, H.; Nakajima, Y.; Shimizu, T.; Yamashita, K.; Yamamoto, M.; Ago, H.; Shen, J. R., Native structure of photosystem II at 1.95 Å resolution viewed by femtosecond X-ray pulses. *Nature* **2015,** *517* (7532), 99-103.
48. Young, I. D.; Ibrahim, M.; Chatterjee, R.; Gul, S.; Fuller, F.; Koroidov, S.; Brewster, A. S.; Tran, R.; Alonso-Mori, R.; Kroll, T.; Michels-Clark, T.; Laksmono, H.; Sierra, R. G.; Stan, C. A.; Hussein, R.; Zhang, M.; Douthit, L.; Kubin, M.; de Lichtenberg, C.; Long Vo, P.; Nilsson, H.; Cheah, M. H.; Shevela, D.; Saracini, C.; Bean, M. A.; Seuffert, I.; Sokaras, D.; Weng, T. C.; Pastor, E.; Weninger, C.; Fransson, T.; Lassalle, L.; Brauer, P.; Aller, P.; Docker, P. T.; Andi, B.; Orville, A. M.; Glownia, J. M.; Nelson, S.; Sikorski, M.; Zhu, D.; Hunter, M. S.; Lane, T. J.; Aquila, A.; Koglin, J. E.; Robinson, J.; Liang, M.; Boutet, S.; Lyubimov, A. Y.; Uervirojnangkoorn, M.; Moriarty, N. W.; Liebschner, D.; Afonine, P. V.; Waterman, D. G.; Evans, G.; Wernet, P.; Dobbek, H.; Weis, W. I.; Brunger, A. T.; Zwart, P. H.; Adams, P. D.; Zouni, A.; Messinger, J.; Bergmann, U.; Sauter, N. K.; Kern, J.; Yachandra, V. K.; Yano, J., Structure of photosystem II and substrate binding at room temperature. *Nature* **2016,** *540* (7633), 453-457.
49. Kern, J.; Alonso-Mori, R.; Tran, R.; Hattne, J.; Gildea, R. J.; Echols, N.; Glockner, C.; Hellmich, J.; Laksmono, H.; Sierra, R. G.; Lassalle-Kaiser, B.; Koroidov, S.; Lampe, A.; Han, G.; Gul, S.; Difiore, D.; Milathianaki, D.; Fry, A. R.; Miahnahri, A.; Schafer, D. W.; Messerschmidt, M.; Seibert, M. M.; Koglin, J. E.; Sokaras, D.; Weng, T. C.; Sellberg, J.; Latimer, M. J.; Grosse-Kunstleve, R. W.; Zwart, P. H.; White, W. E.; Glatzel, P.; Adams, P. D.; Bogan, M. J.; Williams, G. J.; Boutet, S.;

Messinger, J.; Zouni, A.; Sauter, N. K.; Yachandra, V. K.; Bergmann, U.; Yano, J., Simultaneous femtosecond X-ray spectroscopy and diffraction of photosystem II at room temperature. *Science* **2013,** *340* (6131), 491-5.
50. Suga, M.; Akita, F.; Sugahara, M.; Kubo, M.; Nakajima, Y.; Nakane, T.; Yamashita, K.; Umena, Y.; Nakabayashi, M.; Yamane, T.; Nakano, T.; Suzuki, M.; Masuda, T.; Inoue, S.; Kimura, T.; Nomura, T.; Yonekura, S.; Yu, L. J.; Sakamoto, T.; Motomura, T.; Chen, J. H.; Kato, Y.; Noguchi, T.; Tono, K.; Joti, Y.; Kameshima, T.; Hatsui, T.; Nango, E.; Tanaka, R.; Naitow, H.; Matsuura, Y.; Yamashita, A.; Yamamoto, M.; Nureki, O.; Yabashi, M.; Ishikawa, T.; Iwata, S.; Shen, J. R., Light-induced structural changes and the site of O=O bond formation in PSII caught by XFEL. *Nature* **2017,** *543* (7643), 131-135.
51. Kern, J.; Chatterjee, R.; Young, I. D.; Fuller, F. D.; Lassalle, L.; Ibrahim, M.; Gul, S.; Fransson, T.; Brewster, A. S.; Alonso-Mori, R.; Hussein, R.; Zhang, M.; Douthit, L.; de Lichtenberg, C.; Cheah, M. H.; Shevela, D.; Wersig, J.; Seuffert, I.; Sokaras, D.; Pastor, E.; Weninger, C.; Kroll, T.; Sierra, R. G.; Aller, P.; Butryn, A.; Orville, A. M.; Liang, M.; Batyuk, A.; Koglin, J. E.; Carbajo, S.; Boutet, S.; Moriarty, N. W.; Holton, J. M.; Dobbek, H.; Adams, P. D.; Bergmann, U.; Sauter, N. K.; Zouni, A.; Messinger, J.; Yano, J.; Yachandra, V. K., Structures of the intermediates of Kok's photosynthetic water oxidation clock. *Nature* **2018,** *563* (7731), 421-425.
52. Suga, M.; Akita, F.; Yamashita, K.; Nakajima, Y.; Ueno, G.; Li, H.; Yamane, T.; Hirata, K.; Umena, Y.; Yonekura, S.; Yu, L.-J.; Murakami, H.; Nomura, T.; Kimura, T.; Kubo, M.; Baba, S.; Kumasaka, T.; Tono, K.; Yabashi, M.; Isobe, H.; Yamaguchi, K.; Yamamoto, M.; Ago, H.; Shen, J.-R., An oxyl/oxo mechanism for oxygen-oxygen coupling in PSII revealed by an x-ray free-electron laser. *Science* **2019,** *366* (6463), 334-338.
53. Zouni, A.; Kern, J.; Frank, J.; Hellweg, T.; Behlke, J.; Saenger, W.; Irrgang, K.-D., Size determination of cyanobacterial and higher plant photosystem II by gel permeation chromatography, light scattering, and ultracentrifugation. *Biochemistry* **2005,** *44* (11), 4572-4581.
54. Roose, J. L.; Wegener, K. M.; Pakrasi, H. B., The extrinsic proteins of photosystem II. *Photosynthesis research* **2007,** *92* (3), 369-387.
55. Müh, F.; Zouni, A., Cytochrome b 559 in photosystem II. In *Cytochrome complexes: evolution, structures, energy transduction, and signaling*, Springer: 2016; pp 143-175.
56. Chu, H.-A.; Chiu, Y.-F., The roles of cytochrome b559 in assembly and photoprotection of photosystem II revealed by site-directed mutagenesis studies. *Frontiers in plant science* **2016,** *6*, 1261.
57. Pospíšil, P., Enzymatic function of cytochrome b559 in photosystem II. *Journal of Photochemistry and Photobiology B: Biology* **2011,** *104* (1-2), 341-347.
58. Ifuku, K., Localization and functional characterization of the extrinsic subunits of photosystem II: an update. *Bioscience, biotechnology, and biochemistry* **2015,** *79* (8), 1223-1231.
59. Linke, K.; Ho, F. M., Water in Photosystem II: structural, functional and mechanistic considerations. *Biochimica et Biophysica Acta (BBA)-Bioenergetics* **2014,** *1837* (1), 14-32.
60. Vogt, L.; Vinyard, D. J.; Khan, S.; Brudvig, G. W., Oxygen-evolving complex of Photosystem II: an analysis of second-shell residues and hydrogen-bonding networks. *Current opinion in chemical biology* **2015,** *25*, 152-158.
61. Bommer, M.; Coates, L.; Dau, H.; Zouni, A.; Dobbek, H., Protein crystallization and initial neutron diffraction studies of the photosystem II subunit PsbO. *Acta Crystallographica Section F: Structural Biology Communications* **2017,** *73* (9), 525-531.

62. Bondar, A.-N.; Dau, H., Extended protein/water H-bond networks in photosynthetic water oxidation. *Biochimica et Biophysica Acta (BBA)-Bioenergetics* **2012,** *1817* (8), 1177-1190.
63. De Las Rivas, J.; Barber, J., Analysis of the structure of the PsbO protein and its implications. *Photosynthesis Research* **2004,** *81* (3), 329-343.
64. Popelkova, H.; Yocum, C. F., PsbO, the manganese-stabilizing protein: Analysis of the structure–function relations that provide insights into its role in photosystem II. *Journal of Photochemistry and Photobiology B: Biology* **2011,** *104* (1-2), 179-190.
65. Roose, J. L.; Frankel, L. K.; Mummadisetti, M. P.; Bricker, T. M., The extrinsic proteins of photosystem II: update. *Planta* **2016,** *243* (4), 889-908.
66. Guerra, F.; Siemers, M.; Mielack, C.; Bondar, A. N., Dynamics of Long-Distance Hydrogen-Bond Networks in Photosystem II. *J Phys Chem B* **2018,** *122* (17), 4625-4641.
67. Williamson, A. K., Structural and functional aspects of the MSP (PsbO) and study of its differences in thermophilic versus mesophilic organisms. *Photosynthesis research* **2008,** *98* (1), 365-389.
68. Yi, X.; McChargue, M.; Laborde, S.; Frankel, L. K.; Bricker, T. M., The manganese-stabilizing protein is required for photosystem II assembly/stability and photoautotrophy in higher plants. *Journal of Biological Chemistry* **2005,** *280* (16), 16170-16174.
69. Veerman, J.; Bentley, F. K.; Eaton-Rye, J. J.; Mullineaux, C. W.; Vasil'ev, S.; Bruce, D., The PsbU subunit of photosystem ii stabilizes energy transfer and primary photochemistry in the phycobilisome− photosystem ii assembly of synechocystis sp. PCC 6803. *Biochemistry* **2005,** *44* (51), 16939-16948.
70. Guerrero, F.; Sedoud, A.; Kirilovsky, D.; Rutherford, A. W.; Ortega, J. M.; Roncel, M., A high redox potential form of cytochrome c550 in photosystem II from Thermosynechococcus elongatus. *Journal of Biological Chemistry* **2011,** *286* (8), 5985-5994.
71. Roncel, M.; Kirilovsky, D.; Guerrero, F.; Serrano, A.; Ortega, J. M., Photosynthetic cytochrome c550. *Biochimica et Biophysica Acta (BBA)-Bioenergetics* **2012,** *1817* (8), 1152-1163.
72. Ishikita, H.; Knapp, E.-W., Oxidation of the non-heme iron complex in photosystem II. *Biochemistry* **2005,** *44* (45), 14772-14783.
73. Umena, Y.; Kawakami, K.; Shen, J.-R.; Kamiya, N., Crystal structure of oxygen-evolving photosystem II at a resolution of 1.9 Å. *Nature* **2011,** *473* (7345), 55-60.
74. Saito, K.; Rutherford, A. W.; Ishikita, H., Mechanism of tyrosine D oxidation in Photosystem II. *Proceedings of the National Academy of Sciences* **2013,** *110* (19), 7690-7695.
75. Müh, F.; Glöckner, C.; Hellmich, J.; Zouni, A., Light-induced quinone reduction in photosystem II. *Biochimica et Biophysica Acta (BBA)-Bioenergetics* **2012,** *1817* (1), 44-65.
76. Singh, N. K.; Sonani, R. R.; Rastogi, R. P.; Madamwar, D., The phycobilisomes: an early requisite for efficient photosynthesis in cyanobacteria. *EXCLI journal* **2015,** *14*, 268.
77. Renger, G.; Renger, T., Photosystem II: the machinery of photosynthetic water splitting. *Photosynthesis research* **2008,** *98* (1), 53-80.
78. Raszewski, G.; Renger, T., Light harvesting in photosystem II core complexes is limited by the transfer to the trap: can the core complex turn into a photoprotective mode? *Journal of the American Chemical Society* **2008,** *130* (13), 4431-4446.
79. Klimov, V.; Klevanik, A.; Shuvalov, V., Reduction of pheophytin in the primary light reaction of photosystem II. *FEBS letters* **1977,** *82* (2), 183-186.

80. Rappaport, F.; Diner, B. A., Primary photochemistry and energetics leading to the oxidation of the (Mn) 4Ca cluster and to the evolution of molecular oxygen in Photosystem II. *Coordination Chemistry Reviews* **2008,** *252* (3-4), 259-272.
81. Faller, P.; Debus, R. J.; Brettel, K.; Sugiura, M.; Rutherford, A. W.; Boussac, A., Rapid formation of the stable tyrosyl radical in photosystem II. *Proceedings of the National Academy of Sciences* **2001,** *98* (25), 14368-14373.
82. Cox, N.; Pantazis, D. A.; Lubitz, W., Current understanding of the mechanism of water oxidation in photosystem II and its relation to XFEL data. *Annual review of biochemistry* **2020,** *89*, 795-820.
83. Joliot, P.; Barbieri, G.; Chabaud, R., Un nouveau modele des centres photochimiques du systeme II. *Photochemistry and Photobiology* **1969,** *10* (5), 309-329.
84. Shevela, D.; Nöring, B.; Koroidov, S.; Shutova, T.; Samuelsson, G.; Messinger, J., Efficiency of photosynthetic water oxidation at ambient and depleted levels of inorganic carbon. *Photosynthesis research* **2013,** *117* (1), 401-412.
85. Kok, B.; Forbush, B.; McGloin, M., Cooperation of charges in photosynthetic O2 evolution–I. A linear four step mechanism. *Photochemistry and Photobiology* **1970,** *11* (6), 457-475.
86. Dau, H.; Haumann, M., The manganese complex of photosystem II in its reaction cycle—basic framework and possible realization at the atomic level. *Coordination Chemistry Reviews* **2008,** *252* (3-4), 273-295.
87. Styring, S.; Rutherford, A. W., In the oxygen-evolving complex of photosystem II the S0 state is oxidized to the S1 state by D+ (signal IIslow). *Biochemistry* **1987,** *26* (9), 2401-2405.
88. Vass, I.; Styring, S., pH-dependent charge equilibria between tyrosine-D and the S states in photosystem II. Estimation of relative midpoint redox potentials. *Biochemistry* **1991,** *30* (3), 830-839.
89. Messinger, J.; Renger, G., Generation, oxidation by the oxidized form of the tyrosine of polypeptide D2, and possible electronic configuration of the redox states S0, S-1, and S-2 of the water oxidase in isolated spinach thylakoids. *Biochemistry* **1993,** *32* (36), 9379-9386.
90. Ishikita, H.; Knapp, E.-W., Function of redox-active tyrosine in photosystem II. *Biophysical journal* **2006,** *90* (11), 3886-3896.
91. Ibrahim, M.; Fransson, T.; Chatterjee, R.; Cheah, M. H.; Hussein, R.; Lassalle, L.; Sutherlin, K. D.; Young, I. D.; Fuller, F. D.; Gul, S.; Kim, I. S.; Simon, P. S.; de Lichtenberg, C.; Chernev, P.; Bogacz, I.; Pham, C. C.; Orville, A. M.; Saichek, N.; Northen, T.; Batyuk, A.; Carbajo, S.; Alonso-Mori, R.; Tono, K.; Owada, S.; Bhowmick, A.; Bolotovsky, R.; Mendez, D.; Moriarty, N. W.; Holton, J. M.; Dobbek, H.; Brewster, A. S.; Adams, P. D.; Sauter, N. K.; Bergmann, U.; Zouni, A.; Messinger, J.; Kern, J.; Yachandra, V. K.; Yano, J., Untangling the sequence of events during the S_2 --> S_3 transition in photosystem II and implications for the water oxidation mechanism. *Proc Natl Acad Sci U S A* **2020,** *117* (23), 12624-12635.
92. Glöckner, C.; Kern, J.; Broser, M.; Zouni, A.; Yachandra, V.; Yano, J., Structural changes of the oxygen-evolving complex in photosystem II during the catalytic cycle. *Journal of Biological Chemistry* **2013,** *288* (31), 22607-22620.
93. Yano, J.; Pushkar, Y.; Glatzel, P.; Lewis, A.; Sauer, K.; Messinger, J.; Bergmann, U.; Yachandra, V., High-resolution Mn EXAFS of the oxygen-evolving complex in photosystem II: structural implications for the Mn4Ca cluster. *Journal of the American Chemical Society* **2005,** *127* (43), 14974-14975.
94. Kusunoki, M., S1-state Mn4Ca complex of Photosystem II exists in equilibrium between the two most-stable isomeric substates: XRD and EXAFS evidence. *Journal of Photochemistry and Photobiology B: Biology* **2011,** *104* (1-2), 100-110.

95. Yano, J.; Kern, J.; Irrgang, K.-D.; Latimer, M. J.; Bergmann, U.; Glatzel, P.; Pushkar, Y.; Biesiadka, J.; Loll, B.; Sauer, K., X-ray damage to the Mn4Ca complex in single crystals of photosystem II: a case study for metalloprotein crystallography. *Proceedings of the National Academy of Sciences* **2005,** *102* (34), 12047-12052.
96. Grabolle, M.; Haumann, M.; Müller, C.; Liebisch, P.; Dau, H., Rapid loss of structural motifs in the manganese complex of oxygenic photosynthesis by X-ray irradiation at 10–300 K. *Journal of Biological Chemistry* **2006,** *281* (8), 4580-4588.
97. Tanaka, A.; Fukushima, Y.; Kamiya, N., Two different structures of the oxygen-evolving complex in the same polypeptide frameworks of photosystem II. *J. Am. Chem. Soc.* **2017,** *139* (5), 1718-1721.
98. Hattne, J.; Echols, N.; Tran, R.; Kern, J.; Gildea, R. J.; Brewster, A. S.; Alonso-Mori, R.; Glockner, C.; Hellmich, J.; Laksmono, H.; Sierra, R. G.; Lassalle-Kaiser, B.; Lampe, A.; Han, G.; Gul, S.; DiFiore, D.; Milathianaki, D.; Fry, A. R.; Miahnahri, A.; White, W. E.; Schafer, D. W.; Seibert, M. M.; Koglin, J. E.; Sokaras, D.; Weng, T. C.; Sellberg, J.; Latimer, M. J.; Glatzel, P.; Zwart, P. H.; Grosse-Kunstleve, R. W.; Bogan, M. J.; Messerschmidt, M.; Williams, G. J.; Boutet, S.; Messinger, J.; Zouni, A.; Yano, J.; Bergmann, U.; Yachandra, V. K.; Adams, P. D.; Sauter, N. K., Accurate macromolecular structures using minimal measurements from X-ray free-electron lasers. *Nat Methods* **2014,** *11* (5), 545-8.
99. Kern, J.; Yachandra, V. K.; Yano, J., Metalloprotein structures at ambient conditions and in real-time: Biological crystallography and spectroscopy using X-ray free electron lasers. *Current opinion in structural biology* **2015,** *34*, 87-98.
100. Yano, J.; Yachandra, V., Mn_4Ca cluster in photosynthesis: where and how water is oxidized to dioxygen. *Chemical reviews* **2014,** *114* (8), 4175-4205.
101. Vinyard, D. J.; Brudvig, G. W., Progress Toward a Molecular Mechanism of Water Oxidation in Photosystem II. *Annu Rev Phys Chem* **2017,** *68* (0), 101-116.
102. Murray, J. W.; Barber, J., Structural characteristics of channels and pathways in photosystem II including the identification of an oxygen channel. *J Struct Biol* **2007,** *159* (2), 228-37.
103. Ho, F. M.; Styring, S., Access channels and methanol binding site to the CaMn4 cluster in Photosystem II based on solvent accessibility simulations, with implications for substrate water access. *Biochim Biophys Acta* **2008,** *1777* (2), 140-53.
104. Vassiliev, S.; Comte, P.; Mahboob, A.; Bruce, D., Tracking the flow of water through photosystem II using molecular dynamics and streamline tracing. *Biochemistry* **2010,** *49* (9), 1873-81.
105. Vassiliev, S.; Zaraiskaya, T.; Bruce, D., Exploring the energetics of water permeation in photosystem II by multiple steered molecular dynamics simulations. *Biochim Biophys Acta* **2012,** *1817* (9), 1671-8.
106. Sakashita, N.; Ishikita, H.; Saito, K., Rigidly hydrogen-bonded water molecules facilitate proton transfer in photosystem II. *Physical Chemistry Chemical Physics* **2020,** *22* (28), 15831-15841.
107. Stuchebrukhov, A. A., Mechanisms of proton transfer in proteins: localized charge transfer versus delocalized soliton transfer. *Physical Review E* **2009,** *79* (3), 031927.
108. Schutz, C. N.; Warshel, A., The low barrier hydrogen bond (LBHB) proposal revisited: The case of the Asp⋯ His pair in serine proteases. *Proteins: Structure, Function, and Bioinformatics* **2004,** *55* (3), 711-723.
109. Perrin, C. L.; Nielson, J. B., "Strong" hydrogen bonds in chemistry and biology. *Annual review of physical chemistry* **1997,** *48* (1), 511-544.
110. Ishikita, H.; Saito, K., Proton transfer reactions and hydrogen-bond networks in protein environments. *Journal of The Royal Society Interface* **2014,** *11* (91), 20130518.

111. Kuroda, H.; Kawashima, K.; Ueda, K.; Ikeda, T.; Saito, K.; Ninomiya, R.; Hida, C.; Takahashi, Y.; Ishikita, H., Proton transfer pathway from the oxygen-evolving complex in photosystem II substantiated by extensive mutagenesis. *Biochimica et Biophysica Acta (BBA) - Bioenergetics* **2021,** *1862* (1), 148329.
112. Nakamura, A.; Ishida, T.; Kusaka, K.; Yamada, T.; Fushinobu, S.; Tanaka, I.; Kaneko, S.; Ohta, K.; Tanaka, H.; Inaka, K., "Newton's cradle" proton relay with amide–imidic acid tautomerization in inverting cellulase visualized by neutron crystallography. *Science advances* **2015,** *1* (7), e1500263.
113. Miyake, T.; Rolandi, M., Grotthuss mechanisms: from proton transport in proton wires to bioprotonic devices. *Journal of Physics: Condensed Matter* **2015,** *28* (2), 023001.
114. Sakashita, N.; Watanabe, H. C.; Ikeda, T.; Saito, K.; Ishikita, H., Origins of Water Molecules in the Photosystem II Crystal Structure. *Biochemistry* **2017,** *56* (24), 3049-3057.
115. Ho, F. M.; Styring, S., Access channels and methanol binding site to the $CaMn_4$ cluster in Photosystem II based on solvent accessibility simulations, with implications for substrate water access. *Biochim. Biophys. Acta* **2008,** *1777* (2), 140-53.
116. Murray, J. W.; Barber, J., Structural characteristics of channels and pathways in photosystem II including the identification of an oxygen channel. *J. Struct. Biol.* **2007,** *159* (2), 228-37.
117. Gabdulkhakov, A.; Guskov, A.; Broser, M.; Kern, J.; Muh, F.; Saenger, W.; Zouni, A., Probing the accessibility of the Mn_4Ca cluster in photosystem II: channels calculation, noble gas derivatization, and cocrystallization with DMSO. *Structure* **2009,** *17* (9), 1223-34.
118. Vassiliev, S.; Zaraiskaya, T.; Bruce, D., Exploring the energetics of water permeation in photosystem II by multiple steered molecular dynamics simulations. *Biochim. Biophys. Acta* **2012,** *1817* (9), 1671-8.
119. Ogata, K.; Yuki, T.; Hatakeyama, M.; Uchida, W.; Nakamura, S., All-atom molecular dynamics simulation of photosystem II embedded in thylakoid membrane. *J Am Chem Soc* **2013,** *135* (42), 15670-3.
120. Sakashita, N.; Watanabe, H. C.; Ikeda, T.; Saito, K.; Ishikita, H., Origins of water molecules in the photosystem II crystal structure. *Biochemistry* **2017,** *56* (24), 3049-3057.
121. Weisz, D. A.; Gross, M. L.; Pakrasi, H. B., Reactive oxygen species leave a damage trail that reveals water channels in Photosystem II. *Sci. Adv.* **2017,** *3*, eaao3013.
122. Ho, F. M.; Styring, S., Access channels and methanol binding site to the $CaMn_4$ cluster in Photosystem II based on solvent accessibility simulations, with implications for substrate water access. *Biochim. Biophys. Acta* **2008,** *1777* (2), 140-153.
123. Rivalta, I.; Amin, M.; Luber, S.; Vassiliev, S.; Pokhrel, R.; Umena, Y.; Kawakami, K.; Shen, J.-R.; Kamiya, N.; Bruce, D.; Brudvig, G. W.; Gunner, M. R.; Batista, V. S., Structural–Functional Role of Chloride in Photosystem II. *Biochemistry* **2011,** *50* (29), 6312-6315.
124. Saito, K.; Ishida, T.; Sugiura, M.; Kawakami, K.; Umena, Y.; Kamiya, N.; Shen, J.-R.; Ishikita, H., Distribution of the Cationic State over the Chlorophyll Pair of the Photosystem II Reaction Center. *Journal of the American Chemical Society* **2011,** *133* (36), 14379-14388.
125. Nakamura, S.; Nagao, R.; Takahashi, R.; Noguchi, T., Fourier transform infrared detection of a polarizable proton trapped between photooxidized tyrosine Y_Z and a coupled histidine in photosystem II: relevance to the proton transfer mechanism of water oxidation. *Biochemistry* **2014,** *53* (19), 3131-3144.

126. Chrysina, M.; de Mendonça Silva, J. C.; Zahariou, G.; Pantazis, D. A.; Ioannidis, N., Proton translocation via tautomerization of Asn298 during the S_2–S_3 state transition in the oxygen-evolving complex of photosystem II. *The Journal of Physical Chemistry B* **2019,** *123* (14), 3068-3078.
127. Nagao, R.; Ueoka-Nakanishi, H.; Noguchi, T., D1-Asn-298 in photosystem II is involved in a hydrogen-bond network near the redox-active tyrosine Y_Z for proton exit during water oxidation. *J Biol Chem* **2017,** *292* (49), 20046-20057.
128. Åhrling, K. A.; Peterson, S.; Styring, S., An oscillating manganese electron paramagnetic resonance signal from the S0 state of the oxygen evolving complex in photosystem II. *Biochemistry* **1997,** *36* (43), 13148-13152.
129. Messinger, J.; Nugent, J. H.; Evans, M. C., Detection of an EPR multiline signal for the S0* state in photosystem II. *Biochemistry* **1997,** *36* (37), 11055-11060.
130. Messinger, J.; Robblee, J. H.; Yu, W. O.; Sauer, K.; Yachandra, V. K.; Klein, M. P., The S0 state of the oxygen-evolving complex in photosystem II is paramagnetic: detection of an EPR multiline signal. *Journal of the American Chemical Society* **1997,** *119* (46), 11349-11350.
131. Peloquin, J. M.; Campbell, K. A.; Randall, D. W.; Evanchik, M. A.; Pecoraro, V. L.; Armstrong, W. H.; Britt, R. D., 55Mn ENDOR of the S2-state multiline EPR signal of photosystem II: implications on the structure of the tetranuclear Mn cluster. *Journal of the American Chemical Society* **2000,** *122* (44), 10926-10942.
132. Britt, R. D.; Campbell, K. A.; Peloquin, J. M.; Gilchrist, M. L.; Aznar, C. P.; Dicus, M. M.; Robblee, J.; Messinger, J., Recent pulsed EPR studies of the photosystem II oxygen-evolving complex: implications as to water oxidation mechanisms. *Biochimica et Biophysica Acta (BBA)-Bioenergetics* **2004,** *1655*, 158-171.
133. Haddy, A., EPR spectroscopy of the manganese cluster of photosystem II. *Photosynthesis research* **2007,** *92* (3), 357-368.
134. Kulik, L. V.; Epel, B.; Lubitz, W.; Messinger, J., Electronic structure of the Mn4O x Ca cluster in the S0 and S2 States of the oxygen-evolving complex of photosystem II based on pulse 55Mn-ENDOR and EPR spectroscopy. *Journal of the American Chemical Society* **2007,** *129* (44), 13421-13435.
135. Navarro, M. P.; Ames, W. M.; Nilsson, H.; Lohmiller, T.; Pantazis, D. A.; Rapatskiy, L.; Nowaczyk, M. M.; Neese, F.; Boussac, A.; Messinger, J., Ammonia binding to the oxygen-evolving complex of photosystem II identifies the solvent-exchangeable oxygen bridge (μ-oxo) of the manganese tetramer. *Proceedings of the National Academy of Sciences* **2013,** *110* (39), 15561-15566.
136. Debus, R. J., Protein ligation of the photosynthetic oxygen-evolving center. *Coordination chemistry reviews* **2008,** *252* (3), 244-258.
137. Noguchi, T., FTIR detection of water reactions in the oxygen-evolving centre of photosystem II. *Philosophical Transactions of the Royal Society of London B: Biological Sciences* **2008,** *363* (1494), 1189-1195.
138. Noguchi, T., Fourier transform infrared analysis of the photosynthetic oxygen-evolving center. *Coordination Chemistry Reviews* **2008,** *252* (3), 336-346.
139. Noguchi, T., Fourier transform infrared difference and time-resolved infrared detection of the electron and proton transfer dynamics in photosynthetic water oxidation. *Biochimica et Biophysica Acta (BBA)-Bioenergetics* **2015,** *1847* (1), 35-45.
140. Haumann, M.; Müller, C.; Liebisch, P.; Iuzzolino, L.; Dittmer, J.; Grabolle, M.; Neisius, T.; Meyer-Klaucke, W.; Dau, H., Structural and oxidation state changes of the photosystem II manganese complex in four transitions of the water oxidation cycle (S0→ S1, S1→ S2, S2→ S3, and S3, 4→ S0) characterized by X-ray absorption spectroscopy at 20 K and room temperature. *Biochemistry* **2005,** *44* (6), 1894-1908.

141. Yano, J.; Kern, J.; Sauer, K.; Latimer, M. J.; Pushkar, Y.; Biesiadka, J.; Loll, B.; Saenger, W.; Messinger, J.; Zouni, A., Where water is oxidized to dioxygen: structure of the photosynthetic Mn4Ca cluster. *Science* **2006,** *314* (5800), 821-825.
142. Dau, H.; Grundmeier, A.; Loja, P.; Haumann, M., On the structure of the manganese complex of photosystem II: extended-range EXAFS data and specific atomic-resolution models for four S-states. *Philosophical Transactions of the Royal Society of London B: Biological Sciences* **2008,** *363* (1494), 1237-1244.
143. Pushkar, Y.; Yano, J.; Sauer, K.; Boussac, A.; Yachandra, V. K., Structural changes in the Mn4Ca cluster and the mechanism of photosynthetic water splitting. *Proceedings of the National Academy of Sciences* **2008,** *105* (6), 1879-1884.
144. Sauer, K.; Yano, J.; Yachandra, V. K., X-ray spectroscopy of the photosynthetic oxygen-evolving complex. *Coordination chemistry reviews* **2008,** *252* (3), 318-335.
145. Yano, J.; Yachandra, V. K., Where water is oxidized to dioxygen: structure of the photosynthetic Mn4Ca cluster from X-ray spectroscopy. *Inorganic Chemistry* **2008,** *47* (6), 1711.
146. Grundmeier, A.; Dau, H., Structural models of the manganese complex of photosystem II and mechanistic implications. *Biochimica et Biophysica Acta (BBA)-Bioenergetics* **2012,** *1817* (1), 88-105.
147. Ames, W.; Pantazis, D. A.; Krewald, V.; Cox, N.; Messinger, J.; Lubitz, W.; Neese, F., Theoretical evaluation of structural models of the S2 state in the oxygen evolving complex of photosystem II: protonation states and magnetic interactions. *Journal of the American Chemical Society* **2011,** *133* (49), 19743-19757.
148. Corry, T. A.; O'Malley, P. J., Proton isomers rationalize the high-and low-spin forms of the S2 state intermediate in the water-oxidizing reaction of photosystem II. *The journal of physical chemistry letters* **2019,** *10* (17), 5226-5230.
149. Siegbahn, P. E., The S 2 to S 3 transition for water oxidation in PSII (photosystem II), revisited. *Physical Chemistry Chemical Physics* **2018,** *20* (35), 22926-22931.
150. Amin, M.; Kaur, D.; Gunner, M.; Brudvig, G., Toward understanding the S2-S3 transition in the Kok Cycle of Photosystem II: Lessons from Sr-Substituted Structure. *arXiv preprint arXiv:2105.12387* **2021**.
151. Askerka, M.; Brudvig, G. W.; Batista, V. S., The O2-evolving complex of photosystem II: Recent insights from quantum mechanics/molecular mechanics (QM/MM), extended X-ray absorption fine structure (EXAFS), and femtosecond X-ray crystallography data. *Accounts of chemical research* **2017,** *50* (1), 41-48.
152. Pantazis, D. A.; Ames, W.; Cox, N.; Lubitz, W.; Neese, F., Two interconvertible structures that explain the spectroscopic properties of the oxygen-evolving complex of photosystem II in the S_2 state. *Angew. Chem. Int. Ed.* **2012,** *51* (39), 9935-9940.
153. Retegan, M.; Krewald, V.; Mamedov, F.; Neese, F.; Lubitz, W.; Cox, N.; Pantazis, D. A., A five-coordinate Mn (IV) intermediate in biological water oxidation: spectroscopic signature and a pivot mechanism for water binding. *Chemical Science* **2016,** *7* (1), 72-84.
154. Chrysina, M.; Heyno, E.; Kutin, Y.; Reus, M.; Nilsson, H.; Nowaczyk, M. M.; DeBeer, S.; Neese, F.; Messinger, J.; Lubitz, W., Five-coordinate MnIV intermediate in the activation of nature's water splitting cofactor. *Proceedings of the National Academy of Sciences* **2019,** *116* (34), 16841-16846.
155. Liang, W.; Roelofs, T. A.; Cinco, R. M.; Rompel, A.; Latimer, M. J.; Yu, W. O.; Sauer, K.; Klein, M. P.; Yachandra, V. K., Structural change of the Mn cluster during the S2→ S3 state transition of the oxygen-evolving complex of photosystem II. Does it reflect the onset of water/substrate oxidation? Determination by Mn X-ray absorption spectroscopy. *Journal of the American Chemical Society* **2000,** *122* (14), 3399.

156. Cox, N.; Retegan, M.; Neese, F.; Pantazis, D. A.; Boussac, A.; Lubitz, W., Electronic structure of the oxygen-evolving complex in photosystem II prior to OO bond formation. *Science* **2014,** *345* (6198), 804-808.
157. Dau, H.; Haumann, M., Eight Steps Preceding OO Bond Formation in Oxygenic Photosynthesis—A Basic Reaction Cycle of the Photosystem II Manganese Complex. In *Photosynthesis. Energy from the Sun*, Springer: 2008; pp 393-396.
158. Siegbahn, P. E., Water oxidation mechanism in photosystem II, including oxidations, proton release pathways, O—O bond formation and O 2 release. *Biochimica et Biophysica Acta (BBA)-Bioenergetics* **2013,** *1827* (8), 1003-1019.
159. Robblee, J. H.; Messinger, J.; Cinco, R. M.; McFarlane, K. L.; Fernandez, C.; Pizarro, S. A.; Sauer, K.; Yachandra, V. K., The Mn cluster in the S0 state of the oxygen-evolving complex of photosystem II studied by EXAFS spectroscopy: are there three di-μ-oxo-bridged Mn2 moieties in the tetranuclear Mn complex? *Journal of the American Chemical Society* **2002,** *124* (25), 7459.
160. Kulik, L. V.; Epel, B.; Lubitz, W.; Messinger, J., 55Mn pulse ENDOR at 34 GHz of the S0 and S2 states of the oxygen-evolving complex in photosystem II. *Journal of the American Chemical Society* **2005,** *127* (8), 2392-2393.
161. Dau, H.; Zaharieva, I.; Haumann, M., Recent developments in research on water oxidation by photosystem II. *Current opinion in chemical biology* **2012,** *16* (1-2), 3-10.
162. Shimizu, T.; Sugiura, M.; Noguchi, T., Mechanism of Proton-Coupled Electron Transfer in the S_0-to-S_1 Transition of Photosynthetic Water Oxidation As Revealed by Time-Resolved Infrared Spectroscopy. *The Journal of Physical Chemistry B* **2018,** *122* (41), 9460-9470.
163. Bijelic, A.; Rompel, A., Polyoxometalates: more than a phasing tool in protein crystallography. *ChemTexts* **2018,** *4* (3), 1-27.
164. Russo Krauss, I.; Ferraro, G.; Pica, A.; Márquez, J. A.; Helliwell, J. R.; Merlino, A., Principles and methods used to grow and optimize crystals of protein–metallodrug adducts, to determine metal binding sites and to assign metal ligands. *Metallomics* **2017,** *9* (11), 1534-1547.
165. Russo Krauss, I.; Merlino, A.; Vergara, A.; Sica, F., An overview of biological macromolecule crystallization. *International journal of molecular sciences* **2013,** *14* (6), 11643-11691.
166. Chayen, N. E.; Saridakis, E., Protein crystallization: from purified protein to diffraction-quality crystal. *Nature methods* **2008,** *5* (2), 147-153.
167. Rhodes, G., *Crystallography made crystal clear: a guide for users of macromolecular models*. Elsevier: 2010.
168. Shimamura, T., Overview of Membrane Protein Purification and Crystallization. In *Advanced Methods in Structural Biology*, Springer: 2016; pp 105-122.
169. Birch, J.; Axford, D.; Foadi, J.; Meyer, A.; Eckhardt, A.; Thielmann, Y.; Moraes, I., The fine art of integral membrane protein crystallisation. *Methods* **2018,** *147*, 150-162.
170. McPherson, A.; Nguyen, C.; Cudney, R.; Larson, S., The role of small molecule additives and chemical modification in protein crystallization. *Crystal growth & design* **2011,** *11* (5), 1469-1474.
171. McPherson, A.; Gavira, J. A., Introduction to protein crystallization. *Acta Crystallographica Section F: Structural Biology Communications* **2014,** *70* (1), 2-20.
172. Bergfors, T., Seeds to crystals. *Journal of structural biology* **2003,** *142* (1), 66-76.
173. Bergfors, T., Screening and optimization methods for nonautomated crystallization laboratories. In *Macromolecular Crystallography Protocols*, Springer: 2007; pp 131-152.

174. Parambil, J. V.; Heng, J. Y., Seeding in crystallisation. In *Engineering crystallography: from molecule to crystal to functional form*, Springer: 2017; pp 235-245.
175. Fromme, P.; Witt, H. T., Improved isolation and crystallization of photosystem I for structural analysis. *Biochimica et Biophysica Acta (BBA)-Bioenergetics* **1998,** *1365* (1-2), 175-184.
176. Garman, E. F.; Weik, M., Macromolecular crystallography radiation damage research: what's new? International Union of Crystallography: 2011.
177. Andersson, B.; Aro, E.-M., Photodamage and D1 protein turnover in photosystem II. In *Regulation of photosynthesis*, Springer: 2004; pp 377-393.
178. Garman, E. F.; McSweeney, S. M., Progress in research into radiation damage in cryo-cooled macromolecular crystals. *Journal of synchrotron radiation* **2007,** *14* (1), 1-3.
179. Garman, E. F., Radiation Damage in Macromolecular Crystallography: What Is It and Why Do We Care? In *Advancing Methods for Biomolecular Crystallography*, Springer: 2013; pp 69-77.
180. Garman, E. F., Radiation damage in macromolecular crystallography: what is it and why should we care? *Acta Crystallographica Section D: Biological Crystallography* **2010,** *66* (4), 339-351.
181. Garman, E. F.; Nave, C., Radiation damage in protein crystals examined under various conditions by different methods. *Journal of synchrotron radiation* **2009,** *16* (2), 129-132.
182. Lomb, L.; Barends, T. R.; Kassemeyer, S.; Aquila, A.; Epp, S. W.; Erk, B.; Foucar, L.; Hartmann, R.; Rudek, B.; Rolles, D., Radiation damage in protein serial femtosecond crystallography using an x-ray free-electron laser. *Physical Review B* **2011,** *84* (21), 214111.
183. Garman, E. F.; Weik, M., Radiation damage to biological macromolecules: some answers and more questions. *Journal of synchrotron radiation* **2013,** *20* (1), 1-6.
184. Yano, J.; Kern, J.; Irrgang, K.-D.; Latimer, M. J.; Bergmann, U.; Glatzel, P.; Pushkar, Y.; Biesiadka, J.; Loll, B.; Sauer, K., X-ray damage to the Mn4Ca complex in single crystals of photosystem II: a case study for metalloprotein crystallography. *Proceedings of the National Academy of Sciences of the United States of America* **2005,** *102* (34), 12047-12052.
185. Gruner, S. M.; Bilderback, D.; Bazarov, I.; Finkelstein, K.; Krafft, G.; Merminga, L.; Padamsee, H.; Shen, Q.; Sinclair, C.; Tigner, M., Energy recovery linacs as synchrotron radiation sources. *Review of Scientific Instruments* **2002,** *73* (3), 1402-1406.
186. Tenboer, J.; Basu, S.; Zatsepin, N.; Pande, K.; Milathianaki, D.; Frank, M.; Hunter, M.; Boutet, S.; Williams, G. J.; Koglin, J. E., Time-resolved serial crystallography captures high-resolution intermediates of photoactive yellow protein. *Science* **2014,** *346* (6214), 1242-1246.
187. Cusack, S.; Belrhali, H.; Bram, A.; Burghammer, M.; Perrakis, A.; Riekel, C., Small is beautiful: protein micro-crystallography. *Nature structural & molecular biology* **1998,** *5*, 634-637.
188. Kern, J.; Alonso-Mori, R.; Hellmich, J.; Tran, R.; Hattne, J.; Laksmono, H.; Glöckner, C.; Echols, N.; Sierra, R. G.; Sellberg, J., Room temperature femtosecond X-ray diffraction of photosystem II microcrystals. *Proceedings of the National Academy of Sciences* **2012,** *109* (25), 9721-9726.
189. Kern, J.; Alonso-Mori, R.; Tran, R.; Hattne, J.; Gildea, R. J.; Echols, N.; Glöckner, C.; Hellmich, J.; Laksmono, H.; Sierra, R. G., Simultaneous Femtosecond X-ray Spectroscopy and Diffraction of Photosystem II at Room Temperature. *Science* **2013**.

190. Ibrahim, M.; Chatterjee, R.; Hellmich, J.; Tran, R.; Bommer, M.; Yachandra, V. K.; Yano, J.; Kern, J.; Zouni, A., Improvements in serial femtosecond crystallography of photosystem II by optimizing crystal uniformity using microseeding procedures. *Struct. Dyn.* **2015,** *2* (4), 041705.
191. Fuller, F. D.; Gul, S.; Chatterjee, R.; Burgie, E. S.; Young, I. D.; Lebrette, H.; Srinivas, V.; Brewster, A. S.; Michels-Clark, T.; Clinger, J. A.; Andi, B.; Ibrahim, M.; Pastor, E.; de Lichtenberg, C.; Hussein, R.; Pollock, C. J.; Zhang, M.; Stan, C. A.; Kroll, T.; Fransson, T.; Weninger, C.; Kubin, M.; Aller, P.; Lassalle, L.; Bräuer, P.; Miller, M. D.; Amin, M.; Koroidov, S.; Roessler, C. G.; Allaire, M.; Sierra, R. G.; Docker, P. T.; Glownia, J. M.; Nelson, S.; Koglin, J. E.; Zhu, D.; Chollet, M.; Song, S.; Lemke, H.; Liang, M.; Sokaras, D.; Alonso-Mori, R.; Zouni, A.; Messinger, J.; Bergmann, U.; Boal, A. K.; Bollinger, J., J. M. ; Krebs, C.; Högbom, M.; Phillips, J., G. N. ; Vierstra, R. D.; Sauter, N. K.; Orville, A. M.; Kern, J.; Yachandra, V. K.; Yano, J., Drop-on-Demand Sample Delivery for Studying Biocatalysts in Action at XFELs *Nat. Methods* **2017,** *14*, 443-449.
192. Kupitz, C.; Basu, S.; Grotjohann, I.; Fromme, R.; Zatsepin, N. A.; Rendek, K. N.; Hunter, M. S.; Shoeman, R. L.; White, T. A.; Wang, D., Serial time-resolved crystallography of photosystem II using a femtosecond X-ray laser. *Nature* **2014,** *513* (7517), 261-265.
193. Hussein, R.; Ibrahim, M.; Bhowmick, A.; Simon, P. S.; Chatterjee, R.; Lassalle, L.; Doyle, M.; Bogacz, I.; Kim, I.-S.; Cheah, M. H.; Gul, S.; de Lichtenberg, C.; Chernev, P.; Pham, C. C.; Young, I. D.; Carbajo, S.; Fuller, F. D.; Alonso-Mori, R.; Batyuk, A.; Sutherlin, K. D.; Brewster, A. S.; Bolotovsky, R.; Mendez, D.; Holton, J. M.; Moriarty, N. W.; Adams, P. D.; Bergmann, U.; Sauter, N. K.; Dobbek, H.; Messinger, J.; Zouni, A.; Kern, J.; Yachandra, V. K.; Yano, J., Structural dynamics in the water and proton channels of photosystem II during the S2 to S3 transition. *Nature Communications* **2021,** *12* (1), 6531.
194. Blakeley, M. P.; Langan, P.; Niimura, N.; Podjarny, A., Neutron crystallography: opportunities, challenges, and limitations. *Current opinion in structural biology* **2008,** *18* (5), 593-600.
195. O'Dell, W. B.; Bodenheimer, A. M.; Meilleur, F., Neutron protein crystallography: A complementary tool for locating hydrogens in proteins. *Archives of Biochemistry and Biophysics* **2016,** *602*, 48-60.
196. Helliwell, J. R., Fundamentals of neutron crystallography in structural biology. *Methods in enzymology* **2020,** *634*, 1-19.
197. Jha, K. K.; Gruza, B.; Kumar, P.; Chodkiewicz, M. L.; Dominiak, P. M., TAAM: a reliable and user friendly tool for hydrogen-atom location using routine X-ray diffraction data. *Acta Crystallographica Section B: Structural Science, Crystal Engineering and Materials* **2020,** *76* (3), 296-306.
198. Chen, J. C.-H.; Hanson, B. L.; Fisher, S. Z.; Langan, P.; Kovalevsky, A. Y., Direct observation of hydrogen atom dynamics and interactions by ultrahigh resolution neutron protein crystallography. *Proceedings of the National Academy of Sciences* **2012,** *109* (38), 15301-15306.
199. Blakeley, M., Neutron macromolecular crystallography. *Crystallography Reviews* **2009,** *15* (3), 157-218.
200. Blakeley, M. P.; Hasnain, S. S.; Antonyuk, S. V., Sub-atomic resolution X-ray crystallography and neutron crystallography: promise, challenges and potential. *IUCrJ* **2015,** *2* (4), 464-474.
201. Teixeira, S.; Zaccai, G.; Ankner, J.; Bellissent-Funel, M.; Bewley, R.; Blakeley, M.; Callow, P.; Coates, L.; Dahint, R.; Dalgliesh, R., New sources and instrumentation for neutrons in biology. *Chemical physics* **2008,** *345* (2-3), 133-151.

202. Furrer, A.; Mesot, J. F.; Strässle, T., *Neutron scattering in condensed matter physics*. World Scientific Publishing Company: 2009; Vol. 4.
203. Xiang, X.-D.; Wang, G.; Zhang, X.; Xiang, Y.; Wang, H., Individualized pixel synthesis and characterization of combinatorial materials chips. *Engineering* **2015,** *1* (2), 225-233.
204. Coates, L.; Sullivan, B., The macromolecular neutron diffractometer at the spallation neutron source. *Methods in enzymology* **2020,** *634*, 87-99.
205. Blazek, J.; Gilbert, E. P., Application of small-angle X-ray and neutron scattering techniques to the characterisation of starch structure: A review. *Carbohydrate Polymers* **2011,** *85* (2), 281-293.
206. Kikhney, A. G.; Svergun, D. I., A practical guide to small angle X-ray scattering (SAXS) of flexible and intrinsically disordered proteins. *FEBS letters* **2015,** *589* (19), 2570-2577.
207. Müh, F.; Zouni, A., Micelle formation in the presence of photosystem I. *Biochimica et Biophysica Acta (BBA)-Biomembranes* **2008,** *1778* (10), 2298-2307.
208. Müh, F.; DiFiore, D.; Zouni, A., The influence of poly (ethylene glycol) on the micelle formation of alkyl maltosides used in membrane protein crystallization. *Physical Chemistry Chemical Physics* **2015,** *17* (17), 11678-11691.
209. Castellanos, M. M.; McAuley, A.; Curtis, J. E., Investigating structure and dynamics of proteins in amorphous phases using neutron scattering. *Computational and structural biotechnology journal* **2017,** *15*, 117-130.
210. Barré, L., Contribution of Small-Angle X-Ray and Neutron Scattering (SAXS and SANS) to the Characterization of Natural Nanomaterials. In *X-ray and Neutron Techniques for Nanomaterials Characterization*, Springer: 2016; pp 665-716.
211. Golub, M.; Kölsch, A.; Feoktystov, A.; Zouni, A.; Pieper, J., Insights into Solution Structures of Photosynthetic Protein Complexes from Small-Angle Scattering Methods. *Crystals* **2021,** *11* (2), 203.
212. Konarev, P. V.; Volkov, V. V.; Sokolova, A. V.; Koch, M. H.; Svergun, D. I., PRIMUS: a Windows PC-based system for small-angle scattering data analysis. *Journal of applied crystallography* **2003,** *36* (5), 1277-1282.
213. Franke, D.; Svergun, D. I., DAMMIF, a program for rapid ab-initio shape determination in small-angle scattering. *Journal of applied crystallography* **2009,** *42* (2), 342-346.
214. Petoukhov, M. V.; Franke, D.; Shkumatov, A. V.; Tria, G.; Kikhney, A. G.; Gajda, M.; Gorba, C.; Mertens, H. D.; Konarev, P. V.; Svergun, D. I., New developments in the ATSAS program package for small-angle scattering data analysis. *Journal of applied crystallography* **2012,** *45* (2), 342-350.
215. Blanchet, C. E.; Svergun, D. I., Small-angle X-ray scattering on biological macromolecules and nanocomposites in solution. *Annual review of physical chemistry* **2013,** *64*, 37-54.
216. Earnshaw, J., *The application of laser light scattering to the study of biological motion*. Springer Science & Business Media: 2013; Vol. 59.
217. Nelson, N.; Yocum, C. F., Structure and function of photosystems I and II. *Annu. Rev. Plant Biol.* **2006,** *57*, 521-565.
218. Muh, F.; Zouni, A., Light-induced water oxidation in photosystem II. *Frontiers in bioscience (Landmark edition)* **2010,** *16*, 3072-3132.
219. Folea, I. M.; Zhang, P.; Aro, E.-M.; Boekema, E. J., Domain organization of photosystem II in membranes of the cyanobacterium Synechocystis PCC6803 investigated by electron microscopy. *FEBS letters* **2008,** *582* (12), 1749-1754.
220. Kern, J.; Loll, B.; Lüneberg, C.; DiFiore, D.; Biesiadka, J.; Irrgang, K.-D.; Zouni, A., Purification, characterisation and crystallisation of photosystem II from

Thermosynechococcus elongatus cultivated in a new type of photobioreactor. *Biochimica et Biophysica Acta (BBA)-Bioenergetics* **2005,** *1706* (1), 147-157.
221. Shen, J.-R.; Kamiya, N., Crystallization and the crystal properties of the oxygen-evolving photosystem II from Synechococcus vulcanus. *Biochemistry* **2000,** *39* (48), 14739-14744.
222. Shen, J.-R., The structure of photosystem II and the mechanism of water oxidation in photosynthesis. *Annual review of plant biology* **2015,** *66*, 23-48.
223. Joliot, P., Period-four oscillations of the flash-induced oxygen formation in photosynthesis. *Photosynthesis research* **2003,** *76* (1), 65-72.
224. Dau, H.; Haumann, M., The manganese complex of photosystem II in its reaction cycle—basic framework and possible realization at the atomic level. *Coordination Chemistry Reviews* **2008,** *252* (3), 273-295.
225. Tanaka, A.; Fukushima, Y.; Kamiya, N., Two different structures of the oxygen-evolving complex in the same polypeptide frameworks of photosystem II. *Journal of the American Chemical Society* **2017**.
226. Stich, T. A.; Britt, R. D., *Advanced electron paramagnetic resonance studies of the oxygen-evolving complex*. Taylor & Francis Group, LLC: Boca Raton, FL: 2015.
227. Pérez-Navarro, M.; Neese, F.; Lubitz, W.; Pantazis, D. A.; Cox, N., Recent developments in biological water oxidation. *Current opinion in chemical biology* **2016,** *31*, 113-119.
228. Ascone, I.; Meyer-Klaucke, W.; Murphy, L., Experimental aspects of biological X-ray absorption spectroscopy. *Journal of synchrotron radiation* **2003,** *10* (1), 16-22.
229. Eaton, G. R.; Eaton, S. S., *Foundations of modern EPR*. World Scientific: 1998.
230. Hofbauer, W.; Zouni, A.; Bittl, R.; Kern, J.; Orth, P.; Lendzian, F.; Fromme, P.; Witt, H.; Lubitz, W., Photosystem II single crystals studied by EPR spectroscopy at 94 GHz: The tyrosine radical Y. *Proceedings of the National Academy of Sciences* **2001,** *98* (12), 6623-6628.
231. Teixeira, S.; Zaccai, G.; Ankner, J.; Bellissent-Funel, M.; Bewley, R.; Blakeley, M.; Callow, P.; Coates, L.; Dahint, R.; Dalgliesh, R., New sources and instrumentation for neutrons in biology. *Chemical physics* **2008,** *345* (2), 133-151.
232. Niimura, N., Neutrons expand the field of structural biology. *Current opinion in structural biology* **1999,** *9* (5), 602-608.
233. Myles, D. A., Neutron protein crystallography: current status and a brighter future. *Current opinion in structural biology* **2006,** *16* (5), 630-637.
234. Vandavasi, V. G.; Langan, P. S.; Weiss, K. L.; Parks, J. M.; Cooper, J. B.; Ginell, S. L.; Coates, L., Active-site protonation states in an acyl-enzyme intermediate of a class A β-lactamase with a monobactam substrate. *Antimicrobial Agents and Chemotherapy* **2017,** *61* (1), e01636-16.
235. Fromme, P.; Witt, H. T., Improved isolation and crystallization of photosystem I for structural analysis. *Biochimica et Biophysica Acta (BBA)-Bioenergetics* **1998,** *1365* (1), 175-184.
236. Jordan, P.; Fromme, P.; Witt, H. T.; Klukas, O.; Saenger, W.; Krauß, N., Three-dimensional structure of cyanobacterial photosystem I at 2.5 Å resolution. *Nature* **2001,** *411* (6840), 909-917.
237. Bittl, R.; Zech, S. G.; Fromme, P.; Witt, H. T.; Lubitz, W., Pulsed EPR structure analysis of photosystem I single crystals: localization of the phylloquinone acceptor. *Biochemistry* **1997,** *36* (40), 12001-12004.
238. Glusker, J. P., Protein Crystallization. Techniques, Strategies, and Tips Edited by Terese M. Bergfors. International University Line, 1999. ISBN 0963681753. ACS Publications: 2003.

239. Watanabe, M.; Iwai, M.; Narikawa, R.; Ikeuchi, M., Is the photosystem II complex a monomer or a dimer? *Plant and cell physiology* **2009,** *50* (9), 1674-1680.
240. Krug, M.; Weiss, M. S.; Heinemann, U.; Mueller, U., XDSAPP: a graphical user interface for the convenient processing of diffraction data using XDS. *Journal of Applied Crystallography* **2012,** *45* (3), 568-572.
241. Kabsch, W., Xds. *Acta Crystallographica Section D: Biological Crystallography* **2010,** *66* (2), 125-132.
242. Coates, L.; Stoica, A.; Hoffmann, C.; Richards, J.; Cooper, R., The macromolecular neutron diffractometer (MaNDi) at the Spallation Neutron Source, Oak Ridge: enhanced optics design, high-resolution neutron detectors and simulated diffraction. *Journal of Applied Crystallography* **2010,** *43* (3), 570-577.
243. Coates, L.; Cuneo, M. J.; Frost, M. J.; He, J.; Weiss, K. L.; Tomanicek, S. J.; McFeeters, H.; Vandavasi, V. G.; Langan, P.; Iverson, E. B., The macromolecular neutron diffractometer MaNDi at the Spallation Neutron Source. *Journal of Applied Crystallography* **2015,** *48* (4), 1302-1306.
244. Peng, J.; Dong, N.; Dong, Y.; Pan, Z.; Li, W., Solubility, Metastable Zone Width, and Nucleation Kinetics of Boric Acid in the NaCl–KCl–CaCl2–H2O System. *Journal of Chemical & Engineering Data* **2015,** *60* (11), 3341-3346.
245. Hu, B.; Huang, K.; Zhang, X.; Zhang, P.; Yu, S., Solubility and Seeded Metastable Zone width of functional sugar L-arabinose. *Food Science and Technology (Campinas)* **2015,** *35* (1), 51-57.
246. Müh, F.; Zouni, A., Light-induced water oxidation in photosystem II. *Frontiers in bioscience* **2011,** *16*, 3072-3132.
247. Müh, F.; Glöckner, C.; Hellmich, J.; Zouni, A., Light-induced quinone reduction in photosystem II. *Biochim. Biophys. Acta* **2012,** *1817* (1), 44-65.
248. Kern, J.; Renger, G., Photosystem II: Structure and mechanism of the water: plastoquinone oxidoreductase. *Photosynthesis research* **2007,** *94* (2-3), 183-202.
249. Kok, B.; Forbush, B.; McGloin, M., Cooperation of charges in photosynthetic O_2 evolution. 1. A linear 4-step mechanism. *Photochem. Photobiol.* **1970,** *11* (6), 457-475.
250. Renger, G.; Renger, T., Photosystem II: the machinery of photosynthetic water splitting. *Photosynthesis research* **2008,** *98* (1-3), 53-80.
251. Wydrzynski, T.; Satoh, K., Advances in photosynthesis and respiration. *Advances in photosynthesis and respiration* **2005,** *22*, 1-786.
252. Ferreira, K. N.; Iverson, T. M.; Maghlaoui, K.; Barber, J.; Iwata, S., Architecture of the photosynthetic oxygen-evolving center. *Science* **2004,** *303* (5665), 1831-1838.
253. Pieper, J.; Hauss, T.; Buchsteiner, A.; Renger, G., The Effect of Hydration on Protein Flexibility in Photosystem II of Green Plants Studied by Quasielastic Neutron Scattering. *European biophysics journal : EBJ* **2008,** *37* (5), 657-663.
254. Pieper, J.; Trapp, M.; Skomorokhov, A.; Natkaniec, I.; Peters, J.; Renger, G., Temperature-Dependent Vibrational and Conformational Dynamics of Photosystem II Membrane Fragments from Spinach Investigated by Elastic and Inelastic Neutron Scattering. *Biochimica et biophysica acta* **2012,** *1817* (8), 1213-1219.
255. Hussein, R.; Ibrahim, M.; Chatterjee, R.; Coates, L.; Müh, F.; Yachandra, V. K.; Yano, J.; Kern, J.; Dobbek, H.; Zouni, A., Optimizing Crystal Size of Photosystem II by Macroseeding: Toward Neutron Protein Crystallography. *Cryst. Growth. Des.* **2018,** *18* (1), 85-94.
256. le Maire, M.; Champeil, P.; Möller, J. V., Interaction of membrane proteins and lipids with solubilizing detergents. *Biochim. Biophys. Acta* **2000,** *1508* (1-2), 86-111.
257. Müh, F.; Zouni, A., Micelle formation in the presence of photosystem I. *Biochim. Biophys. Acta* **2008,** *1778* (10), 2298-2307.

258. Jacques, D. A.; Trewhella, J., Small-Angle Scattering for Structural Biology--Expanding the Frontier while Avoiding the Pitfalls. *Protein science : a publication of the Protein Society* **2010,** *19* (4), 642-657.
259. Kikhney, A. G.; Svergun, D. I., A practical guide to small angle X-ray scattering (SAXS) of flexible and intrinsically disordered proteins. *FEBS Lett.* **2015,** *589* (19 Pt A), 2570-2577.
260. Petoukhov, M. V.; Svergun, D. I., Joint use of small-angle X-ray and neutron scattering to study biological macromolecules in solution. *European biophysics journal : EBJ* **2006,** *35* (7), 567-576.
261. Petoukhov, M. V.; Svergun, D. I., Analysis of X-ray and neutron scattering from biomacromolecular solutions. *Curr Opin Struc Biol* **2007,** *17* (5), 562-571.
262. Neylon, C., Small angle neutron and X-ray scattering in structural biology: recent examples from the literature. *Eur Biophys J Biophy* **2008,** *37* (5), 531-541.
263. Trewhella, J., Neutrons reveal how nature uses structural themes and variation in biological regulation. *Physica B* **2006,** *385-86*, 825-830.
264. Nagy, G.; Garab, G.; Pieper, J., Neutron Scattering in Photosynthesis Research. In *Contemporary Problems of Photosynthesis* Allakhverdiev, S.; Rubin, A. B.; Shuvalov, V. A., Eds. Institute of Computer Science: Izhevsk, 2014; Vol. 1, pp 69-121.
265. Tiede, D. M.; Thiyagarjan, P., Characterization of photosynthetic supramolecular assemblies using small angle neutron scattering. In *Biophysical Techniques in Photosynthesis*, Amesz, J.; Hoff, A. J., Eds. Springer: Netherlands, 1996; Vol. 3, pp 375-390.
266. Kirkensgaard, J. J. K.; Holm, J. K.; Larsen, J. K.; Posselt, D., Simulation of small-angle X-ray scattering from thylakoid membranes. *J. Appl. Crystallogr.* **2009,** *42*, 649-659.
267. Nagy, G.; Posselt, D.; Kovacs, L.; Holm, J. K.; Szabo, M.; Ughy, B.; Rosta, L.; Peters, J.; Timmins, P.; Garab, G., Reversible membrane reorganizations during photosynthesis in vivo: revealed by small-angle neutron scattering. *The Biochemical journal* **2011,** *436* (2), 225-230.
268. Liberton, M.; Page, L. E.; O'Dell, W. B.; O'Neill, H.; Mamontov, E.; Urban, V. S.; Pakrasi, H. B., Organization and flexibility of cyanobacterial thylakoid membranes examined by neutron scattering. *J. Biol. Chem.* **2013,** *288* (5), 3632-3640.
269. Li, Y.; Lin, Y.; Garvey, C. J.; Birch, D.; Corkery, R. W.; Loughlin, P. C.; Scheer, H.; Willows, R. D.; Chen, M., Characterization of red-shifted phycobilisomes isolated from the chlorophyll f-containing cyanobacterium Halomicronema hongdechloris. *Biochim. Biophys. Acta* **2016,** *1857* (1), 107-114.
270. Tiede, D. M.; Littrell, K.; Marone, P. A.; Zhang, R.; Thiyagarjan, P., Solution Structure of a Biological Bimolecular Electron Transfer Complex: Characterization of the Photosynthetic Reaction Center-Cytochrome C2 Protein Complex by Small Angle Neutron Scattering. *J. Appl. Crystallogr.* **2000,** *33* (1-3), 560-564.
271. Golub, M.; Hejazi, M.; Kolsch, A.; Lokstein, H.; Wieland, D. C.; Zouni, A.; Pieper, J., Solution Structure of Monomeric and Trimeric Photosystem I of Thermosynechococcus Elongatus Investigated by Small-Angle X-ray Scattering. *Photosynth. Res.* **2017,** *133* (1-3), 163-173.
272. Golub, M.; Moldenhauer, M.; Schmitt, F. J.; Feoktystov, A.; Mandar, H.; Maksimov, E.; Friedrich, T.; Pieper, J., Solution Structure and Conformational Flexibility in the Active State of the Orange Carotenoid Protein: Part I. Small-Angle Scattering. *The journal of physical chemistry. B* **2019,** *123* (45), 9525-9535.
273. Cardoso, M. B.; Smolensky, D.; Heller, W. T.; O'Neill, H., Insight into the Structure of Light-Harvesting Complex II and Its Stabilization in Detergent Solution. *The journal of physical chemistry. B* **2009,** *113* (51), 16377-16383.

274. Slowik, D.; Rossmann, M.; Konarev, P. V.; Irrgang, K. D.; Saenger, W., Structural investigation of PsbO from plant and cyanobacterial photosystem II. *Journal of molecular biology* **2011,** *407* (1), 125-137.
275. Tang, K. H.; Blankenship, R. E., Neutron and light scattering studies of light-harvesting photosynthetic antenna complexes. *Photosynth Res.* **2012,** *111* (1-2), 205-217.
276. O'Neill, H.; Heller, W. T.; Helton, K. E.; Urban, V. S.; Greenbaum, E., Small-angle X-ray scattering study of photosystem I-detergent complexes: implications for membrane protein crystallization. *The journal of physical chemistry. B* **2007,** *111* (16), 4211-4219.
277. Le, R. K.; Harris, B. J.; Iwuchukwu, I. J.; Bruce, B. D.; Cheng, X.; Qian, S.; Heller, W. T.; O'Neill, H.; Frymier, P. D., Analysis of the solution structure of Thermosynechococcus elongatus photosystem I in n-dodecyl-beta-D-maltoside using small-angle neutron scattering and molecular dynamics simulation. *Arch. Biochem. Biophys.* **2014,** *550-551*, 50-57.
278. Dewhurst, C. D., D33 - a third small-angle neutron scattering instrument at the Institut Laue Langevin. *Meas Sci Technol* **2008,** *19* (3), 1-8.
279. Comoletti, D.; Flynn, R.; Jennings, L. L.; Chubykin, A.; Matsumura, T.; Hasegawa, H.; Sudhof, T. C.; Taylor, P., Characterization of the interaction of a recombinant soluble neuroligin-1 with neurexin-1beta. *J Biol Chem* **2003,** *278* (50), 50497-50505.
280. Comoletti, D.; Flynn, R. E.; Boucard, A. A.; Demeler, B.; Schirf, V.; Shi, J.; Jennings, L. L.; Newlin, H. R.; Sudhof, T. C.; Taylor, P., Gene selection, alternative splicing, and post-translational processing regulate neuroligin selectivity for beta-neurexins. *Biochemistry* **2006,** *45* (42), 12816-12827.
281. Pernot, P.; Round, A.; Barrett, R.; De Maria Antolinos, A.; Gobbo, A.; Gordon, E.; Huet, J.; Kieffer, J.; Lentini, M.; Mattenet, M.; Morawe, C.; Mueller-Dieckmann, C.; Ohlsson, S.; Schmid, W.; Surr, J.; Theveneau, P.; Zerrad, L.; McSweeney, S., Upgraded ESRF BM29 beamline for SAXS on Macromolecules in Solution. *J. Synchrotron Radiat.* **2013,** *20* (Pt 4), 660-664.
282. Kline, S. R., Reduction and Analysis of SANS and USANS Data Using IGOR Pro. *J. Appl. Crystallogr.* **2006,** *39*, 895-900.
283. Feigin, L. A.; Svergun, D. I., *Structure Analysis by Small-Angle X-Ray and Neutron Scattering*. Plenum Press: New York, 1987.
284. Guinier, A.; Fournet, G., *Small-Angle Scattering of X-Rays"*. John Wiley and Sons: New York, 1955.
285. Svergun, D. I., Determination of the Regularization Parameter in Indirect-Transform Methods Using Perceptual Criteria. *J. Appl. Crystallogr.* **1992,** *25*, 495-503.
286. Svergun, D. I.; Barberato, C.; Koch, M. H. J., CRYSOL -a Program to Evaluate X-ray Solution Scattering of Biological Macromolecules form Atomic Coordinates. *J. Appl. Crystallogr.* **1995,** *28*, 768-773.
287. Pieper, J.; Irrgang, K.-D.; Rätsep, M.; Jankowiak, R.; Schrötter, T.; Voigt, J.; Small, G.; Renger, G., Effects of aggregation on trimeric light-harvesting complex II of green plants: a hole-burning study. *The Journal of Physical Chemistry A* **1999,** *103* (14), 2422-2428.
288. Voigt, B.; Krikunova, M.; Lokstein, H., Influence of detergent concentration on aggregation and spectroscopic properties of light-harvesting complex II. *Photosynthesis research* **2008,** *95* (2-3), 317-325.
289. Hong, X. G.; Weng, Y. X.; Li, M., Determination of the topological shape of integral membrane protein light-harvesting complex LH2 from photosynthetic bacteria in the detergent solution by small-angle X-ray scattering. *Biophys J* **2004,** *86* (2), 1082-1088.

290. Santonicola, M. G.; Lenhoff, A. M.; Kaler, E. W., Binding of alkyl polyglucoside surfactants to bacteriorhodopsin and its relation to protein stability. *Biophys J* **2008,** *94* (9), 3647-3658.
291. Midtgaard, S. R.; Darwish, T. A.; Pedersen, M. C.; Huda, P.; Larsen, A. H.; Jensen, G. V.; Kynde, S. A. R.; Skar-Gislinge, N.; Nielsen, A. J. Z.; Olesen, C., Invisible detergents for structure determination of membrane proteins by small-angle neutron scattering. *The FEBS journal* **2018,** *285* (2), 357-371.
292. Vrandecic, K.; Rätsep, M.; Wilk, L.; Rusevich, L.; Golub, M.; Reppert, M.; Irrgang, K. D.; Kühlbrandt, W.; Pieper, J., Protein Dynamics Tunes Excited State Positions in Light-Harvesting Complex II. *J Phys Chem B* **2015,** *119* (10), 3920-3930.
293. Gerland, L.; Friedrich, D.; Hopf, L.; Donovan, E. J.; Wallmann, A.; Erdmann, N.; Diehl, A.; Bommer, M.; Buzar, K.; Ibrahim, M.; Schmieder, P.; Dobbek, H.; Zouni, A.; Bondar, A. N.; Dau, H.; Oschkinat, H., pH-Dependent Protonation of Surface Carboxylate Groups in PsbO Enables Local Buffering and Triggers Structural Changes. *Chembiochem : a European journal of chemical biology* **2020**.
294. Möller, J. V.; le Maire, M., Detergent binding as a measure of hydrophobic surface area of integral membrane proteins. *J. Biol. Chem.* **1993,** *268* (25), 18659-18672.
295. Neugebauer, J. M., Detergents: an overview. *Methods Enzymol.* **1990,** *182*, 239-253.
296. Decyl beta-D-maltopyranoside. http://pubchem.ncbi.nlm.nih.gov/compound/5288728#section=3D-Conformer.
297. Pebay-Peyroula, E.; Garavito, R. M.; Rosenbusch, J. P.; Zulauf, M.; Timmins, P. A., Detergent structure in tetragonal crystals of OmpF porin. *Structure* **1995,** *3* (10), 1051-1059.
298. Ball, P., Water is an active matrix of life for cell and molecular biology. *Proc Natl Acad Sci U S A* **2017,** *114* (51), 13327-13335.
299. Suzuki, H.; Sugiura, M.; Noguchi, T., Monitoring water reactions during the S-state cycle of the photosynthetic water-oxidizing center: detection of the DOD bending vibrations by means of Fourier transform infrared spectroscopy. *Biochemistry* **2008,** *47* (42), 11024-11030.
300. Noguchi, T.; Sugiura, M., FTIR detection of water reactions during the flash-induced S-state cycle of the photosynthetic water-oxidizing complex. *Biochemistry* **2002,** *41* (52), 15706-15712.
301. Cox, N.; Messinger, J., Reflections on substrate water and dioxygen formation. *Biochimica et Biophysica Acta (BBA)-Bioenergetics* **2013,** *1827* (8), 1020-1030.
302. Hillier, W.; Messinger, J., Mechanism of photosynthetic oxygen production. In *Photosystem II*, Springer: 2005; pp 567-608.
303. Junge, W.; Haumann, M.; Ahlbrink, R.; Mulkidjanian, A.; Clausen, J., Electrostatics and proton transfer in photosynthetic water oxidation. *Philosophical Transactions of the Royal Society of London. Series B: Biological Sciences* **2002,** *357* (1426), 1407-1418.
304. Dau, H.; Haumann, M., Eight steps preceding O–O bond formation in oxygenic photosynthesis—a basic reaction cycle of the photosystem II manganese complex. *Biochimica et Biophysica Acta (BBA)-Bioenergetics* **2007,** *1767* (6), 472-483.
305. Klauss, A.; Haumann, M.; Dau, H., Seven Steps of Alternating Electron and Proton Transfer in Photosystem II Water Oxidation Traced by Time-Resolved Photothermal Beam Deflection at Improved Sensitivity. *The Journal of Physical Chemistry B* **2015,** *119* (6), 2677-2689.
306. Klauss, A.; Haumann, M.; Dau, H., Alternating electron and proton transfer steps in photosynthetic water oxidation. *Proceedings of the National Academy of Sciences* **2012,** *109* (40), 16035.

307. Gabdulkhakov, A.; Guskov, A.; Broser, M.; Kern, J.; Muh, F.; Saenger, W.; Zouni, A., Probing the accessibility of the Mn(4)Ca cluster in photosystem II: channels calculation, noble gas derivatization, and cocrystallization with DMSO. *Structure* **2009,** *17* (9), 1223-34.
308. Gabdulkhakov, A. G.; Kljashtorny, V. G.; Dontsova, M. V., Analysis of molecular oxygen exit pathways in cyanobacterial photosystem II: Molecular dynamics studies. *Crystallography Reports* **2015,** *60* (6), 884-888.
309. Vassiliev, S.; Zaraiskaya, T.; Bruce, D., Molecular dynamics simulations reveal highly permeable oxygen exit channels shared with water uptake channels in photosystem II. *Biochim Biophys Acta* **2013,** *1827* (10), 1148-55.
310. Vassiliev, S.; Zaraiskaya, T.; Bruce, D., Exploring the energetics of water permeation in photosystem II by multiple steered molecular dynamics simulations. *Biochim. Biophys. Acta* **2012,** *1817* (9), 1671-1678.
311. Sakashita, N.; Watanabe, H. C.; Ikeda, T.; Ishikita, H., Structurally conserved channels in cyanobacterial and plant photosystem II. *Photosynthesis research* **2017,** *133* (1), 75-85.
312. Thomaston, J. L.; Woldeyes, R. A.; Nakane, T.; Yamashita, A.; Tanaka, T.; Koiwai, K.; Brewster, A. S.; Barad, B. A.; Chen, Y.; Lemmin, T.; Uervirojnangkoorn, M.; Arima, T.; Kobayashi, J.; Masuda, T.; Suzuki, M.; Sugahara, M.; Sauter, N. K.; Tanaka, R.; Nureki, O.; Tono, K.; Joti, Y.; Nango, E.; Iwata, S.; Yumoto, F.; Fraser, J. S.; DeGrado, W. F., XFEL structures of the influenza M2 proton channel: Room temperature water networks and insights into proton conduction. *Proc Natl Acad Sci U S A* **2017,** *114* (51), 13357-13362.
313. Kato, Y.; Haniu, S.; Nakajima, Y.; Akita, F.; Shen, J.-R.; Noguchi, T., FTIR Microspectroscopic Analysis of the Water Oxidation Reaction in a Single Photosystem II Microcrystal. *The Journal of Physical Chemistry B* **2019,** *124* (1), 121-127.
314. Service, R. J.; Hillier, W.; Debus, R. J., Evidence from FTIR Difference Spectroscopy of an Extensive Network of Hydrogen Bonds near the Oxygen-Evolving Mn_4Ca Cluster of Photosystem II Involving D1-Glu65, D2-Glu312, and D1-Glu329. *Biochemistry* **2010,** *49* (31), 6655-6669.
315. Siegbahn, P. E., The S_2 to S_3 transition for water oxidation in PSII (photosystem II), revisited. *Phys. Chem. Chem. Phys.* **2018,** *20* (35), 22926-22931.
316. Suzuki, H.; Sugiura, M.; Noguchi, T., Monitoring Proton Release during Photosynthetic Water Oxidation in Photosystem II by Means of Isotope-Edited Infrared Spectroscopy. *Journal of the American Chemical Society* **2009,** *131* (22), 7849-7857.
317. Takaoka, T.; Sakashita, N.; Saito, K.; Ishikita, H., p K a of a proton-conducting water chain in photosystem II. *The journal of physical chemistry letters* **2016,** *7* (10), 1925-1932.
318. Zaharieva, I.; Dau, H.; Haumann, M., Sequential and Coupled Proton and Electron Transfer Events in the $S_2 \rightarrow S_3$ Transition of Photosynthetic Water Oxidation Revealed by Time-Resolved X-ray Absorption Spectroscopy. *Biochemistry* **2016,** *55* (50), 6996-7004.
319. Carugo, O., How large B-factors can be in protein crystal structures. *BMC bioinformatics* **2018,** *19* (1), 1-9.
320. Broser, M.; Glöckner, C.; Gabdulkhakov, A.; Guskov, A.; Buchta, J.; Kern, J.; Müh, F.; Dau, H.; Saenger, W.; Zouni, A., Structural basis of cyanobacterial photosystem II inhibition by the herbicide terbutryn. *Journal of Biological Chemistry* **2011,** *286* (18), 15964-15972.
321. Linke, K.; Ho, F. M., Water in Photosystem II: structural, functional and mechanistic considerations. *Biochim. Biophys. Acta* **2014,** *1837* (1), 14-32.

322. Wang, J.; Askerka, M.; Brudvig, G. W.; Batista, V. S., Crystallographic data support the carousel mechanism of water supply to the oxygen-evolving complex of photosystem II. *ACS energy letters* **2017,** *2* (10), 2299-2306.
323. Kawashima, K.; Takaoka, T.; Kimura, H.; Saito, K.; Ishikita, H., O_2 evolution and recovery of the water-oxidizing enzyme. *Nature communications* **2018,** *9* (1), 1-11.
324. Kato, Y.; Akita, F.; Nakajima, Y.; Suga, M.; Umena, Y.; Shen, J.-R.; Noguchi, T., Fourier transform infrared analysis of the S-state cycle of water oxidation in the microcrystals of photosystem II. *The journal of physical chemistry letters* **2018,** *9* (9), 2121-2126.
325. Weisz, D. A.; Gross, M. L.; Pakrasi, H. B., Reactive oxygen species leave a damage trail that reveals water channels in Photosystem II. *Science* **2017,** *3* (11), eaao3013.
326. Ugur, I.; Rutherford, A. W.; Kaila, V. R., Redox-coupled substrate water reorganization in the active site of photosystem II—the role of calcium in substrate water delivery. *Biochimica et Biophysica Acta (BBA)-Bioenergetics* **2016,** *1857* (6), 740-748.
327. Kim, C. J.; Debus, R. J., Evidence from FTIR difference spectroscopy that a substrate H_2O molecule for O_2 formation in photosystem II is provided by the Ca ion of the catalytic Mn_4CaO_5 cluster. *Biochemistry* **2017,** *56* (20), 2558-2570.
328. Ishikita, H.; Saenger, W.; Loll, B.; Biesiadka, J.; Knapp, E.-W., Energetics of a possible proton exit pathway for water oxidation in photosystem II. *Biochemistry* **2006,** *45* (7), 2063-2071.
329. Takemoto, H.; Sugiura, M.; Noguchi, T., Proton release process during the S_2-to-S_3 transition of photosynthetic water oxidation as revealed by the pH dependence of kinetics monitored by time-resolved infrared spectroscopy. *Biochemistry* **2019,** *58* (42), 4276-4283.
330. Saito, K.; Rutherford, A. W.; Ishikita, H. J. N. c., Energetics of proton release on the first oxidation step in the water-oxidizing enzyme. *Nature communications* **2015,** *6* (1), 1-10.
331. Okamoto, Y.; Shimada, Y.; Nagao, R.; Noguchi, T., Proton and Water Transfer Pathways in the $S_2 \rightarrow S_3$ Transition of the Water-Oxidizing Complex in Photosystem II: Time-Resolved Infrared Analysis of the Effects of D1-N298A Mutation and NO_3^- Substitution. *The Journal of Physical Chemistry B* **2021**.
332. Mäusle, S. M.; Abzaliyeva, A.; Greife, P.; Simon, P. S.; Perez, R.; Zilliges, Y.; Dau, H., Activation energies for two steps in the $S_2 \rightarrow S_3$ transition of photosynthetic water oxidation from time-resolved single-frequency infrared spectroscopy. *The Journal of Chemical Physics* **2020,** *153* (21), 215101.
333. Ghosh, I.; Khan, S.; Banerjee, G.; Dziarski, A.; Vinyard, D. J.; Debus, R. J.; Brudvig, G. W., Insights into proton-transfer pathways during water oxidation in photosystem II. *The Journal of Physical Chemistry B* **2019,** *123* (39), 8195-8202.
334. Gerencsér, L.; Dau, H., Water oxidation by photosystem II: $H_2O - D_2O$ exchange and the influence of pH support formation of an intermediate by removal of a proton before dioxygen creation. *Biochemistry* **2010,** *49* (47), 10098-10106.
335. Siegbahn, P. E., Mechanisms for proton release during water oxidation in the S_2 to S_3 and S_3 to S_4 transitions in photosystem II. *Phys Chem Chem Phys* **2012,** *14* (14), 4849-56.
336. Iwata, S.; Barber, J., Structure of photosystem II and molecular architecture of the oxygen-evolving centre. *Current Opinion in Structural Biology* **2004,** *14* (4), 447-453.
337. Yata, H.; Noguchi, T., Mechanism of Methanol Inhibition of Photosynthetic Water Oxidation As Studied by Fourier Transform Infrared Difference and Time-Resolved Infrared Spectroscopies. *Biochemistry* **2018,** *57* (32), 4803-4815.

338. Pal, R.; Negre, C. F. A.; Vogt, L.; Pokhrel, R.; Ertem, M. Z.; Brudvig, G. W.; Batista, V. S., S0-State Model of the Oxygen-Evolving Complex of Photosystem II. *Biochemistry* **2013,** *52* (44), 7703-7706.
339. Fransson, T.; Chatterjee, R.; Fuller, F. D.; Gul, S.; Weninger, C.; Sokaras, D.; Kroll, T.; Alonso-Mori, R.; Bergmann, U.; Kern, J., X-ray emission spectroscopy as an in situ diagnostic tool for X-ray crystallography of metalloproteins using an X-ray free-electron laser. *Biochemistry* **2018,** *57* (31), 4629-4637.
340. Beckmann, K.; Messinger, J.; Badger, M. R.; Wydrzynski, T.; Hillier, W., On-line mass spectrometry: membrane inlet sampling. *Photosynthesis Research* **2009,** *102* (2-3), 511-522.
341. Chovancova, E.; Pavelka, A.; Benes, P.; Strnad, O.; Brezovsky, J.; Kozlikova, B.; Gora, A.; Sustr, V.; Klvana, M.; Medek, P., CAVER 3.0: a tool for the analysis of transport pathways in dynamic protein structures. *PLoS Comput Biol* **2012,** *8* (10), e1002708.
342. Emma, P.; Akre, R.; Arthur, J.; Bionta, R.; Bostedt, C.; Bozek, J.; Brachmann, A.; Bucksbaum, P.; Coffee, R.; Decker, F. J.; Ding, Y.; Dowell, D.; Edstrom, S.; Fisher, A.; Frisch, J.; Gilevich, S.; Hastings, J.; Hays, G.; Hering, P.; Huang, Z.; Iverson, R.; Loos, H.; Messerschmidt, M.; Miahnahri, A.; Moeller, S.; Nuhn, H. D.; Pile, G.; Ratner, D.; Rzepiela, J.; Schultz, D.; Smith, T.; Stefan, P.; Tompkins, H.; Turner, J.; Welch, J.; White, W.; Wu, J.; Yocky, G.; Galayda, J., First lasing and operation of an Ångstrom-wavelength free-electron laser. *Nat. Photonics* **2010,** *4* (9), 641-647.
343. Sierra, R. G.; Batyuk, A.; Sun, Z. B.; Aquila, A.; Hunter, M. S.; Lane, T. J.; Liang, M. N.; Yoon, C. H.; Alonso-Mori, R.; Armenta, R.; Castagna, J. C.; Hollenbeck, M.; Osier, T. O.; Hayes, M.; Aldrich, J.; Curtis, R.; Koglin, J. E.; Rendahl, T.; Rodriguez, E.; Carbajo, S.; Guillet, S.; Paul, R.; Hart, P.; Nakahara, K.; Carini, G.; DeMirci, H.; Dao, E. H.; Hayes, B. M.; Rao, Y. S. P.; Chollet, M.; Feng, Y. P.; Fuller, F. D.; Kupitz, C.; Sato, T.; Seaberg, M. H.; Song, S.; van Driel, T. B.; Yavas, H.; Zhu, D. L.; Cohen, A. E.; Wakatsuki, S.; Boutet, S., The Macromolecular Femtosecond Crystallography Instrument at the Linac Coherent Light Source. *Journal of Synchrotron Radiation* **2019,** *26*, 346-357.
344. Adams, P. D.; Afonine, P. V.; Bunkoczi, G.; Chen, V. B.; Davis, I. W.; Echols, N.; Headd, J. J.; Hung, L. W.; Kapral, G. J.; Grosse-Kunstleve, R. W.; McCoy, A. J.; Moriarty, N. W.; Oeffner, R.; Read, R. J.; Richardson, D. C.; Richardson, J. S.; Terwilliger, T. C.; Zwart, P. H., PHENIX: a comprehensive Python-based system for macromolecular structure solution. *Acta Cryst. D* **2010,** *66* (Pt 2), 213-21.
345. Afonine, P. V.; Grosse-Kunstleve, R. W.; Echols, N.; Headd, J. J.; Moriarty, N. W.; Mustyakimov, M.; Terwilliger, T. C.; Urzhumtsev, A.; Zwart, P. H.; Adams, P. D., Towards automated crystallographic structure refinement with phenix.refine. *Acta Cryst. D* **2012,** *68*, 352-367.
346. Emsley, P.; Lohkamp, B.; Scott, W. G.; Cowtan, K., Features and development of Coot. *Acta Cryst. D* **2010,** *66* (Pt 4), 486-501.
347. Law, N. A.; Caudle, M. T.; Pecoraro, V. L., Manganese redox enzymes and model systems: Properties, structures, and reactivity. In *(Advances in Inorganic Chemistry*, 1999; Vol. 46, pp 305-440.
348. Wieghardt, K., The active-Sites in manganese-containing metalloproteins and inorganic model complexes. *Angew. Chem.-Int. Edit. Engl.* **1989,** *28* (9), 1153-1172.
349. Cinco, R. M.; Rompel, A.; Visser, H.; Aromi, G.; Christou, G.; Sauer, K.; Klein, M. P.; Yachandra, V. K., Comparison of the manganese cluster in oxygen-evolving photosystem II with distorted cubane manganese compounds through X-ray absorption spectroscopy. *Inorganic Chemistry* **1999,** *38* (26), 5988-5998.

350. Mukhopadhyay, S.; Mandal, S. K.; Bhaduri, S.; Armstrong, W. H., Manganese clusters with relevance to photosystem II. *Chemical Reviews* **2004,** *104* (9), 3981-4026.
351. Tsui, E. Y.; Kanady, J. S.; Agapie, T., Synthetic cluster models of biological and heterogeneous manganese catalysts for O_2 evolution. *Inorganic Chemistry* **2013,** *52* (24), 13833-13848.
352. Lang, P. T.; Holton, J. M.; Fraser, J. S.; Alber, T., Protein structural ensembles are revealed by redefining X-ray electron density noise. *Proc. Natl. Acad. Sci. U. S. A.* **2014,** *111* (1), 237-242.
353. Ten Eyck, L. F., Crystallographic fast Fourier transforms. *Acta Crystallographica Section A: Foundations of Crystallography* **1973,** *29* (2), 183-191.
354. Winn, M. D.; Ballard, C. C.; Cowtan, K. D.; Dodson, E. J.; Emsley, P.; Evans, P. R.; Keegan, R. M.; Krissinel, E. B.; Leslie, A. G.; McCoy, A., Overview of the CCP4 suite and current developments. *Acta Crystallographica Section D: Biological Crystallography* **2011,** *67* (4), 235-242.
355. Tanaka, A.; Fukushima, Y.; Kamiya, N., Two different structures of the oxygen-evolving complex in the same polypeptide frameworks of photosystem II. *J. Am. Chem. Soc.* **2017,** *139* (5), 1718-1721.
356. Broser, M.; Gabdulkhakov, A.; Kern, J.; Guskov, A.; Müh, F.; Saenger, W.; Zouni, A., Crystal structure of monomeric photosystem II from Thermosynechococcus elongatus at 3.6-Å resolution. *Journal of Biological Chemistry* **2010,** *285* (34), 26255-26262.
357. Schlodder, E.; Witt, H. T., Stoichiometry of Proton Release from the Catalytic Center in Photosynthetic Water Oxidation: REEXAMINATION BY A GLASS ELECTRODE STUDY AT pH 5.5–7.2. *Journal of Biological Chemistry* **1999,** *274* (43), 30387-30392.
358. Förster, V.; Junge, W., Stoichiometry and kinetics of proton release upon photosynthetic water oxidation. *Photochemistry and Photobiology* **1985,** *41* (2), 183-190.
359. Ho, F. M., Uncovering channels in photosystem II by computer modelling: current progress, future prospects, and lessons from analogous systems. *Photosynthesis research* **2008,** *98* (1-3), 503.
360. Sun, Z.; Liu, Q.; Qu, G.; Feng, Y.; Reetz, M., Utility of B-factors in protein science: interpreting rigidity, flexibility, and internal motion and engineering thermostability. *Chemical reviews* **2019,** *119* (3), 1626-1665.
361. Bayden, A. S.; Moustakas, D. T.; Joseph-McCarthy, D.; Lamb, M. L., Evaluating free energies of binding and conservation of crystallographic waters using SZMAP. *Journal of chemical information modeling* **2015,** *55* (8), 1552-1565.
362. Oksanen, E.; Chen, J. C.-H.; Fisher, S. Z., Neutron crystallography for the study of hydrogen bonds in macromolecules. *Molecules* **2017,** *22* (4), 596.

Acknowledgments

I want to express my sincere gratitude to many people who have given me their support, mentorship, and guidance throughout this adventure. First and foremost, I would like to sincerely thank my academic supervisor Prof. Dr. Athina Zouni, for her mentorship and invitation to the Humboldt University of Berlin. Her patience, enthusiastic supervision allows this research work to produce in the present form by engaging me in new ideas, giving me intellectual freedom in my work, engaging me in several international collaborations, and supporting my attendance at various beam times, meetings and conferences. She is not my an exceptional supervisor but also a wonderful human being. Furthermore, every result described in this thesis was accomplished with the help and support of several collaborators with who I am looking forward to working together in the future. I greatly appreciate Prof. Dr. Holger Dobbek for being my second academic supervisor and his great feedback and excellent guidance in several projects. I would also like to express my deepest gratitude to our collaborators at Berkeley lab, Dr. Junko Yano, Dr. Vittal Yachandra, and Dr. Jan Kern. I am thankful for the extraordinary experiences I gained during working together. It is an honor to learn from them. Additionally, I would like to thank my committee members Prof. Dr. Franz Bartl, Prof. Dr. Thomas Friedrich, Dr. Heiko Lokstein, and Dr. Benedikt Beckmann, for their interest in my work.

I would like to thank the following people for their various contributions to this body of work: - Chapter 2.1: Dr. Mohamed Ibrahim from the group Prof. Holger Dobbek, Dr. Ruchira Chatterjee from Yano/ Yachandra/ Kern group and Dr. Leighton Coates at Oak Ridge National Laboratory for their support during data collection at Oak Ridge National Laboratory. Dr. Frank Müh at Johannes Kepler University Linz for his valuable suggestions throughout this project. Dr. Martin Bommer from the group Prof. Holger Dobbek for his support at BESSY.

- Chapter 2.2: Dr. Maksym Golub and Dr. Jörg Pieper at the University of Tartu for data collection and data analysis. Dr. Mohamed Ibrahim from the group Prof. Holger Dobbek for his valuable inputs throughout this project.

- Chapter 2.3: Dr. Mohamed Ibrahim from the group Prof. Holger Dobbek for his guidance, mentorship, and encouragement. His inputs to this work are invaluable. Within Yano/ Yachandra/ Kern group: Dr. Asmit Bhowmick, Dr. Philipp Simon for their support during data analysis, Dr. Ruchira Chatterjee for her support during XFEL collecting data. She was always with me, leading the protein crystallization team at different XFEL

facilities. I appreciate her encouragement and the friendly environment she created. Dr. Louise Lassalle, Margaret Doyle, Isabel Bogacz, Dr. In-Sik Kim, Dr. Cindy Pham, Dr. Iris Young, Dr. Franklin Fuller, and Dr. Kyle Suetherlin for their support during the beam times. Prof. Dr. Johannes Messinger at Uppsala University and his team members Dr. Mun Hon Cheah, Dr. Petko Chernev, and Dr. Casper de Lichtenberg for their support in the beam times and in characterizing the sample activity. Prof Dr. Uwe Bergmann at the University of Wisconsin–Madison for his support during the beam times and many discussions. Dr. Nicholas Sauter and Dr. Aaron Brewster for their continuous support during XFEL data collection. Within the group of Prof. Zouni, Julia Gaetcke and Gesine Bartels for their technical support.

Moreover, I would like to thank my lab mates Dr. Miao Zhang and Ina Seuffert. Very special thanks to Jelena Boyka for helping me revise the translation of the abstract to German and for her support while teaching the practical courses. I acknowledge the generous financial support I received from the Human Frontiers Science Project (Award No. RGP0063/2013), Sonderforschungsbereich Sfb1078 (Humboldt Universität Berlin), and a Caroline von Humboldt Stipendium, Humboldt University Berlin.

Finally, I am grateful for the continuous support I receive from my family. None of this would be possible without their support. I owe my deepest gratitude to my husband, Mohamed, and my son Aser. I am thankful for their unconditional support and love.

Ehrenwörtliche Erklärung

Hiermit erkläre ich ausdrücklich, dass ich die Dissertation selbstständig und nur unter Verwendung der angegebenen Quellen und zulässigen Hilfsmittel geschrieben habe. Ich versichere außerdem, dass ich die beigefügte Dissertation nur in diesem und keinem anderen Promotionsverfahren eingereicht habe und, dass diesem Promotionsverfahren keine endgültig gescheiterten Promotionsverfahren vorausgegangen sind. Ich habe die Promotionsordnung der Lebenswissenschaftlichen Fakultät der Humboldt-Universität zu Berlin vom 5. März 2015 der das Promotionsverfahren zugrunde liegt, zur Kenntnis genommen. Außerdem erkläre ich, dass die Grundsätze der Humboldt-Universität zu Berlin zur Sicherung guter wissenschaftlicher Praxis eingehalten wurden.